Physics-based Machine Learning Approaches to Complex Systems and Climate Analysis

D I S S E R T A T I O N

zur Erlangung des akademischen Grades

d o c t o r r e r u m n a t u r a l i u m
(Dr. rer. nat.)
im Fach Physik
Spezialisierung: Theoretische Physik

eingereicht an der
Mathematisch-Naturwissenschaftlichen Fakultät
der Humboldt-Universität zu Berlin

von
Maximilian Gelbrecht, MSc.

Präsidentin der Humboldt-Universität zu Berlin:
Prof. Dr.-Ing. Dr. Sabine Kunst

Dekan der Mathematisch-Naturwissenschaftlichen Fakultät:
Prof. Dr. Elmar Kulke

Gutachter:

1. Prof. Dr. Dr. h.c. mult. Jürgen Kurths
2. Prof. Dr. M. Carmen Romano
3. Prof. Dr. Pedro Leite da Silva Dias

eingereicht am: 12.01.2021

Tag der mündlichen Prüfung: 27.05.2021

Abstract

Complex systems and especially those in climate science are often high-dimensional and provide large amounts of data. Systems such as the Earth's climate are comprised of many constituents that are interlinked through an intricate coupling structure. As such, these systems naturally have an inherent network structure. The emerging dynamics of the complex system is then usually nonlinear and often times sufficiently high-dimensional that methods from machine learning can excel. For the analysis of such systems it therefore seems natural to bring together methods and ideas from network theory, dynamical systems theory and machine learning. By combining different concepts from these fields three novel approaches for the study of complex systems are considered throughout this thesis.

In the first part, one particular climate system is investigated: the South American Monsoon system and its variability. For this purpose a novel complex network construction method is introduced that is able to identify the most important wind paths of the South American Monsoon system. In conjunction with analysing composites of precipitation and geopotential height, this enables the study of the variability of the monsoon system. Aside from the importance of cross-equatorial flows, this analysis points to the impact Rossby Wave trains have both on the precipitation and low-level circulation. This connection is then further strengthened by both a conceptual model and by showing that the precipitation is phase coherent to the Rossby Wave trains. As such, the first part of this thesis demonstrates how complex networks can be used to identify spatiotemporal variability patterns within large amounts of data, that are then further analysed with methods from nonlinear dynamics.

In the second part of the thesis, the properties of complex systems are investigated more conceptually. Many complex systems, those in climate science as well, exhibit an enormously complex landscape of possible asymptotic states. To investigate and track the asymptotic states, Monte Carlo Basin Bifurcation analysis, a novel numerical method is introduced. Situated between the classical analysis with macroscopic order parameters and a more thorough, detailed bifurcation analysis, Monte Carlo Basin Bifurcation analysis combines random sampling with clustering methods to identify and characterize the different asymptotic states or classes thereof and their basins of attraction. These capabilities are first demonstrated on three paradigmatic examples from different disciplines: the Dodds-Watts model of social and biological contagion, a second order Kuramoto network and a Stuart-Landau oscillator network, each exhibiting a complex multistable regime that is identified and tracked by Monte Carlo Basin Bifurcation analysis. Subsequently, two conceptual climate models are investigated with the method: a conceptual model for tipping cascades and a bistable climate toy model based on the Lorenz96 model.

After gaining knowledge of dynamical systems with Monte Carlo Basin Bifurcation analysis, a natural next step is to aim to forecast them. When doing so, it is not always straightforward how prior knowledge of the systems, especially in form of partially known governing equations, can be used with data-driven methods. One possibility to do is by using Neural Partial Differential Equations. In this case artificial neural networks, or any other universal function approximator for that matter, are directly integrated into the differential equation. The

resulting hybrid models can be trained e.g. with adjoint-based methods. Here, it is demonstrated how high-dimensional spatiotemporally chaotic systems can be modelled and predicted with such an approach. As paradigmatic examples the Complex Ginsburg-Landau equation, a reaction-diffusion equation, and the Kuramoto-Sivashinsky equation are investigated. With very short integration lengths and a novel trainable finite difference layer these system can be successfully predicted with forecast horizons exceeding the length of the training dataset by far, even when the data is subjected to observational noise.

Both, Monte Carlo Basin Bifurcation analysis and Neural Partial Differential Equations, offer the potential for further applications to more sophisticated climate models. They can also be thought of as a two-part approach to first identify the basins of a system and then use it in a hybrid setup for prediction.

Zusammenfassung

Komplexe Systeme und insbesondere solche in der Klimatologie sind oft hochdimensional und liefern große Datenmengen. Systeme wie das Erdsystem and sein Klima bestehen aus einer Vielzahl miteinander gekoppelter Subsysteme. Daher ergibt sich natürlich eine Form von Netzwerk. Die Gesamtdynamik, die aus diesen komplexen Interaktionen hervorgeht, ist üblicherweise nichtlinear und oft hochdimensional, so dass auch Methoden des maschinellen Lernens Anwendung finden können. Für die Analyse solcher Systeme erscheint es daher naheliegend, Methoden und Ideen aus der Netzwerktheorie, der Theorie dynamischer Systeme und des maschinellen Lernens zusammenzuführen. Durch die Kombination verschiedener Konzepte aus diesen Bereichen werden neuartige Ansätze für die Untersuchung komplexer Systeme in Betracht gezogen. Im Rahmen dieser Arbeit werden drei verschiedene Ansätze verfolgt.

Im ersten Teil wird ein bestimmtes Klimasystem untersucht: das südamerikanische Monsunsystem und seine Variabilität. Zu diesem Zweck wird eine neuartige Konstruktionsmethode für komplexe Netzwerke vorgestellt, die in der Lage ist, die wichtigsten Windpfade des südamerikanischen Monsunsystems zu identifizieren. In Verbindung mit der Analyse von Niederschlagsdaten und geopotentieller Höhe ermöglicht dies, die Variabilität des Monsunsystems zu untersuchen. Abgesehen von der Bedeutung der Windpfade die den Äquator kreuzen, weist diese Analyse auf einen starken Zusammenhang zwischen Rossby-Wellenzügen, dem Niederschlag und der oberflächennahen Zirkulation hin. Dieser Zusammenhang wird dann sowohl durch ein konzeptionelles Modell als auch durch den Nachweis, dass der Niederschlag phasenkohärent zum Rossby-Wellenzug ist, bewiesen. Somit zeigt der erste Teil dieser Arbeit, wie komplexe Netzwerke verwendet werden können, um räumlich-zeitliche Variabilitätsmuster innerhalb großer Datenmengen zu identifizieren, die dann mit Methoden der nichtlinearen Dynamik weiter analysiert werden.

Im zweiten Teil der Arbeit werden die Eigenschaften komplexer Systeme konzeptioneller untersucht. Viele komplexe Systeme, auch in der Klimawissenschaft, weisen eine enorme Vielfalt von möglichen asymptotischen Zuständen auf. Zur Untersuchung der asymptotischen Zustände wird die Monte Carlo Basin Bifurcation Analyse, eine neuartige numerische Methode, eingeführt. Zwischen der klassischen Analyse mit makroskopischen Ordnungsparametern und einer gründlicheren, detaillierteren Bifurkationsanalyse angesiedelt, kombiniert die Monte Carlo Basin Bifurcation Analyse Zufallsstichproben mit Clustering-Methoden, um die verschiedenen asymptotischen Zustände oder Klassen dieser und ihre Einzugsgebiete zu identifizieren und zu charakterisieren. Diese Fähigkeiten werden zunächst an drei paradigmatischen Beispielen aus verschiedenen Disziplinen demonstriert: dem Dodds-Watts-Modell, einem Kuramoto-Netzwerk zweiter Ordnung und einem Stuart-Landau-Oszillator-Netzwerk, die alle jeweils ein komplexes multistabiles Regime aufweisen, das durch die Monte Carlo Basin Bifurcation Analyse identifiziert wird. Anschließend werden zwei konzeptionelle Klimamodelle mit der Methode untersucht: ein konzeptionelles Modell für Kippkaskaden und ein bistabiles konzeptionelles Klimamodell auf der Grundlage des Lorenz96-Modells.

Nachdem mit der Monte Carlo Basin Bifurcation Analyse erste Erkenntnisse über dynamische Systeme gewonnen wurden, ist es ein natürlicher nächster

Schritt, deren Vorhersage anzustreben. Dabei ist es nicht immer klar, wie Vorwissen über die Systeme, insbesondere in Form ihrer Gleichungen, zusammen mit datengetriebenen Methoden genutzt werden kann. Eine Möglichkeit dazu besteht in der Verwendung von neuronalen partiellen Differentialgleichungen. Diese integrieren künstliche neuronale Netze oder andere universeller Funktionsapproximatoren direkt in die Differentialgleichung. Die daraus resultierenden hybriden Modelle können z.B. mit Hilfe adjungierten Methoden trainiert werden. In dieser Arbeit wird gezeigt, wie hochdimensionale räumlich-zeitlich chaotische Systeme mit einem solchen Ansatz modelliert und vorhergesagt werden können. Als paradigmatische Beispiele werden die komplexe Ginsburg-Landau-Gleichung, eine Reaktions-Diffusions-Gleichung und die Kuramoto-Sivashinsky-Gleichung gezeigt. Mit sehr kurzen Integrationslängen und einem neuartigen trainierbaren Finite-Differenzen-Layer können diese Systeme erfolgreich mit Vorhersagehorizonten vorhergesagt werden, die die Länge des Trainingsdatensatzes bei weitem übersteigen, selbst wenn die Daten Messrauschen ausgesetzt sind.

Sowohl die Monte Carlo Basin Bifurcation Analyse als auch die neuronalen partiellen Differentialgleichungen bieten das Potenzial für weitere Anwendungen in anspruchsvolleren Klimamodellen. Man kann sie sich auch als einen zweiteiligen Ansatz vorstellen, um zunächst die Einzugsbereiche der Attraktoren eines Systems zu identifizieren und dieses Wissen dann in einem hybriden Modell zur Vorhersage zu verwenden.

Acknowledgements

First and foremost, I like to deeply thank Professor Jürgen Kurths. Thank you for giving the me the opportunity to work and research at the Potsdam Institute for Climate Impact Research and thank you for the many good pieces of advice and for setting a trustful and free atmosphere in the research group.

Likewise, I want to especially highlight the role of Niklas and thank him for years of stimulating discussions, advice, good ideas, hints and awesome collaborations.

Also I'd like to thank Frank, Valerio and Nico who I collaborated with on projects presented within this thesis for their ideas and advice.

The Research Domain IV at PIK was a wonderful place to do my PhD. I wholeheartedly enjoyed the working atmosphere, the many friendly and helpful colleagues: Fredi, Jacqueline, Forough, Jasper, Nikoo, Hauke, Bedharta, Norbert, Paul, Frank, Marc, just to name a few.

Through my graduate school I could also enjoy a research stay in Brazil and I like to thank everybody at the IAG in São Paulo, especially Prof. Dias, that made my research stay there an inspiring experience and made me feel very welcome.

Thank you Karo, Chris and Hauke for proof-reading.

Thank you to all my friends and my family for being there for me and with me in the bad and good times of this period of my life. I wouldn't have made it without you.

I am deeply thankful for the financial and scientific independence I could enjoy through the IRTG project. This work was developed within the scope of the IRTG 1740/TRP 2015/50122-0, funded by the Deutsche Forschungsgemeinschaft (DFG) and Fundação de Amparo à Pesquisa do Estado de São Paulo (FAPESP). I also acknowledge the German Federal Ministry of Education and Research and the Land Brandenburg for supporting this project by providing resources on the high performance computer system at the Potsdam Institute for Climate Impact Research.

Contents

List of Figures

1. Introduction

Nature, the technology that we use, the world around us that we perceive is made up of thousands of systems that in turn are constituted by many components. The behaviour of such systems is often more than just that of its parts. Intricate interactions and coupling lead to complex behaviour. And while we can predict solar eclipses thousands of years in advance, we cannot reliably predict complex systems such as the weather just a single month in advance [149].

The Earth and its climate is without a doubt a massively complex system. A complex system which is undergoing changes in the last century. Long-term irreversible changes in the Earth's climate, through its tipping elements, are being dangerously close now and could even amplify each other [111]. Even when the anthropogenic climate change is limited to well below 2° C as agreed upon in the Paris Agreement, it still has severe consequences to the life of many millions of humans with the potential of catastrophic droughts, floods, rising sea level and scarce food resources in heavily affected regions [205]. The urgency of the climate crisis makes it even more important to understand the dynamics of climate systems and possibly predict their future.

In the present time, the Earth's climate is also a complex system that is constantly observed and measured. Thousands of satellites, aircraft, balloons, stationary measurement stations and other sources provide a constant flow of observational data [174, e.g.]. Earth system data checks of all four of the 'four Vs' of 'big data': volume, velocity, variety and veracity [171]. It seems therefore natural that we need tools and methods that are able to deal with 'big data'. These can be methods rooted firmly in physics and mathematics from network and dynamical systems theory, but also machine learning methods such as artificial neural networks. The Earth's climate is a prime example of a complex system. It is composed of many nonlinearly interacting components and its dynamics at a macroscopic scale are not easily deducible from the dynamics of its constituents. The dynamics of the Earth system, the short scales that we refer to as weather and the long-term averages that we refer to as climate, arise from the complex interplay of its components. The coupling structure of these components naturally forms a network. Hence, complex networks, the study of these networks, their properties such as their topology is integral to understanding the coupling structure. Whereas both, the individual interactions, and the emergent dynamics of the system as a whole, is usually nonlinear. This makes fundamental knowledge of nonlinear dynamics a prerequisite to investigate them. One example of such nonlinear behaviour are tipping elements, elements of the Earth system that pose the threat of large-scale, abrupt climate changes that are from the standpoint of nonlinear dynamics usually bifurcations of complex systems, often those exhibiting hysteresis [113, e.g.]. Finally, when investigating the Earth's climate from a data-driven perspective, it is

natural to make use of the recent advances in machine learning research, to be able to deal with the large amounts of data that such high-dimensional systems usually provide.

This thesis will therefore address the analysis of complex systems, focusing on those in climate dynamics, in three different parts, each focusing on another aspect of the complex systems in question:

I. The application of principles from network theory and nonlinear dynamics to analyse the spatiotemporal variability of complex systems such as a climate system,

II. The discovery and quantification of the basins of attraction of complex systems,

III. Forecasts of complex system that we only have incomplete knowledge of.

In the first part of this thesis we will use principles from network theory. Climate is a deeply complex system with an intricate coupling structures. While it is fairly obvious that the climate at one location is usually very similar to locations close by, there are long-range couplings, teleconnections, and large-scale climate phenomena such as the El Niño-Southern Oscillation (ENSO) or Madden-Julian Oscillation (MJO) [180, 251, e.g.]. With network approaches we try to encode these couplings structures into a complex network, visualizing and analysing their topology [225, e.g]. Network approaches were successfully used both in uncovering those teleconnection structures [30] and predicting phenomena such as ENSO [142]. Complex networks thus provides us with the appropriate tools for the analysis of climate systems and their variability. We use them in this thesis for one particular climate system, the South American Monsoon System.

Aside from identifying variability patterns in high-dimensional data, we also want to focus on the predictability of high-dimensional systems. In Edward Lorenz' terminology part II and III address predictability of the first and second kind [121]. Here, the first kind refers to predicting the evolution of the system. Due to sensitivity of chaotic complex systems to initial conditions, there is an intrinsic limit to this predictability. The reason why we cannot just perfectly predict the weather a month in advance. The second kind does refer to the uncertainty associated with which asymptotic state of the system is reached and its properties. Most sufficiently complex system exhibit a form of multistability for which multiple several asymptotic states coexist. Understanding their properties is integral also for directly predicting the evolution of the systems.

When predicting systems, we could rely on purely data-driven methods such as artificial neural networks (ANNs). ANNs excel in tasks such as computer vision [236, e.g.]. Yet, where it is difficult to attempt to formulate our knowledge about how to recognise objects in images into mathematical language, in physics and climate research we have centuries of research in our disposal to make use of. Thus, combing data-driven methods with the knowledge that we have of a physical system seems to be a promising idea, especially in Earth system science [171]. In part III we will use Neural Ordinary Differential Equations to do so.

In the sense of machine learning methods, we show both unsupervised and supervised learning methods. Supervised methods learn an input-output relation from examples of both inputs and outputs. We will use these in part III when predicting high-dimensional complex system. Otherwise, both, the network approaches and the clustering methods in part I and II, are unsupervised methods used to identify structures and (variability) patterns without learning these from example.

In the following, first fundamentals of complex systems theory, network theory, dynamical systems and machine learning are introduced that we will use later throughout this thesis. Then the three parts are presented one after the after. First, complex networks and phase synchronization techniques are used to analyse the South American Monsoon System. Then, Monte Carlo Basin Bifurcation Analysis, a novel numerical machine-learning method for identifying and tracking the attractors of high-dimensional systems is introduced. It is tested on three paradigmatic examples before applying it to two conceptual climate models. Lastly, we will show how Neural Partial Differential Equations can be used to forecast only partially known partial differential equations as we will demonstrate on two paradigmatic examples and one conceptual climate model. The thesis closes with a short overarching discussion and outlook.

2. Theoretical Foundations

2.1. Fundamentals of Network Theory

In the first part of the thesis we will use complex networks to uncover spatial patterns of climate data and their variability. A short introduction into fundamentals of network theory that will be used later will be given in the following. For a thorough introduction into the field, the reader is referred to textbooks such as Newman [148].

A network $\mathcal{G}$ is a structure that consists of a set of nodes $\mathcal{N}$ and links $\mathcal{E}$ that connect these nodes. Network theory and its application are an interdisciplinary field, as such different naming conventions for many concepts exist. What we we will call a network here, can also be called a *graph*. Nodes can also be referred to as vertices and links as edges. The information encoded by the links and nodes can also be given in form of the adjacency matrix $\mathbf{A}$, so that

$$A_{ij} = \begin{cases} 1 & \text{if there is a link from } i \text{ to } j \\ 0 & \text{otherwise.} \end{cases} \tag{2.1}$$

Networks can be directed. In this case a link from node i to j does not imply a connection from j to i and the adjacency matrix $\mathbf{A}$ is asymmetric whereas it is symmetric for undirected networks. Usually, self-loops so links from a node to itself are excluded. An undirected network without self-loops is also called a simple graph. Additionally, weights can be associated both with the nodes and the edges. A network with weighted edges is called a weighted network where the node weights usually represent the strength of a connection. In this thesis, our analysis will only use unweighted, directed networks. Therefore we will also not go into further details of the intricacies of weighted networks.

2.1.1. Centrality Measures

The topology of the networks that we are about to construct is evaluated with centrality measures. Centrality measures usually assign a number to each node which tells us how important that node is. There are numerous ways of defining what important means for network nodes and in the following we will introduce only those measures that we we will use later.

Arguably the simplest is the *degree centrality*

$$k_i = \sum_{j=1}^{N} A_{ij} \tag{2.2}$$

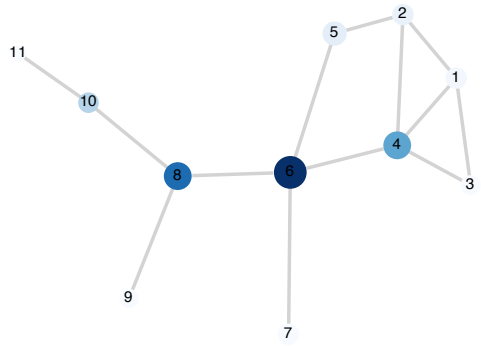

FIGURE 2.1.: Example network made up of eleven nodes. The diameter of each node is proportional to the betweenness of the node and the darker the shade of blue the higher the closeness of the node is. In this example Node 6 has the highest betweenness as almost all shortest paths go through it. Node 4 has the same degree as Node 6 but a considerably smaller betweenness and closeness.

which counts the amount of links connected to each of the N nodes. For directed networks we have to distinguish between the out-degree counting the outgoing links

$$k_i^{(\text{out})} = \sum_{j=1}^{N} A_{ji} \tag{2.3}$$

and the in-degree

$$k_i^{(\text{in})} = \sum_{j=1}^{N} A_{ij}. \tag{2.4}$$

The networks that we are going to propose emphasize paths through the network. A centrality measure suitable to expose nodes which are crucial for the overall path structure is the *betweenness centrality*. It relies on the concept of shortest (or geodesic) paths. The geodesic distance d_{ij} is the length of the geodesic paths (i.e. the smallest number of edges) between two nodes i and j of the network. The betweenness centrality

$$B_i = \sum_{jk} \frac{n_{jk}^{(i)}}{g_{jk}} , \tag{2.5}$$

quantifies the relative number of geodesic paths through a given node i: $n_{jk}^{(i)}$ is the number of geodesic paths between nodes j and k running through i and g_{jk} is total number of geodesic paths between nodes j and k (note that more than one such shortest path may exist) [148]. Another centrality measures relying on geodesic paths

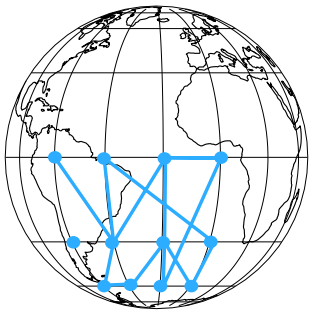

FIGURE 2.2.: Example of a spatially embedded network with nodes and links in blue. Each node represents a certain area. The size of that area may be unequal depending on the grid. If not the complete globe is considered as here, boundary effects will most likely occur during construction.

is the *closeness centrality*

$$C_i = \frac{1}{n} \sum_{j=1} d_{ij} \tag{2.6}$$

which is the mean distance of the geodesic paths from one node to all others. Fig. 2.1 shows an example network with these centrality measures.

2.1.2. Spatially Embedded Networks

We want to analyse climate data with complex networks, said climate data is usually provided on a spatiotemporal grid. When we construct networks from this data, we associate each node with an area, typically one grid point of the dataset and its surrounding area as is shown exemplary in Fig. 2.2.

For a spatially embedded network, the degree centrality can be adjusted to the area each node represents. These are the out- and in-area weighted connectivity (OAWC/IAWC) [225] which are defined as

$$\mathrm{IAWC}_i = \frac{\sum_{j=1}^{N} A_{ij} \cos \lambda_j}{\sum_{j=1}^{N} \cos \lambda_j} \tag{2.7}$$

$$\mathrm{OAWC}_i = \frac{\sum_{j=1}^{N} A_{ji} \cos \lambda_j}{\sum_{j=1}^{N} \cos \lambda_j}. \tag{2.8}$$

Here λ_i is the latitude of the location of node i. The difference between out- and in-area weighted connectivity

$$D_i = \mathrm{OAWC}_i - \mathrm{IAWC}_i \tag{2.9}$$

enables us to uncover possible directional asymmetries in the network, such as sinks and sources. The concept of centrality measures incorporating the area a node represents can be expanded to other centrality measures as well with node splitting invariant measures [85].

Spatially embedded networks or more specifically their centrality measures exhibit boundary effects by the choice of the map section [172]. While there are techniques

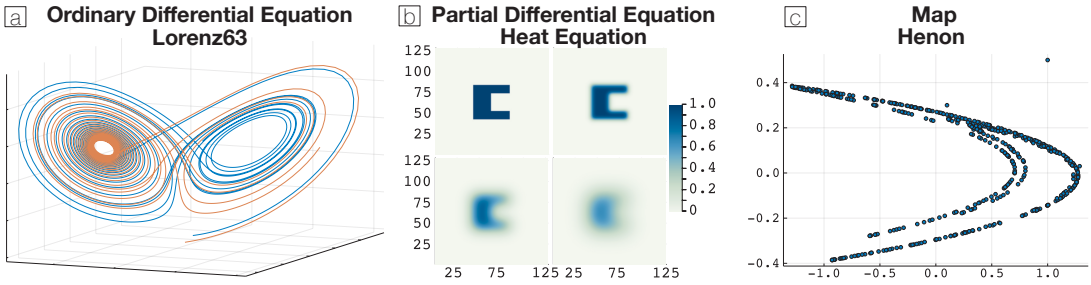

FIGURE 2.3.: Examples of dynamical systems: (a) Two trajectories of a the Lorenz63 system, a ordinary differential equation. Even though the two trajectories start from very close initial conditions, the trajectories quickly move away from each other, showcasing the chaotic behaviour of the system. (b) Four time steps of a solution of the heat equation, a partial differential equation with the initial conditions set in the first, upper left image. (c) Scatter plot of 500 iterations of the Hénon-Map, starting from $(1, 0.5)$.

for networks that are based on pairwise similarity measures to mitigate those at least partially, for the network that we will study this is not so easily possible. In our case we will mitigate boundary effects of the networks that we construct simply by choosing a larger map section. Unfortunately, path-based network measures are affected by spatial embedding in a more complex fashion. While we can thus not mitigate these effects completely, we minimize them by choosing larger map sections as well.

2.2. Fundamentals of Dynamical Systems Theory

A dynamical system is a deterministic mathematical prescription for evolving the state of a system in time [157]. Throughout this thesis we will investigate different types of dynamical systems, which we will briefly introduce here. We will also introduce some concepts and definitions from dynamical systems theory that are used later. For a more detailed description of the concepts introduced in this section, the reader is referred to standard textbooks such as Ott [157], Nicolis and Nicolis [149] and Strogatz [218].

2.2.1. Ordinary Differential Equations

An ordinary differential equation (ODE) is a dynamical systems that evolves the state continuously in time and may be defined in vector form as

$$\frac{d\mathbf{x}}{dt} = f(\mathbf{x}; \Theta). \tag{2.10}$$

Here, $\mathbf{x} \in \mathbb{R}^n$, $f : \mathbb{R}^n \to \mathbb{R}^n$ and Θ are fixed parameters of the function f. Any potential explicit time dependency in the ODE can be eliminated by regarding it as an additional dimension, and hence transforming it into the autonomous form, Eq. 2.10.

As a short-hand we will also write $\dot{\mathbf{x}} = f(\mathbf{x}; \Theta)$. Any solution that follows the equation is called a trajectory $\mathbf{x}(t)$, solving or integrating it from initial conditions $\mathbf{x}_0 = \mathbf{x}(0)$. Fig. 2.3a shows two trajectories of the famous Lorenz63 model that we will introduce later in more detail. While many ODEs can be solved analytically, this is generally not always possible, and we will be mostly interested in such cases where only numerical solutions of the dynamical system are possible. Differential equation solvers rely on numerically estimating the derivative with finite differences and then solving the ODE iteratively. E.g. a first-order finite difference derivative of an arbitrary function $g(x)$ is

$$g'(x) = \frac{g(x + \Delta t) - g(x)}{\Delta t} \tag{2.11}$$

resulting in the Euler method to solve Eq. 2.10

$$\mathbf{x}_{n+1} = \Delta t \cdot f(\mathbf{x}; \Theta) + \mathbf{x}_n \tag{2.12}$$

where time is now discritized in units of Δt. In practice, especially as we deal with nonlinear systems, more sophisticated ODE solvers are used that incorporate higher-order estimates of the derivative and an adaptive time step size. As long as not stated otherwise, we will use the Tsitouras5 solver throughout this thesis [222].

2.2.2. Partial Differential Equations

Partial differential equations (PDEs) are continuous dynamical systems comprised of partial derivatives of different variables, typically one or more spatial variables and time. One example is the heat equation, here in two spatial dimensions $\mathbf{x} = (x, y)$:

$$\frac{\partial}{\partial t} u(\mathbf{x}, t) = \left(\frac{\partial^2}{\partial x^2} + \frac{\partial^2}{\partial y^2} \right) u(\mathbf{x}, t) \tag{2.13}$$

where $u(\mathbf{x}, t)$ is a scalar, spatiotemporal field, e.g. temperature for the heat equation. In short hand we might also write the equation as $\partial_t u = (\partial_{xx} + \partial_{yy})u$. Fig. 2.3b shows four snapshots of the evolution of a solution of the heat equation. PDEs are typically defined on a spatial domain of a certain size and boundary conditions define how the field u is behaving at its boundaries. We may define fixed values of the field itself at its boundaries (Dirichlet boundary conditions) or its derivative (Neumann boundary conditions). Later, we will use periodic boundary conditions, so that if, e.g., the PDE is defined on a one-dimensional interval $x \in [0; L]$, the periodic boundary conditions are $u(0, t) = u(L, t)$. Periodic boundary conditions are common e.g. in molecular dynamics when a very large system is simulated, the PDE then is regarded as modelling one unit cell of a (possibly infinitely) large system [62, e.g]. Throughout this thesis we will rely on solving PDEs numerically. In order to do to so the PDE is transformed into a high-dimensional ODE by discretizing all variables but the time. One way of doing that are finite difference methods. The spatial variables are discretized into a

grid of points with an equal spacing $u(\mathbf{x},t) \to (u_1(t), u_2(t), ...u_N(t))$. The differential operators like ∂_x are then converted into matrices $\mathbf{D}_x$ so that the matrix product $\mathbf{D}_x(u_1(t), u_2(t), ...u_N(t)) = (u_1'(t), u_2'(t), ...u_N'(t))$ equals the finite difference derivative of each component of the now discretized field u. The finite differences matrices also have to account for the boundary conditions of the PDE, e.g. a second-order finite difference matrix of the first derivative with periodic boundary conditions reads

$$\begin{aligned}\mathbf{D}_x \begin{pmatrix} u_1(t) \\ u_2(t) \\ \vdots \\ \vdots \\ u_N(t) \end{pmatrix} &= \frac{1}{2\Delta x} \begin{pmatrix} 0 & 1 & 0 & \cdots & -1 \\ -1 & 0 & 1 & \cdots & 0 \\ 0 & -1 & 0 & \cdots & 0 \\ \vdots & \vdots & \ddots & \ddots & \vdots \\ 1 & 0 & 0 & \cdots & 0 \end{pmatrix} \begin{pmatrix} u_1(t) \\ u_2(t) \\ \vdots \\ \vdots \\ u_N(t) \end{pmatrix} \\ &= \frac{1}{2\Delta x} \begin{pmatrix} u_2(t) - u_N(t) \\ u_3(t) - u_1(t) \\ \vdots \\ \vdots \\ u_1(t) - u_{N-1}(t) \end{pmatrix} = \begin{pmatrix} u_1'(t) \\ u_2'(t) \\ \vdots \\ \vdots \\ u_N'(t) \end{pmatrix}. \end{aligned} \tag{2.14}$$

Finite difference matrices are sparse, banded matrices, hence multiplying them with a vector can be done very efficiently by most modern programming languages. Aside from finite difference methods, it is also possible to use spectral and pseudo-spectral methods. These will however not be used here.

2.2.3. Maps

The third and final kind of dynamical systems that we are investigating are maps. Maps are dynamical systems of the form

$$\mathbf{x}_{n+1} = f(\mathbf{x}_n; \Theta) \tag{2.15}$$

in which time is discretized with the index n and $n+1$ denoting the time step. Any possible further dependencies on prior time steps can be eliminated with suitable transformations. Compared to ODEs and PDEs, trajectories can be trivially generated by following the instruction given by the governing equation starting from initial condition $\mathbf{x}_0$. Fig. 2.3c shows a long trajectory of the Hénon-Map

$$\begin{aligned} x_{n+1} &= 1 - ax_n + y_n \\ y_{n+1} &= bx_n \end{aligned} \tag{2.16}$$

with $a = 1.4$ and $b = 0.3$.

2.2.4. Attractors and Basins

For all these kinds of dynamical systems, the *phase space* is the space spanned by all variables themselves [149]. Let a part of the phase space be $\Delta\Gamma_0$. We then call $\Delta\Gamma_t$ the part of the phase space of all initial conditions inside of $\Delta\Gamma_0$ evolved in time by t. A dynamical system is then called conservative if the volume $|\Delta\Gamma_0| = |\Delta\Gamma_t|$ stays constant for all t [149]. Examples of conservative systems are e.g. harmonic oscillators without damping. *Dissipative* systems are non-conservative systems those dynamics lead to an eventual contraction of the volume $|\Delta\Gamma_t|$ [149]. Dissipative systems are typically characterized by the presence of attracting sets, called *attractors* which are bounded subsets of the phase space to which a set of initial condition with non-zero volume evolves to [157]. The region of the phase space which evolves into an attractors is called its *basin of attraction*, often short *basin*. E.g. for a damped harmonic oscillator $\ddot{x} + \gamma\dot{x} + kx = 0$, all trajectories eventually evolve into the origin due to the damping. It is the only attractor of the system and its basin of attraction is the complete phase space. In this case the attractor is a single point, it is zero-dimensional.

We will call a system that exhibits multiple competing attractors *multistable*. Many complex systems are multistable and exploring these attractors and the size of their basins of attraction is key to understanding the dynamics of the system as, in general, each attractor will exhibit different properties. In Sec. 4.1 we will introduce a method tailor-made to analyse such systems and their basins. In particular we will concentrate on tracking how the basin size changes when parameters of the systems are changed.

2.2.5. Chaos

When the dimension of an attractor is non-integer, i.e. fractal, it is a called a *strange attractor*. The Lorenz63 system and the Hénon-Map shown in Fig. 2.3a and c are two famous examples of such strange attractors. Strange attractors are often, but not necessarily always, a sign of chaotic systems [80]. Chaotic systems are systems which are very sensitive to small deviations of their initial conditions. Fig. 2.3a shows two trajectories of the Lorenz63 system

$$\begin{aligned} \dot{x} &= \sigma(y - x) \\ \dot{y} &= x(\rho - z) - y \\ \dot{z} &= xy - \beta z \end{aligned} \tag{2.17}$$

which was derived as a simplified model for Rayleigh-Benard convection [119]. While ultimately the model fails in accurately modelling convection experiments, it was the birth of the modern research on deterministic chaos [145]. Even the smallest deviations grow exponentially over time. As visible in Fig. 2.3a two trajectories of the Lorenz63 system that start very close to each other quickly diverge and are often on different sites of this strange attractor. In experiments, we will never have exact knowledge of the inital conditions. Even in numerical simulations, rounding errors may eventually lead to two trajectories starting with the same initial conditions to diverge. This is

why chaotic systems are notoriously difficult to forecast. In Chapter 5 we will refer to this and introduce forecasting methods geared towards high-dimensional, chaotic systems.

One way how to quantify if and how chaotic a system is, are the *Lyapunov exponents*. They measure the sensitivity to small perturbations $\delta\mathbf{x}$ relative to a reference trajectory: weather or not these perturbations increase or decrease when the system is evolved in time. Let the initial perturbation be $\delta\mathbf{x}(t_0)$ and $\delta\mathbf{x}(t)$ its evolution in time. In the case for n-dimensional continuous system the Lyapunov exponent may be defined as

$$\lambda = \limsup_{t\to\infty} \frac{1}{t} \ln \frac{|\delta\mathbf{x}(t)|}{|\delta\mathbf{x}(t_0)|} \tag{2.18}$$

[9]. Independent of the reference point, but dependent of the direction of $\delta\mathbf{x}(t_0)$ there are multiple different values for λ. If there is an attractor and the largest, the maximum Lyapunov exponent is positive, the system is chaotic. Computing the maximum Lyapunov exponent λ_{max} will thus be used to check if an attractor of a system we are investigating is indeed chaotic. For this purpose the algorithm of Benettin et al. [18] is applied[1]. The maximum Lyapunov exponent also give us a natural time scale for the system that is independent from the integration time steps. As *Lyapunov time* we refer to the time scaled with λ_{max}, so that $1\lambda_{max}t$ is the time in which a small perturbation grows by a factor of e.

2.2.6. Bifurcations

The qualitative behaviour of dynamical systems, the existence or non-existence of attractors, stable and unstable fixed points, will, in general, depend on the parameters of the systems. Bifurcation analysis explores these changes in qualitative behaviour, often by varying one *control parameter*. Bifurcations are often investigated in their normal forms. This is an algebraically simple and minimal form that exhibits the type of bifurcation. Other systems can usually be approximated by such normal forms, e.g. by using Taylor expansion around the critical points and neglecting higher order terms. In the following we will briefly introduce some types of bifurcation that will appear in systems we investigate throughout this thesis, mostly following Strogatz [218].

Here, we are mostly interested in fixed points x_* for which the dynamical system $\dot{x} = f(x)$ is in a steady state $f(x_*) = 0$. In the one-dimensional case their linear stability can be assessed by inspecting the sign of the derivative $f'(x_*)$. A negative sign means perturbations δx to the fixed point cannot grow, the fixed point is an attractor and stable. Positive sign mean perturbations can grow and the fixed point is, thus, unstable.

For the *saddle-node bifurcation* with the normal form

$$\dot{x} = f(x) = x^2 + \theta \tag{2.19}$$

[1] Implementation from DynamicalSystems.jl used [53]

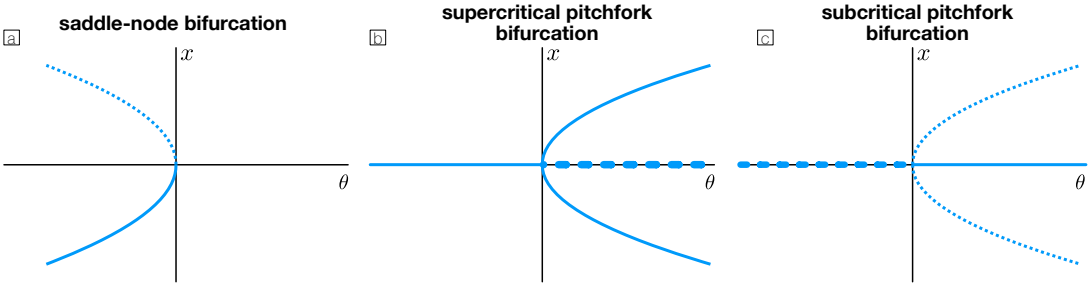

FIGURE 2.4.: Bifurcation types **(a)** saddle-node bifurcation, **(b)** supercritical pitchfork bifurcation, **(c)** subcritical pitchfork bifurcation. Solid lines indicate stable states and dashed lines unstable states.

it is obvious that the system changes its behaviour at $\theta = 0$. For $\theta > 0$, $f(x)$ has no roots, and therefore the system has no fixed points. At $\theta = 0$ there is one fixed point $x_* = 0$ and for $\theta < 0$ two fixed points $x_* = \pm\sqrt{-\theta}$. The fixed point at $x_* = -\sqrt{-\theta}$ is stable as $f'(x) < 0$ and unstable at $x_* = +\sqrt{-\theta}$ as $f'(x) > 0$. This knowledge can be expressed in a *bifurcation diagram*. These diagrams show the control parameter on the x-axis and the value of the fixed point on the y-axis. Stable fixed points are shown in solid lines and unstable fixed points in dashed lines. Fig. 2.4 a summarizes the behaviour of a saddle-node bifurcation: two fixed points, one stable, one unstable exist for $\theta < 0$ and no fixed point exists for $\theta > 0$.

The *pitchfork bifurcation* has the normal form

$$\dot{x} = \theta x \pm x^3. \tag{2.20}$$

The cubic function has either three roots for $\theta > 0$ or only one root at the origin for $\theta < 0$. For $\theta > 0$, the fixed points are at 0 and $\pm\sqrt{\theta}$. Their stability depends on the sign in Eq. 2.20. With a minus sign, the bifurcation is called a *supercritical pitchfork bifurcation* and as shown in Fig. 2.4 b the system changes its behaviour from exhibiting one stable fixed point at the origin to two stable fixed point at $x_* = \pm\sqrt{\theta}$ and one unstable fixed point at the origin at the bifurcation point $\theta = 0$. With a plus sign in Eq. 2.20 the stability of these fixed points is reversed (see Fig. 2.4 c) and the bifurcation is called *subcritical pitchfork bifurcation*.

Adding a constant h to Eq. 2.20

$$\dot{x} = h + \theta x - x^3. \tag{2.21}$$

results in a system that exhibits bifurcations based on changes of both parameters, it is the codimension-2 *cusp bifurcation*. For $h = 0$, we have the aforementioned supercritical pitchfork bifurcation. For $\theta > 0$ and $h \neq 0$, we have a more complex situation. Fig. 2.5a illustrates that for strongly negative or positive h there is only one fixed point, but there are values for h where three fixed points exist. Hence in this scenario, the system has two bifurcation points that occur when the local extremes

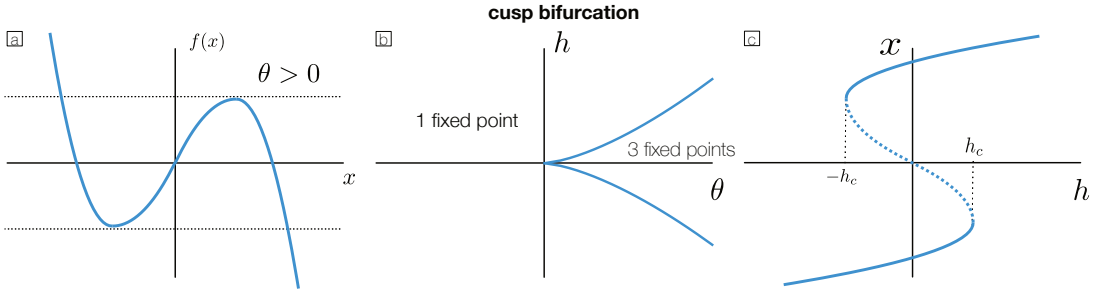

FIGURE 2.5.: (a) The normal form of the cusp bifurcation for $\theta > 0$. When h is strongly negative (positive), the function is shifted downwards (upwards) and it only has one intersection with the x-axis, i.e. a single root, whereas for intermediate values it has three roots. (b) Stability diagram of Eq. 2.21: with parameters h, θ inside the area of the two curves the systems exhibits three fixed points and outside of this area only one fixed point. (c) Bifurcation diagram for a fixed value $\theta > 0$. The critical values h_c are highlighted.

of the cubic function align with the y-axis. These points can be easily found: the extremes of $f(x) = h + \theta x - x^3$ are at $x_m = \pm\sqrt{\theta/3}$, the bifurcation points follow for $f(x_m) = 0$ with $h_c = \pm\frac{2\theta}{3}\sqrt{\frac{\theta}{3}}$. Fig. 2.5b) shows in a *stability diagram* of the system, the part of the parameter space where three fixed points exist. This area is of particular interest for us. Fig. 2.5 shows a bifurcation diagram of the system for a fixed $\theta > 0$. One can regard this as two saddle-node bifurcations. The system is multistable and the special property is that a *cusp catastrophe* can occur: when the system is in the upper state and the parameter h is decreased a sudden jump to the lower state occurs as there is only one stable fixed point of the system for $h < -\frac{2\theta}{3}\sqrt{\frac{\theta}{3}}$. To get the system back into its upper state the parameter has to be increased beyond $h > -\frac{2\theta}{3}\sqrt{\frac{\theta}{3}}$ again. The system is said to exhibit hysteresis. We will use such cusp normal forms in Sec. 4.2.1 to model tipping points in the Earth's climate system. It is a prototypical system for the multistability of many systems that we will investigate throughout this thesis.

Another type of bifurcation that we will encounter are *Hopf bifurcations*. They require the phase space to be at least two-dimensional. One way to express their normal form is using complex numbers $z \in \mathbb{C}$ or the complex plane with

$$\dot{z} = z(\theta + i) + bz|z|^2. \tag{2.22}$$

Here, θ is the control parameter and b is an additional parameter. When a Hopf bifurcation occurs a stable fixed point looses its stability and instead the system exhibits a stable limit cycle. In the two-dimensional case this happens when the eigenvalues of the Jacobian of $f(x)$ are complex conjugated pairs. The bifurcation point is the point at which the eigenvalues are purely imaginary. Thus, the system changes at $\theta = 0$ from a stable spiral to an unstable spiral and a limit cycle (see Fig 2.6).

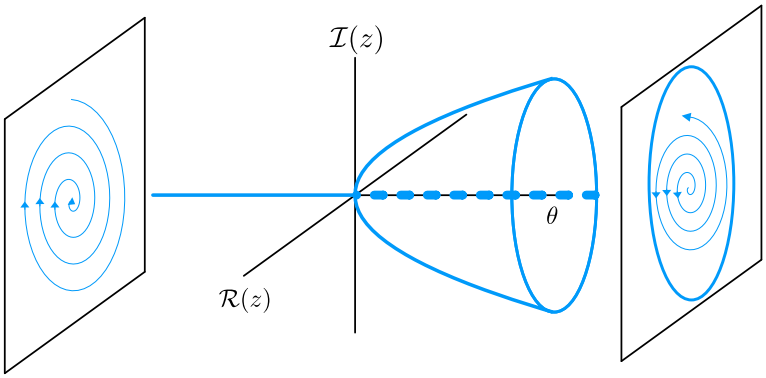

FIGURE 2.6.: Bifurcation diagram of a Hopf bifurcation. To the left the unstable spiral is sketched which is the only fixed point of the system for $\theta < 0$, to the right the unstable spiral and the stable limit cycle are sketched for $\theta > 0$.

In Sec. 4.1 we will introduce a method that takes a new approach on bifurcation analysis focusing on tracking the size of the basin of attraction of the attractors of a system.

2.2.7. Synchronization

When investigating oscillatory systems as we will do later in thesis, synchronization is a phenomenon that we will encounter. Synchronization is a universal phenomenon describing the adjustment of rhythms of oscillating objects due to their weak interaction [163]. Historically this effect was first described scientifically by Christaan Huygens who observed that two pendulum clocks (that he invented before) suspended from the same wooden beam align its movements so that their oscillations coincide aside from their directions being opposite. Synchronization can be found in many areas of science, synchronization of neurons is for example one of the key mechanism for the function of the human brain [68, 197]. The state of an oscillation or oscillator is usually expressed as its phase ϕ, a monotonously growing quantity that grows by 2π for every full oscillation of the system. Synchronization is then often defined as a constant relation between the phases $\phi_{1,2}$ of the individual oscillators $|n\phi_1 - m\phi_2| < const$ where $n, m \in \mathbb{N}$. In this thesis our primary focus are chaotic systems and their dynamics. Chaotic oscillators such as the previously introduced Lorenz63 system can synchronize to each other too, as we will see in the next section. Networks of oscillators also tend to synchronize, a phenomenon that we will explore in Sec. 4.1 when investigating networks of Stuart-Landau oscillators and the Kuramoto model.

2.2.8. Phase Synchronization of Chaotic Systems

Following Rosenblum et al. [182], chaotic oscillators like the Lorenz63 system introduced with Eq. 2.17 can synchronize to each other. To investigate the synchronization of such oscillators first a suitable phase has to be defined. Whereas for harmonic

oscillators a phase arises naturally as the argument of e.g. a sine wave, this is not obvious for a chaotic oscillator. One way to define a phase of a chaotic oscillator is using the analytical signal approach [74] by finding a suitable embedding for one of the observables $x(t)$ to turn it into a complex time series

$$\tilde{x}(t) = x(t) + i\hat{x}(t) = A(t)\exp\left(i\phi(t)\right) \tag{2.23}$$

from which an amplitude $A(t)$ and phase $\phi(t)$ arise. The imaginary part $\hat{x}(t)$ is computed with the Hilbert transform $\mathcal{H}\left(f(x)\right)$ which is defined as

$$\mathcal{H}\left(f(x)\right) = \frac{1}{\pi}\text{P.V.}\int_{-\infty}^{+\infty}\frac{f(\tau)}{x-t}\mathrm{d}\tau, \tag{2.24}$$

where P.V. denotes the Cauchy principal value of the integral. The Hilbert transform induces a 90° phase shift to every frequency component of the time series. Another way to arrive as the same $\tilde{x}(t)$ is to perform a Fourier transform, setting all negative frequencies equal to zero and transforming it back. The phase $\phi(t)$ thus follows as

$$\phi(t) = \arctan\frac{\Im(\tilde{x})}{\Re(\tilde{x})} = \arctan\frac{\mathcal{H}(x(t)}{x(t)}. \tag{2.25}$$

After each full period, 2π is added in order to unwrap the phase. For Eq. 2.25 to provide a meaningful phase of the time series, the signal $\tilde{x}(t)$ needs to exhibit a well-centered oscillation around a common reference point in the complex plane. Instead of the time series itself, Osipov et al. [155] argue that it is also possible to define a phase by using the derivative and its Hilbert transform. This results in a more concise definition of the phase, since the derivative is better centered than the time series itself, and slow variations are eliminated [134]. The derivatives can be calculated with the standard 4th-order finite differences formulas. Thus, denoting $x\left(t\right)$ as any of the observables of the oscillator series, we define its phase as

$$\phi\left(t\right) = \arctan\frac{\mathcal{H}\{\dot{x}\}\left(t\right)}{\dot{x}\left(t\right)}. \tag{2.26}$$

The *phase synchronization* of two chaotic oscillators can then by investigated by computing the phase difference $\Delta\phi = |\phi_1 - \phi_2|$. If the phase difference stays constant the two oscillators exhibit phase synchronization. As Rosenblum et al. [182] show, this phase synchronization indeed occurs when two complex oscillators such as the Rössler system, but also the Lorenz63 system, are weakly coupled to each other. At the same time though the amplitudes $A(t)$ are not synchronous at all.

We will use the phase synchronization approach in Sec. 3.5 on observational data where we want to proof a relation between two different climate phenomena in South America.

2.3. Dimension Reduction and Clustering

When dealing with large amounts of data, as we often do in climate science when investigating present day climate, we need ways to find patterns in the data or to group similar data points together. This can be used either to directly infer certain properties from these patterns or groups or as a pre-processing step before another analysis is conducted. In climate science one is particularly interested in the most dominant spatiotemporal variability pattern. These are often associated with large-scale phenomena like the El Niño-Southern Oscillation or the North Atlantic Oscillation. In the following we will introduce some techniques of extracting variability patterns and find groups of similar behaviour, i.e. clustering, that are used in this thesis.

2.3.1. Principal Component Analysis

Principal component analysis, in meteorology also often called empirical orthogonal function analysis (EOF), projects the input data onto a new coordinate system that maximizes the variance of data along the first coordinate axes. It can therefore also be used as a dimension reduction technique when coordinate axes that carry almost no variance are subsequently neglected. We can quickly derive the needed transformation, following Alpaydin [7], when we formulate the wanted transformation as a Lagrange problem. The new coordinate is z_1 and $\mathbf{v}_1$ is the projection vector that projects a data sample $\mathbf{v}$ so that $z_1 = \mathbf{v}_1^T\mathbf{x}$ maximizes the variance along z_1. The new coordinate system should be orthonormal so that the constraints are $||\mathbf{v}_i|| = 1$ and $\mathbf{v}_i\mathbf{v}_j = \delta_{ij}$. With the Lagrange multiplier α, it follows that

$$\begin{aligned} &\max_{\mathbf{v}_1} \left(\mathrm{Var}(z_1)\right) - \alpha\left(\mathbf{v}_1^T\mathbf{v}_1 - 1\right) \\ =&\max_{\mathbf{v}_1} \left(\mathbf{v}_1^T\Sigma\mathbf{v}_1\right) - \alpha\left(\mathbf{v}_1^T\mathbf{v}_1 - 1\right) \end{aligned} \tag{2.27}$$

where we used that $\mathrm{Var}(z_1) = \mathrm{Var}(\mathbf{v}_1^T\mathbf{x}) = \mathbf{v}_1^T\Sigma\mathbf{v}_1$ with $\Sigma = \mathrm{Cov}(\mathbf{x})$ being the covariance matrix of x. Taking the derivative while ignoring the maximum for a brief moment leads to $2\Sigma\mathbf{v} - 2\alpha\mathbf{v} = 0$ and therefore $\Sigma\mathbf{v} = \alpha\mathbf{v}$ which only holds true for eigenvalues and eigenvectors of Σ. As the maximum is searched, α also has to be largest eigenvalue and associated eigenvector. We can continue this procedure by always adding a new constraint like $\mathbf{v}_1\mathbf{v}_2 = 0$ to Eq. 2.27. Eventually these will all result in eigenvalue problems that are solved by the largest remaining eigenvalue. Hence, the new coordinate system that maximizes variance along the first axes is spanned by the eigenvectors of the covariance matrix in descending order of the associated eigenvalues. As briefly mentioned in the beginning of this section, PCA can be used as a method for dimension reduction when the axes that do not carry significant variance are neglected and only the first few coordinate dimensions are used for the further analysis. One other way to use PCA, is to use it as a method to extract the dominant variability patterns from spatiotemporal datasets. This is especially common in meteorology.

The leading eigenvectors, often called Empirical Orthogonal Functions (EOFs)[2], are visualized to inspect the dominant variability patterns that often correspondent to known large-scale climate phenomena as for example the North Atlantic Oscillation (NAO) [237, e.g.].

2.3.2. Complex Empirical Orthogonal Functions

The Complex EOF analysis (CEOF) extends the standard EOF analysis by applying the principal component analysis to the complexified time series, i.e. the analytical signal [91, e.g.]. The analytical signal $\tilde{x}(t)$, as introduced in Sec. 2.2.8, is usually computed by augmenting the time series with its Hilbert transform as its imaginary part. This two-dimensional embedding of the time series enables us to analyse oscillations in time series with methods that rely on phase information. Hence, the CEOF method is especially well suited for identifying oscillatory patterns and propagating waves [14]. We follow here the notation of Barnett [14]: The eigenvectors $B_n(\mathbf{x})$ of the covariance matrix of the spatiotemporal complexified data $\tilde{X}(\mathbf{x}, t)$ and its principal components $A_n(t) = \sum_{\mathbf{x}} \tilde{X}(\mathbf{x}, t) B_n^*(\mathbf{x})$ are all complex valued and can therefore not be analysed directly as it is the case for the standard EOF analysis. Thus, we investigate the following three measures, which separate the temporal and spatial domain, as well as the phase and amplitude information:

- spatial phase function $\theta_n(\mathbf{x}) = \arctan\left(\frac{\Im(B_n(\mathbf{x}))}{\Re(B_n(\mathbf{x}))}\right)$,
- spatial amplitude function $S_n(\mathbf{x}) = \left(B_n(\mathbf{x})\, B_n^*(\mathbf{x})\right)^{1/2}$,
- temporal phase function $\phi_n(t) = \arctan\left(\frac{\Im(A_n(t))}{\Re(A_n(t))}\right)$.

$\Im$ and $\Re$ denote the imaginary and real part respectively. For more details on CEOF analysis, the reader is referred to Barnett [14].

2.3.3. Singular Spectrum Analysis

Another method that is related to PCA is Singular Spectrum Analysis (SSA). Similar to PCA, but focusing on the temporal rather than the spatial domain, SSA solves an eigenvalue problem and decomposes a single time series into several components that can be ordered by the amount of variance of the time series they account for [36, 228]. To accomplish this, first the time series $x(t)$ is delay-embedded into a $M \times N$ matrix $\mathbf{X}$ with the k-th row given by $x(t + k)$, the time series delayed by k. The time series has length N and is embedded up to a delay M. Thereafter, the eigenvalue problem of the covariance matrix of $\mathbf{X}$ is solved. It can be shown that the magnitude of the eigenvalues is directly proportional to the amount of variance that is accounted for by

[2] Meteorological literature can sometimes be a bit contradictory of what is named a EOF and what is named a principal component. We adopt the terminology here that EOFs are the eigenvectors of the covariance matrix.

the respective eigenvectors in the same manner as we did for PCA in Sec. 2.3.1. With the eigenvectors $\mathbf{v}_i$, we can construct the principal components

$$A_k(t) = \sum_{j=1}^{M} x(t+j-1)\mathbf{v}_k(j). \tag{2.28}$$

As these principal components are in a different coordinate system than the original time series, SSA also performs a coordinate transform like PCA, they cannot be directly compared to the time series. We therefore reconstruct the time series from individual principal components or a set of principal components $\mathcal{K}$ with

$$\hat{x}_{\mathcal{K}}(t) = \frac{1}{M_t} \sum_{k\in\mathcal{K}} \sum_{L_t}^{U_t} A_k(t-j+1)\mathbf{v}_k(j), \tag{2.29}$$

where the normalization M_t and bounds of the summation L_t, U_t are subject to boundary effects [229]:

$$(M_t, L_t, U_t) = \begin{cases} (1/t, 1, t) & \text{if } 1 \le t \le M-1 \\ (1/M, 1, M) & \text{if } M \le t \le N-M+1 \\ (1/(N-t+1), t-N+M, M) & \text{if } N-M+2 \le t \le N. \end{cases}$$

The different reconstructed components correspond to different variability patterns of the original time series. This allows, e.g., to filter out certain variability modes or frequency bands from a given time series like the annual cycle of a climate time series. The reconstructed components have been shown to capture the phase of the time series well [78], which is a necessary condition for the phase coherence investigations we will do in Sec. 3.5. This leaves us with the task of selecting the right components for our investigation.

One specific approach to select only significant components is Monte Carlo SSA (MCSSA) [6]. MCSSA computes significance thresholds by performing SSA with the same parameters on an ensemble of surrogate time series. The exact proprieties of MCSSA obviously depend on the type of surrogate used. When shuffle surrogates are used, MCSSA provides a way how to distinguish a SSA component from (high-frequency) noise. If the eigenvalue of the k-th component is lower than 95-percentile of eigenvalues of the k-th shuffle MCSSA surrogate component, the corresponding reconstructed component is regarded as noise. This yields similar results to the visual check of the cumulative eigenvalue series approaching a horizontal line [204]. Another possibility is to use AR1 or AR2 surrogates as their spectrum is closer to that of a typical climate time series.

2.3.4. Clustering

Another way of extracting patterns from data in an unsupervised manner, is clustering. Clustering methods aim to partition data into groups, called clusters, so that the

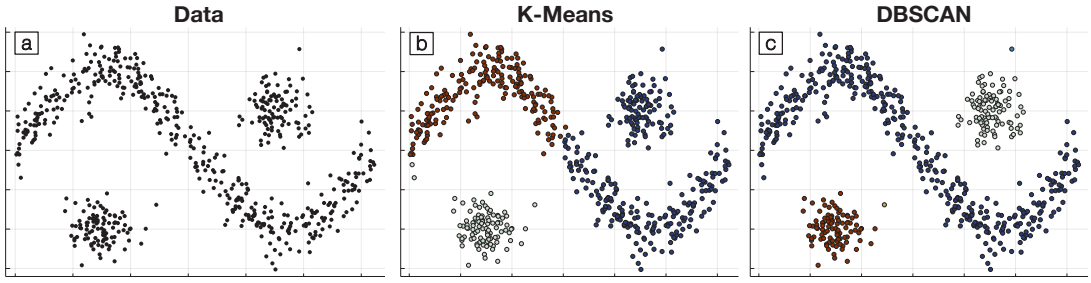

FIGURE 2.7.: Clustering example, the data **(a)** is generated from two two-dimensional normal distributions and a sine wave with added normal distributed noise. **(b)** K-means clustering (with $k = 3$) identifies only one of the clusters correctly, the sine wave is split in two clusters, one of them joined with the upper right cluster. **(c)** DBSCAN identifies all clusters correctly except for two single points which are labelled as outliers by DBSCAN.

members of each group exhibit similar behaviour to each other but dissimilar behaviour to members of other clusters. What exactly similar and dissimilar means in this context depends very much on the exact clustering algorithms and often on the choice of an appropriate similarity measure by its user. In this thesis, we will use clustering algorithms to distinguish and identify different qualitative behaviour of dynamical systems, e.g. we want to group initial conditions that lead to oscillating solutions into one cluster and those who lead to a stable fixed point to into another cluster.

As an example, one of the conceptually simplest clustering algorithms is k-means clustering [117]. It partitions the data $\mathbf{X}$ into k groups, whereas k is chosen a priori, by minimizing the reconstruction error

$$E(\mathbf{m}_i; \mathbf{X}) = \sum_{j}^{k} \sum_{i} b_i^{(j)} ||\mathbf{x}_i - \mathbf{m}_j|| \tag{2.30}$$

$$b_i^{(j)} = \begin{cases} 1 & \text{if} \quad ||\mathbf{x}_i - \mathbf{m}_j|| = \min_j ||\mathbf{x}_i - \mathbf{m}_j|| \\ 0 & \text{otherwise.} \end{cases} \tag{2.31}$$

Here, $\mathbf{m}_i$ are the centers or means of each of the k clusters, $b_i^{(j)}$ is the label that indicates that the i-th data point belongs to the j-th cluster and $||.||$ is most commonly the L2 norm. The values for $\mathbf{m}_i$ are found using an iterative procedure. Starting points for $\mathbf{m}_i$ are random. In each interaction all labels $b_i^{(j)}$ are computed and the means are updated by solving $\partial E / \partial \mathbf{m}_i = 0$ for $\mathbf{m_i}$. The exact formula depends on the chosen norm $||.||$. PCA can be used to provide reasonable starting values for $\mathbf{m}_i$[7]. K-means returns clusters that are convex or almost spherically shaped as only the distance to the center of the cluster is minimized. While this can already give good insights into the data, it will not be enough for complex systems that potentially exhibit more complex behaviour.

2.3.5. Density-based Clustering

Like k-means clustering many clustering algorithms, partition the data by minimizing a similarity measure of the data points to each other into a predefined number of groups, often resulting in convex or spherical-shaped clusters [104]. We are interested in complex systems where the shape of groups of data points exhibiting similar behaviour can be quite complex as well and generally we will not know the number of clusters that we want to detect a priori. One class of clustering algorithms able to deal with these constraints is density-based clustering (see Fig. 2.7). Density-based clustering groups contiguous regions with a high density of data points that are separated by regions with a low density of data points into clusters [104]. The regions with a low density of data points are typically considered as noise or outliers. Thus density-based clustering algorithms can also be used for outlier detection.

Probably the most used, and also one of the first widely used, density-based clustering algorithms is density-based spatial clustering of applications with noise (DBSCAN) [65]. As an input DBSCAN needs the distance from each point to other D_{ij}. This can be the L2 norm, but it can also be another norm, as we will also derive a specialized norm for application to dynamical systems, later. In order to determine the contiguous regions with high density, several definitions have to me made, following Ester et al. [65]:

- ϵ-*neighborhood*: All points $\mathcal{N}_\epsilon(p)$ that have a distance D_{ip} smaller than ϵ to p,
- Point p is *directly density reachable* from point q if $p \in \mathcal{N}_\epsilon(q)$ and $|\mathcal{N}_\epsilon(q)| \geq$ minPts,
- Point p is *density reachable* from point q, if there is a chain of connection $q \to p_1 \to p_2 \quad ... \to p$ where for all subsequent pairs (p_i, p_{i+1}) of points p_{i+1} are directly density reachable from p_i,
- Points p and q are *density connected* if there is another point o from which both are density reachable.

The difference between definition three and four is made to distinguish between points at the edge and at the core of clusters. minPts is a parameter of the method and can be thought of as a lower threshold for what is considered as a high density of points within a radius ϵ. A *cluster* $\mathcal{C}$ then is the set of points for which

- $\forall p, q \in \mathcal{C}$, p and q are density connected,
- $\forall p, q$, if $p \in \mathcal{C}$ and q is density reachable from p, then $q \in \mathcal{C}$

hold. All points that are not part of a cluster are considered as noise or outliers. This chain of connection, is a feature of the DBSCAN algorithm, that will be particularly useful for our application to dynamical systems later. Given data, the DBSCAN clusters are computed by starting with an arbitrary data point, determining its cluster and all the points that belong to it with the rules introduced above. Then, the algorithm proceeds until all nodes are either assigned a cluster or marked as noise. The

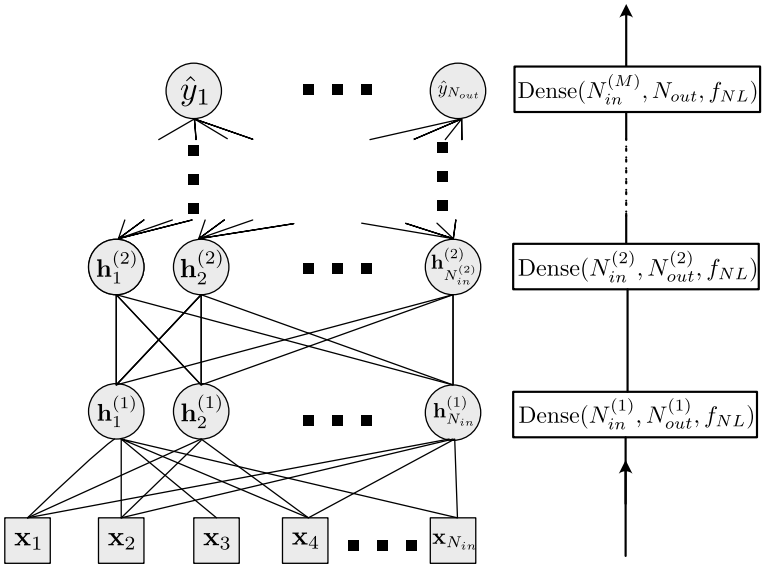

FIGURE 2.8.: Schematic of a multilayer perceptron feed-forward neural network (MLP). The left part is the full schematic of the network with all nodes and connections sketched. Circles symbolize nodes of the network and squares inputs. The MLP has M layers. The last layer defines the output $\hat{\mathbf{y}}$ of the MLP, all other layers are also referred to as 'hidden layers'. On the right the analogous shorthand that is used later in this thesis is shown.

parameters of DBSCAN are ϵ and minPts, Ester et al. [65] recommend in their original paper to find them by computing the sorted k-dist graph. The k-dist is the distance of a point to its k-th nearest neighbor. The sorted k-dist graph then is the graph of all k-dists of the dataset in descending order. ϵ is then chosen as the value at the first visual knee in the graph and minPts as k. We will discuss other possibilities for our specific application later.

2.4. Fundamentals of Artificial Neural Networks

Another machine learning technique that we will make use of are artificial neural networks (ANNs). They are powerful, data-driven universal function approximators [52, 92] that are inspired by biological neural networks such as the human brain. This means that ANNs can approximate every function, it could be an analytical expression such as $f(x) = \sin(x^2)$, or even a more general question such as: 'Given a 128×128-sized image, what is the probability that there is a cat in the image?'. ANNs do not try to mimic an actual biological neural network though, they are multi-purpose statistical tools. Early forms of ANNs were already used in the 1950s [67, 175, 181]. They became more useful when backpropagation and automatic differentiation, now standard techniques to fit ANNs to data, were first formulated in the 1970s and -80s

[116, 185, 242]. However, only the recent advance of "big data", readily available large datasets, and increasing computational power have allowed ANNs to become a crucial technology in many science disciplines, and also for commercial applications [79]. In the last years, ANNs made the headlines of international news for achievements such as beating the world's best Go players, a feat that was for a long time thought to be impossible for a computer program [208].

Essentially, ANNs are nonlinear models with an enormous amount of parameters and an associated set of techniques to learn the right parameter values from data. ANNs are comprised of many artificial neurons, also called nodes, that are connected with each other to form a network. One of the simplest forms of ANNs are multilayer perceptron feed-forward neural networks (MLP)[3]. A MLP is comprised of M layers of nodes, each layer i consisting of $N^{(i)}$ nodes. All nodes of subsequent layers are densely connected with each other and each connection has a weight $w_{ik}^{(j)}$ (see Fig. 2.8), where $w_{ik}^{(j)}$ is the weight of the connection from the k-th node in the j-th layer to the i-th node in the $j+1$-th layer. Each node sums all its inputs and applies a nonlinear function f_{NL}. The output $\mathbf{h}$ of the i-th node of the j-th layer with the N_{in}-dimensional input $\mathbf{x}$ follows as

$$\mathbf{h}_i^{(j)} = f_{NL}(\sum_k^{N_{in}} w_{ik}^{(j)} x_k + b_i^{(j)}), \tag{2.32}$$

where $b_i^{(j)}$ is an additional bias parameter of each node. Without the nonlinear function f_{NL}, also called activation function, the output of the MLP would just be a polynomial and the MLP thus only be able to approximate polynomial functions. The nonlinearity eliminates this shortcoming. There are many possible choices for this function. Traditionally, $\tanh(x)$, sigmoid $(1/(1+e^{-x}))$, and ReLu $(\max(0,x))$ are popular choices. In the following we will use the swish function $f_{NL}(x) = x/(1+\exp(-x))$ as it potentially improves the accuracy of the ANN [169]. Due to its dense connections a MLP layer is also referred to as a *dense* layer, especially within machine learning software libraries. In matrix form, a complete dense layer reads

$$\text{Dense}(\mathbf{x}; N_{in}, N_{out}, f_{NL}) = f_{NL}(\mathbf{W}\mathbf{x} + \mathbf{b}), \tag{2.33}$$

where the $(N_{out} \times N_{in})$-matrix $\mathbf{W}$ and the N_{out}-dimensional bias vector $\mathbf{b}$ are the learnable parameters $\Theta_i = \{\mathbf{W}, \mathbf{b}\}$. The last layer of the MLP forms the output $\hat{\mathbf{y}}$ of the MLP and we will refer to the collection of all parameters of all layers as Θ.

MLPs, as most ANNs, are a supervised machine learning method: we seek the optimal parameters for the MLP by minimizing a loss function on example data which consists of pairs of input and output values $(\mathbf{x}, \mathbf{y})$. For regression tasks this loss func-

[3]Some authors only call nodes or networks a (multi-layer) perceptron when its purpose is binary classification, for others perceptron is (almost) synonymous with node and a MLP can also be set up for regression tasks. We will adopt the latter terminology.

tion is usually the sum of the squared errors between the output of the $\text{MLP}(\mathbf{x};\Theta) = \hat{\mathbf{y}}$ and values of the training set $\mathbf{y}$, the loss function thus follows as

$$\mathcal{L}(\Theta) = \sum_i (\mathbf{y}_i - \text{MLP}(\mathbf{x}_i;\Theta)))^2. \tag{2.34}$$

In order to minimize the loss function $\mathcal{L}(\Theta)$ with respect to Θ, we have to compute the gradients of the loss function $\mathcal{L}$ with respect to all parameters $\partial\mathcal{L}/\partial\theta_i$. As an example, following Alpaydin [7], let us consider a 2-layer MLP with a vector as an input, a single number as an output, with α_{ij} as the parameters of the first layer and β_i as the parameters of the second layer which has no activation function. For simplicity both layers have no bias parameters. The output of this MLP for the j-th data sample then is $\hat{y}_j = \sum_i \beta_i h_i^{(1,j)}$ where $h_i^{(1,j)}$ is the output of the i-th node of the first, hidden layer given input x_j. The derivatives with respect to the parameters of the second, last layer $\partial\mathcal{L}/\partial\beta_i$ can be computed by applying the chain rule

$$\frac{\partial\mathcal{L}}{\partial\beta_i} = \sum_j \frac{\partial\mathcal{L}}{\partial\hat{y}_j}\frac{\partial\hat{y}_j}{\partial\beta_i} = \sum_j -2(y_j - \hat{y}_j)h_i^{(1,j)} = \sum_j \delta_j h_i^{(1,j)}, \tag{2.35}$$

where we define $\delta_i = -2(y_j - \hat{y}_j)$. The derivatives with respect to the first layer follow consequently by applying the chain rule once more as

$$\frac{\partial\mathcal{L}}{\partial\alpha_{ik}} = \sum_j \frac{\partial\mathcal{L}}{\partial\hat{y}_j}\frac{\partial\hat{y}_j}{\partial h_i^{(1,j)}}\frac{\partial h_i^{(1,j)}}{\partial\alpha_{ik}} = \sum_j -2(y_j - \hat{y}_j)\beta_i\frac{\partial f_{NL}(x)}{\partial x}x_j = \sum_j \delta_j\beta_i\frac{\partial f_{NL}(x)}{\partial x}x_j.$$

The first two factors are the loss δ_j which has already been computed in Eq. 2.35, weighted by β_i, the weights of the second layer, which can be interpreted as the error of node i of the second layer [7]. The errors of the MLP are thus propagated backwards by repeatedly applying the chain rule, hence this algorithm is named *backpropagation* [185]. In practice, most software libraries compute these derivatives with automatic differentiation (AD). AD is a set of techniques that augment code in such a way that when executing a function, it is able to track each elementary operation performed by the function, computing its derivative and ultimately also computing the derivative of the function itself by applying the chain rule to all tracked elementary operations that lead to the output of the function [17]. As soon as we obtain the derivatives of $\mathcal{L}$ for all parameters θ_i, we are able to update the parameters by

$$\Delta\theta_i = \eta \cdot \frac{\partial\mathcal{L}}{\partial\theta_i} \tag{2.36}$$

where η is the learning rate. The learning rate has to be small enough so that minima of $\mathcal{L}$ are not missed, but large enough for the update procedure to converge quickly. It is a hyperparameter of the MLP approach. This is the most basic form of a gradient descent optimization. In practice more sophisticated versions decrease the learning rate over time [99], feature a per parameter learning rate [101] and weight decay. We

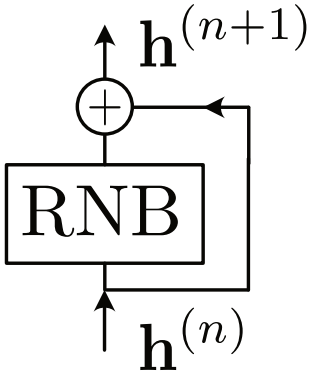

FIGURE 2.9.: Schematic of a residual network block: the input $\mathbf{h}$ is both put into a block of layers (e.g. dense or convolutional layers) $\mathrm{RNB}(\mathbf{h}^{(n)};\Theta)$ with parameters Θ and skips past this block of layers via a shortcut. The output RNB and is then summed with its input to form the output of the residual network block $\mathbf{h}^{(n+1)}$

will use an optimization method that uses all of these, adaptive moment estimation with decoupled weight decay regularization (AdamW) [123].

ANNs can have enormously many parameters and thus are prone to overfitting. There are many different techniques to combat this. In this thesis we will concentrate on just two techniques as our ANNs are comparably shallow. These are regularization and monitoring the loss and accuracy on a validation set. The ANN is overfitted if the loss on the data it was trained with is very small, while it generalizes very poorly on previously unseen data. We thus split the dataset into two parts, a training set and a validation set, to test how well the ANN generalizes. In the beginning of the learning procedure both the loss on the training and the validation set will decrease. As soon as the loss on the validation set rises again while the loss on the training set still decreases, the ANN is beginning to overfit and the training procedure should be stopped. Regularization on the other hand means that we penalize the weights in the loss function by adding an additional term, the complete, new loss function then becomes

$$\mathcal{L}(\Theta) = \sum_i (\mathbf{y}_i - \mathrm{MLP}(\mathbf{x}_i;\Theta)))^2 + \gamma \sum_j ||\theta_j||. \tag{2.37}$$

The regularization constant γ is another hyperparameter of training the MLP and $||.||$ is typically the L1 or L2 norm. Regularization is also part of the AdamW optimizer used throughout this thesis as it features a weight decay term in every parameter update.

For ANNs with many layers, deep neural networks, gradients computed through backpropagation are potentially getting very small, effectively obstructing the training of deep ANNs. This is the vanishing gradient problem [89]. One way to mitigate or at least attenuate it is the introduction of additional shortcuts or skip connections to the ANN. A particularly successful technique are Residual Networks (ResNets) [84]. ResNets connect the input $\mathbf{h}^{(n)}$ of a layer or block of layers (RNB) directly back to its output $\mathbf{h}^{(n+1)}$

$$\mathbf{h}^{(n+1)} = \mathrm{RNB}(\mathbf{h}^{(n)};\Theta) + \mathbf{h}^{(n)} \tag{2.38}$$

as is shown in Fig. 2.9. In Chapter 5 we will see that these ResNets also bare strong similarities to differential equations.

Aside from MLPs, another important ANN class are convolutional neural networks (CNN). They are inspired by the visual vortex of animals [73]. In contrast to the densely connected layers of a MLP where each connection has its own weight, the CNN layers share a lot of weights and react to local features of the input. As the name suggests CNNs perform a discrete convolution on the input, in the 1-dimensional case the i-th element of the output follows as

$$h_i^{(n+1)} = \sum_j k_j h_{i-j}^{(n)} \tag{2.39}$$

with the filter kernels $\mathbf{k}$ as parameters. Typically multiple convolutions with multiple different filters are applied simultaneously, which is referred to as the convolutional layer having multiple channels. In an image recognition task the individual filters correspond to the recognition of specific features and shapes such as corners, circles or edges [79]. When working with convolutional layers, one also often uses pooling layers that reduce the (spatial) dimension of the data by downsampling. For us, CNNs will be useful when dealing with spatiotemporal dynamical systems and data.

3. Analysis of the South American Monsoon System: Networks & Phase Synchronicity

When we want to understand the climatology of a region, understand repeating patterns of e.g. heavy rainfall or we desire to predict the onset of a monsoon, we need to be able to understand the complex spatiotemporal variability and intricate coupling structure that constitutes its climate. Networks have proven to be a valuable tool to investigate spatiotemporal coupling structures in the climate system [59, 223]. Networks are able to uncover and, upon a suitable quantification of the network topology, visualize these coupling structures remarkably well.

Networks from climate data, climate networks, are usually constructed by thresholding a pairwise similarity measure of spatiotemporally gridded data. As such they are spatially embedded networks (see Sec. 2.1.2). If the similarity between the time series at two distinct grid points is larger than a certain threshold, a link is placed. This similarity measure can be e.g. a correlation coefficient [59, 225] like the Pearson correlation, but also event synchronization when one is more interested into the spatiotemporal dynamics of extreme events [132]. These networks are then usually studied with centrality measures like those that we have introduced in Sec. 2.1. The centrality measures highlight regions that are particularly important for the climate of the studied region. Climate networks constructed from the pairwise correlation of global surface temperature data for example strongly highlight the region in the Pacific Ocean that is associated with the El Niño-Southern Oscillation (ENSO) which is otherwise not immediately visible in the raw data [59].

Due to the large-scale seasonal changes in precipitation, wind and other observables, complex networks are especially well suited for the analysis of spatiotemporal couplings in monsoon systems [24, 29, 30, 132]. Additionally, complex networks have also proven to be an effective tool for the analysis of larger-scale, interannual variability due to phenomena like ENSO [224, 250]. By utilizing climate networks it is also possible to distinguish different types of El Niño events [243]. Recent advances even suggest that networks can serve as early warning precursors of ENSO events or even predict them [142, 177]. Aside from ENSO, climate networks are also a powerful tool to uncover other teleconnections pattern [27, 30, 173, 253].

Networks excel in uncovering patterns from large amounts of spatiotemporal data. They can tell where to look for further investigations. Two particularly successful examples of this approach are the prediction of extreme floods in the eastern Andes [23] and the prediction of the onset of the Indian summer monsoon [216]. Both studies

based on an initial network analysis of the respective region. In the following we will approach this in a similar manner. First we will give a short introduction into the climate system in question, the South American Monsoon System (SAMS), then we will introduce a novel network construction, streamflow networks. Subsequently, the streamflow networks will be used to investigate the low-level circulation of the SAMS. One feature of the SAMS that is highlighted by the networks, the rainfall dipole of the SAMS and its connection to Rossby Waves, will then be further investigated with phase synchronization techniques.

Sec. 3.3 - 3.3.2 follow the publication „A complex network representation of wind flows“, reproduced from [MG1], with the permission of AIP Publishing, Sec. 3.1, 3.2 and 3.4 follow closely text and results of parts of the publication „Variability of the Low-Level Circulation of the South American Monsoon Analysed with Complex Networks“ [MG4] and Sec. 3.5 follows the publication „Phase coherence between precipitation in South America and Rossby waves“ [MG3].

3.1. The South American Monsoon System

The region whose climate we are investigating primarily throughout this chapter is South America and the monsoon system it is characterized by. The South American Monsoon System (SAMS) was not categorized as a monsoon system until Zhou and Lau [254] showed that the climate of South America actually fulfills a slightly loosened criteria of a monsoon system: The key difference between the SAMS and other monsoon systems is that there is no seasonal reversal in the prevailing wind direction. However, as Zhou and Lau [254] showed this reversal does happen for the anomaly wind vector field, instead. The reversal in the anomaly wind directions around the equator can be understood as an effect of the stronger atmospheric heating over the South American continent as compared to the tropical Atlantic ocean, which enhances the low-level winds from the Atlantic ocean toward the South American continent, superimposed on the year-round easterly direction of the trade winds. The largest precipitation differences between dry and wet seasons can be found in the southern Amazon (at about 10°S), where precipitation peaks during austral summer (DJF) [34].

The differential heating between the tropical Atlantic Ocean and the South American continent, together with the trade winds that are strong year-round, are the key ingredients of the South American Monsoon System (SAMS) [34]. The trade winds are responsible for the low-level moisture transport from the tropical Atlantic ocean to the continent. The trade winds are, after crossing the Amazon basin, deflected by the Andes and channeled southward into the South American Low-Level Jet (SALLJ) (see Fig. 3.1). The SALLJ is a synoptic-scale wind system with highest speeds typically attained in Bolivia near Santa Cruz de la Sierra [136, 206, 230]. There are different definitions of Low-Level Jets (LLJs) in general and of the SALLJ in particular. Bonner [33] defines LLJs as events which have to fulfill a certain velocity criterion: the Bonner criterion 1 demands a velocity of $15\,\mathrm{m\,s^{-1}}$ and a velocity decrease of at least $6\,\mathrm{m\,s^{-1}}$ at 3 km altitude. This is well above the mean velocities observed in the regions

associated with the SALLJ. Typically, Bonner 1 events occur between 5 and 50 times per year depending on the exact observation point and year [137]. In contrast to this event-type definition, Rodwell and Hoskins [178, e.g.], regard LLJs as essential and permanent features of every subtropical monsoon system. Here, we follow the line of Rodwell and Hoskins [178] and speak of an enhanced SALLJ when there are positive velocity anomalies with a poleward direction at the eastern slopes of the Andes and of an suppressed SALLJ when there are negative velocity anomalies.

The SALLJ transports moisture from tropical South America (including the Amazon) to southeastern South America (SESA) (Fig. 3.1). The intensity and position of the SALLJ is connected to the occurrence of floods and droughts in SESA, as well as to the frequency, intensity, and size of Mesoscale Convective Systems (MCS) forming in SESA [136, 230]. We will therefore put significant emphasis on the variability of the SALLJ. Depending on prevailing atmospheric conditions, the SALLJ exhibits two different regimes: it either has a pronounced southward component exiting in the Gran Chaco area (the so-called Chaco Jet), or a more pronounced eastward component exiting in southern Brazil (the No-Chaco Jet) [188, 191].

Monsoon systems like the SAMS are the result of a complex interplay of atmospheric processes on various spatial and temporal scales [240]. The strength or activity of a monsoon is most easily noticeable in terms of anomalously high precipitation. This strength of precipitation is naturally coupled to the low-level circulation of the monsoon system as well, so that different criteria for active and break monsoon phases based on precipitation, pressure systems and wind have been suggested [167, 170]. The active and break phases are strongly connected to changes in the low-level circulation [240]. In the latter study, the authors formulated a criterion for the Asian-Australian Monsoon to distinguish between active and break phases solely based on the wind velocity at 850 hPa and the outgoing longwave radiation (OLR, merely a proxy for precipitation) in certain reference regions. This concept was applied to the South American Monsoon System (SAMS) as well: Jones and Carvalho [94] showed that the direction of the anomaly wind vectors in the Brazilian state Rondônia is an indicator for this activity. Based on previous observations, Jones and Carvalho [94] picked a region in Rondônia (9°-13°S, 60°-64°W) as a reference for classifying the wind. Rondônia is situated south of the Amazon basin and north of Bolivia. It is therefore heavily affected by the strength of the monsoon. Whereas the absolute wind field in Rondônia is northerly throughout the austral summer season (DJF), the direction of the anomaly wind field exhibits two distinct regimes: a westerly and an easterly regime. These regimes can be identified with active and break phases of the SAMS, as they are related to large-scale differences in precipitation [94]. They will be further investigated in Sec. 3.4.1 and Sec. 3.4.3.

FIGURE 3.1.: Overview of important features of the low-level atmospheric circulation of the South American Monsoon System (SAMS). The incoming trade winds and the South American Low-Level Jet (SALLJ) are marked in red. The South Atlantic Convergence Zone (SACZ) and southeastern South America (SESA) are marked in black. In Sec. 3.4, active and break phases of the SAMS are studied. For this purpose several additional regions are marked. The active and break phases are distinguished based on the wind direction in the Bolivian districts Beni and Santa Cruz (BSC, marked in dark blue). The original study used a reference region slightly to the north, in the Brazilian province of Rondônia (marked in orange, see text) [94]. Various regions in South America that are referenced in later sections are marked in yellow. These include (from north to south) the Llanos Plain (LLA), the Guyana Highlands (GH), the Guyanas without the Guyana Highlands (GUY), the eastern slopes of the Andes in northern Bolivia and western Paraguay (NBP) and Patagonia (PAT).

3.2. Data

In our analysis we will use reanalysis data. Climate data is measured from a variety of sources and in a variety of manners, ground-based stations, satellites, aircraft, ships, buoys, radar and more [174, e.g]. All contribute to the available database of climate data. Reanalysis models take in all of these data sources and interpolate them onto a regular spatiotemporal grid. This makes the analysis for us much easier as we do not have to deal with any effects from irregular temporal or spatial grids. We utilize two different reanalysis data sources throughout our investigations, NASA's Modern-Era Retrospective analysis for Research and Applications (MERRA) and its updated version MERRA2 [174]. The datasets that we use cover the period from 1980 to 2016 and consist of 6-hourly or daily data on a $1/3° \times 2/3°$ rectangular grid. Especially the atmospheric circulation can be very different in different heights above ground. Instead of using fixed heights in meters, the observables are usually tracked on isobaric surfaces, the geopeotential height (GPH). In the following, observables at 850 hPa which correspondent to an altitude of roughly $1.4 - 1.5$ km are used to investigate the low-level atmosphere and observables at 250 hPa which correspondent

to an altitude of roughly $10-11$ km are used to investigate the upper-level atmosphere such as the jet stream and Rossby waves. The GPH itself is one of those observables and one of our main data sources for the state of the atmosphere. GPH as an observable is the height in meters of a isobaric surface with a certain pressure. Wind, given in its meridional and zonal component at a specific pressure level, and precipitation are other observables that we will use in our analysis. Often, we will limit our analysis to the months November to February (NDJF), as this is roughly the wet season of the SAMS. Anomalies are computed with respect to the seasonal climatology of NDJF, i.e. its mean, for the composite analyses accompanying the network analysis.

The networks constructed in the following are computed from a dataset of a large map section spanning 0°W-110°W; 70°S-25°N and thus comprising $N = 33,366$ nodes. In order to minimize biases due to boundary effects of these spatially embedded networks (see Sec. 2.1.2), we choose a region that is substantially larger than the South American continent and the area we are interested in. The resulting centrality measures of the networks are cropped to a smaller map section that is also used for composites of geopotential height and precipitation: 20°W-90°W; 60°S-20°N.

3.3. Streamflow Networks

Climate Networks, typically involving similarity measures, are mostly applied to temperature and precipitation data. One climatic observables that have so far not been considered for a complex network analysis is the atmospheric wind field. Wind data provide crucial information about Earth's atmospheric circulation and as we've seen in Sec. 3.1 the SAMS like other monsoon systems is characterized by large-scale changes in the wind direction. Furthermore, global-scale phenomena like the El Niño-Southern Oscillation also directly impact regional wind fields. Wind is, in contrast to other quantities that were previously used to construct climate networks like temperature or rainfall, not a scalar but a three-dimensional observable. Large-scale atmospheric motions are dominated by a balance between the Coriolis and pressure-gradient forces. This *geostrophic equilibrium* causes the wind vectors to be approximately parallel with isobaric surfaces, as long as the Coriolis force has a horizontal component, which is the case everywhere except along the equator [187]. For our application, we are interested mainly in advective processes (i.e., horizontal transport of air masses) associated with the South American monsoon system (SAMS), because these determine the characteristic, large-scale coupling patterns which we intend to analyze with the network approach. For the investigation of the SAMS, it is therefore sufficient to investigate the two-dimensional wind on isobaric surfaces, even though heat transfer causes vertical winds, which play a key role for the formation of the large-scale circulation cells of Earth's atmosphere. This vertical motion is usually slower than the geostrophic motion, which at 850 hPa is typically of $\mathcal{O}\left(1\,\mathrm{m\,s^{-1}} - 10\,\mathrm{m\,s^{-1}}\right)$. The restriction to two-dimensional isobaric surfaces also allows for an easier interpretation of the methods and results: although the three-dimensional field could technically be analyzed with the method introduced in the following, it would make the results harder to vi-

sualize and most data sources wouldn't offer vertical levels close enough to each other for our approach.

In the following, a construction method for climate networks from two-dimensional flows like the low-level atmospheric wind field is introduced. The majority of existing climate network construction methods are based on pairwise correlations of scalar observables. Of course, even from a two-dimensional observable, like the wind field on a given geopotential height, we could derive a network representation solely based on correlations. For example, correlations could be computed between the zonal and meridional components separately, from the absolute values of the two-dimensional vectors, or by a form of scalar vector product. Several successful approaches to construct networks from flows based on correlations have been introduced [143, 226, e.g.]. Complementary, we intend here to introduce a method that directly utilizes the characteristics of multidimensional vector fields. Approaches for a direct network representation of flows have been introduced, e.g., by Ser-Giacomi et al. [202] and Viebahn and Dijkstra [232]. Viebahn and Dijkstra [232] investigated critical transitions of the wind-driven ocean circulation in a model basin by utilizing complex networks that were constructed with links along or across the streamlines of the flux. Ser-Giacomi et al. [202] used Lagrangian simulations to construct complex networks of the surface flow of the Mediterranean sea. Further studies investigated atmospheric blocking with these Lagrangian flow networks as well [203]. Here, we intend to propose a new construction method for the analysis of flow data. We will introduce a simple model of the local flow and propose two different approaches to ensure the significance of the links that we set. We will test and validate the method by applying it to observational wind data of the South American monsoon system before turning to a deeper analysis of the variability of the SAMS. As large-scale changes in the wind field are a substantial feature of every monsoon system, they serve as an ideal application for the proposed methodology.

3.3.1. Network Construction

Most climate networks focused on statistical co-variability measures to compare two time series, placing a link between the corresponding nodes if their co-variability is particularly high. For the case of the two-dimensional isobaric wind field, we propose an alternative approach that focuses on the directed properties of this two-dimensional vector field: Wind mainly transports air and moisture from one location to another. Given the wind data at a specific location, we can calculate how far the wind transports matter during a specific time and link all nodes reached by the wind. We call networks based on this idea subsequently *streamflow networks*. They will most suitably be analyzed by measures that focus on the paths which these streamflow links create. In the following, we will present two ways to construct such networks: One where the corresponding significance tests are based on numerical simulations, and one where they are based on an analytical approximation.

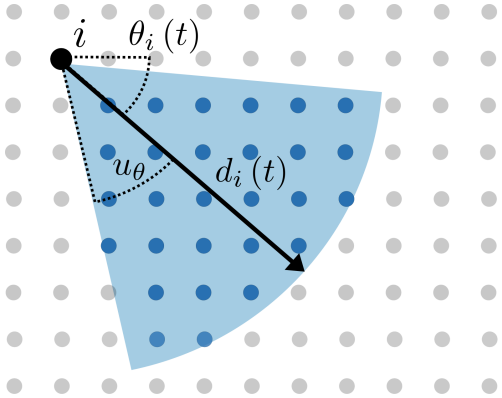

FIGURE 3.2.: Basic concept of the streamflow networks: The blue filled nodes are considered to be reachable by the wind of the black filled node i. The covered distance $d_i(t)$ is directly proportional to the velocity of the wind, the vector has the same direction as the original wind vector $(u_i(t), v_i(t))$ and the angle uncertainty u_θ is a parameter of the network. The blue shaded area indicates the central angle referred to in the text.

The streamflow networks rely on the basic idea of networks directly representing the flow of the wind fields. To implement this idea, we derive a strongly simplified model of the wind flow. For this purpose, we first focus on a single node i and a single step t in the time series. Introducing a fixed travel time T, the distance the wind can reach in T is $|(u_i(t), v_i(t))| \cdot T$. We add an additional uncertainty $u_{d_i}(\lambda_i)$. This uncertainty is chosen to ensure that two nodes will be linked when the distance the wind can reach passed more than halfway through the distance between two neighboring nodes as nodes represent the entire grid cell area surrounding them, and not just their precise location. This way, we also lower the chances of having dead ends in the paths of the network. For a given rectangular grid this uncertainty will depend on the latitude λ of node i. We define this uncertainty as the average of the distance to the next neighbor in the meridional direction d_m and the zonal direction d_z:

$$u_{d_i}(\lambda_i) = \frac{1}{2}\left(d_m + d_z(\lambda_i)\right) \ . \tag{3.1}$$

The distance in the zonal direction depends on the latitude, whereas the distance in the meridional direction is a constant for a given rectangular grid. The total distance that is considered to be covered by a given wind vector thus follows as

$$d_i(t) = |(u_i(t), v_i(t))| \cdot T + u_{d_i}(\lambda) \, . \tag{3.2}$$

For grids with a very fine resolution, u_{d_i} will be small in comparison to $|(u_i(t), v_i(t))| \cdot T$. Note, however, that it would become more important for coarser grids.

Focusing on the actual wind flow, we also have to account for the direction of the wind. The arctangent of the meridional and zonal wind component yields the wind

angle $\theta_i(t)$. Next, we also introduce an angle uncertainty u_θ. We define a circle section with the spatial position of node i as its center for every time step. The radius is $d_i(t)$, the central angle is $2 \cdot u_\theta$ and $\theta_i(t)$ its direction (see Fig. 3.2). All nodes that lie within this circle sector are considered to be reachable by the wind at time t from node i. The angle uncertainty u_θ introduced here remains a parameter to be set. It governs how wide the circle section is and therefore directly influences the degree centrality and link density of the resulting network (see Sec. 3.3.2 below regarding suitable choices of this parameter).

Next, we apply this method to the whole time series at node i and count how often each other node j lies within the circle sections determined for each time step t. This provides the hit counts h_{ij}. There are two different approaches how we can derive a significance threshold for these hit counts. If h_{ij} is larger than this significance threshold we set a link between i and j, otherwise not.

Simulation Method

The first approach to compute a significance threshold is with surrogate data. By computing N_{stat} surrogate hit counts $\eta_{ij}^{(k)}$ that tell us how often node j lies within the circle section spanned by node i in the k-th surrogate, we can derive a significance threshold for the actual hit counts h_{ij} of the real data. The surrogates are based on uniformly distributed angles as their direction and velocities drawn from the velocity time series of the node. These hit counts are approximately normally distributed (see Figure A.5) and therefore it seems reasonable to calculate the mean $\mu_{\eta,ij}$ and standard deviation $\sigma_{\eta,ij}$ of $\eta_{ij}^{(k)}$ with respect to k, the surrogate number, to estimate a significance threshold for h_{ij}. Thus, we define the adjacency matrix of the network as

$$A_{ij} = \begin{cases} 1 & \text{if } h_{ij} > \mu_{\eta,ij} + n \cdot \sigma_{\eta,ij} \quad \text{with } n \in \mathbb{N} \\ 0 & \text{otherwise.} \end{cases} \tag{3.3}$$

The parameter n is either 2 for a 95.5% significance or 3 for a 99.7% significance, assuming a normal distribution. A pseudocode representation of the complete algorithm is shown in the Appendix Sec. A.1.1.

The resulting network is directed. Its out-degree thus strongly depends on the absolute value of the wind velocity and does not provide much additional information. A path-based measure like the betweenness centrality seems to be ideal for these kind of networks. The resulting networks will exhibit strong boundary effects due to the underlying wind fields and the directed nature of the network.

Semi-analytic Method

The previously proposed method to compute significance thresholds for the *streamflow networks* has one significant flaw: the computation of the surrogates is costly and scales with $\mathcal{O}(N_{stat} \cdot N_t \cdot N_{Node})$ in computation time for every node. Using the same basic

concept (see Fig. 3.2), we can, alternatively, analytically estimate how likely it is that a hit count h_{ij} occurs just by chance.

The probability for a single hit from node i to node j can be assumed to be binomially distributed because either a hit occurs with the probability p_{ij} or it does not with probability $1 - p_{ij}$. Hence, we compute the probability for k hits to occur with a cumulative binomial distribution:

$$P_{ij}\left(k \geq h_{ij}\right) = 1 - P_{ij}\left(k < h_{ij}\right) \tag{3.4}$$

$$= 1 - \sum_{k=0}^{h_{ij}} \binom{N_t}{k} p_{ij}^k \left(1 - p_{ij}\right)^{N_t - k}. \tag{3.5}$$

Looking at time series with large N_t, the binomial distribution can be approximated either by a Poisson distribution for small $N_t p_{ij}$ or a normal distribution otherwise:

$$P_{ij}\left(k \geq h_{ij}\right) = \begin{cases} 1 - \sum_{k=0}^{h_{ij}} \frac{\left(N_t p_{ij}\right)^k \exp -N_t p_{ij}}{k!} & N_t p_{ij} \text{ small} \\ 1 - \frac{1}{\sqrt{2\pi N_t p_{ij}\left(1-p_{ij}\right)}} \sum_{k=0}^{h_{ij}} \exp \frac{-\left(k - N_t p_{ij}\right)^2}{2 N_t p_{ij}\left(1-p_{ij}\right)} & \text{otherwise.} \end{cases} \tag{3.6}$$

Both situations will occur when looking at large datasets with big map sections. The approximation with the Poisson distribution is typically used for pairs of nodes with a large spatial distance.

We introduced the streamflow network method by first looking at the absolute value of the velocity and then at its direction, one after the other. Hence it seems reasonable to split the elementary probability p_{ij} into a velocity component $p_{|\mathbf{v}|_{ij}}$ and an angular component $p_{\theta_{ij}}$, too. In first order we may approximate these two probabilities as independent from each other. Therefore the elementary probability p_{ij} follows as

$$p_{ij} \approx p_{|\mathbf{v}|_{ij}} \cdot p_{\theta_{ij}}. \tag{3.7}$$

The velocity probability $p_{|\mathbf{v}|_{ij}}$ is the probability to have a velocity large enough that the node j is reachable for wind from node i. Hence, it is the probability that $|\mathbf{v}|_i > \frac{d_{ij}}{T}$. Formally this probability can be calculated using the velocity probability density function $p\left(|\mathbf{v}|\right) \mathrm{d}v$ with the integral

$$p_{|\mathbf{v}|_{ij}} = \int_{\frac{d_{ij}}{T}}^{\infty} p\left(|\mathbf{v}|\right) \mathrm{d}v. \tag{3.8}$$

However, given a discrete sample time series for $|\mathbf{v}\left(t\right)|_i$, this integral can be estimated by sorting the time series and then finding the value closest to $\frac{d_{ij}}{T}$. The relative position of this value in the sorted series is then the estimated value of $p_{|\mathbf{v}|_{ij}}$. This estimate for $p_{|\mathbf{v}|_{ij}}$ mirrors the procedure when generating surrogates where we also only draw a random value from the time series.

The angular probability $p_{\theta_{ij}}$ is the probability to randomly draw a direction in the interval $[\theta_{ij} - u_\theta, \theta_{ij} + u_\theta]$. Assuming a uniform distribution for this random process

as when calculating the surrogates before, this probability is just the fraction of the whole circle which the corresponding circle section occupies. Thus,

$$p_{\theta_{ij}} = \frac{u_\theta}{\pi}. \tag{3.9}$$

Using the elementary probability p_{ij}, we can now calculate the probability $P_{ij}\,(k \geq h_{ij})$ which tells us how likely it is that h_{ij} (or more) hits occur just by chance. The adjacency matrix of networks follows by thresholding this probability with

$$A_{ij} = \begin{cases} 1 & \text{if } P_{ij}\,(k \geq h_{ij}) < \psi \\ 0 & \text{otherwise} \end{cases}. \tag{3.10}$$

It seems reasonable to choose the threshold ψ to fit the probability enclosed by $\mu_{\eta,ij} \pm n \cdot \sigma_{\eta,ij}$ when calculating the surrogates, so that both methods yield comparable networks.
This semi-analytic approach is just another way of calculating a streamflow network with similar properties as with the surrogates. It is an unweighted, directed network that emphasizes on the importance of paths through the network. The semi-analytic approach should save us a lot of computation time, though. The only computationally intensive task remaining is the integral for $p_{|\mathbf{v}|_{ij}}$. Solved by sorting the time series, with e.g. quicksort, and then searching for the position in the sorted array with a binary search, its computation time scales with $\mathcal{O}\,(N_t \cdot \log N_t \cdot \log N_t)$. This is much less than the computation of the surrogates for the simulation method.

3.3.2. Application to the SAMS

Before we utilize the streamflow networks for a thorough analysis of the variability of the low-level circulation of the SAMS, we will test them and compare the two different construction methods to each other to see which one we will use in our further analysis later and find suitable values of the parameters used in the construction.

Parameters

Table 3.1.: Overview over most used parameter choices for streamflow networks.

Travel time T	1 d
Angle uncertainty u_θ	$\frac{\pi}{6}$
Number of surrogates (simulation method) N_{stat}	200
Significance parameter n (simulation method)	2
Threshold probability ψ (semi-analytic method)	0.05

The travel time T and angle uncertainty u_θ are crucial for streamflow networks. T sets the radius of the circle section (Eq. 3.2) used to determine the network links.

Hence, there is a direct connection of T to the out-degree and thus also the link density of the network, ρ scales almost linearly with T (see Fig. A.1). We choose a travel distance $T = 1$ d as it results in a link density of about $\rho \approx 0.04$ which we consider large enough for the network to feature enough interesting features but not too large to show mostly spurious links.

The angle uncertainty u_θ is the central angle of the circle section and therefore also affects the out-degree of all nodes. However, the angle uncertainty will also affect paths through the network and the overall structure: The extreme case of $u_\theta = \pi$ would, e.g., result in an undirected network as the circle section becomes a whole circle. We should therefore choose an angle uncertainty that is large enough, so that enough connections are possible, but not too large, such that the directed nature of the streamflow networks is not lost. In fact, the link density ρ scales almost linearly with u_θ. We chose a fixed uncertainty of $u_\theta = \frac{\pi}{6}$. Future work could investigate variable angle uncertainties, e.g. by relating them to the variance of the wind direction. However, sensitivity analyses with varying choices of u_θ reveal that the qualitative spatial structure of the networks is very robust to small changes of u_θ (see Fig. A.3 and A.4), which also justifies to choose a fixed value of u_θ as a network parameter. Such a fixed angle uncertainty leads to a significantly simpler and computationally faster model. Furthermore, the almost linear increase of the link density with larger time lags (Fig. A.1) indicates that $u_\theta = \frac{\pi}{6}$ is a reasonable choice given the spatial grid resolution, since this increase would scale quadratically if the angle uncertainty were too large. In different settings and applications, however, we suggest to always explicitly check the robustness of the results to different choices of u_θ, and modify it in accordance to the local dispersion of the wind field if necessary.

Both of the statistical parameters n (simulation method) and ψ (semi-analytic method) will have a direct influence on the link density as well. However, we introduced both parameters as a threshold for statistical significance and therefore set these parameters such that a 95% confidence level is obtained. Here, we choose to set both statistical parameters to a similar level of significance with $n = 2$, which represents 95.45% for normal distributed values, and $\psi = 5\%$. This leads to both methods using a comparable parameter set.

In the Appendix Sec. A.1.2 there is an extended discussion of the parameter choices with additional results from varying the parameters T and u_θ, further justifying the parameter choices that we take.

Results

Given the parameter values that we just set, we compute streamflow networks for the core monsoon season in South America (DJF) using the MERRA dataset of wind fields at 850 hPa introduced in Sec. 3.2. Spatial distributions of centrality measures (see Sec. 2.1), computed for both the analytically and the numerically constructed network, can be seen in Fig. 3.3 to 3.5.

As mentioned in Sec. 3.2, in order to reduce boundary effects the networks are computed on a larger dataset with the centrality measures then cropped for the figures.

Boundary effects of the OAWC and IAWC of streamflow networks can be mitigated by choosing a larger map section because streamflow networks possess, by construction, a maximum link distance. By extending the map section by 20° of longitude, we add about 2000 km at 20°S or about 1000 km at 60°S in zonal direction to the map section. Low-level winds have a typical velocity of $\mathcal{O}\left(1\,\mathrm{m\,s^{-1}} - 10\,\mathrm{m\,s^{-1}}\right)$. When using a travel time $T = 1\,\mathrm{d}$ this yields a maximum link distance of approximately 900 km. The spatial embedding is therefore only relevant for the OAWC and IAWC for strong winds in high latitudes. Unfortunately, path-based centrality measures like betweenness are affected by spatial embedding in a more complex fashion. While we can thus not mitigate these effects completely, we reduce them by choosing larger map sections as well.

The OAWC of both network types exhibits the largest values south of 40°S. However, these values are smaller at the eastern than at the western boundary of the map section. Qualitatively, the spatial distribution of OAWC is very similar for both network construction methods. In fact, the relative difference between the semi-analytic and the simulated network is rather small. The semi-analytic network has a 0%-20% larger OAWC (and out-degree) for most parts of the network. The only larger area with an OAWC that is more than 50% larger for the semi-analytic method can be found in southern Brazil close to the border with Paraguay. This region (10°-30°S, 40°-50°W) exhibits a relatively small average wind velocity of only $2.87\,\mathrm{m\,s^{-1}}$, compared to the average wind velocity of the complete map section, $5.86\,\mathrm{m\,s^{-1}}$, and there is a change in wind direction in this area as there is a anticyclone east of it and the SALLJ west of it. Possible reasons for the relatively large differences between the simulation-based and analytical networks in this area are discussed below.

In order to investigate directional asymmetries of the streamflow networks, we consider the difference between out- and in-area weighted connectivity D_i. We find that the OAWC of both network types is much larger than the IAWC south-east of 50°S; 30°W, on both sides of the southern Andes in central Argentina and Chile, as well as in SESA. The OAWC is much larger over the Atlantic Ocean south of the continent as well as along the eastern slopes of the Andes in Bolivia, Paraguay, and northern Argentina. The area weighted connectivity difference D_i in this region is larger for the simulation method than for the semi-analytic one. Most parts of northern and central South America exhibit a very similar OAWC and IAWC.

The betweenness centrality of both network types is high along the eastern slopes of the Andes as well as in large parts of eastern and northeastern Brazil. Relatively, the simulation-based network shows larger values in these region and exhibits a more concise pattern. In particular, the simulation-based network has very high betweenness centrality along the Amazon river.

To investigate the seasonal dependence of these spatial patterns, we construct another simulation-based network for the austral winter season (JJA), which is also the dry season in most parts of South America. Fig. 3.6 shows the difference of the betweenness centrality between this JJA-network and the simulation-based DJF-network discussed above. During DJF, the betweenness is much higher along the eastern slopes of the Andes and most parts of northern South America, especially along three narrow bands: one around Los Llanos (0°N-10°N, 60°W-75°W), one south of the Guyana

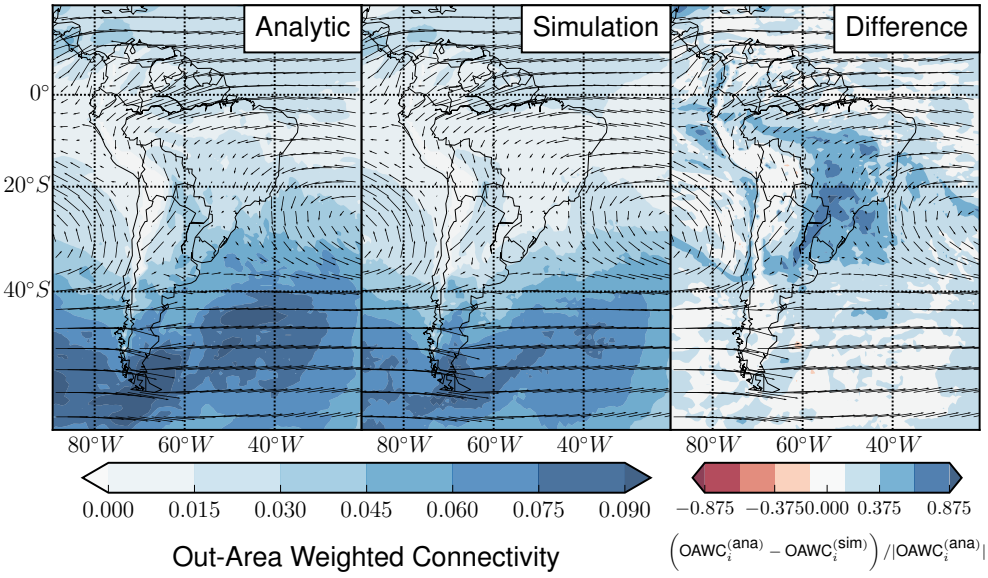

FIGURE 3.3.: OAWC of streamflow networks for both the semi-analytic (a) and the simulation-based (b) network construction method. The relative difference between both networks is shown in (c). The strong eastward winds south of 40°S dominate the OAWC. Qualitatively both methods produce networks with similar OAWC. The largest difference can be found in central and southern Brazil.

Shield (0°N-5°N, 55°W-70°W) and one along the Amazon river (0°S-5°S, 50°W-65°W) (all are marked in Figure 3.6). These bands align very well with the average wind field in these areas as well. The JJA-network exhibits higher betweenness centrality in Paraguay and south-western Brazil.

Comparing the Two Network Construction Methods

While some of the properties of the spatial distribution of the centrality measures shown before can be attributed to the network construction method itself and the boundaries of the map section we choose, other properties unveil important parts of the South American climate. We will compare the two network construction methods and the results of the centrality measures we evaluate them with.

The OAWC of the streamflow networks is, by construction, directly related to the wind velocity. The OAWC is largest in the south of the map section where strong eastward winds prevail. Overall, the OAWC of both networks types is very similar. The main difference (around 25°S, 55°N) is in a region with very low average wind velocities, east of the SALLJ and west of an anticyclone. It is not clear what exactly causes the difference between both network types in this region, apart from the approximations involved in the semi-analytic method. In particular, the assumption of the semi-analytic method that velocities and directions are independent, might not hold true in

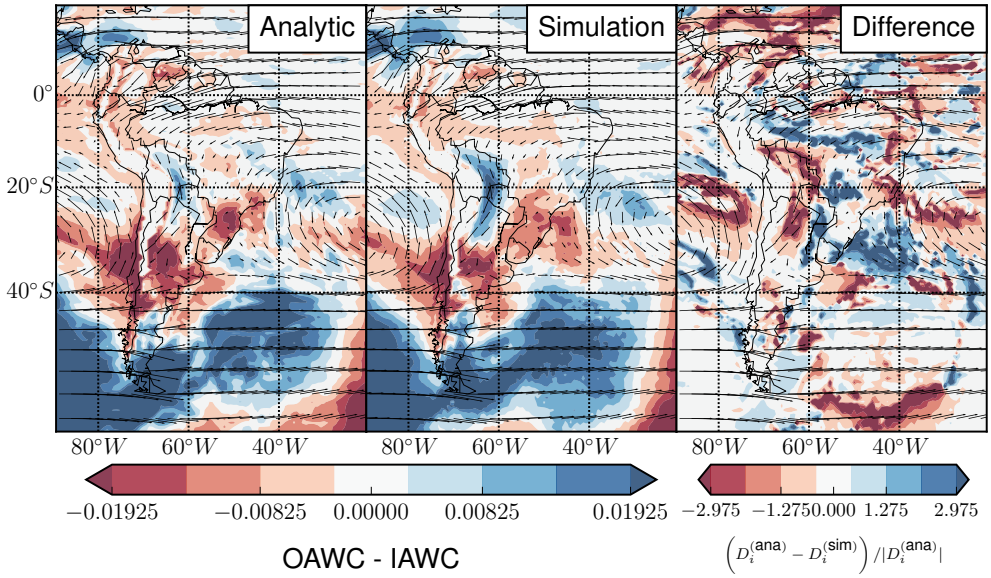

FIGURE 3.4.: Difference of out- and in-area weighted connectivity of streamflow networks representing the South American low-level circulation, for both the semi-analytic (a) and the simulation-based (b) network construction method. The relative difference between both networks is shown in (c). While the high values south of 40°S are caused by the spatial embedding, the large values along the eastern slopes of the Andes in Bolivia and northern Argentina indicate jet-like behavior caused by the South American Low-Level Jet (SALLJ).

this case. However, one should expect a low OAWC in this region due to the relatively low wind velocities which favors the simulation-based network.

The streamflow networks exhibit strong boundary effects due to their spatial embedding. These effects are especially visible for the OAWC and area weighted connectivity difference D_i (see Fig. 3.3 and 3.4): Nodes in the south-eastern corner of the map section show a smaller OAWC than in the south-west, although the average wind velocities are similar in both regions. As mentioned before, boundary effects are strongest in high latitudes and for strong winds. The wind field at these nodes is predominantly eastward and thus the nodes in the south-east would connect to nodes farther east, which are however not part of the considered map section anymore. A correction of these boundary effects with spatially embedded random networks (SERN) is not possible here for networks not based on correlation measures [172]. Fortunately though, the boundary effects are mostly restricted to the actual boundary, because the spatial link distance is limited by the wind velocity as discussed in the previous section.

D_i, the difference of OAWC and IAWC, encodes information about directional asymmetries of the network. Even though much of this difference at the edges of the map section is caused by boundary effects, it also contains valuable information about the wind field itself. Regions where the winds are slowed down and deflected by orographic

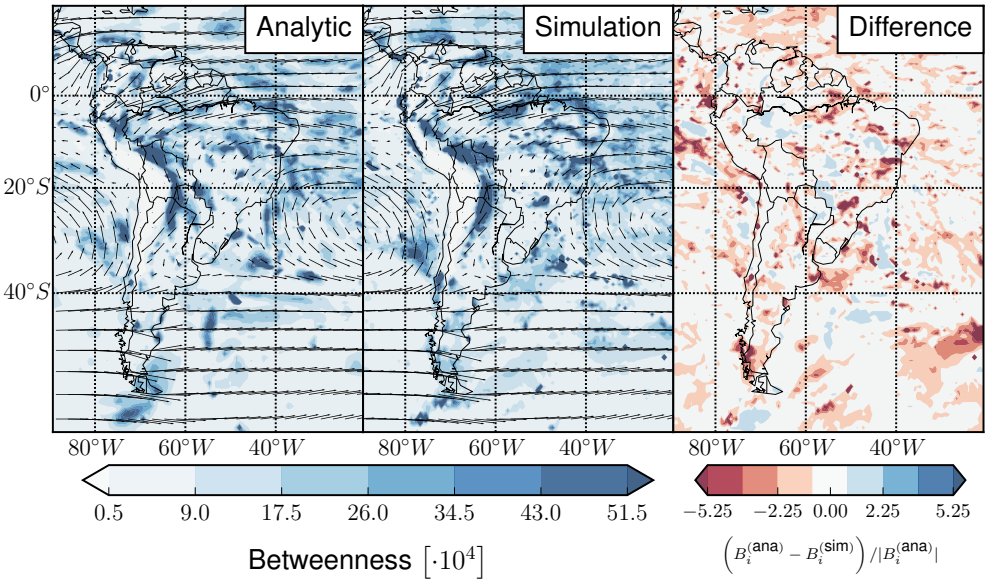

FIGURE 3.5.: Betweenness centrality of streamflow networks representing the South American low-level circulation, for both the semi-analytic (a) and the simulation-based (b) network construction method. The relative difference between both networks is shown in (c). A major difference between both methods is the high betweenness of the simulation network along the Amazon river.

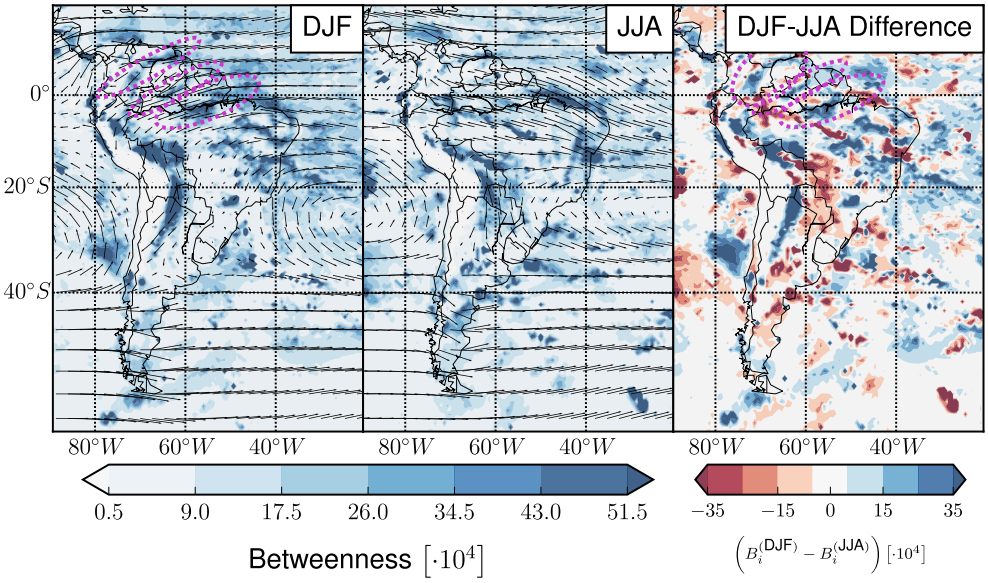

FIGURE 3.6.: Difference between wet and dry season of betweenness centrality of streamflow networks of South America, constructed with the numerical simulation method. Note the high betweenness during DJF along the eastern slopes of the Andes and along the three narrow band marked in magenta in northern South America.

barriers like the Andes result in large differences as well. More importantly, the SALLJ region has a much higher out- than in-area weighted connectivity. The winds leading into this region from the Amazon region are deflected by the Andes and are typically quite slow, which results in a low IAWC in the SALLJ region. Additionally, the wind speeds of the SALLJ are higher and the wind direction possesses multiple regimes, so that connections in multiple directions are possible. The observed difference in out- and in-area weighted connectivity can therefore be used to infer such a jet-like behavior. This is also true for the area along the Amazon river and around Los Llanos, which are the only regions in northern South America with a slightly larger out- than in-area weighted connectivity. This effect is present in both methods but it is stronger for the simulation method. The difference of OAWC and IAWC can thus be used to study the variability of the SALLJ as we will do in the next section.

The betweenness is probably the most important measure for the streamflow networks, which by construction call for a path-based analysis of their topology. Due to our choice of a construction method based on the local flows, we associate network paths with paths the wind could take in terms of an uninterrupted transport of air masses. The betweenness centrality, as a measure of the number of shortest paths running through a node, is therefore a key measure to evaluate which areas are the most important ones for the overall path structure. Jet-like structures that interconnect different areas of the network are particularly emphasized by the betweenness centrality.

The difference between the betweenness of both methods is spread over the whole map section. The largest and most important difference is a region of high betweenness along the Amazon river for the simulation method that is only very weakly present for the semi-analytic method.
Both methods produce networks which are overall very similar to each other. Differences appear only in the detail and thus one can safely pick the semi-analytic method when computation time is an issue. However, the simulation method might be able to reveal important wind paths slightly better and is therefore picked for our further investigations.

Climatic Interpretation of the Results

The streamflow networks provide a network representation of the low-level atmospheric circulation. By evaluating centrality measures and their spatial distribution we can identify many key features of the South American climate and its low-level circulation pattern. Aside from the strong winds south of South America, this pattern is dominated by the incoming trade winds in northern South America that are, after crossing the Amazon basin, deflected southward by the Andes and channeled into the SALLJ (see Sec. 3.1). The streamflow networks identify these important features: networks of both construction methods (simulation-based and semi-analytic) exhibit high betweenness values in the SALLJ and the Amazon region, thus indicating the

relevance of these areas in terms of important transport routes of the low-level circulation. Additionally, the wind paths of the incoming trade winds over the northern Amazon basin are clearly visible in the betweenness in terms of three narrow bands of high betweenness as well (see Fig. 3.5).

Furthermore, the climate of South American is strongly influenced by frontal systems originating from the southern extra-tropics, caused by Rossby waves that propagate across the southern Pacific ocean [25, 32, 209, 210]. In the vicinity of the southern tip of the South American continent, the absolute value of the mean wind field strongly influences the OAWC as visible in Fig. 3.4. However, the spatial pattern of the difference between out- and in-area weighted connectivity D_i is not solely determined by this climatologically westerly wind direction. The large areas of positive differences of out- and in-area weighted connectivity around $50°S$ in combination with the negative differences over southern South America around $40°S$ can be associated with the northward propagating frontal systems, which transport cold, dry air northward at low atmospheric levels. In this sense, the difference between out- and in-area weighted connectivity gives us a form of divergence, a notion of sources and sinks of the dominant circulation patterns.

Regarding interseasonal variability, we compare networks of the wet season (DJF) against networks of the dry season (JJA) in Fig. 3.6. The results shows that the betweenness centrality is able to capture the activity of the monsoon: During the wet season the betweenness along the slopes of the Andes and northern South America, where most moisture is transported to southern South America, is much larger than during the dry season (JJA). As mentioned in the previous paragraph, these incoming north-easterly trade winds are visible in the spatial distribution of the betweenness for DJF, but are strongly diminished for JJA.

As we have shown, the streamflow networks are able able to unveil important characteristics of a regional climate system like the South American monsoon. They provide an accurate, coarse-grained representation of the low-level atmospheric circulation that focuses on the key features thereof and can thus serve as a tool for the deeper in analysis of the variability of the low-level atmospheric circulation in the next section. For this purpose we will choose the simulation-based method to construct the streamflow networks. Even though both methods, the simulation-based and the semi-analytic method yield qualitatively similar networks, the simulation-based seem to be advantageous when evaluating the important path-based measures that a lot of analysis will focus on. Especially the betweenness centrality captures important wind paths like trade winds and the SALLJ very well. The large difference observed between the wet and dry season networks indicates that the betweenness centrality of the proposed networks can also be an indicator for the overall activity of the monsoon. The enhanced trade winds and SALLJ during the wet season are in accordance with the literature about the South American Monsoon System. Additionally, the spatial pattern of the difference between out- and in-area weighted connectivity provide information about jet-like behavior, as well as about sources and sinks of the dominant circulation patterns.

3.4. Variability of the Low-Level Circulation

As we established streamflow networks as a suitable tool for the analysis of the low-level circulation, we will now focus on analysing the variability of the low-level circulation of the SAMS. In particular, we focus on the strength of the monsoon, in terms of its active and break phases, which is an intraseasonal variability and the impact of the ENSO, an intraannual variability.

In Sec. 3.1, we already introduced the active and break phase of the SAMS and a criterion based on the anomalous wind direction introduced by Jones and Carvalho [94] to classify them. Monsoon systems like the SAMS are the result of a complex interplay of atmospheric processes on various spatial and temporal scales [240]. The strength or activity of a monsoon is most easily noticeable in terms of anomalously high precipitation. The strength of the precipitation is naturally coupled to the low-level circulation of the monsoon system. The spatiotemporal characteristics of the active and break regimes, as well as the variability of some key features of the SAMS in response to them, has not been thoroughly explored yet. The subdivision into active and break phase is solely based on the low-level wind direction in a small reference region, yet both phases exhibit large-scale differences [94]. This makes active and break phases an ideal study object for our streamflow networks. However, we will also investigate composites of other observables such as the precipitation during the phases further corroborate the network results.

The active and break phases are part of the intraseasonal variability of the SAMS. On the intraannual scale, the ENSO is one of the major factors of variability. Existing studies investigating the impact of the ENSO on the low-level circulation of the SAMS have mainly focused on case studies of single events [e.g. 207, and references therein]. Hence, we will study the impact of ENSO on the spatiotemporal characteristics of low-level circulation over the last decades.

3.4.1. Intraseasonal Variability of the SAMS Caused by Active and Break Phases

In the original study on active and break phases of the SAMS, the reference region used to distinguish the two phases was placed in the brazilian state Rondônia [94]. When investigating the SAMS with the MERRA dataset (see Sec. 3.2), it became apparent that there are differences to the NCEP/NCAR dataset used by Jones and Carvalho [94]. Whereas the NCEP/NCAR dataset exhibits an overall westerly wind regime in Rondônia, the MERRA dataset exhibits a broad northerly wind regime in Rondônia. We therefore shift the reference region southward by 4° to (13°-18°S, 59°-65°W) to retain a narrower, westerly wind distribution in the reference region with the MERRA dataset as well. This area corresponds roughly to the Bolivian districts Beni and Santa Cruz. Fig. 3.1 shows both, the location of the Rondônia reference region and the new reference region in Beni and Santa Cruz (BSC). A more detailed discussion of the choice of the reference region can be found in the Appendix Sec. A.1.4.

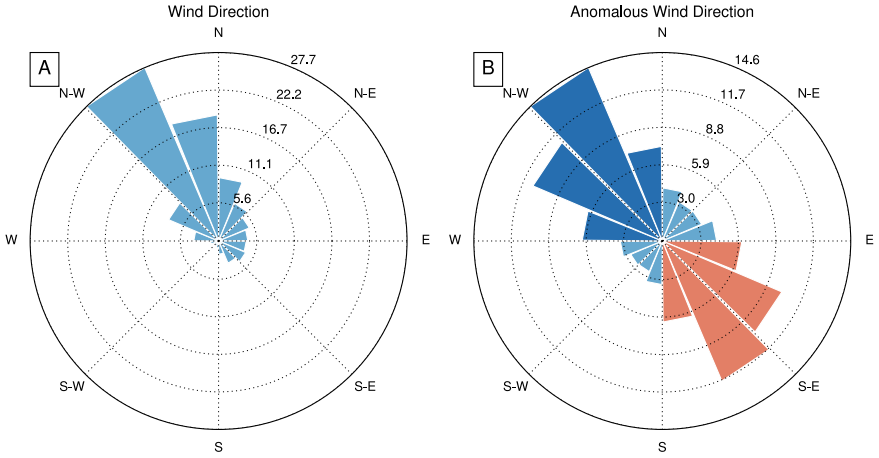

FIGURE 3.7.: Histograms of wind directions at 850 hPa in the Bolivian districts of Beni and Santa Cruz (13°-18°S, 59°-65°W, see Fig. 3.1). While the normal wind direction (A) exhibits only one broad regime, the direction of the anomaly wind vector field (B) exhibits two distinct regimes: the easterly regime (orange) and the westerly regime (dark blue). Fig. 3.8 shows the corresponding wind fields. The wind direction is, by convention, the direction the wind originates from.

The wind direction within this reference region exhibits the two distinct regimes when the seasonal climatology is removed from the wind field component-wise (see Fig. 3.7). As introduced in Sec. 3.1, these regimes can be identified with active and break phases of the monsoon. The active regime exhibits an north-westerly wind direction ($[\pi/2, \pi]$, when east is identified with the angle zero). The break regime exhibits the opposing south-easterly wind direction ($[-\pi/2, 0]$). Based on these two wind regimes, we subdivide the time series into an active (westerly) time series and a break (easterly) time series by applying the following rule: A time step is considered to be in the active or break regime, respectively, if 75 % or more of the nodes in BSC exhibit an anomaly wind direction of the corresponding direction interval. This classification is robust to small changes of this percent value. For the examined time series from 1985 to 2010, 26 % of the days during the DJF seasons are classified as active and 21 % of the days of the DJF seasons are classified as break. Time steps for which the wind direction is between these two regimes are not further investigated.

Wind and Precipitation Composites

The wind fields for both regimes is shown in Fig. 3.8. While the active regime exhibits a stronger cross-equatorial flux with faster winds along the eastern slopes of the Andes, during the break phase easterly winds from southern Brazil flow towards Paraguay and Bolivia.

The strongest absolute winds are the year-long strong westerly winds in the southern Atlantic and Pacific. These exhibit a south-westerly direction in Patagonia during

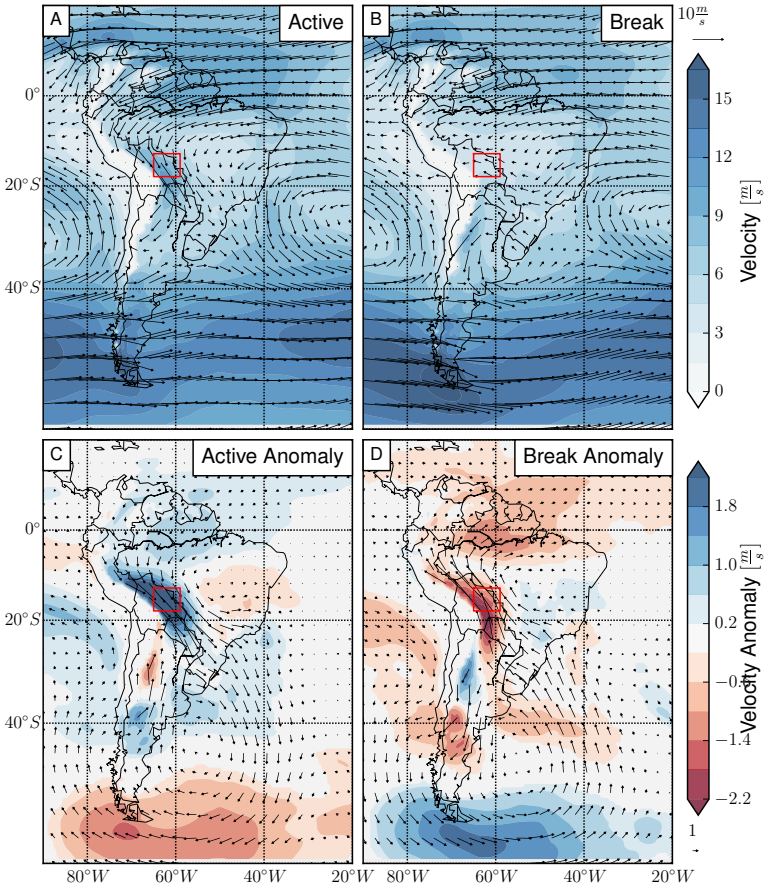

FIGURE 3.8.: Wind fields at 850 hPa during active (A) and break (B) regimes for the DJF season. The arrows indicate the wind direction and strength. The top row uses the regular meridional and zonal wind components during the active and break phases, respectively. The bottom row shows anomalous wind fields. The absolute value of the wind is color-coded in all subfigures. The bottom row panels show the anomalous absolute value. Only absolute value anomalies at a 95 % significance level due to a t-test are shown. During the active phase the South American Low-Level Jet (SALLJ) is visibly enhanced. Between the active and the break phase the direction of the anomalous wind vectors is reversed.

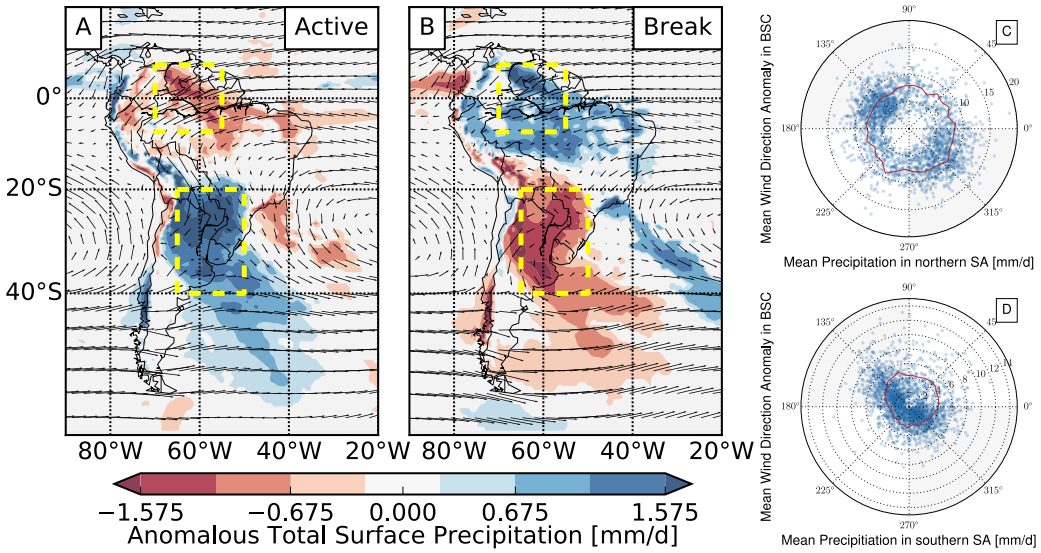

FIGURE 3.9.: Anomalous total surface precipitation of the active (A) and the break (B) regimes based on MERRA. The anomalies are computed with respect to the DJF climatology. Statistical significance was determined with a one-sample t-test, and non-significant ($p > 0.05$) anomalies are shown in white. The active phase is characterized by enhanced precipitation in southern Brazil, SESA and Bolivia, whereas the break phase exhibits strong precipitation in Venezuela, Peru and the Amazon basin. The rose plots in the right panel show the mean daily precipitation of all nodes within the yellow, dashed rectangles in northern South America (C) and southern South America (D), depending on the wind direction in Beni and Santa Cruz. The wind direction in Beni and Santa Cruz is the circular mean of the wind direction of all nodes within this reference region (see Fig. 3.1). Note, that the wind direction, per convention, is the direction the wind originates from. In southern South America, highest precipitation occurs when the region of Beni and Santa Cruz exhibits a northwesterly wind direction, whereas less precipitation occurs for southeasterly anomalies. The red, solid line indicates the mean precipitation of all data within the corresponding 1/32 of the whole circle.

the active phase and a westerly to north-west-westerly direction during the break phase. The anomaly wind field of the active phase is characterized by strong north-westerly winds close to the eastern slopes of the Andes, which indicates a substantially strengthened SALLJ. These north-westerly winds lead into a cyclone south of Uruguay over Argentina and the adjacent Atlantic ocean. The anomalous wind direction of the break phase is almost exactly reversed, with a suppressed SALLJ and the cyclone replaced by an anticyclone. All the anomalies shown, e.g. in Fig. 3.8, were subject to a one-sample t-test. Non-significant anomalies ($p > 0.05$) are not shown.

The role of the wind regimes to classify the activity of the SAMS becomes clear when investigating the precipitation anomaly composites of the two regimes (Fig. 3.9). During the active phase there is substantially more precipitation in SESA and southern Brazil. While the daily mean precipitation is about 3 mm when there are predominately easterly winds in BSC, it increases to 4.1 mm when they are predominately westerly winds in BSC. During the break phase there is more precipitation in the Amazon and northern South America. While the absolute differences in precipitation in these regions are similar to the differences induced in SESA, the relative differences are smaller. The spatial distribution of precipitation shows that the westerly and easterly anomaly wind regimes have a strong impact on the activity of the SAMS. For this reason, these monsoon phases provide an ideal application for our streamflow networks.

These results on wind and precipitation composites for the active and break phases are, although derived from distinct datasets, qualitatively inline with the earlier results of Jones and Carvalho [94].

Network Results

The streamflow networks were constructed with the same parameters and from the same dataset as in the previous section when first introducing them. In the following analysis we want to analyse the intraseasonal variability of the SAMS with the networks by computing different networks from the active and break phases. We choose to present both normal network measures and network measure anomalies. For this purpose, we compute a reference streamflow network representing the DJF climatology with the same parameter set that we use for all other networks. For each node-based centrality measure X, its anomalies follow as the difference between the centrality measure of the corresponding phase X_i^{phase}, and the centrality measure of the DJF-network X_i^{DJF}: $\hat{X}_i = X_i^{\text{phase}} - X_i^{\text{DJF}}$. The difference between two phases is the same for anomalies and normal network measures, since we do not rescale the anomalies: $X_i^{\text{Diff}} = X_i^{\text{phase 1}} - X_i^{\text{phase 2}} = \hat{X}_i^{\text{Diff}}$.

The link density ρ of the networks ranges between 0.023 and 0.028. The network of the full DJF season exhibits the largest value of ρ. Generally, larger variances of the wind direction tend to result in larger link densities and the variance of the wind direction is naturally lower when we consider only subsets of the time series, based on the wind direction of the reference region BSC. In contrast to studies using climate networks based on pairwise similarity measures where the link density is usually kept

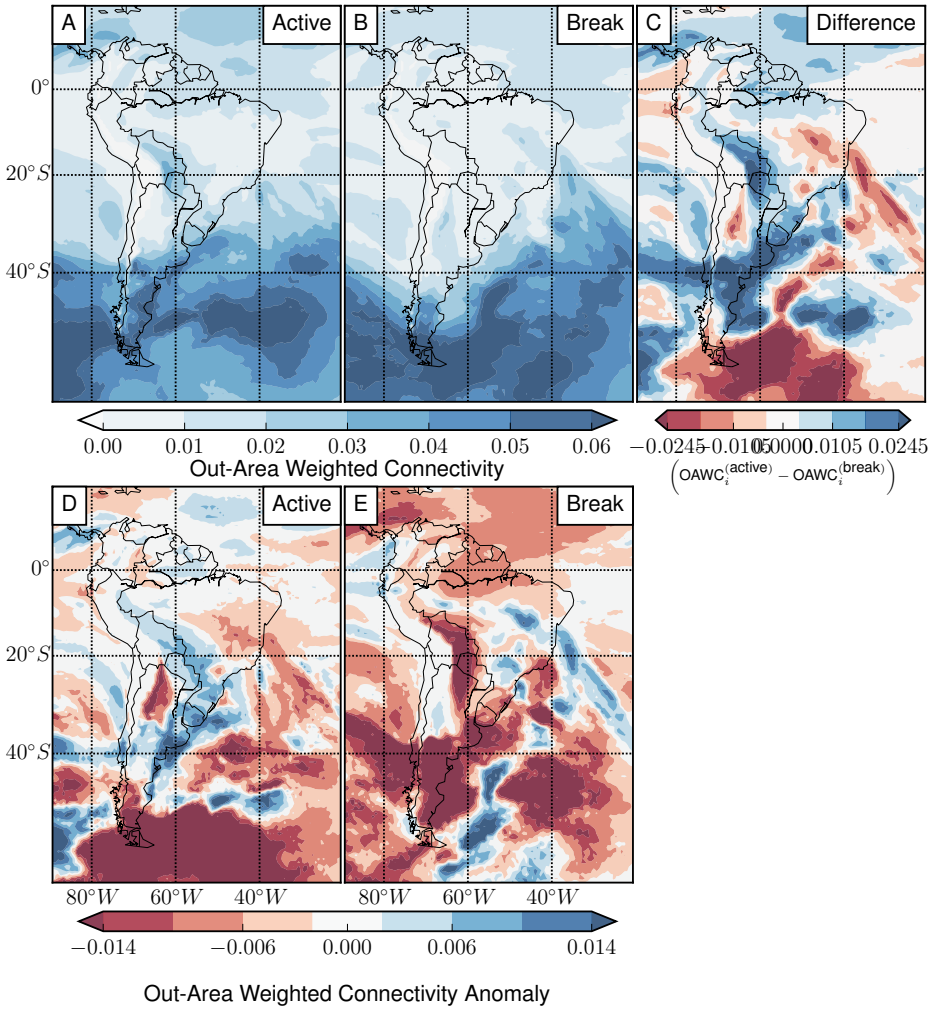

FIGURE 3.10.: Out-area weighted connectivity (OAWC) of streamflow networks computed separately for the active and break phase of the SAMS, as well as the difference between these phases, are shown in the top row. The bottom row shows anomaly measures that were calculated by subtracting the network measures of a streamflow network of the complete DJF season. The OAWC is dominated by the strong eastward winds in the south of South America. Key differences between both phases can be found along the eastern slopes of the Andes.

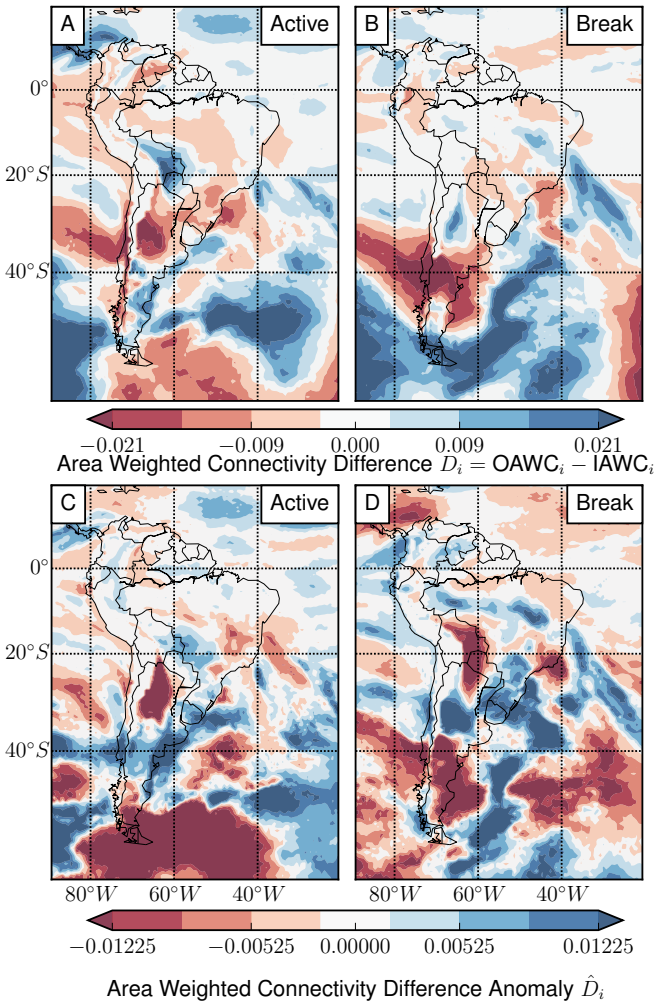

FIGURE 3.11.: Difference between out- and in-area weighted connectivity D (see eq. 2.9) of wind networks for the active and break phase of the SAMS. Like in the other figures showing network measures, the anomaly measures were calculated by subtracting the network measures of a streamflow network for the complete DJF season. The SALLJ area in Bolivia and Paraguay exhibits high values during the active phase. This area of high values is shifted southward during the break phase.

constant when comparing multiple networks [59, e.g.], we do not keep it constant. The streamflow networks are directly related to the underlying wind field, and in such a case the link density is just another network measure. However, to be certain, we tested a constant link density by adjusting the statistical parameter n (see Sec. 3.3). The resulting, corrected anomalies for the path-based network measures are almost identical to the non-corrected anomalies (not shown). This is due to path-based measures like the betweenness relying shortest paths through the network. A larger variance of the wind direction adds only relatively few shortest paths to the network, and path-based measures are relatively resilient to small changes of ρ. This also supports our association of important wind paths with path-based measures of streamflow wind networks (see Sec. 3.3.2). In the following the spatial distribution of the centrality measures is discussed, please refer to Fig. 3.1 for some of the geographical regions and abbreviations used from them. Primarily focusing on the measures on the continent, the spatial distributions of the OAWC of the networks computed for the active and break phases

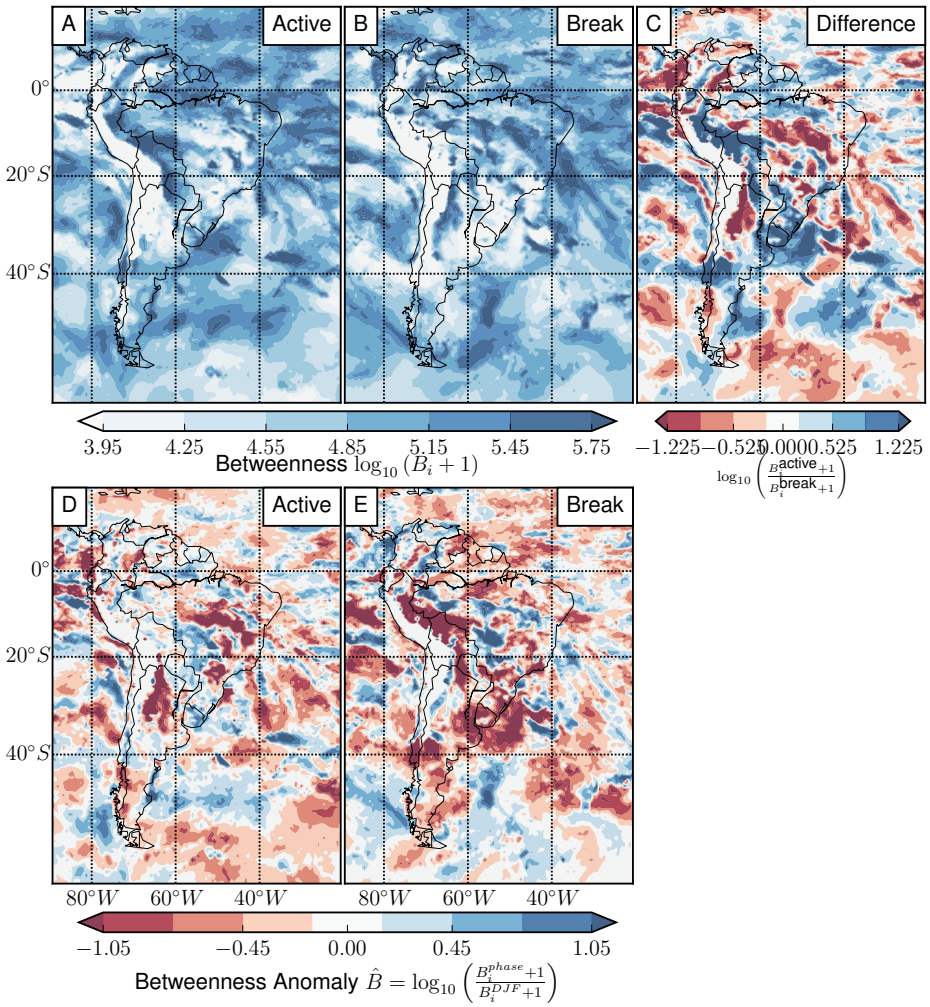

FIGURE 3.12.: Betweenness centrality (see eq. 2.5) of wind networks of the active and break phase and the difference between them. During the active phase the SALLJ along the eastern slopes of the Andes is much more pronounced. As the range between the minimum and maximum betweenness of a network is quite large and scales with the number of nodes [148], it is common to show the logarithm of the betweenness. The anomaly is shown as the difference of logarithms as well.

are, overall, quite similar (top row of Fig. 3.10): largest values can be observed in the south, where strong eastward winds dominate. Furthermore, both phases exhibit a west-east asymmetry in high latitudes due to the spatial embedding that was already discussed in Sec. 3.3.2. The OAWC displays the largest difference between the active and the break phase in central and southern South America. The eastern slopes of the Andes exhibit a stronger OAWC for the active phase in Venezuela, Peru, Bolivia, Paraguay and southern Argentina. Furthermore, the whole Argentinian coast exhibits a much larger OAWC during the active phase. The Amazon has higher OAWC values during the active phase as well. In contrast, the break phase exhibits substantially higher OAWC values in northern Argentina in the Gran Chaco area, as well as in eastern and central Brazil. The network measure anomalies (bottom row of Fig. 3.10) are qualitatively similar to the difference between both phases, which implies that the DJF-network used to calculate the anomalies exhibits values in the middle between the extreme cases (active and break phases). It is most apparent that the break phase exhibits strongly negative anomalies along the eastern slopes of the Andes.

For both phases, the difference of out- and in-area weighted connectivity D (see Fig. 3.11) exhibits the largest values in southern South America and over the subtropical Atlantic ocean. During the active phase there is a small band of positive difference in Los Llanos (LLA) and more prominent areas of positive D in northern Bolivia and Peru (NBP), where the network of the break phase exhibits D values close to zero. The break phase exhibits strongly positive D values in the Gran Chaco area, where the active phase on the other hand boasts negative D values. During the active phase, there are positive D_i values in Patagonia (PAT), which is even more apparent in the anomaly measure. Furthermore, there is an area with a strongly negative D north of it.

The betweenness centrality over the South American continent (Fig. 3.12) exhibits large values along the eastern slopes of the Andes. This band is much longer and stronger during the active phase. Especially the betweenness anomaly (bottom row of Fig. 3.12) shows strongly negative values along the eastern slopes of the Andes during the break phase. We observe only few mid- or large-sized areas on the South American continent where the break phase exhibits larger betweenness values than the active phase: the Guyana highlands (GUY), eastern Brazil, and the Gran Chaco area.

Geopotential Height Composites

In addition to the network analysis and the investigation of precipitation anomalies, geopotential height composites also provide information about the state of the atmospheric circulation during the active and break phases (see Fig. 3.13 and 3.15). These composites were formed by averaging the geopotential height of the corresponding time series of the active and break phases, and subtracting the climatology for DJF.

The geopotential height at 850 hPa (GPH850) exhibits negative (positive) anomalies along the eastern slopes of the Andes during the active (break) phase, starting in Bolivia and extending further southward. There is a local minimum (maximum) in the Gran Chaco area, indicating the enhanced (suppressed) northern Argentinean Low

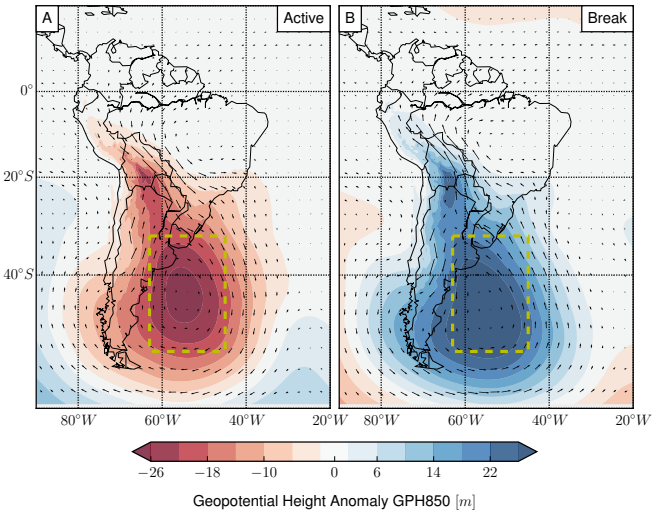

FIGURE 3.13.: Geopotential height at 850 hPa during the active and break phase. The anomalies were calculated by subtracting the DJF-mean and are significant at a 95 % level. Black arrows represent the mean anomaly wind field at 850 hPa during the corresponding phase. The yellow, dashed line marks the area with the largest differences that is referred to in the text.

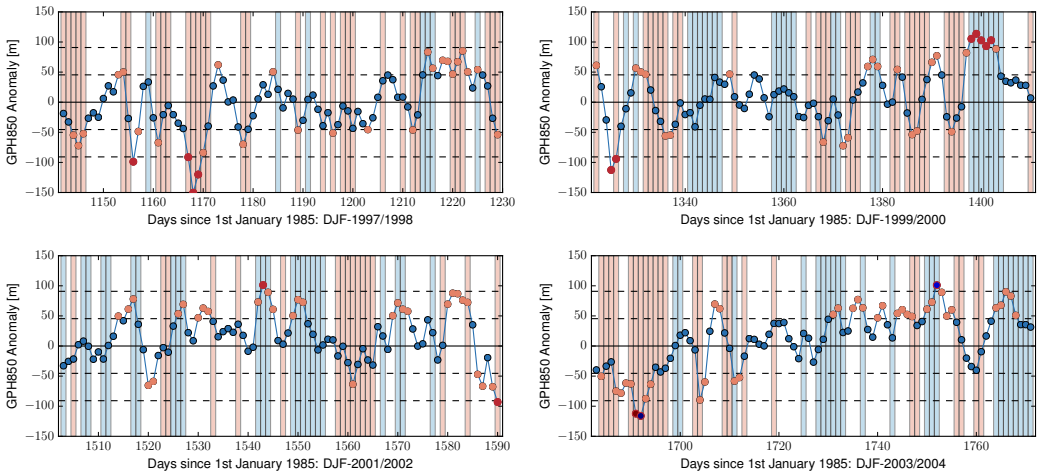

FIGURE 3.14.: Spatial mean of the anomaly of the geopotential height at 850 hPa (GPH850) in the southern Atlantic (refer to Fig. 3.13 for the exact region). In order to demonstrate the intraseasonal evolution of the GPH850 and the relation to the active and break phases, four years of the time series have been chosen at random. The horizontal dashed lines mark multiples of the empirical standard deviation σ_{GPH850}. Spatially averaged GPH850 values are marked in orange if $|\mathrm{GPH850}| \geq \sigma_{\mathrm{GPH850}}$, and in red if $|\mathrm{GPH850}| \geq 2 \cdot \sigma_{\mathrm{GPH850}}$. In the background, all days that belong to the active phase are colored in light red and all days that are part of the break phase are colored in light blue.

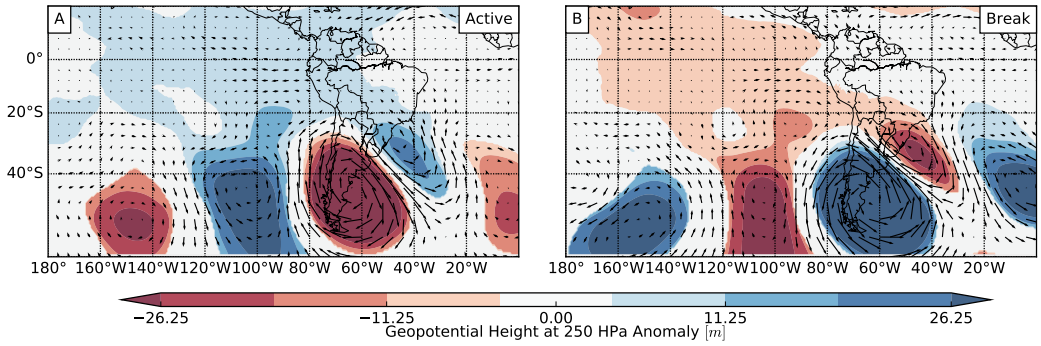

FIGURE 3.15.: Geopotential height anomaly at 250 hPa of the active (A) and break (B) phase of the SAMS, calculated by removing the DJF-mean from time series and averaging over all time steps of the respective phase. Black arrows are proportional in length to the anomalous wind field at 250 hPa of the corresponding phase.

(NAL) during the active (break) phase. The largest differences can be found in an anomalous cyclone over the southern Atlantic ocean east of Argentina, which extends into the aforementioned pressure anomaly at the eastern Andean slopes. The low-pressure cell that can be observed east of southern Argentina results in strong south-westerly winds in southern Argentina and over the adjacent Atlantic ocean during the active phase. In contrast, the wind direction during the break phase is westerly to north-westerly.

As this anomalous low/high pressure system in the subtropical Atlantic is one of the most distinctive differences between the active and break phase, it is subject to further investigation. Fig. 3.14 shows the intraseasonal evolution of the GPH850 in relation to the active and break phases. The GPH850 anomaly varies around zero in a close-to-periodic fashion, with active events generally occurring more often during negative anomalies and break events occurring more often during positive anomalies. The mean of the GPH850 during active phases is $\text{GPH850}_{\text{active}} = -22.7 \pm 44.5$ m, compared to $\text{GPH850}_{\text{break}} = 25.6 \pm 42$ m during break phases. Here, the empirical standard deviation of all GPH850 values that belong to the corresponding phase is used to estimate the uncertainty of the mean. There is an overlap between the GPH850 values of the regimes, however this overlap does not include the mean values of the opposing phase.

The average length of an active phase is 2.52 ± 1.8 days and the length of break phases is 2.26 ± 1.77 days. However, as already recognizable in Fig. 3.14, there are many occasions when only single days interrupt the active phase. If one would choose to loosen the criterion or smoothen the wind direction signal, it would most likely result in much longer average lengths.

The upper-level circulation is primarily characterized by Rossby Waves, the westerlies, and the Bolivian high. The geopotential height anomalies at 250 hPa (see Fig. 3.15) reveal opposing patterns of Rossby wave trains for the two composites: The active phase exhibits negative anomalies over southern South America and posi-

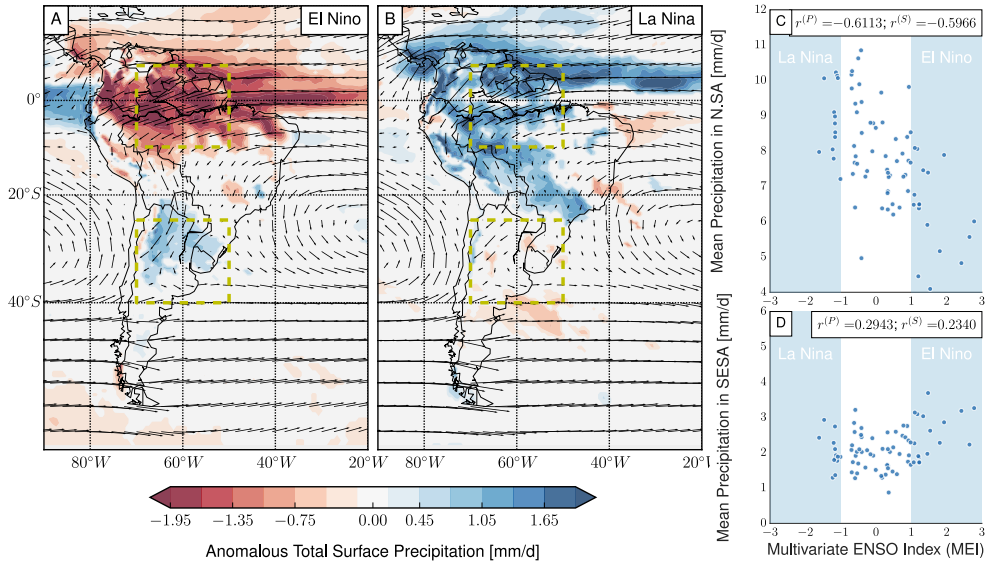

FIGURE 3.16.: Anomalous total surface precipitation during El Niño (A) and La Niña events (B). The anomalies were computed with respect to the DJF climatology. Regions with non-significant ($p > 0.05$) anomalies, as calculated with a one-sample t-test, are shown in white. The black arrows encode the mean magnitude and direction of the wind field during El Niño or La Niña events, respectively. For the correlation analysis mean daily precipitation for each month was computed separately for northern South America (C) and southern South America (D) (marked by yellow, dashed lines, respectively). The correlation between this mean precipitation value and the monthly Multivariate ENSO Index (MEI) was estimated with the Pearson correlation coefficient $r^{(P)}$ and Spearman's rank correlation coefficient $r^{(S)}$.

tive anomalies in southern Brazil. Central and northern South America exhibit slightly positive anomalies. In contrast, the break phase has positive anomalies at the southern South America, negative anomalies in southern Brazil, and slightly negative values in central South America. The position and the sign of the largest GPH250 anomalies in southern South America correspond well to the GPH850 anomalies.

3.4.2. Interannual Variability of the SAMS Caused by the ENSO

The El Niño Southern Oscillation (ENSO) is one of the most important sources of interannual variation for the SAMS [34]. For our investigation of the variability of the low-level circulation to the ENSO, we subdivide the time series in a positive ENSO (El Niño) and a negative ENSO (La Niña) part according to the Multivariate ENSO Index (MEI) [247]. When MEI ≥ 1 a month is considered to be an El Niño month and when MEI ≤ -1 a month is considered to be a La Niña month. Given the dataset that spans from 1985 to 2010, restricted to the austral summer, this results in 17 El Niño and 13 La Niña months.

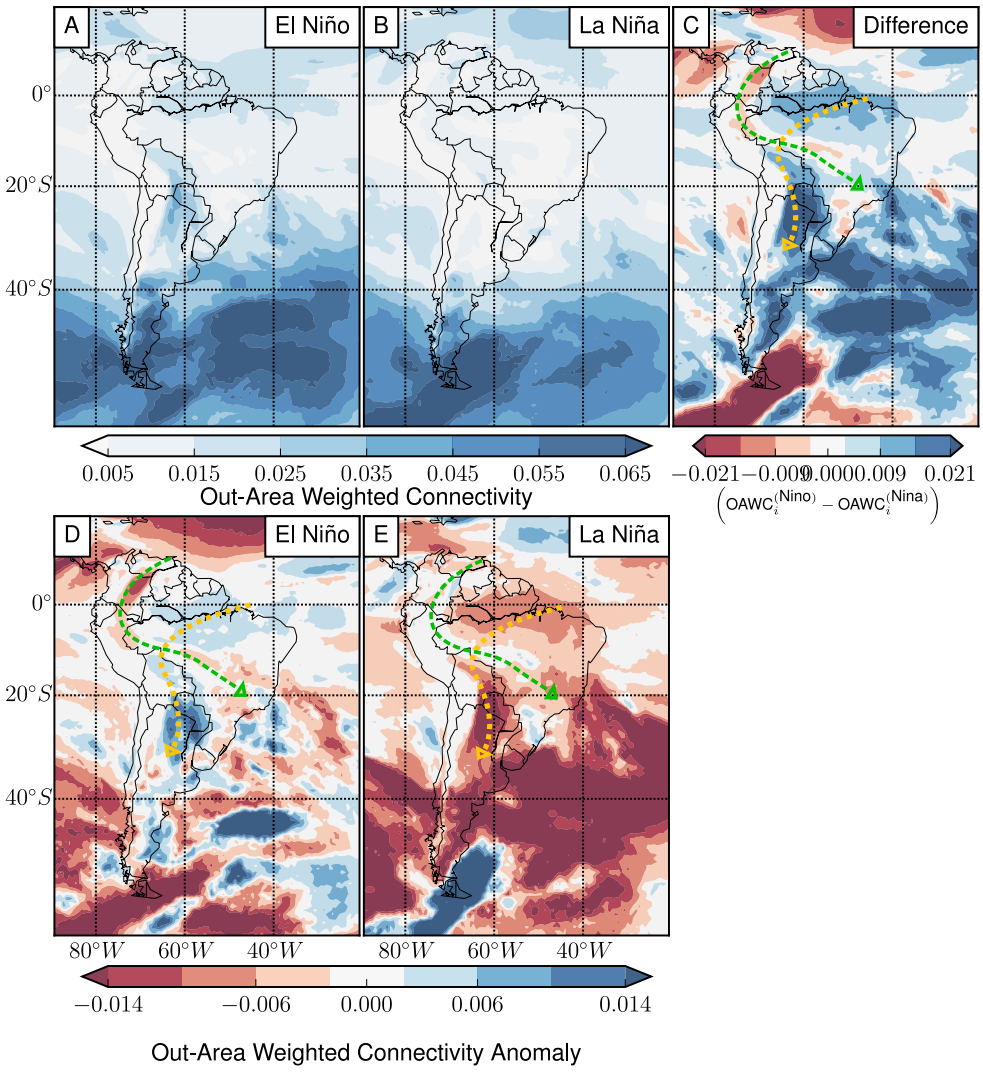

FIGURE 3.17.: Out-area weighted connectivity (OAWC, see Eq. 2.8) of streamflow wind networks during El Niño and La Niña phases. The top row shows the normal network measures and the difference between the two ENSO phases. The bottom row shows anomaly OAWC which are, as before, computed as the differences between the OAWC of the respective phase and the OAWC of the complete DJF season. The El Niño network exhibits larger values for most parts of the map. Especially noteworthy is the large OAWC during El Niño phases at the eastern slopes of the central Andes in Bolivia, Paraguay and northern Argentina. The La Niña network exhibits slightly larger OAWC along the eastern slopes of the northern Andes. The dominant enhanced large-scale wind path during El Niño conditions is marked in yellow, whereas the weakened wind path is shown green. Conversely, the yellow wind path is attenuated and the green wind path enhanced during La Niña events.

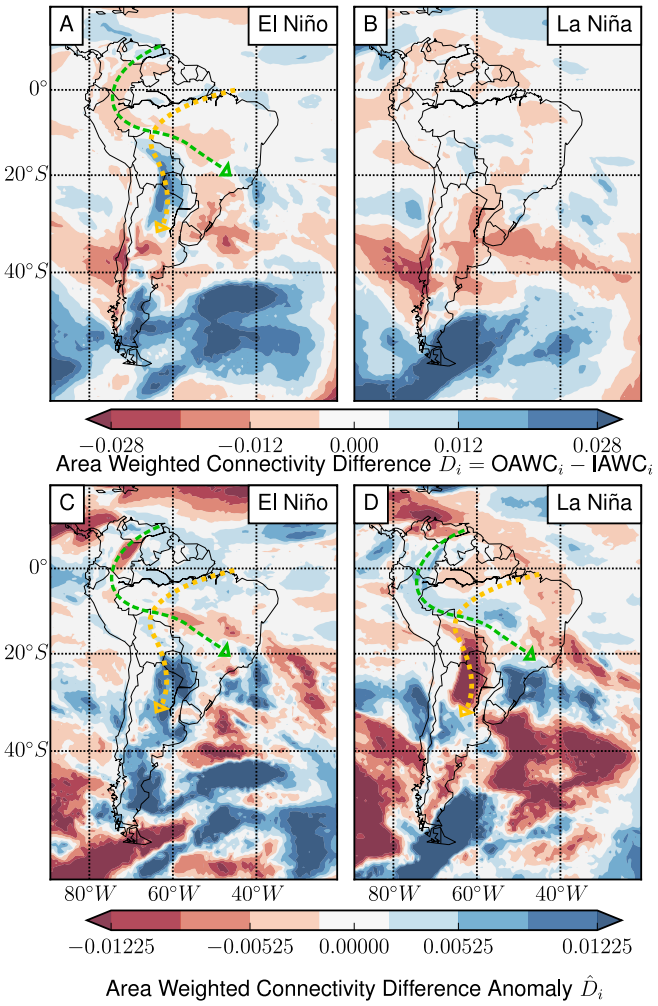

FIGURE 3.18.: Difference of out- and in-area weighted connectivity D (see Eq. 2.9) of the El Niño and La Niña phases. The anomalies were calculated with respect to a network of the complete DJF season. Note the strongly negative anomalies along the eastern slopes of the Andes in Bolivia and northern Argentina during La Niña events. As in Fig. 3.17, the dominant large-scale wind paths are shown.

Fig. 3.16 shows the precipitation anomalies of El Niño and La Niña months as well as scatter plot of the MEI against precipitation in northern and southern South America. There is a negative correlation between the MEI and the precipitation in northern South America, including most parts of the Amazon. In contrast, average precipitation in SESA is larger during El Niño. However, there is no clear correlation between the precipitation in SESA and the MEI as the Pearson coefficient is only $r^{(P)} = 0.29$ and the Spearman coefficient is $\rho^{(S)} = 0.23$. The low-level circulation is affected by the ENSO as well, as studies suggest a strengthening of the SALLJ during El Niño events [207].

The network of the El Niño phase exhibits a larger link density than the La Niña network for otherwise constant parameters ($\rho_{\text{Niño}} = 2.6\%$ and $\rho_{\text{Niña}} = 2.3\%$). On the South American continent, the OAWC is distinctively larger during El Niño events along the eastern slopes of the central Andes in Argentina, Paraguay and Bolivia. The El Niño anomaly exhibits distinctly negative values at the slopes of the northern Andes,

but positive anomalies in the Amazon. Contrarily, the La Niña network exhibits larger OAWC values on the eastern slopes of the Andes in Venezuela and Peru (see Fig. 3.17) and strongly negative anomalies in Argentina, Paraguay and the Amazon.

The area weighted connectivity difference D exhibits key differences between the ENSO types at the eastern slopes of the Andes as well (Figure 3.18). The El Niño network exhibits negative values both in the normal and the anomaly measure in Llanos and south of it, where the La Niña network exhibits positive D anomalies. These positive anomalies extend eastward to central Brazil. In NBP and Gran Chaco the El Niño network exhibits positive D values with positive anomalies extending southward until the southern tip of South America. Contrarily, the La Niña network only shows small area weighted connectivity difference in these regions, but exhibits strongly negative anomalies in NBP and Gran Chaco.

3.4.3. Discussion

Active and Break Phases of the SAMS

Cross-equatorial Flow and Low-Level Jet

We subdivided the wind field time series based on a small reference region in northern Bolivia (BSC). Although the strength of the anomaly wind fields for the active and break monsoon phases weakens the further away from BSC one goes, both network types exhibit large differences across the South American continent and the adjacent oceans in all network measures that were investigated.

There is hardly any cross equatorial flow in the break phase. The investigation of the OAWC and betweenness shows that both, the trade winds toward and across the Amazon, and the southward flow along the slopes of the Andes, are much stronger during the active phase. This flow along the eastern slopes of the central Andes constitutes the SALLJ. The betweenness and area weighted connectivity difference D furthermore suggest Llanos as an important pathway for the cross-equatorial flow of the active phases. However, only the No-Chaco Jet is enhanced during the active phase, as there are negative anomalies in the Gran Chaco area. The break phases exhibit the opposite behavior, as shown by all network measures and the wind field itself: the SALLJ is strongly suppressed, as noticeable by the absence of large betweenness and D values along the eastern slopes of the Andes, but especially by distinctly high, negative anomalies of all network measures in these areas. The SALLJ is the key feature for transporting moisture from the Amazon to SESA [230], and the enhanced SALLJ can thus be considered one of the main reasons of the strong precipitation difference between both regimes (see Fig. 3.9). The generally positive anomalies of the geopotential height at 250 hPa over Bolivia additionally suggest a strengthening of the Bolivian high.

The break phase exhibits strong southward winds in the Gran Chaco area, which are strongly suppressed during the active phases. These are highlighted by differences of all shown network measures as well. However, these are not indicating a Chaco Jet, as the SALLJ in Bolivia is still strongly suppressed during the break phase. This

wind system, which is sometimes referred to as Argentinian low-level jet [189], is instead directly related to the anomalous high/low pressure systems forming over the subtropical Atlantic ocean that are further investigated in the following.

Large-Scale Atmospheric Circulation in Southern South America

One of the most distinct differences in the low-level atmosphere between the active and the break phase of the SAMS is the striking difference in the geopotential height at 850 hPa, showing pronounced cyclonic (anti-cyclonic) activity over southern South America and the adjacent Atlantic ocean during the active (break) phase. This pressure anomaly is related to a Rossby wave train that is most apparent in the geopotential height at 250 hPa. This wave train, a longitudinal oscillation of low- and high-pressure anomalies, originates from the southern Pacific ocean and propagates eastward across the southern part of the South American continent [24, 26]. The further analysis of the mean GPH850 over the subtropical Atlantic indicates the substantial relationship between the GPH850 over the subtropical Atlantic and the active and break monsoon phases.

During the active phase, the negative GPH850 anomalies extend further north as well, showing an intensified northern Argentinian Low (NAL) that further amplifies the moisture flux from the Amazon to SESA during this phase. The negative GPH850 anomalies are forming an anomalous cyclone in the south Atlantic during the active phase that results in more northwards winds originating from Patagonia. These are especially highlighted by the concise pattern of large OAWC and D. D can here provide information about sources and sinks of the wind field. This is visible for example in Fig. 3.11 between 20°S and 40°S, where we observe low OAWC, but large IAWC, and directly south of it we find nodes which exhibit high OAWC, but low IAWC. This encodes the information about northward propagating frontal systems that transport cold, dry air to South America from the South during so-called cold surges [26, 28, 77]. The anomalous cyclone also causes northward anomaly winds in the Gran Chaco area. These in turn result in the suppressed Chaco Jet that is visible in the networks.

Contrarily, the break phase exhibits an anomalous anticyclone that accelerates southwards winds in the Gran Chaco area but overall suppresses the SALLJ. This is notably apparent in the anomalous betweenness field. The most concise patterns of the betweenness of the break network are the strongly negative anomalies along the eastern slopes of the Andes and the strongly negative anomalies in the center of the anticyclone over the Atlantic ocean south of Uruguay.

The described differences in the geopotential height fields between active and break monsoon phases suggest that the alternation between the two phases is modulated by the Rossby wave train. In addition to the spatial composite maps, this hypothesis is strongly supported by the approximately periodic switching between active and break phases, which happens in concert with alternating low and high pressure anomalies over the subtropical Atlantic ocean (see Fig. 3.14), caused by the eastward propagation of the Rossby wave train.

We note that both lower and upper level pressure configurations during the active phase strikingly resemble corresponding geopotential height anomalies studied in the context of extreme precipitation events in SESA and at the eastern slopes of the central Andes [24, 26]. This suggests a close connection between the active monsoon phase and extreme event occurrences associated with cold surges which propagate northward into subtropical South America [77], modulated by the Rossby wave train. This serves as an ideal starting point for further investigations that will discussed later in Sec. 3.5.

Impact of ENSO on SAMS low-level circulation

The networks presented above were computed with wind data that include all El Niño and La Niño events during austral summer between 1985 and 2010. The SALLJ is enhanced during the El Niño phase as shown by the OAWC and betweenness centrality. This is in accordance with case observations that were made during El Niño events in 1998 and 2003 [69, 206]. The network results presented here comprise data from a multitude of El Niño events and thus support the claim that the enhanced SALLJ is a general effect of El Niño, which did not only happen in single years. Especially the more southward Chaco Jet exhibits a much larger OAWC, D and betweenness during El Niño events. The eastward No-Chaco Jet is less affected by the ENSO, which is in agreement with the precipitation differences (see Fig. 3.16): While SESA, which is typically more affected by the Chaco Jet, exhibits slightly enhanced precipitation, southeast and central-west Brazil, which are more affected by No-Chaco Jets, exhibit positive precipitation anomalies during La Niña.

On a large-scale, the dominant wind pathway from the tropics to the subtropics is shifted and rotated during positive and negative ENSO anomalies. This is suggested by the described differences between the ENSO network measures in Llanos, along the Amazon river and east of the central Andes: While the low-level flow during El Niño events is dominated by trade winds that flow toward the South American continent in zonal direction and are then channeled into a strong SALLJ with Chaco Jet characteristics, the low-level flow during La Niña events exhibits stronger cross-equatorial flow along the slopes of the Andes in northern South America, which is subsequently channeled into a less strong No-Chaco SALLJ. These flow paths are marked in the corresponding network figures (green and yellow dashed lines in Fig. 3.17 and 3.18).

The comparison of the subsets of the time series based on the MEI and the active and break regime shows that the occurrence of active phases is relatively independent from the ENSO. The frequency of active time steps is only marginally different during El Niño and La Niña months. However, break phases occur less often during El Niño events (13 % during El Niño events, 23 % during La Niña). This is conceivable, as the El Niño events enhance the SALLJ which results in less easterly anomaly winds in the reference region used to distinguish the active and break phase.

3.4.4. Conclusion and Summary

We have analyzed the spatiotemporal circulation characteristics of the South American Monsoon System (SAMS) in terms of intraseasonal variability associated with the active and break monsoon phases, as well as in terms of interannual variability associated with the El Niño Southern Oscillation (ENSO). Our analysis is based on high-resolution data provided by NASA's Modern Era Retrospective-Analysis for Research and Applications. By combining composite analyses of the anomalies of wind, precipitation and geopotential height fields with the recently introduced streamflow wind networks, we were able to reveal how each of these phases influences the low-level circulation of the SAMS. The streamflow network approach is able to unveil the crucial differences between the active and break phase of the SAMS, but also between El Niño and La Niña conditions. The constructed streamflow networks have revealed the dominant wind pathways of the monsoonal circulation. They are particularly responsive to associated changes in the South American Low-Level Jet (SALLJ), which is the most important low-level moisture transport system of the SAMS.

The main findings for intraseasonal and intraannual variability can be summarized as follows:

1. *Intraseasonal:* The low-level circulation of the active monsoon phase is characterized by a strong cross-equatorial flow along the eastern slopes of the Andes, a strongly enhanced, southeastward-directed South American Low-Level Jet, and southerly winds over southern South America. While the Low-Level Jet is distinctly strong in Peru, Bolivia and Paraguay, it is suppressed in the Gran Chaco Area. The active monsoon phase is associated with an anomalous cyclone at low atmospheric levels over the Atlantic ocean south of Uruguay. The low-level circulation of the break monsoon phase is characterized by a pattern opposing the one observed for the active phase. In particular, the SALLJ is strongly suppressed and the anomalous cyclone over the subtropical Atlantic ocean is replaced by an anomalous anti-cyclone.

2. *Intraseasonal:* The opposing circulation patterns for the active and break monsoon phases occur in concert with approximately periodic oscillations between low and high pressure anomalies at 850 hPa over the subtropical Atlantic ocean, which are part of a Rossby wave train emanating from the southern Pacific ocean. We thus infer that this Rossby wave train is the modulator of the alternations between active and break phases of the South American monsoon.

3. *Intraannual:* The dominant low-level wind pathways, and thus also the most important moisture transport routes, are strongly affected by ENSO: During El Niño events, the Chaco Jet (a southward extension of the SALLJ) is substantially enhanced, leading to above average precipitation in southeastern South America, while the cross-equatorial flow in northern South America is suppressed. These differences are part of a large-scale re-organization of the dominant wind paths, which is modulated by the ENSO: For El Niño conditions, the main wind path

is directed westward along the Amazon river and closely follows the slopes of the central Andes southward to the Gran Chaco area. For La Niña conditions, this pathway is considerably shifted northward and rotated counterclockwise, leading to an enhanced cross-equatorial flow over northern South America, together with an enhanced eastward flow toward the subtropics.

Especially the result 2) points to the strong connection of the intraseasonal variability of the SAMS to Rossby Waves. Previous studies already linked those to extreme precipiation in South Eastern South America as well [24, 26]. Seemingly the connection to Rossby Waves does not only affect extreme precipitation in one of most densely populated areas in South Amercia, but also the entire low-level circulation. Therefore, we will study this connection in more detail in the following.

3.5. Phase Coherence between Precipitation in South America and Rossby Waves

In the previous section we explored the variability of the low-level circulation of the SAMS with complex networks. This pointed us to the influence the upper-level atmosphere Rossby waves have both on the low-level circulation itself, but also on the precipitation as these go hand in hand in a monsoon system. As introduced in Sec. 3.1 the SAMS during the austral summer, the wet season, is characterized by a pronounced low-level moisture inflow from the tropical Atlantic ocean toward the South American tropics that is channeled into the SALLJ. In the previous section we already saw how the SALLJ constitutes as the most important feature of the low-level circulation regarding active and break phases. However, there is also a considerable variability in the direction of the SALLJ to the subtropics. Related to this, precipitation in South America during the monsoon season exhibits significant intraseasonal variability. The most pronounced precipitation variability mode is typically described as a precipitation dipole [114, 135, 152, 158], with strongest amplitudes of this alternating pattern found between Southeastern Brasil (SEBRA) and Southeastern South America (SESA) (see Fig. 3.19). These two regions are also the northernmost and southernmost exit regions of the SALLJ, respectively. SEBRA is usually part of the climatological position of the South Atlantic Convergence Zone (SACZ [43, 114, 150]), one of the key characteristics of the SAMS. SERBA and SESA, the most affected regions by this variability pattern are among the most densely populated and agriculturally important areas in South America. We will refer to this variability pattern between the two exit regions and the associated variability in precipitation as a precipitation dipole. Later, we will see the spatiotemporal pattern that illustrates the choice of this name.

While the relation between the active and break phases that we explored in the previous chapter and the two phases of the dipole is not completely clear, we will focus for now on directly on the connection of the precipitation and its variability to Rossby Wave trains that we already saw having an impact on the active and break phase as well. Prior research suggested that the precipitation variability is related to

the Madden-Julien Oscillation (MJO) and the Bolivian high [110, 114, 135, 231]. In addition, evidence has also been reported that the dipole is related to Rossby wave trains emanating from the southern Pacific region and their relative phasing with the MJO [51, 81, 114].

The aim of our investigation in the following is a detailed analysis of the relationship between the eastward propagating Rossby waves and the dominant modes of precipitation variability in South America during the monsoon season. Previous studies mainly used principal component analysis (PCA) and composite analyses to analyze the characteristics of the precipitation variability in South America [51, 152, 158]. More recently, complex network approaches based on event synchronization were also already able to complement these approaches [31]. However, aside from studying composite anomalies during or before precipitation events, or the network topology induced by the synchronization of these events, these methods are not suitable to further investigate the detailed atmospheric mechanisms behind the dipolar precipitation variability and its relationship to the Rossby wave trains. In particular, a direct statistical test of this relationship on the basis of suitably identified time series has, as far as is known, not been performed so far.

In the following, we therefore intend to shed further light on the mechanism behind the dipole pattern by directly investigating its dynamical properties in terms of its statistical relationship with the relevant atmospheric dynamics. This will be done, on the one hand, by setting up a conceptual model that explains the observed structure of the PCA and, on the other hand, by showing that the reconstructed phases of the relevant observables, the precipitation in the dipole regions and the upper-level GPH in southern South America representing the Rossby wave train, are coherent with each other. The latter approach relies on the concepts that have first been explored to study dependencies of chaotic oscillators in nonlinear dynamical systems theory (see Sec. 2.2.8 for an introduction). This framework has been applied successfully to climate time series before, investigating the coherence between ENSO and the Indian Monsoon [134]. Utilizing the methodological concept of phase coherence will allow us, in particular, to establish statistical significance of the relationship between the dipolar precipitation pattern and the Rossby wave train.

3.5.1. Data

For this part of our investigation we will rely on data from the MERRA2 project, the successor of the MERRA project dataset used in the previous sections (see Sec. 3.2). In contrast to the network analyses of the previous sections in which we used daily data, we will use 6-hourly here in the following. The precipitation data is smoothed using a moving average with a window size of 4 days. The two reference regions for the precipitation dipole are chosen in accordance with prior research [31], and the mean of all grid cells within these boxes is used as an index for the precipitation in SEBRA and SESA, respectively. The reference region for inferring Rossby wave activity is chosen over Southern South America (see Fig. 3.19) similar to the reference region that we used during the network analysis before. The results that are reported in

the following are very robust to changes in position and size of this box. However, it is important that the reference region is not much larger than half of a typical wavelength of the wave train, to still properly capture its oscillating behavior. The mean of the geopotential height at 250 HPa of all grid nodes within this reference region then serves as an index for the Rossby wave train. Fig. 3.19 (A) and (B) show the reference regions and the typical opposing configuration of the Rossby Wave trains in the geopotential height anomaly fields during extreme precipitation (above the 90th percentile) in SEBRA and SESA. The precipitation itself is shown in Fig. 3.19 (C) and (D). The South American precipitation dipole is a phenomenon restricted to the austral summer from November to February (NDJF). Because some of the methods used here are easier to handle with data that exhibits a regular time axis without jumps, all-year data is used at first. The crucial parts of the analysis are however limited to NDJF data. When anomaly data is used, it is computed with the daily climatology computed from the same dataset and standardized.

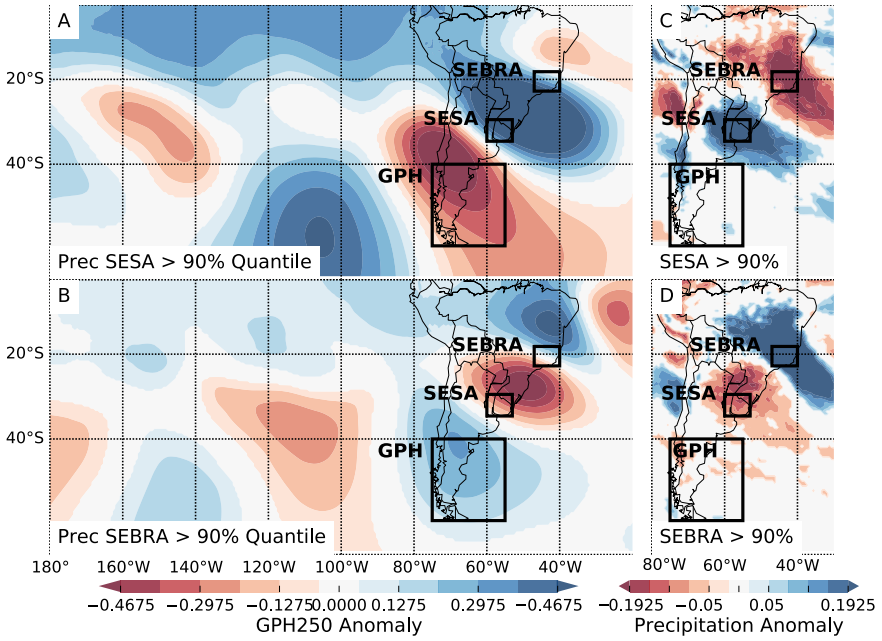

FIGURE 3.19.: Geopotential height at 250 hPa and precipitation anomalies (with respect to the NDJF climatology) for times when (A) & (C) precipitation in South Eastern South America (SESA) is above its 90% percentile, and (B) & (D) when precipitation in South Eastern Brasil (SEBRA) is above its 90% percentile. For the calculation of the percentiles, only time steps with precipitation larger than 0.01 mm/d are considered. The reference regions SESA and SEBRA serve as a proxy for the South American precipitation dipole in this study, and the geopotential height in southern South America (GPH) as a proxy for Rossby wave activity. The size and position of the GPH reference region is chosen such that it roughly covers one half of the spatial wavelength.

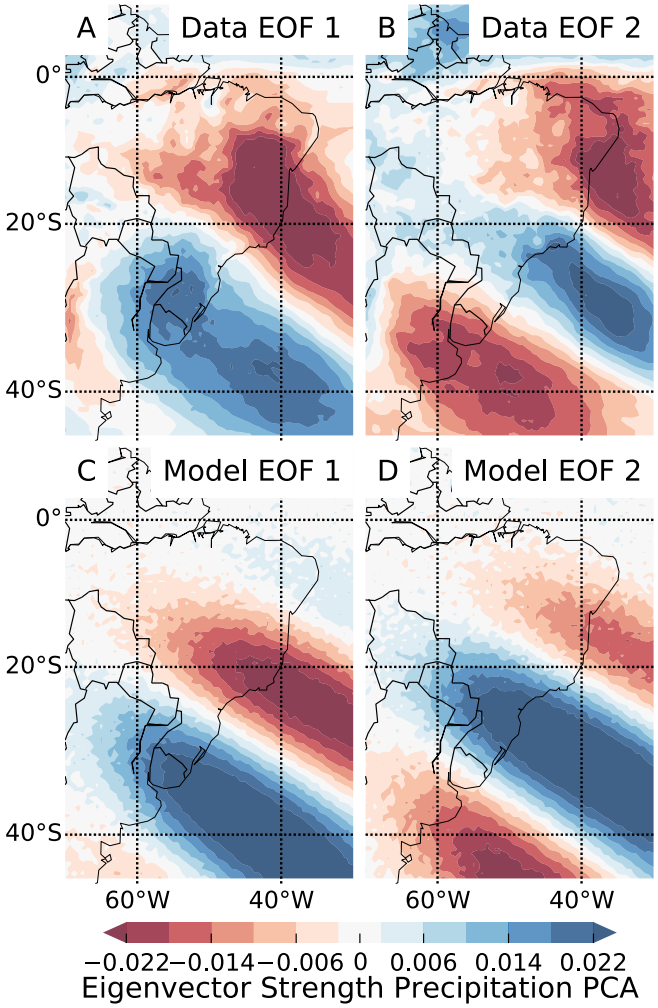

FIGURE 3.20.: (A & B) First and second EOFs of the precipitation data. NDJF precipitation anomalies were used to calculate these EOFs, which account for 9% of the total precipitation variability. A plot of the eigenvalue spectrum can be found in the Appendix. (C & D) First and second EOFs of the data generated by the conceptual model.

3.5.2. Conceptual Model

Typically, dominant modes of variability are identified and visualized from a principal component analysis (PCA) of the covariance matrix (see Sec. 2.3.1). A PCA of outgoing long-wave radiation data, also led to the first description of the South American precipitation dipole [152]. The dipole pattern is clearly recognizable in the two leading empirical orthogonal functions (EOFs) of the precipitation anomalies as well (top row of Fig. 3.20), which emphasizes the importance of this variability mode for South American climate.

The key hypothesis we intend to test is that the variability mode corresponding to the South American precipitation dipole can be explained by northward propagating waves. For this purpose we set up a conceptual model which corroborates that hypothesis by reproducing the pattern of the EOFs. We choose to model the dimensionless

geopotential height h along an arbitrary direction x with a wave equation

$$\Box h\left(x,t\right)=0 \tag{3.11}$$

with the 1-dimensional d'Alembertian $\Box = \frac{1}{c}\frac{\partial^2}{\partial t^2} - \frac{\partial^2}{\partial x^2}$ and p, the dimensionless precipitation, as its spatial derivative

$$p(x,t)=\frac{\partial}{\partial x}h\left(x,t\right) \tag{3.12}$$

since precipitation, on a large-scale, typically occurs at the fronts between highs and subsequent lows. This equation solves to a traveling wave for $p\left(x,t\right)$. By embedding this traveling wave in the same spatiotemporal grid as the data, and adding Gaussian damping along and perpendicular to the propagation direction, we generate the model data $P_M\left(\lambda,\varphi,t\right)$. Its parameters are the mean values of the Gaussian damping λ_0, φ_0, their standard deviations σ_λ, σ_φ, the wavelength L, and the direction θ of the wave. In Appendix Sec. A.2.1 the full model equation and more details regarding the fitting procedure can be found. The model data $P_M\left(\lambda,\varphi,t\right)$ can be used to compute the first two EOFs of the conceptual model. These EOFs are then fitted, by optimizing the model parameters via minimizing the least squares error to the EOFs of the precipitation data (see Fig. 3.20). While the parameters referring to the Gaussian damping and the direction θ roughly account for the location and orography, the wavelength or wavenumber is an important parameter of the modelled wave.

Fig. 3.20 shows the two leading EOFs of the observed precipitation anomaly data and the conceptual model. The qualitative structure of the EOFs of the observational data is reproduced well by the conceptual model. The wavelength of the model wave L after the fitting procedure is roughly 4000 km, while the alternating Rossby Wave train pattern in Fig. 3.19 also exhibits a wavelength of about 4000 to 6000 km, measured as the distance between subsequent maxima. While small deviations from the data EOFs that could be caused by the orography or other external effects are to be expected with such a simple conceptual model, it can be inferred that the type of alternating EOF pattern that is present for the South American precipitation dipole can be caused by a propagating wave such as a Rossby Wave train, and the resulting pressure anomalies.

We can further validate this hypothesis by performing a Complex EOF (CEOF) analysis. CEOF recovers phase information from the data in the same way as we will do in our further analysis of the phase coherence: with a Hilbert transform. The data is embedded with a Hilbert transform and then a PCA of this now complex-valued spatiotemporal field is performed. For a more thorough description of CEOF including all resulting quantities, see Sec. 2.3.2. Through its two-dimensional embedding with the Hilbert transform, CEOFs allow to assess oscillatory patterns, and in particular patterns due to propagating waves, better than standard EOFs [14, 91, e.g.]. Fig. 3.21 shows the spatial phase $\theta_0\left(\lambda,\varphi\right)$ and amplitude $S_0\left(\lambda,\varphi\right)$ of the first CEOF, i.e. the dominant oscillatory pattern, in the upper panel. For a propagating wave one would expect a monotonously, constantly growing spatial phase along the propagation direction and constant values on lines perpendicular to this direction. This is exactly what

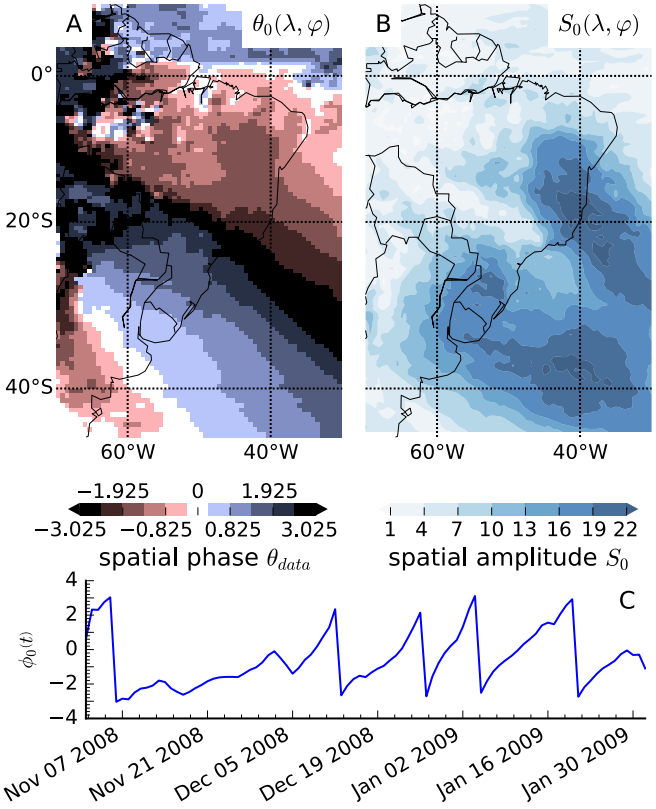

FIGURE 3.21.: First Complex EOF (CEOF) of the NDJF precipitation anomalies. (A) Spatial phase $\theta_0(\lambda, \varphi)$ and (B) spatial amplitude $S_0(\lambda, \varphi)$ of the first CEOF component. (C & D) Temporal phase and temporal amplitude of the 2008/09 season. Only one season is shown to representativly show the qualitative behaviour of these measures. The other seasons exhibit a similar behaviour.

the conceptual model exhibits (see Fig. A.8) and the data closely resembles these as well. The spatial phase shows the propagation of a wave along the eastern coast of South America in a remarkably clear pattern extending from Argentina to the eastern tip of Brazil, with its spatial amplitude maxima on the continent close to the SESA and SEBRA reference regions. The temporal phase (Fig. 3.21C) exhibits a distinct oscillatory pattern as well: a seesaw pattern with roughly similar periods indicating the temporal dynamics of the dominant oscillation pattern. The CEOF thus also shows a south-west to north-east propagating oscillation pattern with its maxima close to SESA and SEBRA and temporal periods similar to those of Rossby Wave trains.

3.5.3. Data-driven Phase Coherence Investigation

Singular Spectrum Analysis

Complementary to the conceptual approach, a data-driven analysis of the dynamical properties of the precipitation dipole is performed by investigating the reconstructed phases of the three proxies of precipitation in SESA and SEBRA and GPH for the Rossby Waves, and their dependencies to each other. As we are investigating an intraseasonal variability, we utilize singular spectrum analysis (SSA) in order to remove the annual cycle and high frequency noise from the time series (see Sec. 2.3.3). We note that Paegle et al. [158] had also used SSA to study specific frequency bands of

variability related to the dipole pattern under study. According to the intraseasonal frequency range that we are interested in, the SSA is carried out with a delay $\tau = 60\,\mathrm{d}$. The eigenspectrum of all investigated time series is shown in Fig. A.9. SSA decomposes the signal into $60{\cdot}4$ components ordered by the magnitude of their eigenvalues, as there are four data points per day in the dataset. We consider three different approaches to identify the right components for our analysis, and ultimately combine our knowledge from all three of them.

First of all, Monte Carlo SSA (MCSSA) [6](see Sec. 2.3.3) can be used. Here, we use 1000 shuffle surrogates for the significance bounds. The eigenvalues of the first 25 components, and those of the corresponding surrogates, are shown in Fig. A.9. If the eigenvalue of the k-th component is lower than the eigenvalue of the k-th shuffle MCSSA surrogate, the corresponding reconstructed components are regarded as noise. This yields similar results to the visual check of the cumulative eigenvalue series approaching a horizontal line [204]. In our case, the cumulative explained variance of the eigenvalues, which is directly proportional to the cumulative eigenvalue series itself, is larger than 95% for all three observables at this point. As the eigenvalue spectrum differs for each of the observables, the MCSSA significance test does so as well. The break point is at $k = 19$ for SESA, $k = 16$ for SEBRA and $k = 25$ for GPH.

Another way of approaching the problem to select the right components is to directly choose those component ranges that induce the smallest phase differences (the phase reconstruction is described in the next section). As we have three sets of components to choose from, this is a highly nontrivial optimization problem. A genetic algorithm [72] whose individuals are lists of the starts and ends of the component ranges of the three time series is used for this purpose. The fitness used in this algorithm is the phase difference at the end of the series, modified with extra penalties in order to favor larger component ranges. This results in the ranges 4-15 for SEBRA, 3-13 for SESA and 2-14 for GPH.

Finally, it should be assured that the components which we choose actually exhibit oscillations within the intraseasonal frequency band that we are interested in. For this purpose, we calculate the dominant frequencies of all components. The first two reconstructed components of all three observables contain the annual cycle, the third components exhibits dominant frequencies between $1/(40\,\mathrm{d})$ and $1/(50\,\mathrm{d})$. SESA's and GPH's fourth component are within this range as well. Reconstructed components with $k > 12$ exhibit frequencies $f_{dom} > 1/(10\,\mathrm{d})$ and components with $k > 15$ exhibit frequencies $f_{dom} > 1/(8\,\mathrm{d})$. Thus, the ranges suggested by the optimization routine described in the previous paragraph include only significant reconstructed components, and all reconstructed components with intraseasonal dominant frequencies except for those with frequencies around $1/(40\,\mathrm{d})$. The latter frequency range is not typically associated with Rossby wave trains. However, we also tested to include these components and found qualitatively similar results, indicating that this approach is robust.

All further investigations are carried out with time series attained by summing the components found by the optimization. Since the data is linearly detrended prior to the SSA, and the annual cycle removed via SSA, the time series oscillate around

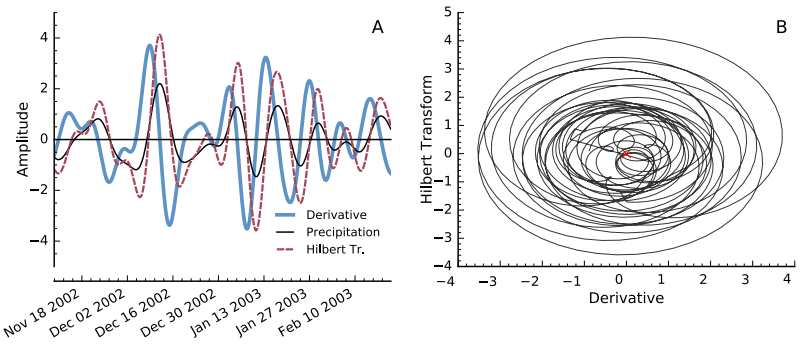

FIGURE 3.22.: (A) Example of a SSA-processed observable (precipitation in SEBRA), its derivative, and the Hilbert transform of the derivative for the 2002/2003 NDJF season. (B) Example of the embedding of a processed observable (precipitation in SEBRA) via Hilbert transform, for three consecutive seasons 2002/2003, 2003/2004 and 2004/2005 that are joined together with an end-point matching.

zero. To validate that the SSA-filtered time series still reflect the precipitation dipole, we check whether the extreme events in the two dipole reference regions (defined as time points with precipitation above the 90th percentile of the unprocessed data) still exhibit positive values in the processed time series. This is the case for 95% of the SEBRA events and 97% of the SESA events. Since an extreme event-based definition was able to capture the characteristics of the precipitation dipole in a previous study [31], we are convinced that the SSA-filtered time series, which preserve these events and consists of most of the reconstructed components with dominant frequencies in the intraseasonal range, still represent the precipitation dipole.

The results on the coherence of phases presented below are robust for different approaches to preprocess the data: Alternatively to SSA, it would also be possible to process the data with a regular bandpass filter. However, one needs to carefully select a filter with constant phase response in the frequency range we are interested in, and one also needs a priori knowledge about the cutoff frequencies. We used a Lanczos 10-50-day bandpass filter with a high number of weights [61] and found qualitatively similar results: phase differences at the end of the time series are slightly larger than for the optimization approach described above, but still significantly smaller than those of the surrogates. Corresponding results can be found in the Appendix in Fig. A.11-A.14. We additionally tested Ensemble Empirical Mode Decomposition (EEMD) [248] as an alternative. With it similar results can be obtained; however, identifying the right intrinsic mode functions of the EEMD is more challenging.

Phase Reconstruction

In Sec. 2.2.8 we saw how the phase synchronization of chaotic oscillators can be investigated by reconstructing their phases with Hilbert transforms. In the following we will apply this approach to the SSA-processed observables. As we are dealing with

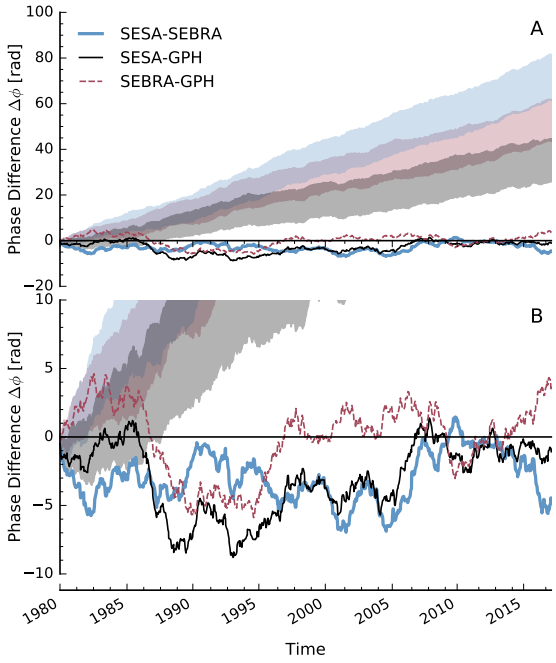

FIGURE 3.23.: Phase difference time series: (A) The grey shaded area marks the 5% and 95% percentiles of phase difference time series from the 250 AR2 surrogates of the time series computed with maximum likelihood estimates of the AR2 parameters. (B) Zoomed in view of (A).

a seasonal phenomena, we only consider NDJF data in the analysis and perform an end-point matching to concatenate the data of the different seasons. The end-point matching minimizes the euclidean distance between the joint vector of all three time series, their derivatives and Hilbert transforms, as well as an additional penalty that is linear in time, and favors end points late in the season and start points early in the season. As described in Sec. 2.2.8 the phase of each of the observables $x(t)$ than follows as

$$\phi(t) = \arctan \frac{\mathcal{H}\{\dot{x}\}(t)}{\dot{x}(t)}. \tag{3.13}$$

Fig. 3.22 shows an example of a time series and its embedding. We see that the definition of the phase in the above described way is justified, since most oscillations revolve around the origin. This demonstrates that the phase can be defined meaningfully even across seasons, and the relation of the phase time series of the two precipitation proxies and the Rossby Wave train proxy can be compared to each other.

Phase Relation

Temporal Evolution There are two approaches how we can study the phase relation of the dipole. First as explained in Sec. 2.2.8, we directly investigate the temporal evolution of the phase differences

$$\Delta\phi(t) = \phi_i(t) - \phi_j(t) \tag{3.14}$$

with the indices i and j representing either of SEBRA, SESA and GPH. If i oscillates faster (slower) than j, the phase differences are positive (negative). We test the statistical significance of these phase differences by comparing it to surrogate time series. For this purporse 250 autoregressive surrogates of order 2 (AR2) for each of the time series were calculated. AR2 surrogates are chosen because they can oscillate with a preferred frequency [217, e.g]. The surrogates were generated based on the Yule-Walker estimates of the AR2 coefficients of the unprocessed data, and then processed in the same way as the actual data, including the SSA filtering. The k-th surrogate difference is calculated as

$$\Delta\phi_k^{(s)_k}(t) = \frac{1}{2}\left(\left(\phi_i(t) - \phi_j^{(s)_k}(t)\right) + \left(\phi_i^{(s)_k}(t) - \phi_j(t)\right)\right) \tag{3.15}$$

where the superscript (s) denotes a phase generated from surrogates. Hence, we test whether the phase differences induced by the two observables are small against the difference induced by one of the observables and a surrogate of the other one. Similar schemes have been utilized to test for the statistical significance of phase coherence in previous studies [221, e.g]. The upper panel of Fig. 3.23 shows the 5% and 95% percentiles of the 250 surrogate phase differences. Similar results can be obtained with AR1 surrogates as well (Fig. A.11).

Examining Fig. 3.23, we see that the phase differences of the data are well below the surrogates and in fact very close to zero: The phase differences remain below 9 full periods, which is remarkable since the potential maximum of $\Delta\phi$ is 350 periods, given by the number of periods the time series goes through for the complete duration of the studied interval. While it could be expected that the SEBRA-to-SESA phase difference stays close to zero, the SESA-to-GPH and SEBRA-to-GPH phases do not exhibit larger differences over the course of the dataset. More pronounced (negative) excursions of the phase differences are seen between 1985 and 1988 for SEBRA-to-GPH and SESA-to-GPH differences, indicating that GPH oscillates faster than the precipitation proxies during these time. The maximum absolute phase difference between the start and the end of a season is about 3.5, occurring during this time interval, while the mean value over all seasons is about 1.0. Additionally, larger phase differences can be observed between 2005 and 2007 for the SESA-to-SEBRA and SESA-to-GPH differences, indicating a faster oscillation of the average precipitation in SESA. On average, however, the SESA-to-GPH and SEBRA-to-GPH phase differences are typically negative, indicating that the oscillations of the atmospheric waves are slightly faster than the oscillations of the precipitation dipole.

The surrogates exhibit a spectrum similar to those of most climatic time series. However, by construction their spectra still slightly differ from the spectra of the investigated time series themselves, and one can see that these rather small differences lead to phase differences that are far larger than those of the three proxy time series in question to each other.

Phase Difference Distribution Another possibility to study the phase relation is to directly examine the distribution of the phase differences. For this purpose, phase differences are mapped back into the interval $[0, 2\pi]$ and histograms $H(i,j)$ of all observable pairs i, j are computed (Fig. 3.24). As a comparison and significance test iAAFT surrogates [198] are used. These surrogates are refined Fourier transform surrogates. Fourier transform surrogates are computed by multiplying the Fourier transformed time series with a random phase vector and transforming it back into the original space. Therefore, the surrogates exhibit the same spectrum as the original time series but have randomized phases.

If the phases of the observable have no relation to each other, the histograms show a uniform distribution. A KS-test of the phase difference distributions against those of the iAAFT shows that the observed distributions differ from the surrogate distributions at a significance level of $\alpha < 0.0001$ for all three observable pairs. While $H(\text{SESA}, \text{SEBRA})$ and $H(\text{SESA}, \text{GPH})$ exhibit phase differences in the complete interval, they both have a broad peak around π. $H(\text{SEBRA}, \text{GPH})$ displays less pronounced, but still visible peaks around 0 and 2π, respectively.

As a measure of the spread of the distribution, and thus of how coherent the phases of the observables are, we perform a maximum likelihood fit (MLE) of a vonMises distribution to the data [71]. The vonMises distribution is an approximation to the circular wrapped normal function that exhibits an easier mathematical form than the latter. Its probability density function is $f_{vM}(x) = \exp(\kappa \cos(x - \mu)) / (2\pi I_0(\kappa))$ with the dispersion κ and location μ. $I_0(\kappa)$ denotes the modified Bessel function of order zero. If the dispersion parameter κ of the vonMises distribution is zero, the distribution is uniform and thus the observables are incoherent. If κ is large, the distribution resembles a normal distribution with κ^{-1} as its standard deviation and μ as its mean. Thus, a κ significantly different from 0 and from those of the iAAFT surrogates hints a phase coherence between the observables: the larger κ, the clearer. We can fit the data for each season separately and investigate the temporal evolution of the phase coherence with these time series $\kappa_{i,j}(t)$ (see Fig. 3.24 D). While the more recent years since 2009 exhibit strong phase coherence for all observable pairs (large κ), there are, especially for $\kappa_{\text{SEBRA,GPH}}(t)$, some seasons where the phase difference is more spread out. This occurred in particular in 1994/95, 95/96 and 2005/06 and 06/07. Except for these seasons, $\kappa_{\text{SEBRA,GPH}}$ boasts higher values. $\kappa_{\text{SESA,GPH}}$ and $\kappa_{\text{SESA,SEBRA}}$ exhibit a very similar behavior, apart from some dips for $\kappa_{\text{SESA,GPH}}$ in 2003/04 and 2008/09.

3.5.4. Discussion

After the initial network analysis pointed us to the relation between Rossby Wave trains and the precipitation in the SAMS. We presented two complementary approaches to show how precipitation in South America, and in particular its dominant, dipolar variability mode during the monsoon season, is coupled to the southern-hemisphere Rossby wave trains. This dipole is characterized by alternating wet and dry conditions between SEBRA and SESA, two of the most densely populated areas

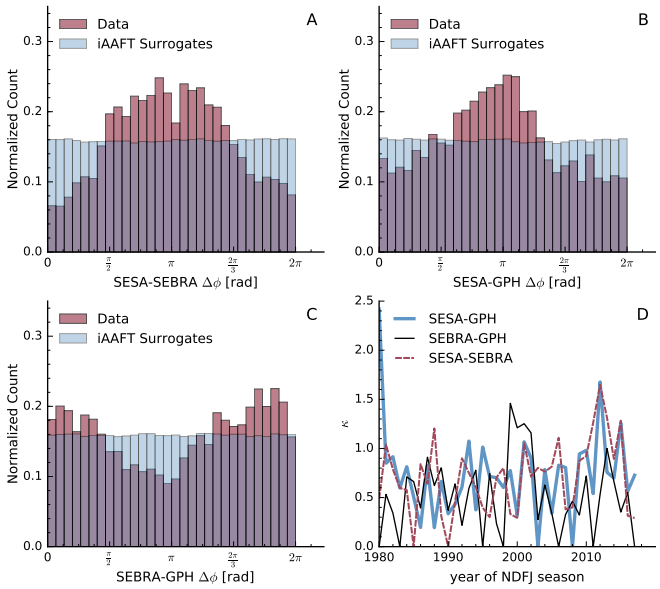

FIGURE 3.24.: (A-C) Histograms $H(x, y)$ of phase difference of all proxy time series. The empirical distributions of the observables are significantly different from iAAFT surrogates at a significance level $\alpha < 0.0001$ due to a KS test. (D) Temporal evolution of the dispersion parameter κ of a maximum likelihood fitted vonMises distribution to the phase differences for each season.

of South America. Composites of geopotential height data for times of strong precipitation in SESA and SEBRA, respectively, show concise atmospheric waves originating from the southern Pacific ocean, which exhibit opposite phases for the two modes of the dipole

We first showed that the spatial patterns of the two leading EOFs of the precipitation anomalies in South America can be well reproduced by a conceptual model of a travelling atmospheric pressure wave. In this conceptual model, precipitation is proportional to the spatial derivative of the wave, and is hence highest at the boundary from high to subsequent low-pressure cells in analogy with frontal systems. The EOFs of this conceptual model are remarkably close to those of the observational data. The CEOF analysis complements this approach and the propagation of a wave along the eastern South American coast can clearly be identified in its leading component, i.e. eigenvector. Together with the successful reproduction of the spatial EOF patterns, this provides strong evidence that the leading variability mode is indeed determined by the Rossby wave activity.

To further support this statement, and in particular to quantify the dependencies caused by the corresponding mechanism, we analyzed the phase coherence between three distinct time series: Two representing the precipitation in the two reference regions in SESA and SEBRA, respectively, and one representing the upper-level geopotential height, and hence Rossby wave activity, over southern South America. Specifi-

cally, we embedded the SSA-processed observables with a Hilbert transformation and calculated the corresponding phase time series for each of them.

The observed phase differences are small for the entire time period. Given that a phenomenon at intraseasonal time scales is studied, and that each observable completes roughly 350 periods over the course of the studied time span, this is a remarkable coherence. Of course, the three investigated observables cannot be expected to be in perfect phase synchronization for the entire span of the studied interval, given that many different factors, such as orographic barriers and nonlinear effects related to convection potentially play a role.

The dominant moisture source of precipitation in subtropical South America is the southward flow from the tropics related to the South American Low-Level Jet (SALLJ, [114, 135, 138]). The flow direction at the outlet of this jet is determined by the pressure configuration between SESA and SEBRA, and hence by the alternation of low and high pressure cells caused by the Rossby waves. If a low-pressure cell is located just south of SESA, this flow transports moisture along the isobars toward SESA, and correspondingly for SEBRA. The fact that the GPH-derived Rossby wave time series tend to oscillate slightly faster than the precipitation in SESA and SEBRA can be explained along these lines: If the northward propagating pressure waves occasionally fail to pick up the moisture flow from the tropics along the isobars, one would effectively obtain slightly faster oscillations in the driving pressure waves than in the responding precipitation waves.

In addition, positive feedbacks between moisture flow and convection related to the release of latent heat may lead to slight deviations from a perfect phase coherence. Notably, the atmospheric waves propagating northward across the South American subtropics occasionally become stationary, establishing prolonged episodes of an active SACZ at the order of five days [43, 114, 151].

The phase coherence also becomes clear as histograms of the phase differences exhibit visible peaks that are significantly different from those of phase randomized surrogates. To make a justified assertion about the phase coherence of the precipitation dipole and Rossby wave we need both, the fact that their phase differences stay close to zero for the whole duration of the study period, and that their distributions exhibit distinguished peaks.

Since we included most of the intraseasonal SSA components in our analysis, our results show that the interaction of the precipitation dipole with the Rossby waves is the dominant factor of intraseasonal precipitation variability in South America: Our results indicate that the dipole-like pattern is not present due to some direct interaction between the climatic subsystems in SESA and SEBRA, but is rather caused by the propagation of Rossby wave trains from the southern Pacific ocean, along the southern tip of the South American continent, and then northward toward the subtropical Atlantic ocean. The identification of this causal mechanism, which explains the dominant variability mode of monsoonal precipitation in South America, should help to improve the synoptic-scale predictability of precipitation in particular in SESA and SEBRA, which are the two regions which are most affected by this mode. Potentially a simplified forecast model could be set up using some of the machine learning

techniques that are later discussed in this thesis. The presented framework also enables us to investigate the temporal evolution of phase coherence at longer time scales, and hence the interannual variability of the South American precipitation dipole. Seasons with larger phase difference should be investigated for dependencies with other variabilities like the El Niño Southern Oscillation or the Madden-Julian Oscillation in future work.

Summary

In this chapter we explored the South American Monsoon System (SAMS) with a two-part approach. We first introduced a novel network construction method, stream-flow networks, that deliver us a network representation of the low-level circulation of the monsoon system. In conjunction with composites of the geopotential height and precipitation we analysed the spatiotemporal characteristics of the intraseasonal variability of the SAMS in the form of its active and break phases and the interannual variability in form of the El-Ninõ Southern Oscillation (ENSO). When investigating the variability due to ENSO we observed a shift in the dominant low-level circulation pattern. For the active and break phases our investigation did not only highlight the flow pattern the South American Low-Level Jet takes in each of the respective phases but also pointed us to an anomalous cyclone over the subtropical Atlantic Ocean that is present during active phases and replaced by an anomalous anti-cyclone during break phases. This cyclone is part of an periodic oscillating behaviour which we suspected to be part of a Rossby Wave train. We thus proceeded with an in-depth analysis of the connection of these Rossby Wave trains to the precipitation variability of the SAMS. By setting up a conceptual model that is able to reproduce the pattern of a PCA of the precipitation data on the one hand and by proving phase coherence between the Rossby Wave and the precipitation in the two most affected regions on the other hand, we are able to infer the connection between the Rossby Wave train and the most prominent precipitation variability of the SAMS.

The two approaches that we took in this chapter have demonstrated how techniques and methods from network theory and dynamical systems can be applied to climate data. A network theory approach can uncover interesting phenomena and regions of interest. It pointed us where to investigate further. This further investigation can then be done with e.g. with phase synchronization techniques.

4. Monte Carlo Basin Bifurcation Analysis

After we utilized tools from network theory and dynamical systems for a thorough analysis of observational data from the South American Monsoon System, we now turn to more conceptional approaches as we are looking at the qualitative behaviour of high-dimensional dynamical systems those governing equations we know and apply this knowledge later to climate models. Many high-dimensional complex systems such as climate models exhibit an enormously complex landscape of possible asymptotic states. In Sec. 2.2.6 we introduced simple examples of low-dimensional normal forms of bifurcations that also lead to multistability. Identifying bifurcations and multistability for high-dimensional systems that are not analytically solvable can often be more challenging. We tackle this challenge with a numerical approach that focuses on quantifying and tracking the basins of attraction (see Sec. 2.2.4) of the attractors of the system. The approach that we present is situated between a classical analysis with macroscopic order parameters and a more thorough, detailed bifurcation analysis. By using random sampling and clustering methods, we set up an physics-based machine learning method, that is able to characterize the different asymptotic states or classes thereof and their basins of attraction.

In this chapter, we will first introduce the idea and formalism behind the method in the following section. Then, the algorithm will be explained in Sec. 4.1.5 in detail. First, we will apply the method to a number of paradigmatic examples that showcase the wide variety of possible real world applications: the Dodds-Watts model of social and biological contagion, a network of second order Kuramoto oscillators, used e.g. to model power grids and a network of Stuart-Landau oscillators, of importance for many chemical and biological systems. Subsequently the method will be applied to two conceptual climate models, one conceptual model for tipping cascades in Sec. 4.2.1 and a climate toy model comprised of a energy balance model and the Lorenz96 model in Sec. 4.2.2.

The following Sec. 4.1 to 4.1.10 closely follow the publication „Monte Carlo basin bifurcation analysis“ [MG5].

4.1. Monte Carlo Basin Bifurcation Analysis

Multistability is a universal phenomenon of complex systems. Whether it is hysteresis effects in physics, the human brain [12, 130], gene expression networks [212], in human perception [200], power grids [131] or the climate system [46, 88, 128, 140], almost every sufficiently complex system has a multitude of stable asymptotic states and bifurcations that occur when control parameters are changed. Most traditional methods of bifurcation analysis, such as AUTO [58] rely on tracking states by continuation

of the integration, and become increasingly challenging for high-dimensional systems. Further, for high-dimensional systems, often one is also more broadly interested in classes of asymptotic states such as synchronized versus unsynchronized states of oscillator network or states that share a common symmetry. In the following, we aim to fill a gap between a coarse analysis with macroscopic order parameters and more thorough bifurcation analysis.

To do so, we introduce a novel physics-based machine learning approach, Monte Carlo Basin Bifurcation Analysis (MCBB), based on random sampling and clustering methods. Its aim is to resolve different classes of asymptotic behaviour into different clusters. Rather than studying the existence of states and orbits on the one hand, or only tracking changes in a single order parameter on the other, MCBB learns which type of attractors are most dominant in terms of the volume of their basin of attraction, and quantifies the changing size of the basin of attraction of each of these classes as a function of a control parameter. This provides new insights into the bifurcation structure of multistable high-dimensional systems. Thus, we can regard MCBB as a way to interpolate between detailed studies of asymptotic bifurcations tracking every change in asymptotic structure on the one hand, and statistical physics using specialized order parameters to study the macroscopic behavior at the other end.

4.1.1. Motivation

For the purpose of identifying the different attractors of a system in question, we will adopt the formalism of Eckmann and Ruelle [63, e.g] and speak of invariant measures of the system. An invariant measure $\rho(x)$ satisfies the condition

$$\rho\left(T_{-t}(E)\right) = \rho\left(E\right) \tag{4.1}$$

where E is a subset of points of the phase space and $T_{-t}(E)$ is the time evolution of E by the time $-t$ (so backwards in time). Physically, invariant measures may be thought of as experimental time averages. The invariant measures enable us to speak about the properties of attractors that we want to find and classify in a more general and abstract manner.

With MCBB it is our goal to find classes of similar attractors of a high-dimensional system that collectively have the largest basin of attraction with respect to a measure of initial conditions ρ_0 and we want to address the question of how these classes of attractors and their basin volumes change when a control parameter p is changed in a range I_p. As a class of attractors $\mathcal{C}$ we understand an equivalence class of attractors, potentially at different p, that exhibit similar invariant measures. We interpret ρ_0 as a probability density and in this way draw initial conditions from ρ_0 and parameter values from I_p to generate trajectories of the system. Assuming ergodicity, the tail of these trajectories samples the invariant measures on the attractor. We use these samples to estimate if they are drawn from similar measures in the sense of the equivalence classes $\mathcal{C}$ and cluster them accordingly, such that all members of a cluster are drawn from the same class. Then, by normalizing the amount of samples at a partic-

ular parameter value p, we can derive an estimate of the relative volume of the basin of attraction of a class. The samples themselves can be used to study the properties of the corresponding class. The most important and intricate point is how we define the similarity in this case. Also, in high-dimensional systems that potentially have extremely large numbers of different asymptotic states, we might be interested in a coarser understanding of similar behaviour or measures. We will therefore define the similarity in terms of statistics of the invariant measures that can be computed easily using the samples that we gather. In the following, we will formally outline what we understand as an equivalence classes and how to built the similarity measures.

4.1.2. Classes of Attractors and their Basin Volumes

We are investigating dynamical systems, these can be ordinary differential equations $\dot{\mathbf{x}} = F(\mathbf{x}, t; p)$ or maps $\mathbf{x}_{n+1} = F(\mathbf{x}_n; p)$ with a control parameter p. Integrating or iterating them from initial conditions $\mathbf{x}_0$ yields a trajectory $\mathbf{x}(t; \mathbf{x}_0, p)$. Assuming that we are dealing with a sufficiently well behaved dynamical system, the measure ρ_0 will asymptotically evolve into

$$\rho_\infty = \sum_{\mathcal{A}} b_{\mathcal{A}} \rho_{\mathcal{A}} \tag{4.2}$$

a linear combination of invariant measures $\rho_{\mathcal{A}}$ on the attractors $\mathcal{A}$ of the system with linear expansion coefficients $b_{\mathcal{A}}$. In general, the set of attractors and their invariant measures $\rho_{\mathcal{A}}$ will change, when the control parameter p is varied. Given the yet to be defined notion of similarity of invariant measures, we have classes of asymptotic states $\mathcal{C}$. When the control parameter p is varied, we denote as $\mathcal{C}_p$ the states that belong to class $\mathcal{C}$ at parameter p. We therefore have a parameterized space of measures for each class. Its elements

$$\rho_{\mathcal{C}}(p) = \sum_{\mathcal{A} \in \mathcal{C}_p} c_{\mathcal{A}} \rho_{\mathcal{A}} \tag{4.3}$$

are given as linear combinations of the measures $\rho_{\mathcal{A}}$ on the attractors inside $\mathcal{C}_p$ with coefficients $c_{\mathcal{A}}$, assuming that they are only finitely many attractors at each p. We can use this to decompose ρ_∞ into

$$\rho_\infty(p) = \sum_{\mathcal{C}} b_{\mathcal{C}}(p) \rho_{\mathcal{C}}(p), \tag{4.4}$$

a linear combination of the measures of each class $\rho_{\mathcal{C}}(p)$ at parameter value p with coefficient $b_{\mathcal{C}}(p)$. Here we assume $\rho_{\mathcal{C}}(p) = 0$ and $b_{\mathcal{C}}(p) = 0$ if the class is empty at p. When we integrate or iterate the dynamical systems from parameters sampled from I_p and initial conditions from ρ_0, the resulting trajectory will have probability $b_{\mathcal{C}}(p)$ to asymptotically sample an invariant measure in $\mathcal{C}$. Therefore, $b_{\mathcal{C}}(p)$ is the relative volume of the basin of attraction of class $\mathcal{C}$ at parameter p.

4.1.3. Similarity of Asymptotic Measures

In order to compute the coefficients $b_{\mathcal{C}}(p)$ and make the approach operational, we still need to define the notion of similarity of the classes $\mathcal{C}$.

Let us first consider two extreme cases. As the first case, a linear response of asymptotic measures suggests to identify $\rho_{\mathcal{A}}(p)$ and $\rho_{\mathcal{A}}(p + \Delta p)$ as belonging to the same class if they are connected by a smooth continuum of measures. This means that $\rho_{\mathcal{A}}(p + \Delta p) - \rho_{\mathcal{A}}(p)$ vanishes smoothly in an appropriate sense as Δp goes to zero, e.g. in the sense of Ruelle [183, 184]. When applying this to our sampling approach, we could built clusters of samples (and thereby the classes) by requiring a discrete notion of continuity that converges to the right continuum condition in the appropriate limit. Classes that are built like this, would put us close to a bifurcation analysis by resolving every potential difference in asymptotic states. For high-dimensional systems this might not be desirable, as noted before. When the number of asymptotic states is very large we might be interested in a coarser definition of classes of asymptotic states. Additionally, evaluating a discrete similarity measure on the high dimensional space is potentially prohibitively expensive to compute for large numbers of samples.

The other extreme case are order parameters. We could consider $\rho_{\mathcal{A}}(p)$ and $\rho_{\mathcal{A}}(p + \Delta p)$ as similar if they lead to the same order parameter up to some finite bound. This would place us directly into the realm of statistical physics, but we would need to know the meaningful order parameters for our system a priori.

We try to situate MCBB between these two extreme cases and build the classes by making use of a pseudometric on the space of measures built from a weighted sum of differences of statistics $S_k(\rho)$ of the measures. These statistics can be estimated with the sampled trajectories. The pseudometric distance between the underlying invariant measures of the i-th and j-th trial follows as

$$D(\rho^i, \rho^j) = \sum_k w_k |S_k(\rho^i) - S_k(\rho^j)|, \tag{4.5}$$

with additional weights $\mathbf{w}$. Specifically, we will show that for the examples considered it is sufficient to track the mean and the variance of the measures, encoding the position and size of the attractor in phase space:

- The position of the attractor: $E_k = \langle x \rangle_{\rho_k}$
- The size of the attractor: $\mathrm{Var}_k = \left\langle (x - E_k)^2 \right\rangle_{\rho_k}$

where ρ_k denotes the marginal distribution on system dimension k.

We further consider the histograms of these statistics over the dimensions of the system. This is particularly useful when the system consists of many identical elements, and it allows us to identify asymptotic states related by permutation symmetry. This is critical for the application to networked systems, for example a dynamical system on a fully connected network will have a symmetry group S_n. A more detailed discussion of the technical aspects is given in the next section.

Dependent on the investigated systems, other statistics, such as higher moments or entropy measures such as the non-normality, measured with the Kullback–Leibler

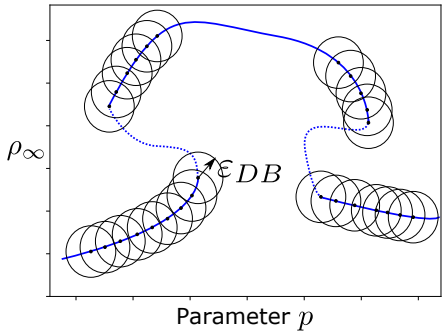

FIGURE 4.1.: Schematic illustration of an example dynamic with stable asymptotic states (solid blue lines) and unstable asymptotic states (dashed blue lines). Two trials i and j are classified as belonging to the same asymptotic state if they are connected via a common ϵ_{DB}-neighbourhood.

divergence, $\mathrm{KL}_k = \mathrm{KL}(\rho_k||\mathcal{N}(E_k, \mathrm{Var}_k))$ can be used as well. The implementation of the algorithm provides a flexible framework for this purpose (see Appendix B.4).

4.1.4. Clustering

Finally, we construct clusters of samples, and thereby the classes of asymptotic states, from the estimates of the distance of statistics $\mathbf{D}$ that we just defined. Again following the argument from the previous section, we want to identify two samples as from the same class of asymptotic states if there is a smooth response of the distance measure between them (see Fig. 4.1). We can require that the observed distance is (up to a factor) a finite scaling of the linear response of the asymptotic state to the parameter change. For every sample with a parameter p^i we continue the integration with $p^i \pm \delta p$ where $\delta p \approx< \min_j(||p^{(i)} - p^{(j)}||) >_i$ should be a typical parameter spacing, leading to samples from the measure $\rho^{i\pm}$. Then, we compare the difference $D(\rho^i, \rho^j)$ between trial i and j with the difference to the results of the continuation of the integration $\delta_i^\pm = D(\rho^i, \rho^{i\pm})$. If the former is much larger we assume that there is no direct continuation between the states. Two states are then in the same cluster if there is a chain of states connecting them.

Instead of this computationally intensive continuation study we can also try to extract sensible values for the distance between samples directly from the data. This leads then to a constant response size parameter ϵ_{DB} for all trials that is ideally a specific percentile $Q_k(p(\delta_i^\pm))$ of the distribution of actual responses $\delta_i^\pm$. When we incorporate the parameter proximity constraint with a weight w_p in the distance calculation as well, the new condition then reads

$$\begin{aligned} &i \text{ and } j \text{ are connected if} \\ &\sum_k w_k |S_k(\rho^i) - S_k(\rho^j)| + w_p |p^{(i)} - p^{(j)}| < \epsilon_{DB}. \end{aligned} \tag{4.6}$$

Such a criterion is part of density-based clustering algorithms that we introduced in Sec. 2.3.5. These algorithms are also ideal as they do not require a priori knowledge of the number of clusters. We can thus use them to distinguish the different classes of asymptotic states given a certain set of suitable statistics. If a single, constant threshold like ϵ_{DB} is used, it also allows us to vary this threshold in order to resolve different classes of asymptotic states finer or coarser: if we choose a large ϵ_{DB} many similar asymptotic states will be grouped into a single cluster that corresponds to a coarser class of asymptotic states. Contrary, a smaller ϵ_{DB} will result in more different clusters, hence resolving the asymptotic states finer. Fig. 4.1 schematically illustrates that: As long as this constant threshold is smaller than the minimal distance between trajectories of the two asymptotic states in question, they will be resolved into different clusters. Alternatively to the regular density-based clustering algorithms, we outline a specialized clustering algorithm in Appendix B.2.

Crucially, all steps described here can be performed in a time that scales at most quadratic in the system dimension. This means that high dimensional systems are amenable to being studied in this way.

4.1.5. Algorithm

We now describe the algorithm that implements the ideas described above in more detail.

MCBB is a modular algorithm: most steps can be modified to suit the dynamical system in question. Algorithm 1 summarizes this procedure in pseudocode and in the following a detailed description of every step is given.

Setup We aim to distinguish different classes of asymptotic states by using clustering algorithms on sets of statistics that each evaluate one of the N Monte Carlo trials. Given a dynamical system such as an ordinary differential equation system $\dot{\mathbf{x}} = F(\mathbf{x}, t; p)$ or a map $\mathbf{x}_{n+1} = F(\mathbf{x}_n; p)$ with $\mathbf{x} \in \mathbb{R}^{N_d}$, we draw N initial conditions $\mathbf{x}_0^{(i)}$ from the distribution $\mathcal{U}_{IC}$ and N parameter values $p^{(i)}$ from the distribution $\mathcal{U}_p$. In what follows, we will use uniform distributions for $\mathcal{U}_{IC}$ and $\mathcal{U}_p$. In the Appendix B.1 the dependence on the choice of the distributions is briefly discussed. While we will mostly focus on systems with one parameter dimension, it is in principal also possible to investigate systems with more than one parameter dimension. In particular setups with two varying parameters can provide useful insights into the dynamics of the investigated systems as we will see later in two examples in Sec. 4.1.9 and 4.2.1. However, results for systems with three or more parameter dimensions are harder to visualize and will need exponentially more trial runs to create sufficient density in the parameter space. In contrast, just as for basin stability, the number of necessary samples does not scale with the dimension of the space of initial conditions.

Integration Subsequently, the system is solved for all of the N drawn configurations $(\mathbf{x}_0^{(i)}, p^{(i)})$. The integration time has to be set appropriately to the system, so that the

asymptotic states are reached. After discarding the transient, the system is integrated for a sufficiently long time. While in theory, this choice of a suitable integration time and transient time is highly non-trivial, in practice, one should have prior knowledge about the time scales of the system. In most situations choosing these times at reasonably large values and checking them for individual trajectories is sufficient. A more sophisticated approach will be discussed in future work.

In case of very long transients, if the system has not truly converged, we may instead observe the basins of attraction of metastable states. See e.g. Lindner and Hellmann [115] for a related discussion of such basins. In this case the results will depend on simulation time.

The Julia package (see Appendix B.4) uses DifferentialEquations.jl [40] to solve ODE systems and from that we will mostly rely on the Tsitouras5 solver [222]. Even though it features an adaptive step size during integration, we save the trajectories at a constant step size, so that the results of all N trials are saved at the same time steps.

Evaluation of the Integration On each of the tail samples generated this way we evaluate a set of statistics, typically we consider some number N_s of statistics per system dimension N_d. These include per default the position and size of the attractor as the mean and standard deviation of the tail sample. Other statistics such as entropy are possible as well, though. Thus, we obtain N matrices of statistics $\mathbf{S}_i$ each $(N_d \times N_s)$-sized with elements $S_{i,kl}$.

Clustering For most clustering algorithms a distance matrix between all samples is needed. This $(N \times N)$-sized distance matrix can be computed from the $\mathbf{S}_i$s with two different approaches. First, by calculating

$$D_{ij} = \sum_{l}^{N_s} w_l \sum_{k}^{N_d} |S_{i,kl} - S_{j,kl}| + w_{N_m+1}|p^{(i)} - p^{(j)}| \tag{4.7}$$

where each measure is weighted with w_i. The parameter values can be included in the distance metric with weight w_{N_m+1} to ensure that similar asymptotic states with strongly different parameter values are distinguished from each other. The other possibility is to first fit a one dimensional histogram $H_{i,k}$ to each statistic k across all system dimensions. This is advantageous when symmetric configuration of asymptotic states should not be distinguished which is often the case for networks of identical units. The distance matrix then follows with a suitable histogram distance $\mathcal{D}_H(H_{i,k}, H_{j,k})$ such as the 1-Wasserstein metric with

$$D_{ij} = \sum_{l}^{N_m} w_l \mathcal{D}_H(H_{i,l}, H_{j,l}) + w_{N_m+1}|p^{(i)} - p^{(j)}|. \tag{4.8}$$

When all $H_{i,k}$ for one specific statistic k share the same binning and norm, the 1-Wasserstein metric can be computed very efficiently from the empirical CDF of each

histogram. While the algorithm also works without the weights, i.e. $w_i = 1 \quad \forall i$, introducing them gives more flexibility when using higher order moments and entropies as statistics. The choice of the weights $\mathbf{w}$ depends on the statistics used and the expected asymptotic states. Generally, a good first guess is to give higher moments such as variance and non-normality measures lower weight than the mean those weight is set to 1. Given the distance matrix, a clustering algorithm such as DBSCAN [65], is used. In Sec. 2.3.5 we already introduced DBSCAN, it classifies all points that can be reached through a common ϵ_{DB}-area as one cluster. Estimating an appropriate ϵ_{DB} parameter is a non-trivial task and there are different possibilities. As discussed in Sec. 2.3.5 the k-nearest neighbour (kNN) distance, more specifically the 4NN distance, can be used to estimate ϵ_{DB} as the the value of the kNN distance at the first visual knee in the ordered kNN distance graph of all data points. Another, yet similar possibility is to use the median of the cumulative kNN distance, where k is a certain percentage of all points, e.g. 0.5%. As explained in Sec. 4.1.4, the ϵ_{DB} can also be estimated by continuing the integration and tracking the response of $\mathbf{D}$. In the examples we have studied, this yields similar values like the more empirical kNN-based methods, but is computationally more expensive. This is why the kNN-based methods are preferred for the estimation of the parameter. Fundamentally there is no "right" choice of ϵ_{DB}, in combination with the choice of distance measures it determines how finely we want to resolve the classes of asymptotic states. While the choice of statistics and weights determines what aspects we look at, ϵ_{DB} provides us with an overall resolution that we can vary. As the clustering itself can be computed very fast, it is easy to scan a variety of values. We will see an example in Sec. 4.1.9 where two clusters that are somewhat similar are no longer resolved as two when we increase ϵ_{DB}. Density-based clustering algorithms such as DBSCAN are sensible to outliers. Input that is strongly dissimilar to all other data is classified as an outlier. For our purpose, this will typically happen when an explosion of multistability, many different, yet dissimilar, asymptotic states occur.

Evaluation of the Clustering The clustering algorithm $\mathcal{C}$ thus returns the cluster assignments

$$\mathbf{C} = \mathcal{C}(\{\mathbf{S}_i\}; \epsilon_{DB}) \tag{4.9}$$

which map each of the N trials to one of the N_C clusters, with $C_i \in [1, N_C]$ being the number of this cluster for trial i. The cluster assignments $\mathbf{C}$ enable us to further analyse the system in question. First of all, we can track the size of the basin of each class of asymptotic states for changing parameters and thus quantify bifurcations and multistability within the system. This is done by computing the amount of trials within a parameter window $[p_{min}; p_{max}]$ and sliding this window over the complete parameter range. We thus have an estimator for the relative basin volume at parameter p that

we derived earlier in Eq. 4.4 for each cluster $\mathcal{C}_i$:

$$\hat{b}_{\mathcal{C}_i}(p) = ||CL_i^{(p)}||/\sum_j^{N_C} ||CL_j^{(p)}|| \tag{4.10}$$
$$CL_i^{(p)} = \left\{ j | (C_j = i) \cap \left(p^{(j)} \in [p_{min}; p_{max}] \right) \right\}.$$

In order to further investigate the dynamics of each class of asymptotic sets, the statistics are subdivided into sets corresponding to each of the clusters as well. This way we can track, e.g., how the position or size of samples in a cluster change as a function of p. Investigating solutions of typical trajectories within each cluster can provide insights as well. In Sec. 4.1.6 examples of such analyses are shown.

All in all, the two main parameters of the method are the weights $\mathbf{w}$ of the distance calculation and the clustering parameter, in case of DBSCAN ϵ_{DB}. As a default for $\mathbf{w}$, we take $w_E = 1$, $w_{Var} = 0.5$, $w_p = 1$. In Sec. 4.1.6 we will explain in more detail why we chose the weights presented for the systems under study. For the clustering parameter, an estimate with the kNN distance or a response analysis is made and if needed this value is increased (decreased) if one wants to resolve more (fewer) clusters. As for most Monte Carlo methods, the number of trials N should be chosen sufficiently large so that the results are independent from it. A reasonable test is therefore to run the experiment twice: if the results differ qualitatively, one has to increase N.

The computational complexity of MCBB very much depends on the system in question. The most expensive parts of the approach are N times integrating the system and the computation of the distance matrix. The integration scales with $\mathcal{O}(N \cdot N_d)$ for sparsely coupled systems, whereas the integration of more densely coupled systems scales with higher powers of N_d. The computation of the distance matrix scales with $\mathcal{O}(N^2)$ and is typically the bottleneck only for systems that integrate very fast and very large N as e.g. the conceptual model for tipping cascades that is shown in Sec. 4.2.1.

Algorithm 1 Monte Carlo Basin Bifurcation Analysis (MCBB)

Given: A dynamical system $\dot{\mathbf{x}} = F(\mathbf{x}, t; \mathbf{p})$ or $\mathbf{x}_{n+1} = F(\mathbf{x}_n; \mathbf{p})$ with system dimension N_d
Given: A set of N_s statistics $\{\mathcal{S}\}$ on the components of trajectories $\mathbb{R}^{N_t} \to \mathbb{R}$ (e.g. mean and variance)
Given: A distribution $\mathcal{U}_{IC}$ of the initial conditions and parameters $\mathcal{U}_p$

for $i \leftarrow 1, N$ **do**
    Sample N initial conditions $\mathbf{x}_0$ from $\mathcal{U}_{IC}$ and N parameter values from $\mathcal{U}_p$
    Solve system for a long trajectory $\mathbf{x}(t; \mathbf{x}_0, \mathbf{p})$
    for $dim \leftarrow 1, N_d$ **do**
        for $meas \leftarrow 1, N_s$ **do**
            compute $S_{i,dim,meas} = \mathcal{S}_{meas}(x_{dim}(t))$ from the tail of the trajectories.
Obtained: N $(N_d \times N_s)$-matrices $\mathbf{S}_i$

Compute $(N \times N)$-sized distance matrix $\mathbf{D}$ of all $\mathbf{S}_i$ to each other.
Density-based clustering (e.g. DBSCAN) of $\mathbf{D}$
Analyze cluster memberships and statistics $\mathcal{S}$ for each cluster dependent on the parameter values $\mathbf{p}$
Obtained: Estimated relative basin volume $\hat{b}_{\mathcal{C}_i}(p)$

4.1.6. Results

MCBB is a method that can be applied to a wide range of dynamical systems. Both, systems with discrete and with continuous state spaces are possible to investigate. Typical applications are networks of oscillators as will be shown in the following, but also discrete agent-based models such as the Dodds-Watts model. Every system that returns a trajectory given an initial condition and parameter can in principal be analyzed with MCBB. In the following we will first analyse three prototypical systems with MCBB: the Dodds-Watts model, Kuramoto oscillator networks and Stuart-Landau oscillator networks. Then, in Sec. 4.2 we will apply MCBB to conceptual climate models as well.

The source code of all these results is available in the GitHub repository of the accompanying software implementation (see Appendix B.4).

4.1.7. Dodds-Watts model

The Dodds-Watts model of social and biological contagion [56, 57] is a generalization of contagion models such as the SIS and SIR model [146, e.g.]. Given is a population of N_I individuals that are connected to all other individuals. Each of the individuals is either in the susceptible (S), infected (I) or recovered (R) state and has a memory of doses they received within the last T time steps $\mathcal{D}_{t,i}$. Thus, showcasing the ability of MCBB to also deal with systems with finite delays or memories. At each time

step each individual i comes into contact with another individual j that is randomly selected from all other individuals. If j is infected, i receives a dose d with exposure probability p. The amount of the dose d is drawn from a distribution $f_d(d)$. The dose adds to the dose memory $\mathcal{D}_{t,i}$ of i at time step t so that $\mathcal{D}_{t,i} = \sum_{t-T+1}^{t} d_{t',i}$. If the dose memory of an individual exceeds the dose threshold d_i^*, it becomes infected. Latter dose threshold d_i^* is drawn from a distribution $g(d^*)$. As soon as $\mathcal{D}_{t,i}$ drops below the threshold, the individual recovers with probability r at each time step. A recovered individual becomes susceptible again with probability s. One gets the classic SIS model e.g. for the configuration $s = 1$, $g(d^*) = \delta(d^* - 1)$, $f_d(d) = \delta(d - 1)$, $T = 1$ with p and r as free parameters. For more details on the model, see Dodds and Watts [56]. For this N_I dimensional model with discrete states $s_{i,t} \in [S, I, R]$ and discrete time $t \in [1, 2, .., t_N]$ we directly evaluate the count of susceptible $N(S)$ and infected states $N(I)$ within the time evolution of each individual as statistics for the algorithm. As shown by Dodds and Watts [56], there are several configurations which possess multistable regimes where also a mixed population with $N(I)$ unequal 0 or N_I can be stable.

In particular, we are investigating the two configurations: (A) with $N_I = 1,000$, $T = 12$, $r = 1$, $g(d) = \delta(d-3)$, $s = 1$ and (B) with $N_I = 1,000$ $g(d) = 0.075\delta(d-1) + 0.4\delta(d-2) + 0.525\delta(d-12)$, $T = 20$, $r = 1$ and $s = 1$. The number of initially infected individuals is drawn from a uniform distributed over $[0; N_I]$. We evolve the system for 1000 time steps from which we regard the first 800 time steps as the transient. Configuration (B) is roughly similar to the SIS model but with a dosage memory of 20 steps and a dosage threshold distribution so that roughly half of the population is quite resilient against becoming infected. For both configurations $N = 5,000$ trajectories with random initial conditions and parameter values were computed. As both of the measures are equally important, we choose $w_I = w_S = 1$ and $w_p = 0$, so that we do not use the parameter value in the distance calculation. The distance $\mathbf{D}$ was constructed using histograms of the statistics as described in Sec. 4.1.5.

Based on a visual inspection of a 4NN-distance graph, the clustering parameter $\epsilon_{DB} = 0.15$ was chosen for configuration (A). Fig. 4.2 shows the results of the analysis. Similar to the results reported in Dodds and Watts [56], we see for such a configuration a bifurcation occur around $p \approx 0.4$. For values larger than this the fully infected state becomes stable. Its basin of attraction quickly grows, but the fully healthy state remains stable as well with a very small basin of attraction for large p values.

Configuration (B) exhibits a slightly more complex structure as Fig. 4.3 reveals, in accordance with the results in Dodds and Watts [56]. Additionally, Fig. 4.3 features sliding histograms as well. These can be helpful to identify the dynamics of the clusters. For each sliding parameter window a histogram is fitted to all statistics results within this window. These histograms are then plotted directly next to each other so that we can visualize changes of the statistics within each cluster for changing parameter values. In the case of the Dodds-Watts model where we measure the fraction of time an individual agent was infected and susceptible, these are predominantly either 1 or 0 as most agents are either infected or susceptible the whole time. Fig. 4.3a shows the behaviour of the system. For small values p only the fully healthy state is stable

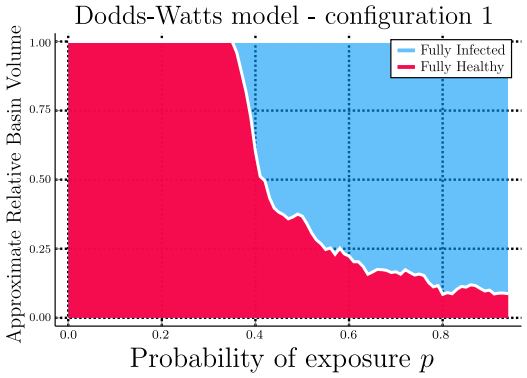

FIGURE 4.2.: Approximate relative basin volume of the two different classes of asymptotic states, fully infected (blue) and fully healthy (red), for configuration (A) of the Dodds-Watts model. The colored areas in the plot represents the basin volume of the respective state. Computed by using a sliding parameter window over the clustering results (see Sec. 4.1.5), a window length of 0.05 and an offset of 0.01 were used.

(see also Fig. 4.3b). The first bifurcation occurs around $p = 0.3$ when a mixed state, for which susceptible and infected individuals coexist, becomes stable. Its basin of attraction quickly grows, while the healthy state remains stable but with a very small basin of attraction. For growing p the amount of infected individuals rises. Eventually, around $p = 0.7$ a fully (or almost fully) infected state becomes stables. As Fig. 4.3 d, shows directly at the bifurcation point not all individuals of the fully infected state are infected which is the case for larger p. Comparing the results to the ones reported in Dodds and Watts [56] we see that the fully infected and the mixed state are indeed two distinctive stable branches of the system and thus rightfully classified by MCBB into two separate clusters.

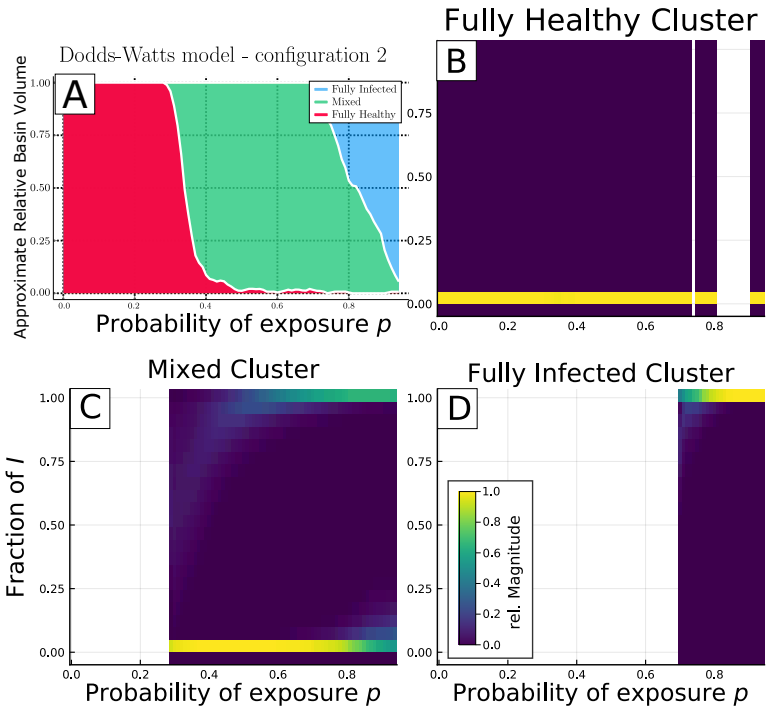

FIGURE 4.3.: (A) Approximate relative basin volume of the different asymptotic states of configuration (B) of the Dodds-Watts model. It exhibits a fully infected (blue), fully healthy (red) and mixed state (green). Computed by using a sliding parameter window over the clustering results (see Sec. 4.1.5), a window length of 0.05 and an offset of 0.01 were used.

4.1.8. Kuramoto Networks

The Kuramoto model is one of the fundamental examples of synchronization theory and network science. Yoshiki Kuramoto derived his model of coupled phase oscillators as the simplest nontrivial model for a temporally organized system that exhibits synchronization or self-entrainment, as he referred to it [107]. The version with inertia, often called second-order Kuramoto model, has been used in a variety of contexts, most importantly to model nodes in power grids [19, 70, 86, 141, 144, 179]. When the coupling of the oscillators to each other is increased, an onset of synchronization can be observed. In the transition towards this globally stable synchronization, the Kuramoto model with inertia exhibits an extreme form of multistability, with a large number of different attractors. Studying the dominant patterns of synchronization in the transition region was one of the motivating questions for the development of MCBB. While we are not interested in resolving every single one of these attractors, we want to gain insights into the dynamics of the model beyond just computing an order parameter.

The system is given by the equations

$$\dot{\phi}_i = \omega_i \,, \tag{4.11}$$
$$\dot{\omega}_i = \pm 1 - 0.1\,\omega - K \sum_j A_{ij} \sin(\phi_i - \phi_j) \quad \text{with } + \forall i \in [1, N/2], -\forall i \in [N/2+1, N]$$

which describe the time evolution of the phase ϕ_i and frequency ω_i of N oscillators that are connected to each other via a network with adjacency matrix $\mathbf{A}$. Equally many oscillators have a $+1$ and -1 in the frequency equation as their drive. For $K = 0$ the oscillators rotate freely with $\omega = \pm 10$. As K increases synchronization starts to occur in the network. At $K = 10$ the system typically synchronizes completely.

While a large number of works have studied the stability of this synchronous state as a function of the local network topology [11, 54, 86, 100, 133, 141, 176, 193, 196, 199, e.g.], comparatively little is known about the intermediate regime. As the aforementioned previous studies have shown, the main dynamics, especially concerning the synchronization of the network, is in the frequency. Hence, we will only consider the frequency dimensions in the analysis here. Fig. 4.4a shows the network on which the oscillators are coupled and the sign of their drive in Eq. 4.12. It is a random regular graph for which every node has degree $k = 3$. The single statistic we will use on the asymptotic state are the positions of the frequency of all the nodes and the distance matrix $\mathbf{D}$ is computed according to Eq. 4.7 from $N = 25,000$ trajectories.

Fig. 4.4b shows the MCBB results for the basin bifurcation structure $\hat{b}_{\mathcal{C}}(p)$, based on distances computed from the per-dimension mean of the frequency. For $K = 0$, i.e. no coupling, the oscillators rotate freely with their natural freely with their natural frequencies $\omega = \pm 10$. This state persists for small K, until its basin volume decreases rapidly from $K \approx 1$ onward. In the intermediate regime between $K \approx 1$ and $K \approx 5$ there are many different asymptotic states. They are classified together in the outlier cluster here because each of these states occurs so infrequently that not enough samples are obtained for a statistical treatment and for a separate cluster to be identified. Hence, the basin structure is not dominated by a single transitional state, instead an explosion of multistability occurs. Two transitional states do achieve a significantly large basin in the transition region though (green and red in Fig. 4.4b), as each of these classes of states occurred in more than 0.5% of the total runs with a maximum relative basin volume of about 10% at $2 < K < 4$. We can look a bit deeper into these clusters, as we do in Fig. 4.5, to find out that these clusters represent a partially synchronized state, in which a region of the network is synchronized in the upper right corner of the network, while all other oscillators rotate at their natural frequency.

To understand how the network synchronizes when K is increased and the unsynchronized and partially synchronized states loose their stability, we can inspect closer the size of the attractor, i.e. the measured per dimension standard deviation of the trajectories, as presented in Fig. 4.6. There we see that with increasing K the size of the attractor increases as well. Thus, the frequency of the oscillators starts to oscillator itself around a stable average frequency. This suggests an interesting insight into the transition regime and how the network synchronizes. When the coupling K

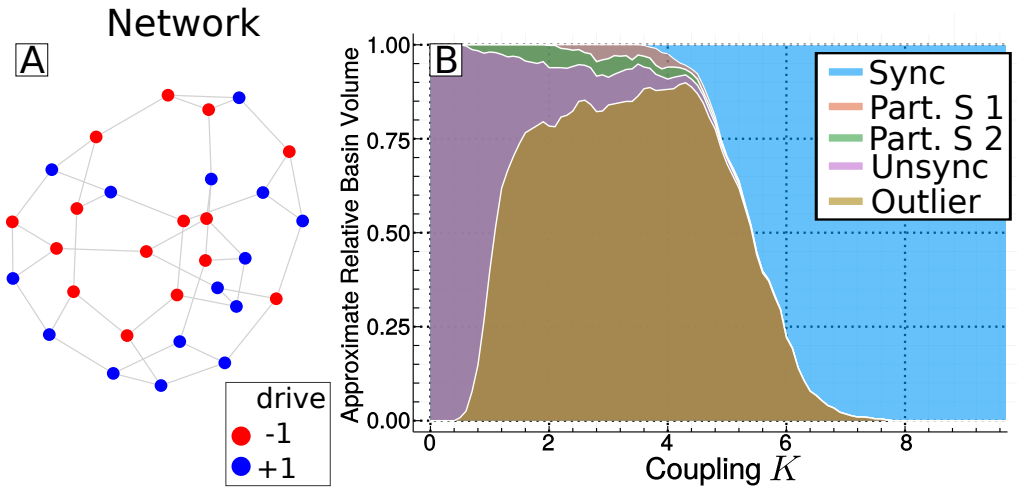

FIGURE 4.4.: (A) Network structure of the investigated Kuramoto system. Red nodes have a negative drive (minus sign in Eq. 4.12) and blue nodes a positive one. (B) The basin bifurcation diagram for the system with the synchronized, partially synchronized and synchronized regimes.

increases some neighbouring oscillators couple and synchronize (as shown e.g. in the partially synchronized states). The basin of the partially synchronized state grows. At the same time when K increases, the frequency oscillations of the non-synchronized oscillators grow and these oscillators spend more and more time far from their natural frequency. Once the frequency oscillations get so large that they are close to the frequency of a synchronized component, the formerly non-synchronized oscillators get entrained. It is beyond the scope of MCBB to accurately verify this mechanism. However, the parameter dependent basin volume that is computed by MCBB, already provides immediate and crucial insights into how the attractors of the systems and their basin structure change during the transition from a fully unsynchronized to a fully synchronized network. Most importantly, the approach shows that the attractors grow in size until they loose their stability.

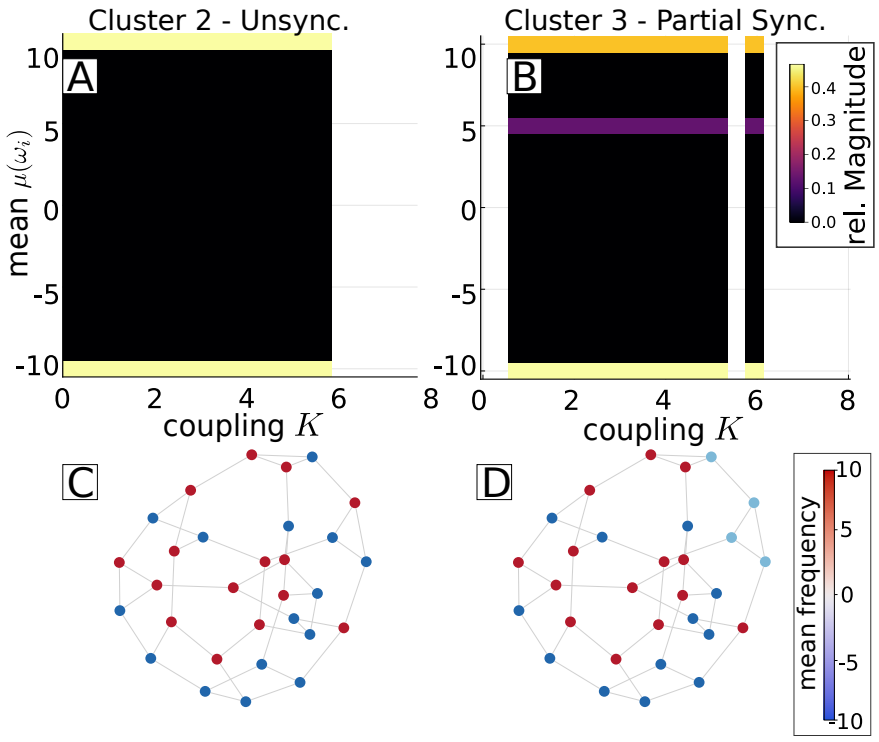

FIGURE 4.5.: Analysis of the clusters exhibiting no synchronization (A) and partial synchronization (B). (A) and (B) are sliding histogram plots, similar to Fig. 4.3 and show the means of the frequencies over all nodes as histograms depending on the coupling parameter. (C) and (D) show the mean frequency of each individual oscillators over all samples in the cluster for cluster 2 (left) and cluster 3 (right).

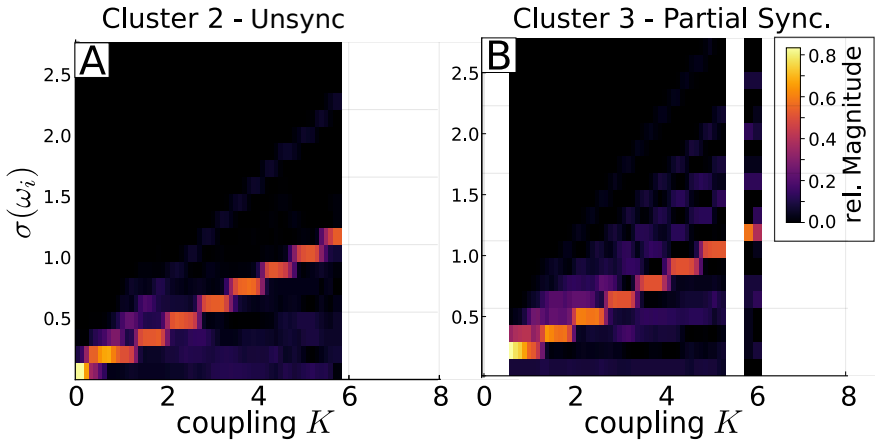

FIGURE 4.6.: Sliding histogram plot similar to Fig. 4.5. Here, the standard deviation of all frequency time series is shown depending on the coupling parameter.

4.1.9. Stuart-Landau Oscillator Networks

Another paradigmatic type of oscillator is the Stuart-Landau oscillator which can be written as

$$\dot{z} = (\lambda + i\omega - |z|^2)z \tag{4.12}$$

where $z \in \mathbb{C}$, λ is the bifurcation parameter and ω is its eigenfrequency. Originally derived by Lev Landau and later by Stuart and Watson [108, 219, 238] to describe the transition to disturbance in hydrodynamics, it is also a normal form of the Andronov-Hopf bifurcation (see Sec. 2.2.6) and hence widely applicable and of great importance in many fields [8]. Coupling Stuart-Landau oscillators can lead to several interesting phenomena. Most importantly oscillator quenching in the form of amplitude death (AD) and oscillator death (OD) [103, 192, e.g]. Also, chimera states [5, 168, e.g.] which describe states of systems of coupled identical oscillators that exhibit an inhomogeneous pattern in which phase-locked, synchronized states coexist with drifting states. To apply MCBB to Stuart-Landau systems, we use the configuration of Sathiyadevi et al. [190] as it prominently features a multistable regime with travelling wave (TW), oscillation death (OD) and what the authors refer to as stable amplitude chimera (SAC) dynamics. In this setup N_N Stuart-Landau oscillators with identical eigenfrequency ω are coupled by attractive coupling to its P_1 nearest neighbours and repulsive coupling to its P_2 nearest neighbours via the following equations:

$$\begin{aligned}\dot{z}_i = (1 + i\omega - |z_i|^2)z_i + \frac{K}{2P_i}\sum_{k=i-P_1}^{i+P_1} \Re(z_k - z_i) \\ -i\frac{K}{2P_2}\sum_{k=i-P_2}^{i+P_2} \Im(z_k - z_i).\end{aligned} \tag{4.13}$$

where $\Re(x)$ is the real part and $\Im(x)$ the imaginary part. We can also investigate this setup with the coupling mediated on two Watts-Strogatz random graphs [239], one for the repulsive and one for the attractive coupling. With the rewiring probability $p_r = 0$, we get the same equation as above, for $p_r \neq 0$ we expect changes in the dynamics.

Parameter Configuration

We choose the same parameter configuration as in Sathiyadevi et al. [190]: $\omega = 2$, $N_N = 100$, $P_1 = 1$ and $P_2 = 22$. In our experiments we vary K, $r_2 = P_2/N_N$ and p_r. We use random initial conditions with real and imaginary part uniformly distributed between -1 and 1 (in contrast to the cluster initial conditions used for some calculations in [190]) and vary K from 1.8 to 2.5. As per dimension measures we use mean and standard deviation. Since the Stuart-Landau oscillators are complex valued, all measures are applied separately to the real and imaginary part. From our a priori knowledge about Stuart-Landau Oscillators, we know that their asymptotic states will exhibit different kinds of oscillatory behaviour, thus it is a good choice to

put the largest weight on the standard deviation. We choose $w_E = 0.25$, $w_{SD} = 1$, $w_p = 1$ and run $N = 15,000$ trials that are integrated from $t_0 = 0$ to $t_f = 200$. The first 70% of this time span are regarded as the transient and are not used for the evaluation. The first experiment is performed with $p_r = 0$ and $r_2 = 0.22$ and the distance matrix $\mathbf{D}$ is calculated using histograms according to Eq. 4.8.

Varying the coupling

After running the experiment and calculating the distance matrix $\mathbf{D}$, the associated 4-dist graph exhibits the knee point at around 0.01. We slightly decreased this value to 0.009 and 0.008 in the reported results. Fig. 4.7a and b show these results for the approximate relative basin volume. Similar to the results reported in Sathiyadevi et al. [190] we see a multistable regime, in which TW dynamics are prevalent for $K < 1.95$ and OD dynamics for $K > 2.2$. In between there are various states in which some oscillators show OD-like behaviour and others exhibit a synchronized oscillation. We thus prefer to refer to these kinds of states as partially synchronized (PS) states. Importantly, the PS states are a mixture of many similarly partially synchronized states and not just a single asymptotic state. If we choose a larger ϵ_{DB} like in Fig. 4.7A, the states with full OD and the PS states with only few partially synchronized oscillators and otherwise mostly OD dynamics are merged into one cluster (OD+PS). For smaller ϵ_{DB} they are separated into two distinct clusters (Fig. 4.7A). One particular structured and more common kind of partially synchronized states can be found for $1.9 < K < 2.0$. As Fig. 4.8 shows, these states are highly regular stationary waves, interrupted by oscillators exhibiting OD. We thus refer to these states as regularly clustered stationary wave states (RCSW). Aside from these more regular dynamics, there are all kinds of different mixed states between wave-like dynamics and oscillation death. Many are so dissimilar to each other that they fall into the outlier cluster. The outlier cluster has the most members during the transitions from TW to PS via RCSW at $K \approx 2.0$ and at the transition between OD and PS at $K \approx 2.2$. A handful of smaller clusters with less than 60 members (or 0.4% of all trials) were neglected. They contain partially synchronized states with more similarities to each other than to those in the outlier cluster. We identified these dynamics by further analyzing the statistics within each cluster. Fig. 4.8 shows example plots and sliding histogram plots for two of these clusters. The RCSW states mostly oscillate and thus almost all oscillators have a mean of zero and a constant standard deviation different from zero. We see that these histograms change little for different coupling values. The cluster is very homogeneous with almost all members looking like the example shown in Fig. 4.8 C. The PS cluster, on the other hand, is much more inhomogenous. Its members have in common that most of the oscillators exhibit OD, thus as Fig. 4.8 confirms, they exhibit nonzero means, with both positive and negative values while having a vanishing standard deviation which corresponds to the typical stable fixed points of OD dynamics. Fig. 4.8 D shows one example, the amount of oscillators still exhibiting synchrony is different within the cluster, though. Additional results for the other clusters can be found in the Appendix.

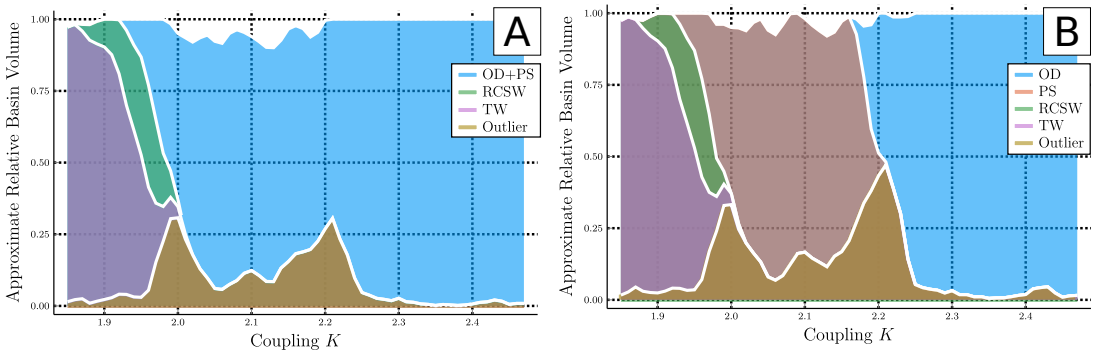

FIGURE 4.7.: Cluster diagram of the Stuart-Landau Oscillator network with $p_r = 0$ for two different values of the clustering parameter ϵ_{DB}. For (A) $\epsilon_{DB} = 0.009$ and for (C)&(D) $\epsilon_{DB} = 0.008$. MCBB resolves the different classes of asymptotic states: travelling wave (TW), regular clustered stationary waves (RCSW), (full) oscillation death (OD) and mixed partial synchronized / oscillation death (PS) states. When increasing ϵ_{DB} states in which most (but not all) oscillators exhibit OD, while the remaining few oscillators are synchronized (PS) and the states in which all oscillators exhibit OD (OD) are merged to one cluster (OD+PS). The window size used is 0.025 and the window offset is 0.01.

Varying the coupling and amount of coupled neighbours

Similarly to the additional setup in Sathiyadevi et al. [190], we can also investigate this system with two varying parameters using MCBB. First, we choose to vary K, the coupling strength, and r_2, the relative amount of neighbours the oscillators are coupled to repulsively. Fig. 4.9 shows similar clusters of similar asymptotic behaviour as in the one-dimensional setup. We see that TW dynamics are present only for small K and large r_2 values, while OD+PS dynamics are present even for small K values when r_2 is small. For very small r_2 there is also a desynchronized (DS) cluster. Most notably the distinctive RCSW type dynamics are only present for $r_2 > 0.1$ and its basin becomes larger for larger r_2 values.

Rewiring of the network

When we start to randomize the coupling by rewiring it according to the scheme of Watts-Strogatz random graphs, we get the results presented in Fig. 4.10. Here, we added the outlier cluster together with several smaller clusters that all exhibit mixed, partially synchronized, partially OD dynamics to the mixed states (MS) cluster. The range of K for which these kinds of dynamics appear gets wider when the rewiring p_r increases. TW dynamics appear less for larger p_r values. RSCW type dynamics do not appear when the network is rewired.

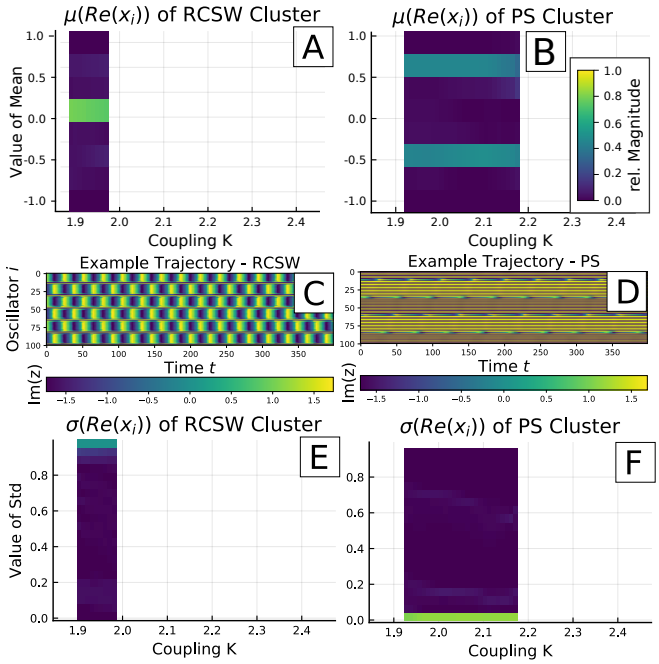

FIGURE 4.8.: Introspective analysis of the two of the clusters also shown in Fig. 4.7. Plots (A),(B),(E),(F) are sliding histogram plots. For each sliding window of coupling values K, the respective measures of trajectories within the said cluster are plotted as a histogram in y-Direction. (A-C) inspect the RCSW cluster. (A),(B) show the mean and the standard deviation of the RSCW cluster. (C) and (D) are example trajectories from the respective clusters. (E), (F) show the mean and standard deviation of the PS cluster.

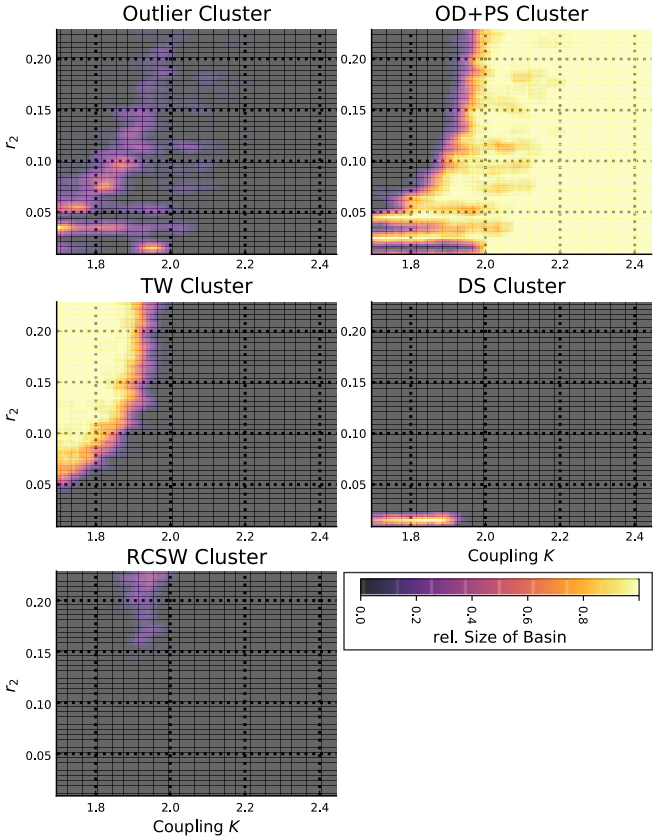

FIGURE 4.9.: Results from the setup with two parameters, varying the amount of coupled neighbours r_2 and the coupling strength K.

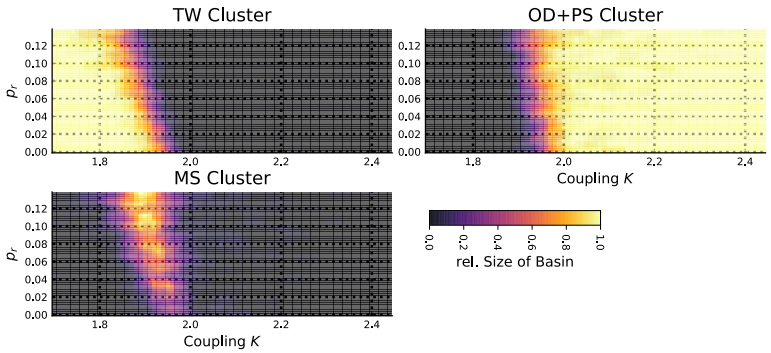

FIGURE 4.10.: Results from the setup with two parameters, varying rewiring p_r of the Watts-Strogatz random graph that mediates the repulsive coupling and the coupling strength K.

4.1.10. Discussion

Given a complex system, such as an ODE system, like the Kuramoto and Stuart-Landau networks demonstrated in Sec. 4.1.8 and 4.1.9, or a map like the Dodds-Watts model presented in Sec. 4.1.7, MCBB is able to analyze and quantify which classes of asymptotic states are occuring. As demonstrated with the paradigmatic example systems MCBB is a widely applicable approach. It is suitable to analyze the behaviour of every high-dimensional system that returns a trajectory, be it agent-based models such as the Dodds-Watts model or differential equations like the Kuramoto and Stuart-Landau networks. The known bifurcations of these systems were reproduced by MCBB as shown for example with the Dodds-Watts model. Additionally, it enables us to reveal clusters of qualitatively similar asymptotic states for all these systems as the results investigated in Sec. 4.1.9 show. It does successfully identify the sizes of the basins of the most important asymptotic states even in transition regimes, which a traditional bifurcation analysis cannot reveal. For the Kuramoto system we see how and when the basin of the unsynchronized states shrink and how the basins of the completely synchronized states emerge. We also get an insight into the transition between these states, as we can see how the size of the attractors increases before they destabilize. Hence, for the Kuramoto model it provides an intuitive way of visualizing the synchronization process. When applying MCBB to a Stuart-Landau system the different asymptotic behaviours, travelling wave states, oscillator quenching phenomena such as oscillator death and mixed states, are classified in different clusters and interesting dynamics such as regularly clustered stationary wave states are revealed and their basins are quantified.

The analysis can always be fine tuned by changing the clustering parameters to resolve the asymptotic states finer or coarser. Additionally, the weights of the distance calculation provide another mean of adjustment. The flexible nature of the method also allows for experimentation with the statistics used to evaluate the trajectories and the exact clustering algorithm. In particular various entropy-based statistics

seem promising to use. While designing the method we already used the per dimension Kullback-Leibler divergence as a statistic to track structural changes of investigated systems. This was especially useful for relatively low-dimensional systems. The curve entropy [13] of the complete trajectory was tested as well. Additionally, we also experimented with a distance between histograms of the covariance matrices as a statistic. This expands variance-based size measure to also take cross-correlation between the dimensions into consideration which could be useful for systems that exhibit multiple possible cross-correlations structures in the asymptotic states that otherwise behave similar, e.g. different kinds of collective oscillations. For the example systems presented here, it was however sufficient to only use the position and size of the attractors as measures. Additional measures were not necessary to resolve the different classes of asymptotic states. This should not stop experimentation with additional measures though, as some of them are already implemented in the accompanying software as well with further additional ones easy to add.

Aside from the approximate basin volume and the sliding histograms shown here, it is also possible to further investigate the clusters found by the clustering algorithm, e.g. by analyzing which kind of initial conditions lead to certain class of asymptotic states or by analyzing how each dimension is changing with the control parameters separately and not in histogram form. These options are already implemented in the Julia package (see Appendix B.4) and more could be envisioned in the future.

A distinct limit of the approach is that it is only able to detect and track stable solutions of the investigated systems. Unstable solutions are not accessible with MCBB. A further important avenue of investigation is to study the mathematical properties of the algorithm described here in much more detail. In particular it would be highly desirable to understand the convergence properties of the algorithm. We also suspect that there is considerable scope for improving the clustering by making use of information from the continuation, rather than reverting to a standard density-based algorithm. In Appendix B.2 one modified algorithm that needs further investigations is already outlined. One other avenue of investigation where we will improve the method further is to use the statistics of the tail sample we record in order to track when the integration has reached the asymptotic regime in a suitable sense.

So far we focused on introducing the method, testing it with paradigmatic examples and discussing the results on these models. MCBB opens the door to studying a wide variety of systems in novel ways. In the following we will investigate two conceptual climate models and show how MCBB can be useful for the analysis of these types of models as well.

4.2. MCBB for Climate Models

In the previous sections we demonstrated on paradigmatic examples that MCBB is able to uncover and quantify the largest basins of attraction of high-dimensional complex systems. And, as aforementioned mentioned, most climate models exhibit multistabilty as well, e.g. energy-balance climate models exhibit a bistability between a cold

and warm state [39, 127, 201], but also regional climate can exhibit multistability such as between savannah and rainforest states [46, 88]. In the following sections we will first explore a conceptual model for tipping cascades with MCBB. This follows parts of the publication „Basin stability and limit cycles in a conceptual model for climate tipping cascades“ [MG7] with additional MCBB results added here that replace the original basin stability results. Afterwards we will analyse a bistable climate toy model. This follows the first part of the publication „Analysis of a bistable climate toy model with physics-based machine learning methods“ [MG6].

4.2.1. Conceptual Model for Climate Tipping Cascades

The Model

Several large-scale sub-regions of the Earth exhibit a multistability that could lead to a "tipping" from one state into another when a certain threshold of e.g. the global mean temperature is transgressed. Lenton et al. [113] identified several of these tipping elements of the Earth. All of the Earth's climate sub-regions are connected in some direct or indirect manner and thus it is natural that a massive change of the behaviour of one sub-region will impact others. A potential domino-like effect, a tipping cascade, has been hypothesized [37, 214]. Here, we want to investigate the properties of a conceptual model of interlinked tipping points, in particular its attractors, to understand the dynamics of tipping cascades. We restrict the model to five elements that are potentially the most vulnerable to tipping when the 2.0°C goal of the Paris Agreement is transgressed. These are the Greenland Ice Sheet (GIS), the West Antartic Icesheet (WAIS), the Atlantic Meridional Overturning Circulation (AMOC), the Amazon rainforest (AMAZ) and the El-Niño Southern Oscillation (ENSO). For a more detailed view on the choice of the tipping elements, the reader is referred to [MG7].

Each individual tipping element is represented by the cusp normal form that we already introduced in Sec. 2.21:

$$f_i\left(x_i\right) = -a_i x_i^3 + b_i x_i + c_i \qquad\qquad a_i, b_i, c_i \in \mathbb{R}. \tag{4.14}$$

It exhibits hysteresis and two critical points where a tipping from one state into the other can occur and is therefore a good candidate for a conceptual tipping element [37]. We couple five of these together with an individual link strength s_{ij} and assume, a simplified, linear interaction between the elements. Reformulating the constants in Eq. 4.14 in order to give them a physical meaning, then results in the full model

$$\frac{dx_i}{dt} = \left[-x_i^3 + x_i + \frac{\sqrt{4/27}}{T_{\text{limit, i}}} \cdot \Delta\text{GMT} + \frac{d}{10} \cdot \sum_{\substack{j \\ j \neq i}} s_{ij}\left(x_j + 1\right) \right] \frac{1}{\tau_i}. \tag{4.15}$$

In this model τ_i is the typical time scale one tipping element needs to undergo the transition from one state to another and $T_{\text{limit, i}}$ is the critical temperature threshold of each element (see Tab. 4.1). The 1 is added in the coupling term, to ensure that the

coupling term is positive and its sign, determining whether or not there is a positive or negative feedback, is only determined by s_{ij}. The factor $\sqrt{4/27}$ stems from the location of the tipping points of the cusp equation. We derived these for a very similar equation in Sec. 2.2.6. An untipped element will exhibit a value of around -1 and a tipped element a value of around $+1$. The change in global mean temperature to pre-industrial levels ΔGMT is the first control parameter in our analysis. Furthermore we will treat the overall interaction strength d as an additional control parameter. The interaction strength is normalized to $d \in [0; 1]$, whereas $d = 0$ equals to no coupling at all, $d = 1$ means that the coupling term has a similar magnitude as the dynamics of the individual sub-element. Therefore small values around $d \approx 0.2$ seem the most realistic. The parameters of the model are thus τ_i, s_{ij} and $T_{\text{limit},i}$ and the control parameters ΔGMT and d. Values of these parameters are based on expert survey and given in Tab. 4.1 and B.1. Most of the parameters have large uncertainties. Importantly, for some of the links the sign of s_{ij} is also uncertain.

TABLE 4.1.: Parameters of the model: critical temperature range $T_{\text{limit, i}}$ of the five tipping elements as taken from the literature [194]. The typical tipping time scale τ_i is given in model years (in arbitrary units).

Tipping element	$\mathbf{T_{limit,\,i}}$ **[°C]**	$\tau_\mathbf{i}$ **[a.u.]**
Greenland	0.8 – 3.2	4900
West Antarctica	0.8 – 5.5	2400
AMOC	3.5 – 6.0	300
ENSO	3.5 – 7.0	300
Amazon rainforest	3.5 – 4.5	50

Adjustments to MCBB

We are interested in investigating the attractors of this model which mostly correspond to the different combinations of elements being tipped or not. With MCBB we can compute the relative size of the basins of these attractors and how these change when the global mean temperature increases or the interaction strength is increased. All parameters of the model have large uncertainties. Any analysis of the system needs to account for those. When generating sample trajectories during the MCBB procedure, we therefore also always draw these parameters randomly. Whereas we regard the interaction strength d and the change in global mean temperature to pre-industrial levels ΔGMT as the control parameters, all other parameters are considered background parameters and are uniformly randomly drawn from within their uncertainties. The basin information is then computed only with regard to the control parameters. To cover the phase space and the parameter uncertainties sufficiently well a larger number of samples N than in our previous examples is therefore needed. The presence of these background parameters changes the notion of what we understand as a class of similar attractors within MCBB and their basins. However with this change, we

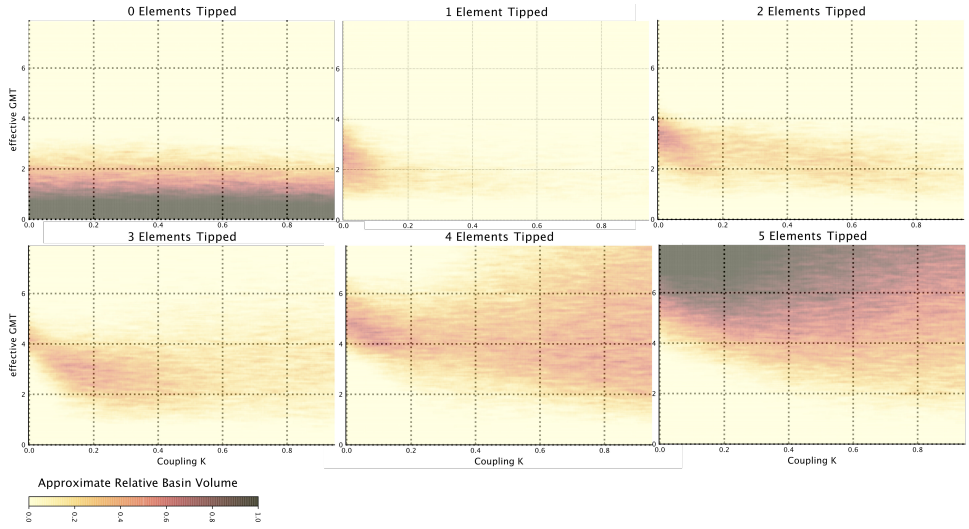

FIGURE 4.11.: MCBB results of the Conceptual Model for Tipping Cascades. For this analysis all initial conditions were set to the untipped state. Additionally, limit cycle oscillations are found that are looked at in detail in Fig. 4.13.

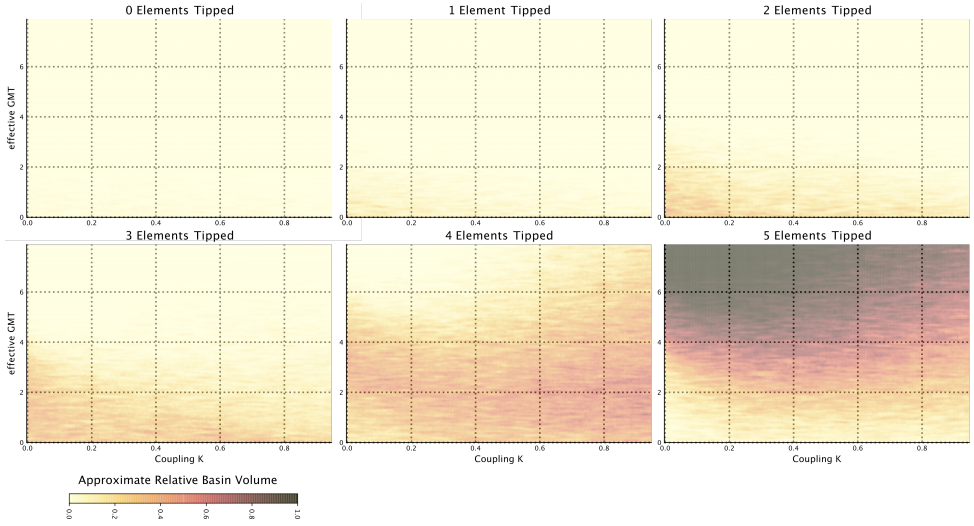

FIGURE 4.12.: MCBB results of the Conceptual Model for Tipping Cascades. For this analysis all initial conditions were randomly set within $[-1; 1]$. Additionally, limit cycle oscillations are found that are looked at in detail in Fig. 4.14.

are still able to make qualitative judgements on tipping cascades in the model even if this model has large uncertainties. Furthermore, we can also restrict the analysis to run only from initial conditions that are untipped. This would correspond to the current state of the Earth and enable us to study the actual tipping cascades better. For instance a system that starts with all but one element tipped, is highly unlikely to induce a cascade. However as we are not only interested in the cascades but also in the basin structure of the attractors of the model itself, both approaches, random initial conditions as usual with MCBB, and a restriction to untipped initial conditions are performed. Aside from the uncertainties of the model, the model is used with two control parameters. Extending the definition for the relative basin volume (Eq. 4.10) to two-dimensional parameter setups is straightforward by sliding a two-dimensional parameter window over the clustering results as we have already done when investigating the Stuart-Landau oscillator network in Sec. 4.1.9.

Results

The MCBB analysis was conducted by integrating $N = 175,000$ trajectories for a time of $52,000$ $a.u.$. This very long integration time was chosen to avoid any transient dynamics as some elements can also still tip after a considerable amount of time due to the large τ_i values. As statistics for MCBB only the mean and the variance per dimension was used and the distance matrix was computed with the histogram approach (see Eq. 4.8) and both statistics have the same weight. The ϵ_{DB} value for the clustering was found with the kdist-method at $\epsilon_{DB} = 0.2$. However, the results are not very sensitive to this value. When evaluating the clustering results, it is easy to identify the amount of tipped elements, as in this model, aside from transient dynamics, all tipped states will exhibit stationary values of around $+1$ and all untipped states exhibit stationary values of around -1. Fig. 4.11 shows the MCBB results when the initial conditions are all in the untipped state. Increasing ΔGMT increases the amount of tipped elements. One, two or three tipped elements are only possible for $\Delta\text{GMT} \lessapprox 4$. Larger temperature lead to four or all five elements tipped. Compared to the values of $T_{\text{limit},i}$, more elements tip at lower ΔGMT values with increasing d. Whereas three of the five elements have a minimal $T_{\text{limit},i} \geq 3.5$ on their own, already for $\Delta\text{GMT} \approx 2$ and $d \approx 0.2$, states with three tipped elements become stable. By inspecting the results gathered during the MCBB run, one sees that these states are mostly those of the GIS, WAIS and AMOC beeing tipped. Increasing either d or ΔGMT only slightly results in four and five tipped elements.
Looking at the results of the analysis of the basins with random initial conditions (see Fig. 4.12), shows that the volume of the basin of attraction with respect to initial conditions in the complete phase space of the model is very small for states with zero, one or two tipped elements. At the $d = 0.2$ and $\Delta\text{GMT} = 2$ point only states with three, four or five elements have a large basin of attraction, increasing either of d or ΔGMT leads to states with four or five elements beeing tipped.
Furthermore, limit cycle attractors are found by MCBB, identifying the parameter regimes where Hopf bifurcations occur and the tipping elements start to show Kadyrov

oscillations. Such Kadyrov oscillations have already been found in the early literature on dynamical systems of the cusp type [1]. As shown in Fig. 4.13 for initial conditions at -1 for all tipping elements, this is most prominently the case for large interaction strengths and medium temperature increase values. Here, about every tenth solution is oscillating. For smaller interaction strength values, limit cycles can still occur but are much rarer with an occurrence at about 1% of all solutions. Of all these limit cycle oscillations almost all (95%) have a significant amplitude (Standard deviation $>$ 0.1) in at least one tipping element. The most common limit cycles are simultaneous oscillations of AMOC and GIS as shown in Fig. 4.13d. They make up about 86% of all oscillating states found. The reason for this predominant oscillation is that there is a strong negative feedback loop between the Greenland Ice Sheet and the AMOC via freshwater input from Greenland that weakens the AMOC, while on the other side a weaker AMOC cools the northern hemisphere [see e.g. 41, 105]. Still, whether such oscillations could indeed exist in the climate system remains speculative, but in principle there is evidence of oscillatory behavior in paleo data of the Earth system [50].

Discussion

For temperatures above 4.0°ΔGMT, we find that the only dominating stable states are those with four or five tipped elements. Even for lower temperature increases states with two to four tipped elements already have a considerably large basin of attraction. The analysis that was performed from all-untipped states also shows that tipping elements may tip earlier than their individual critical temperature, due to tipping cascades. The most common combination of tipping elements for this to happen is that of GIS, WAIS and AMOC. The difference between running the analysis from all-untipped states or randomly chosen initial conditions also shows the hysteresis of the model. Once an element is tipped, it is almost impossible for it to revert its state back to the untipped state. Even when there is only a small but nonzero coupling or increase in GMT, the states with all states tipped already exhibit a significant basin of attraction. Limit cycle oscillations between the tipping of some elements have been detected at some rare parameter configurations, particularly at large interaction strength levels. These occur mainly between the Greenland Ice Sheet and the AMOC. Although it remains unclear whether such (Kadyrov) oscillations have occurred in the climate system, they point towards possible internal modes of variability in the climate system. However, in principle such limit cycle behavior could have played a role during paleo times such as the Pleistocene [50, 55].

One of the advantages of using MCBB for this analysis is that it is computationally cheaper than a thorough basin stability analysis and the adjustments made to the method also allowed for the analysis of a model with considerable uncertainties and two control parameters. This further extends the capabilities of MCBB.

Here, we present results for a dynamical network approach with strongly simplified individual dynamics of each tipping element. It has to be clear that no direct forecast of tipping cascades can be derived from such a conceptual model which simplifies the nature of tipping elements as well as their interaction structure. However, it can still

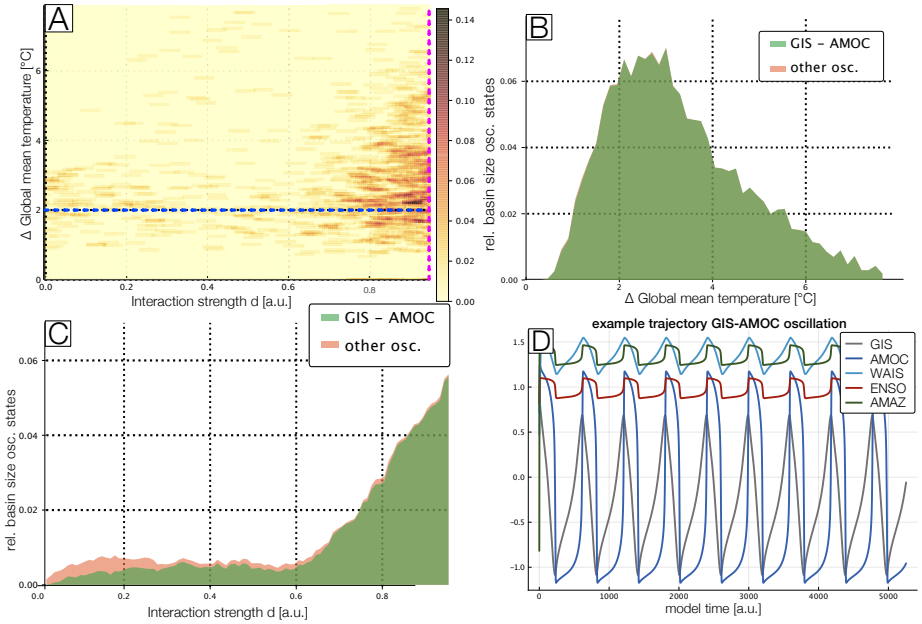

FIGURE 4.13.: Detailed view of the oscillating states. Here, the initial conditions of all tipping elements are $[-1, -1, -1, -1, -1]$. For random initial conditions, see Fig. 4.14. **(a)** Occurrence of oscillating states with respect to global mean temperature above pre-industrial level GMT and interaction strength parameter d. **(b)** 1D Slice of (a) along the dashed magenta line, dependence of limit cycles and their main type on the temperature increase at high interaction strength. **(c)** 1D Slice of (a) along the dashed blue line, dependence of limit cycles and their main type on the coupling strength at a temperature increase of 2 °C above pre-industrial. **(d)** Example time series for a limit cycle of AMOC and GIS.

be helpful to get insights into potential threats of tipping events and investigate the possibility of tipping cascades with such simplified models until coupled, process-based models are developed that can resolve the involved processes and coupling structures in more detail. At the very least, these simplified models can tell us where potential dangers are and where to investigate further with future, more sophisticated models.

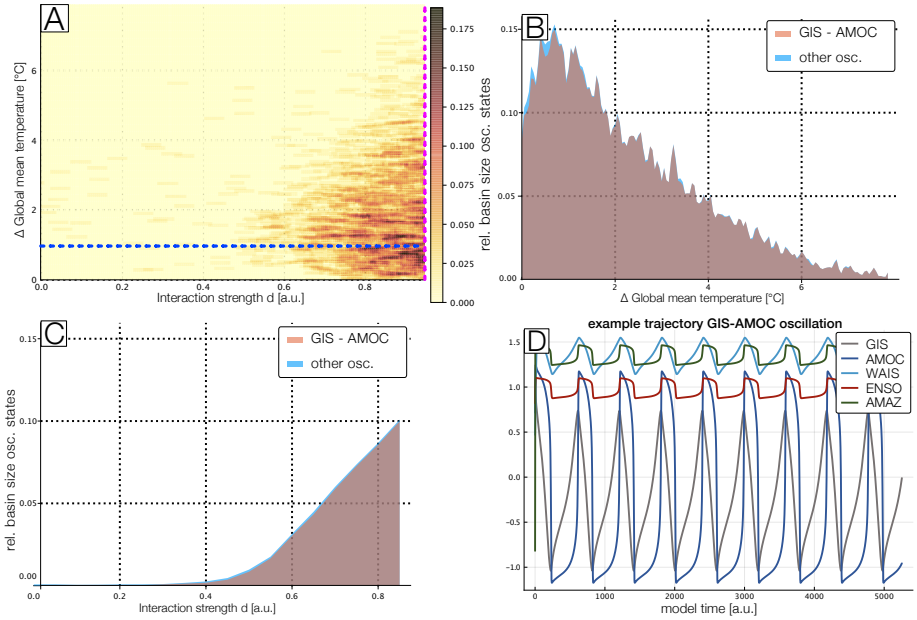

FIGURE 4.14.: Detailed view of the oscillating states. Same plot as in Fig. 4.14 but with random initial conditions.

4.2.2. Bistable Climate Toy Model

Energy-balance climate models exhibit a well-known bistability between a cold state, often called "snowball earth" and a warm state that corresponds to the present day climate [39, 201]. This is not only an effect of models, as paleoclimatic evidence reveal that such a snowball earth state of global glaciation has most likely occurred in the past [90, 102]. In between these states saddle-like Melancholia states may exist [127]. Towards the goal of applying MCBB to realistic models such as a quasigeostrophic atmosphere model or even Earth Models of Intermediate Complexity (EMICs), we start with a simplified Bistable Climate Toy Model.

Model description

The Bistable Climate Toy Model (BCTM) consists of a Lorenz96 model (L96) [118, 120] that is coupled to a zero-dimensional energy balance model (EBM). The L96 model can be thought of as a representation of atmospheric dynamics along one latitudinal circle as it also features simplified processes of advection, forcing and dissipation. However, it does not correspond to any known actual fluid dynamical system and therefore does not model the atmosphere directly. It was rather set up as a toy model to study chaotic spatially extended systems and their predictability. The L96 model has rapidly gained relevance in many different research areas in order to study

bifurcations [35, 96–98, 154, 156, 227], to test parametrizations [2, 10, 44, 153, 233, 234, 246], to investigate extreme events [20, 21, 93, 215], and ensemble forecasting techniques [60, 109, 245], to develop new tools for investigating predictability [42, 83, 95, 162], and for addressing basic issues in non-equilibrium statistical mechanics [3, 4, 75, 125, 126].

In its simple one-layer form the L96 model is formulated as follows:

$$\dot{X}_n = (X_{n+1} - X_{n-2})\, X_{n-1} - X_n + F, \quad n = 1, \ldots, N \tag{4.16}$$

with periodic boundary conditions given by $X_{j-N} = X_j = x_{j+N}\ \forall j = 1, \ldots, N$. The first, nonlinear term describes a non-standard advection, the term $-X_n$ dissipation and the parameter F describes the forcing acting on the model. The energy of the system is $E = 1/2 \sum_{n=1}^{N} X_n^2$. For a detailed analysis of the mechanics and energetics of the L96 model and of a generalisation thereof, the reader is referred to [235].

If $N \gg 1$, the model exhibits a fixed point for low forcing values $0 \leq F \leq 8/9$ at $X_k = F$, $k = 1, \ldots, N$. The fixed point loses stability as F is increased and, after a complex set of bifurcations [96, 97, 227], the system becomes chaotic for $F \geq 5.0$ [118].

In order to introduce multistability in the L96 model, an efficient strategy is to suitably couple it with a multistable model, as described in Bódai and Lucarini [22]. Our simple bistable model of reference is the zero-dimensional EBM of the form:

$$\dot{T} = -\frac{\mathrm{d}V(T)}{\mathrm{d}T} \tag{4.17}$$

where $V(T)$ is a confining potential ($V(T) \to \infty$ sufficiently fast as $|T| \to \infty$) with two local minima separated by a local maximum. Additional stable states could be introduced with a $V(T)$ that features more minima. The full BCTM then follows as

$$\begin{aligned} \dot{T} &= S\left(1 - a_0 + \frac{a_1}{2}\left(\tanh\left(T - \tilde{T}\right)\right)\right) - \sigma T^4 - \alpha\left(\frac{\mathcal{E}}{0.6 \cdot F^{\frac{4}{3}}} - 1\right) \\ \dot{X}_n &= (X_{n+1} - X_{n-2})\, X_{n-1} - X_n + F\left(1 + \beta\frac{T - \tilde{T}}{\Delta_T}\right) \end{aligned} \tag{4.18}$$

where the usual periodic boundary conditions of the L96 apply ($X_{j-N} = X_j = x_{j+N}$ $\forall j = 1, \ldots, N$), and $\mathcal{E}$ is the energy per site of the L96 model $\mathcal{E} = E/N$. The values and meaning of all parameters of the model can be found in Tab. 4.2. The coupling of EBM to the L96 is set up so that if the temperature of the EBM is higher than its reference $\tilde{T}$ (very roughly a state of higher energy in the atmosphere) the L96 is forced with a forcing larger than its reference forcing F (and vice versa). The strength of the coupling is controlled with the parameters α, β. In the EBM the first term describes the incoming (solar energy), modulated by the temperature-dependent albedo, due to tanh in the term, the albedo is $a_0 + a_1/2$ for very low temperatures and $a_0 - a_1/2$ for very high temperature. The second term corresponds to the outgoing energy through the Stefan-Boltzmann law. In the third term a negative feedback in the system is introduced, so that if the energy per site $\mathcal{E}$ is larger than the average value in the

TABLE 4.2.: Parameters of the Bistable Climate Toy Model

Solar Constant	S	$[5; 20]$
Albedo	a_0	0.5
Albedo	a_1	0.4
Reduced Stefan-Boltzmann Constant	σ	$1/180^4$
Reference Forcing	F	8
Number of Grid Points	N	40
Reference Temperature	$\tilde{T}$	270
Temperature Scale	Δ_T	60
Coupling $X \to T$	α	2
Coupling $T \to X$	β	1

uncoupled case, which is $\bar{\mathcal{E}} \approx 0.6F^{4/3}$ [75], the temperature of the system is reduced. The system also exhibits Melancholia states in form of a chaotic saddle sitting between the two competing attractors [MG6, 127].

Results

We apply MCBB to the Bistable Climate Toy Model by sampling $N = 15,000$ trajectories with initial conditions drawn from $\mathcal{U}(-7; 7)$ for the L96 state variables X and $\mathcal{U}(240, 300)$ for the temperature T. The solar constant, the control parameter, is varied within $S \in [5; 20]$. The trajectories are integrated for 400 time units and the first 80% of the trajectory are not included in the analysis to avoid transient effects. Only the statistics E_k, Var_k, KL_k of the L96 model are used for the identification of the attractors, but the EBM mean E_{EBM} is saved for further analysis as well. Fig. 4.15 shows the approximate relative basin volume estimated by MCBB. Two classes, i.e. clusters, are found. The system is multistable in the interval of around $S \in [7; 15]$ with each of the basins being approximately equal-sized with respect to the distributions of initial conditions chosen. For $\epsilon_{DB} = 0.05$ the clustering algorithm detects several outliers. These are mostly the trajectories that go through the Melancholia state (M). As shown in Fig. 4.17 they exhibit a saddle-like behaviour for the EBM variable. When ϵ_{DB} is increased to 0.1 or larger these states are not resolved anymore and the algorithm only finds the cold and warm state as shown in Fig. 4.15. Further insights can be gained with a sliding-histogram approach. For each sliding parameter window a histogram is fitted to all collected values of the EBM mean for each of the two attractors. Fig. 4.16 clearly shows the two stable branches of the EBM and its respective values of the forcing F. As one can expect the "blue" cluster in Fig. 4.15 exhibits the much larger values of the forcing (see Fig. 4.16b)) and is thus the warm state of the model and the "red" cluster in Fig. 4.15 is the cold state of the model. Again, the hysteresis behaviour of the model is evidently shown. For $S < 7$ only the cold state is stable and for $S > 15$ only the warm state is stable.

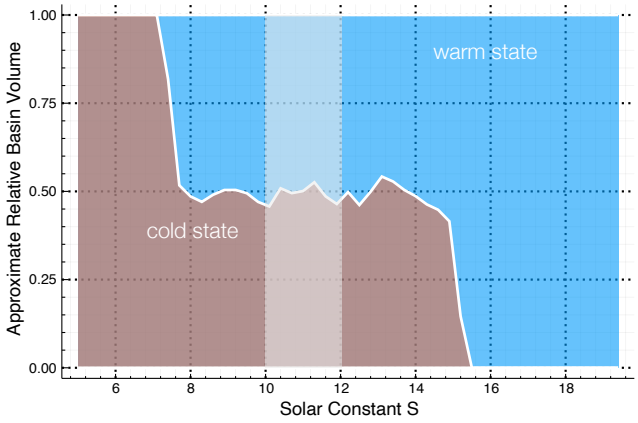

FIGURE 4.15.: Approximate relative basin size of the Bistable Climate Toy Model when changing the solar constant S estimated with MCBB. The model exhibits a cold and a warm state. Trajectories from the shaded area are used later as training data for predictions of the model in Sec. 5.6.5

Discussion

With MCBB we correctly identified the two competing attractors of the BCTM, their basins and how their volumes change when the solar constant is varied. We were thus able to show the typical hysteresis of energy balance climate models.

Interestingly, even though MCBB is tailored towards identifying the largest basins of attractions, we were also able to identify some of the saddle-like Melancholia states of the system that are rarely occurring. As the Melancholia states have a finite lifetime, they are unstable states, it is no surprise that we did not find a basin of attraction with MCBB, but when the clustering parameter is set sufficiently low, these were classified as outliers and a closer inspection releaved their saddle-like trajectory. When the clustering parameter is larger they are classified as part of the cold or warm state depending on where their trajectory ends.

We also experimented with further modifying the BCTM. One can add stochastic noise to the EBM or L96, or introduce more stable states by modifying the EBM. MCBB was also able to identify and track those additional states.

Understanding what the attractors of a system are is also essential when it comes to predictions of such systems. In the following chapter we will introduce a method that is able to do so and then we will also come back to the Bistable Climate Toy Model and use the knowledge that we gathered here for predictions of future states of the system. In this regard MCBB can also be seen as the first part of a two-part approach to analyse and predict high-dimensional chaotic systems.

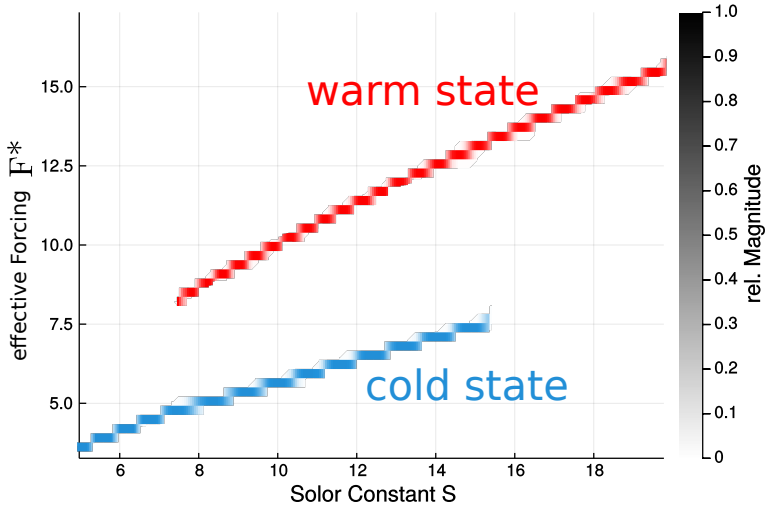

FIGURE 4.16.: Sliding histogram plot of the mean of the EBM dimension of the Bistable Climate Toy Model computed with MCBB. The two histogram plots of each of the identified states are joined together to better illustrate the two stable branches of the EBM and their hysteresis behaviour. On the y-axis the value of complete effective forcing term of the L96, so $F* = F\left(1 + \beta\frac{T-\tilde{T}}{\Delta_T}\right)$, is shown. The relative magnitude of each of these values appearing in the individual sliding histograms is shown in shades of blue and red, however in this case are mostly all zero or one.

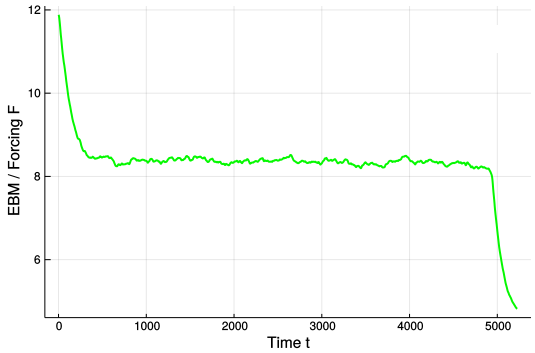

FIGURE 4.17.: Example of the trajectory of the energy balance model for one of the Melancholia states found by MCBB as an outlier. Visible is a trajectory typical for a saddle. The trajectory remains close to the Melancholia state for some finite time until it collapses into the snowball/cold state.

4.3. Discussion

While the work with MCBB so far focused on introducing the method and testing it with paradigmatic models and conceptual climate models, we believe that this opens the door for studying a wide variety of systems in novel ways. We expect that the method will be fruitful in diverse contexts where a mix of multistability and high dimensional behaviour are important. Most notable among those would be biological networks and climate systems. Already the first three examples that we presented in Sec. 4.1, showcase the broad possibilities of MCBB for many interdisciplinary fields, be it disease and opinion spreading (Dodds-Watts model), power grid dynamics (Kuramoto network) or chemical and biological systems (Stuart-Landau network). The application to the conceptual tipping cascades model and the climate toy model also showcase MCBB's potential for further applications in climate dynamics.

MCBB provides an excellent way to visualize the complex behaviour of systems where a traditional bifurcation analysis is often not useful or difficult to implement. It resolves the most important classes of asymptotic states and enables the user to track the size of its basins along changing parameters.

One possible realm of applications that we haven't studied yet in more detail are partial differential equations (PDE). As they are usually discretized into high-dimensional ODEs, MCBB could be an ideal tool to analyse them. One example are ecology models studying the resilience of ecosystems through modelling the interplay of precipitation and vegetation [15]. These models exhibit a form of multistable spatial pattern formation that could be studied with MCBB. More realistic climate models, or more specifically atmosphere models, could also be investigated. While large general circulation models are computationally too complex, PDEs from atmospheric dynamics such as quasigeostrophic models could work [139], or in future research also Earth models of intermediate complexity (EMICs).

Summary

In this chapter we introduced Monte Carlo Basin Bifurcation Analysis (MCBB), a novel, numerical method for analysing dynamical systems that is situated between an analysis with macroscopic order parameters and a more thorough, detailed bifurcation analysis. MCBB identifies the largest basins of attraction of the system and tracks their relative volume for changing parameters. This is done by combining a random sampling approach with clustering techniques: suitable, easy to compute statistics of trajectories integrated from randomly generated initial conditions and parameters are clustered by density-based clustering algorithms such as DBSCAN. Typical applications are oscillator networks as we have demonstrated with the Kuramoto and Stuart-Landau models. Especially for the Kuramoto model MCBB was also able to give some new insights into the synchronization behaviour as it highlighted the growing frequency fluctuations of unsynchronized states with increased coupling strengths.

Subsequently we applied MCBB to a conceptual model for tipping cascades and a bistable climate toy model based on the Lorenz96 model.

In the next chapter, we will turn our attention to forecasts of complex, high-dimensional systems. Different attractors of a system generally exhibit different properties such as different Lyapunov exponent. For the forecast of physical systems knowledge of its attractors is often a requirement to make meaningful predictions. Training a numerical model with data from one attractor and then testing it on another, could potentially result in big errors. We can have this knowledge from prior research or find it ourselves with MCBB.

5. Hybrid Modelling Approaches

Traditionally predictions of complex systems were mostly done by composing models in the form of e.g. differential equations. Over the recent decades models such as the numerical weather prediction models made large progress. Nowadays a 5-day forecast is as precise as a 3-day forecast was 20 years ago [16]. But, as Edward Lorenz already recognized in the 1960s there is a predictability limit due to the chaotic nature of the partial differential equations and involved processes that they model [122]. For the scales that we refer to as *weather* the limit is currently estimated to be about two weeks [252]. Whereas larger scale climate phenomena like the El Niño Southern Oscillation can be predicted much farther in advance, typically by several months [47] and even larger trends like the anthropogenic climate change are predicted decades ahead with large-scale climate simulations, models and their comparisons like the Coupled Model Intercomparison Project Phase 6 (CMIP6) [66].

On the other side, there is the recent advance of purely data-driven machine learning methods such as artificial neural network models. From this standpoint, forecasting a time series is a supervised learning problem. We try to learn the evolution of a time series from examples. The simplest way to do this is to group the time series into input-output pairs $(\mathbf{x}_t; \mathbf{x}_{t+1})$ and learn the function $f(\mathbf{x}_t; t) = \mathbf{x}_{t+1}$ from these examples. Recently, weather and climate models also attracted the attention of leading machine learning researchers, as Google Research's MetNet shows [213]. It is able to outperform the 8-hour precipitation forecast of the National Oceanic and Atmospheric Administration of the USA (NOAA).

In the following, it is our aim to bring these two spheres of models, equation-based and data-driven, together. The resulting hybrid models hopefully profit from both approaches. In order to do so, we will introduce our approach of combining them with neural partial differential equations and test them on three paradigmatic and prototypical systems.

The results reported in this chapter closely follow the publication „Neural partial differential equations for chaotic systems“ [MG2] from Sec. 5.1 to 5.7, except for Sec. 5.6.5 which follows the second part of the publication „Analysis of a bistable climate toy model with physics-based machine learning methods“ [MG6].

5.1. Introduction to Hybrid Modelling Approaches

For centuries, differential equation models derived from physical principles have been the preferred tool to forecast the behavior of complex natural systems and only more recently the advance of data-driven methods, like the ANNs, that we introduced in Sec. 2.4 enabled many promising approaches for forecasting spatiotemporal system,

e.g. with feed-forward neural networks [159], convolutional neural networks [87] or reservoir computing [160]. When we already have some degree of knowledge of a system it seems natural that we want to use this knowledge even when we work with data-driven methods. However, it is not always straightforward how prior knowledge can be integrated into data-driven methods. This combination of physical models and data-driven models is often referred to as hybrid modelling or hybrid models [171]. Reichstein et al. [171] identified five potential areas where these hybrid approaches can excel: 1) improving parameterizations of existing physical models, 2) replacing a physical sub-model with a data-driven model, 3) analysis of model-observation mismatch, 4) constraining sub-models and 5) emulating physical models with data-driven models to increase computational efficiency. As 1) and 2) are advancing the models itself, possibly increasing their accuracy, we see these as the most important areas and will present one approach able to do both at the same time.

The complex systems that we are interested in are chaotic. Systems exhibiting chaos are inherently difficult to forecast, as already the smallest deviations will lead to large errors later. Key challenges remain in predicting complex systems that are high dimensional and chaotic, when only short time series and spatially incomplete data are available. We tackle these challenges by combining knowledge that we have about the governing equations of these systems with a universal function approximator such as an artificial neural networks (ANNs). The aim is predicting complex, chaotic systems of which we only have incomplete and sparse knowledge. Every process-based model of a natural system is incomplete in some sense, for example due to unknown parts of the dynamics, or due to deliberately omitting higher-order effects. Hybrid models can fill these deficiencies by combining process-based knowledge with data-driven approximations for a closed description of the system. In contrast to purely data-driven models, the dynamics of hybrid models is often easier to analyse and to interpret and, as we will show, hybrid methods potentially need much less data to train than purely data-driven approaches.

There are different approaches to combine differential equations, specifically partial differential equations (PDEs), with ANNs. First of all, there is the possibility to directly integrate an ANN in the equation itself. In this case one cannot use the standard backpropagation algorithm (see Sec. 2.4) that is usually used to train the ANN anymore. Chen et al. [45] showed an efficient algorithm to train through an ODE solver based on the adjoint sensitivity method. Rackauckas et al. [165] expanded on this idea and developed the universal differential equations framework that allows to freely augment most types of differential equations with universal approximators such as ANNs. They also showed that by using methods such as SINDy [38] on these hybrid models, it is possible to recover and identify missing parts of the governing equation analytically.

Another approach to combining system knowledge with data-driven models are Physics-informed Neural Networks, which can approximate solutions of PDEs with ANNs and also set up ANNs whose outputs are solutions of a specific PDE. This is particularly useful in fluid dynamics where every output should adhere to the Navier-Stokes equation [166].

A different kind of hybrid method combining a knowledge-based differential-equation model with a reservoir computer has recently shown great promise for predicting chaotic systems [161]. This setup was able to make accurate predictions of chaotic systems like the Lorenz63 and the Kuramoto-Sivashinksy model. Wikner et al. [244] proposed a parallel implementation of the hybrid reservoir approach that is also able to predict higher dimensional systems, but only with local short-time causal interactions.

We focus on a particular challenging situation: We want to predict the dynamics of high-dimensional chaotic systems by combining discretized partial differential equations with ANNs, under the condition of very short training datasets and with parts of the spatial data missing. The universal differential equations framework [165] provides the basis for the introduction of the Neural Partial Differential Equations (NPDE) that we will use.

5.2. Neural Partial Differential Equations

In Sec. 2.4 we introduced the fundamentals of artificial neural networks (ANNs), powerful data-driven function approximators. ANNs with skip connections, ResNets (see Sec. 2.4), and differential equations are more similar than immediately visible as Weinan [241] and Haber et al. [82] pointed out. ResNet blocks (RNB) whose output $\mathbf{h}_{n+1}$ given an input $\mathbf{h}_n$ is defined by

$$\mathbf{h}_{n+1} = \mathrm{RNB}(\mathbf{h}_n; \Theta) + \mathbf{h}_n \tag{5.1}$$

bare strong similarities to the forward Euler step that can be used to iteratively solve ODEs $\dot{\mathbf{y}} = f(\mathbf{y}; t)$ with

$$\mathbf{y}_{t+1} = \Delta t \cdot f(\mathbf{y}_t, t; \Theta) + \mathbf{y}_t. \tag{5.2}$$

An ODE can thus be seen as the continuous limit of deep ResNets [82]. Initially, this was used to study purely data-driven ANNs [82, 186, 241], but the potential for setting up hybrid models was soon realised by Rackauckas et al. [165]. The framework of universal differential equations [165] enables us to use universal approximators such as ANNs within partial differential equations (PDEs). The resulting NPDEs are hybrid models that are able to compensate missing parts of the PDE by learning them from data, thereby attenuating structural model errors. NPDEs are thus discretized PDEs with an ANN $\mathcal{N}$ as part of the equation, e.g. in the form

$$\partial_t u = f(u) + \mathcal{N}(u; \boldsymbol{\Theta}). \tag{5.3}$$

5.2.1. Training NPDEs

When training a NPDE, the standard backpropagation rule (see Sec. 2.4) cannot be utilized anymore, since we need to be able to compute gradients of the solution of a differential equation with respect to its parameters. Algorithms that accomplish this were previously used e.g. in meteorology to study the sensitivity of weather

and climate models [64]. Most of these algorithms rely on appending the differential equations with adjoint functions, an idea originally conceived by Pontryagin et al. [164] in the context of optimal control theory. Chen et al. [45] were the first to propose a suitably adapted algorithm, reverse-mode automatic differentiation of ODE solutions, which can be used to train neural ODEs. We outline this algorithm briefly in the following. Aside from this algorithm there are several other variants, for these we refer to Rackauckas et al. [165, e.g.].

Given is an ODE $\dot{\mathbf{x}} = f(\mathbf{x}, t; \theta)$ that is integrated from t_0 to t_1 with parameters θ and a scalar loss function $\mathcal{L}(\mathbf{x}(t_1))$ of the ODE solution that is supposed to be minimized by the training procedure. The parameters θ can include those of data-driven models like ANNs. To compute the gradient $\frac{\partial \mathcal{L}}{\partial \theta}$, the ODE is appended with the adjoint

$$\mathbf{a}(t) = \frac{\partial \mathcal{L}}{\partial \mathbf{x}(t)}. \tag{5.4}$$

The adjoint follows the dynamics

$$\frac{d\mathbf{a}}{dt} = -\mathbf{a}^T(t)\frac{\partial f(\mathbf{x}(t), t, \theta)}{\partial \mathbf{x}(t)} \tag{5.5}$$

and tracks how the gradient of the loss depends on the trajectory. This is needed to compute the desired $\frac{\partial \mathcal{L}}{\partial \theta}$ with another adjoint

$$\mathbf{a}_\theta = \frac{\partial \mathcal{L}}{\partial \theta(t)} \tag{5.6}$$

$$\frac{d\mathbf{a}_\theta}{dt} = -\mathbf{a}^T(t)\frac{\partial f(\mathbf{x}(t), t, \theta)}{\partial \theta} \tag{5.7}$$

The proof of these dynamics following Chen et al. [45] can be seen as a continuous backpropagation. Similar to the traditional, discrete backprogation the chain rule is applied with

$$\frac{\partial \mathcal{L}}{\partial \mathbf{x}(t)} = \frac{\partial \mathcal{L}}{\partial \mathbf{x}(t+\epsilon)}\frac{\partial \mathbf{x}(t+\epsilon)}{\partial \mathbf{x}(t)} \tag{5.8}$$

by inserting a state of the trajectory evolved by an incremental time step ϵ. Evolving the trajectory can be approximated with

$$\mathbf{x}(t+\epsilon) = \int_t^{t+\epsilon} f(\mathbf{x}(t), t; \theta)dt + \mathbf{x}(t) = T_\epsilon(\mathbf{x}(t), t; \theta) \overset{\epsilon \to 0}{\approx} \epsilon f(\mathbf{x}(t), t; \theta) + \mathbf{x}(t) \tag{5.9}$$

to rewrite Eq. 5.8 as

$$\mathbf{a}(t) = \mathbf{a}(t+\epsilon)\frac{\partial T_\epsilon(\mathbf{x}(t), t)}{\partial \mathbf{x}(t)}. \tag{5.10}$$

These results can be used to get the dynamics of $\mathbf{a}(t)$ by inserting them into the definition of its derivative

$$\frac{d\mathbf{a}(t)}{dt} = \lim_{\epsilon \to 0} \frac{1}{\epsilon}(\mathbf{a}(t+\epsilon) - \mathbf{a}(t)) \tag{5.11}$$

$$= \lim_{\epsilon \to 0} \frac{1}{\epsilon}(\mathbf{a}(t+\epsilon) - \mathbf{a}(t+\epsilon)\frac{\partial}{\partial \mathbf{x}(t)}(\mathbf{x}(t) + \epsilon f(\mathbf{x}(t), t; \theta)) \tag{5.12}$$

$$= \lim_{\epsilon \to 0} -\mathbf{a}(t+\epsilon)\frac{\partial f(\mathbf{x}(t), t; \theta)}{\partial \mathbf{x}(t)} = -\mathbf{a}(t)\frac{\partial f(\mathbf{x}(t), t, \theta)}{\partial \mathbf{x}(t)}. \tag{5.13}$$

The dynamics of $\mathbf{a}_\theta$ can be derived analogously. Similar to how a traditional backpropagation traverses the chain of the ANN from the output back to the input, the appended ODE with the adjoints needs to be solved backwards in time as the initial values of the augmented dynamics are only known at the end point of the integration t_1. To compute $\frac{\partial \mathcal{L}}{\partial \theta}$, we thus need to solve the appended ODE

$$\begin{pmatrix} \frac{d\mathbf{x}}{dt} \\ \frac{d\mathbf{a}}{dt} \\ \frac{d\mathbf{a}_\theta}{dt} \end{pmatrix} = \begin{pmatrix} f(\mathbf{x}, t, \theta) \\ -\mathbf{a}^T(t)\frac{\partial f(\mathbf{x}(t), t, \theta)}{\partial \mathbf{x}(t)} \\ -\mathbf{a}^T(t)\frac{\partial f(\mathbf{x}(t), t, \theta)}{\partial \theta} \end{pmatrix} \tag{5.14}$$

backwards in time from t_1 to t_0 with initial conditions $[\mathbf{x}(t_1); \frac{\partial \mathcal{L}}{\partial \mathbf{x}(t_1)}; \mathbf{0}]$ to eventually get $\frac{\partial \mathcal{L}}{\partial \theta} = \mathbf{a}_\theta(t_0)$. The partial derivatives in Eq. 5.14 are computed using automatic differentiation (AD).

However, Chen et al. [45] primary application of this algorithm was training regular ANNs, more specifically ResNets [84], with ODE solvers. Rackauckas et al. [165] expanded the Neural ODE approach into the universal differential equations framework. A universal ordinary equation is any equation of the form

$$u' = f(u, t, U_\theta(u, t)) \tag{5.15}$$

where $U_\theta(u, t)$ is a universal function approximator such as an ANN. As we know how to compute the gradients through a differential equation solver, virtually every combination of analytical terms and universal approximators such as ANNs is thinkable. Due to the powerful underlying differential equation solver library DifferentialEquations.jl [40], this approach works with stochastic and delay differential equations as well. This includes PDEs, as they are usually numerically solved by discritizing them into ordinary differential equations (see Sec. 2.2.2).

5.3. NPDEs for Chaotic Systems

We aim to apply universal differential equations to chaotic systems and train the resulting NPDEs. Similar to the purely data-driven ANN approach introduced in Sec. 2.4, the NPDE is trained by minimizing a loss function that is comprised of the

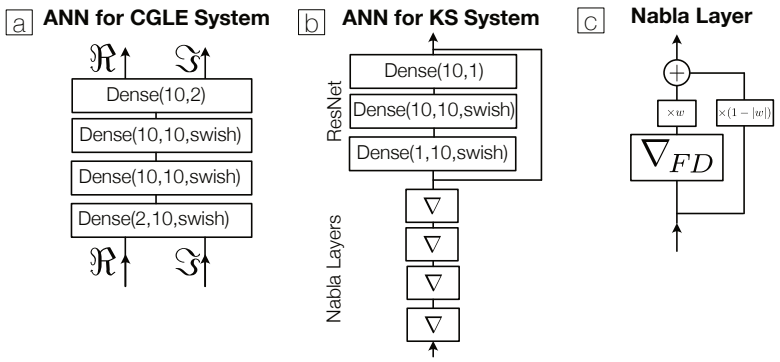

FIGURE 5.1.: Overview of the ANNs used for the NPDEs. **a)** ANN setup for the CGLE system. $\Re$ is the real part of the value of $u(\mathbf{x}, t)$ and $\Im$ is the real part of $u(\mathbf{x}, t)$. **b)** The ANN setup for the KS system consists of four Nabla layers and a ResNet, with three dense layers. **c)** Nabla layers used in b), the parameter w is trainable and subject to an additional penalty to approximately constrain it to $[-1, 1]$. $\nabla_{\mathbf{FD}}$ is the finite difference derivative matrix.

sum of the least square errors of the predictions made by the NPDE $\hat{u}(\mathbf{x}, t; \Theta)$ and an additional L1 parameter regularization of the ANN:

$$\mathcal{L}(\Theta) = \sum_{i_t, \mathbf{x}} (u(\mathbf{x}, i_t) - \hat{u}(\mathbf{x}, i_t; \Theta))^2 + \gamma \sum_{i}^{N_\Theta} ||\theta_i||. \tag{5.16}$$

The sum is taken over all discretized spatial coordinates $\mathbf{x}$ and time steps i_t of the predicted trajectory, $||.||$ the L1 norm and $\gamma = 10^{-5}$. $\mathcal{L}$ is minimized using an AdamW optimizer (see Sec. 2.4) [123].

In Rackauckas et al. [165] many non-chaotic applications of universal differential equations are discussed. These are usually trained by minimizing the mean square error of a relatively long trajectory predicted by the universal or neural differential equations. This approach is not suitable to train models for chaotic systems as inherently small deviations at the start of the trajectory can lead to massive deviations later. We thus integrate the NPDE only from t_0 to $t_0 + N_f \Delta t$ for a small N_f and repeat this from every initial condition in the training dataset. For chaotic systems, Δt needs to be typically very small to ensure stable training as we will see later. For $N_f = 1$ we therefore train on the one-step-ahead forecast error. Increasing the integration time also increases the computational complexity massively. We thus first integrate with $N_f = 1$ until the forecast error on a validation set does not decrease anymore. Then, we slowly increase N_f to its final value τ. When integrating the NPDE the solvers will typically use an adaptive step size, however we are saving the trajectories at constant intervals Δt for better comparability. As the datasets that we use are very short,

training is repeated over many epochs.

5.4. Nabla Layer

The unknown or missing part of the dynamics that we aim to model with the ANN in the NPDE can of course also include a derivative. One possibility is to model derivatives with convolutional layers as e.g. a convolution with the filter $[1, -2, 1]$ is identical to applying a first-order second derivative finite difference matrix [165]. However, we don't have to fit the kernel parameters during a lengthy training procedure to be close to a derivative when we already know what the parameters of derivatives look like. We just have to recognize if we need to model a derivative or not. In order to do so we introduce a novel trainable layer, the Nabla layer ∇. As illustrated in Fig. 5.1 it is defined by

$$\nabla(\mathbf{x}; \Theta = \{w\}) = (1 - |w|)\mathbf{x} + w\nabla_{\mathbf{FD}}\mathbf{x} \tag{5.17}$$

where $\nabla_{\mathbf{FD}}$ is the finite difference derivative matrix and w is a trainable parameter. The parameter w is approximately bound to the interval $[-1; 1]$ by an additional penalty in the overall loss function. For this function we chose $p(w) = \max(x^6 - 1, -x^4 + x^2)$ as it has large values outside of $[-1; 1]$ and local minima at 0 and ± 1. When stacking k of these layers and a MLP together, we are able to model functions of derivatives up to order k. It seems reasonable to use four Nabla layers if no prior knowledge of the system indicates otherwise, as rarely higher order derivatives are found in governing equations of natural systems. To increase the numerical precision of the layer, we use alternating forward and backward finite difference schemes when stacking Nabla layers as we noticed an impact of the accuracy of the finite difference schemes on the results, especially when higher order derivatives are modelled. Additional skip connections can help training these models if they are comprised of many layers, resulting in a ResNet (see Sec. 2.4).

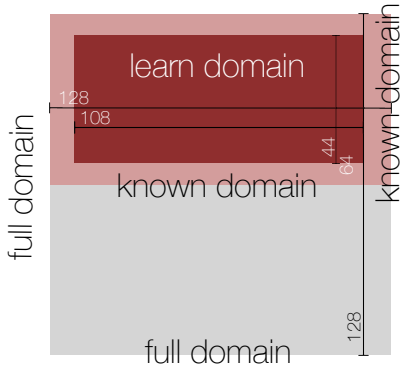

FIGURE 5.2.: Sketch outlining the setup to learn the NPDE from incomplete data. In this example only the upper half of the spatial data is known. The learn domain is then defined to be well within this known domain.

5.5. Training with Incomplete Data

Since we directly augment the differential equation, the NPDE approach is very flexible. It does not have a fixed input or output dimension. This leads to several possibilities. First of all, we can train the NPDE with data in a lower spatial resolution and then use it to predict in a higher resolution or the other way around. This could for example be useful as it eliminates the need for data pre-processing when training a NPDE with data from different sources on different spatial grids.

The NPDE approach enables us to deal with spatially incomplete data as well. We can learn the missing part of the equations from the incomplete data and predict the complete systems by defining a 'learn domain' ξ that is situated well within the known data ζ (see Fig. 5.2). This approach is limited to systems where local interactions are dominant as we of course cannot learn long-range interactions to points that are outside of the learn domain like this. The loss function is computed only from points within ξ with

$$\mathcal{L}(\Theta) = \sum_{\mathbf{x}_\xi \in \xi, i_t} (u(\mathbf{x}_\xi, i_t) - \hat{u}(\mathbf{x}^*, i_t; \Theta))^2 + \gamma \sum_{i}^{N_\Theta} ||\theta_i||, \tag{5.18}$$

but the input of the NPDE $\mathbf{x}^*$ is the complete known data $\mathbf{x}_\zeta$ appended with zeros where the data is missing. Appending the zeros is necessary when the PDE has a defined boundary with boundary conditions.

5.6. Results

In the following we will apply NPDEs to three prototypical systems. We will assume that we know only a part of the equation we are investigating and "forget" about another part of the equation, which is instead modelled by an ANN $\mathcal{N}$. The ANN will be trained with data. For this theoretical setup, we generate data from the true, known system and then compare the prediction of the trained NPDE to the simulations of the true system and train it with the algorithm presented in Sec. 5.2.1.

We asses how well the NPDEs perform by first integrating them from initial conditions that were not part of the training part for a suitably long time. Importantly, when integrating we save the trajectory at the same regular intervals Δt as when generating the initial true data. We then define the following measures of forecast accuracy: the non-normalized error

$$E(\mathbf{x}, t) = u(\mathbf{x}, t) - \hat{u}(\mathbf{x}, t) \tag{5.19}$$

and the normalized error [161]

$$e(t) = \frac{||u(\mathbf{x}, t) - \hat{u}(\mathbf{x}, t)||}{< ||u(\mathbf{x}, t)||^2 >^{1/2}}. \tag{5.20}$$

As defined in Pathak et al. [161], we also compute a valid time t_v as the first time when $e(t_v) > 0.4$.

The results of our NPDE approach will be compared to other methods. The first benchmark is a convolutional neural network (CNN) with a bottleneck, that is set up in a recursive loop so that the output of the CNN is fed back into it to forecast the next step. This is an architecture that could successfully approximate simple general circulation models [195]. Another comparison is a hybrid reservoir computer [161] that also combines a knowledge-based model with a data-driven model, i.e., the incomplete PDE with a reservoir computer. Reservoir computers, which are also referred to as Echo State Networks, are recursive neural networks which rely on a large random network and a trainable output layer. For high-dimensional systems, the size of the reservoir network needs to be increased accordingly. For the systems investigated here, the necessary reservoir size potentially becomes prohibitory large. For our comparative purposes, we thus compute the hybrid reservoir with a lower-dimensional system with the same inter-grid spacing. Additionally, we also show how the incomplete model on its own performs as a predictor. Further details on these comparisons can be found in the Appendix (see Sec. C.2.1 and C.2.2).

5.6.1. Complex Ginsburg-Landau Equation

The Complex Ginsburg-Landau equation (CGLE) [76, 147], a reaction-diffusion type equation, is defined by

$$\partial_t u = (1 + i\alpha)\Delta u - (1 + i\beta)|u|^2 u \tag{5.21}$$

where $u(\mathbf{x}, t)$ is a complex valued field on two spatial dimensions. The CGLE is a prototypical equation that models every reaction-diffusion system close to the onset of oscillation [76]. We discretize the equation with a finite difference scheme to a 128×128 grid with size 192×192 and apply periodic boundary conditions. For various parameter configuration, like $\alpha = 2$, $\beta = -1$ as chosen here, this system exhibits chaotic behaviour as indicated by a maximum Lyapunov exponent[1] of $\lambda_{max} = 0.17$. Here, we focus on modelling the reaction term, so $(1 + i\beta)|u|^2 u$, with an ANN. Note, however, that for the NPDE approach it would also be possible to make the parameter α trainable or to 'forget' the diffusion part of the equation. The NPDE we investigate here is given by

$$\partial_t u = (1 + i\alpha)\Delta u + \mathcal{N}_{CGLE}(u; \boldsymbol{\Theta}). \tag{5.22}$$

As part of the NPDE $\mathcal{N}_{CGLE}$ is defined in a way that it only has as a single input: the value of the spatiotemporal field u at one specific position. Since u is complex valued, the real and imaginary part are split as separate inputs. $\mathcal{N}_{CGLE}$ is a multilayer perceptron with two hidden layers, each with 10 densely connected nodes (see Fig. 5.1).

[1] Computed with the algorithm of Benettin et al. [18], implemented in DynamicalSystems.jl [53]

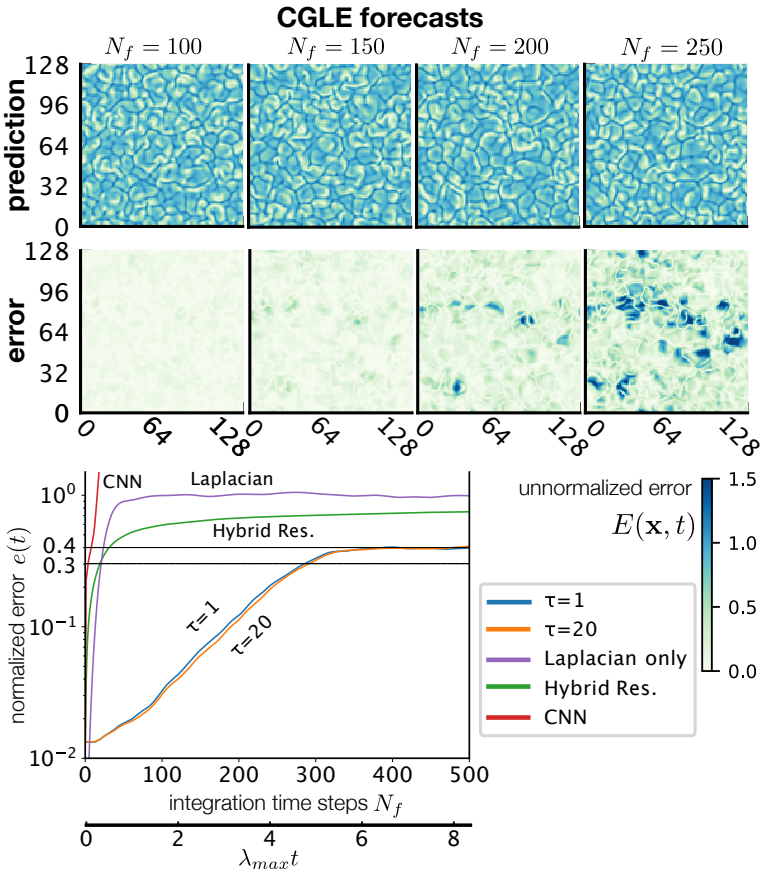

FIGURE 5.3.: NPDE forecast for the CLGE. The upper row shows the prediction made by the NPDE for two different time steps N_f and the lower row the difference of this prediction to the true value. As the CGLE is complex valued, we show the absolute value of these fields here. Also shown is the evolution of the normalized error $e(t)$ for two different integration length and compared to a hybrid reservoir, a CNN and the forecast made by integrating the Laplacian only. The upper x axis is given in units of integration time steps with $\Delta t = 0.1$ and the lower axis is in units of the Lyapunov time.

A single long trajectory of the CGLE is integrated with a Tsitouras solver [222]. The initial conditions are uniformly random within the interval $[-0.005; 0.005]$ for both the real and imaginary part. Although the solver has an adaptive step size, the trajectory is saved every $\Delta t = 0.1$. The first 2000 steps are not saved to avoid any transient dynamics. Only the next 25 steps after the transient are the training set and the remainder of the trajectory is saved for the validation and test set. The NPDE is trained minimizing the loss function Eq. 5.16 using an AdamW optimizer [123].

Fig. 5.3 shows the prediction of the trained NPDE for different time steps N_f and how the normalized error (Eq. 5.20) evolves. We found that the NPDE makes accurate predictions that exceed the length of the training set by far. The normalized error increases exponentially with increasing t until it levels off at around 0.4, which coincides with the threshold of the valid time t_v for the CGLE NPDE. Therefore, we additionally measure when $e(t) = 0.3$ is reached for the first time.

The valid time increases slightly when the integration length τ is increased (see Fig. 5.3), however increasing τ needs considerably more computation time. Ultimately, this increase is so small that it does not seem to justify the much higher computation time in the case of the CGLE. The valid time is $N_f = 388$ integration time steps, for $\tau = 1$ and $N_f = 479$ for $\tau = 20$, whereas $e(t) = 0.3$ is reached for $N_f = 286$ for $\tau = 1$ and $N_f = 292$ for $\tau = 20$. Given a maximum Lyapunov exponent of $\lambda_{max} = 0.16724655$ and $\Delta t = 0.1$, this is equivalent to $4.88\lambda_{max}t$ to reach $e(t) = 0.3$ and a valid time of $8.01\lambda_{max}t$ for $\tau = 20$. In comparison, the valid time of the hybrid reservoir is $N_f = 25$ or $0.44\lambda_{max}t$. Its error levels off at a larger value ($e(t) \approx 0.7$) as well. For the CNN, the valid time is $N_f = 8$ integration steps or $0.13\lambda_{max}t$. Its error quickly grows and does not level off at all.

5.6.2. Influence of Observational Noise

Additionally, we can test the performance of the forecast when the training data is subject to noise. For this purpose one iteration of Gaussian noise with standard deviation σ is added to the training data to simulate observational noise with

$$\mathbf{x}_\eta(t) = \mathbf{x}(t) + \eta(t) \tag{5.23}$$

where each element of $\eta(t)$ is independently drawn from a normal distribution $\mathcal{N}(0, \sigma)$. For a given σ, the model is trained in the same manner as before with 25 time steps of training data $\mathbf{x}_\eta$. The forecast error $e(t)$ can be evaluated by comparing the NPDE forecast against the original time series $\mathbf{x}$ or the series with noise $\mathbf{x}_\eta$. In our trials the forecast length did not differ significant in either case. In Fig. 5.4 and Tab. 5.1 the results for noise with a standard deviation between 0.01 and 0.2 are reported. There is a relatively smooth response to the increased observational noise. The forecast length decreases but even at $\sigma = 0.2$ reliable forecasts can still be made as an error of $e(t) = 0.3$ was reached after $N_f = 97$ or $1.62\lambda_{max}t$. Compared to the mean standard deviation of the CGLE data of $\sigma \approx 1.3$, this is about 15% of the system's variability.

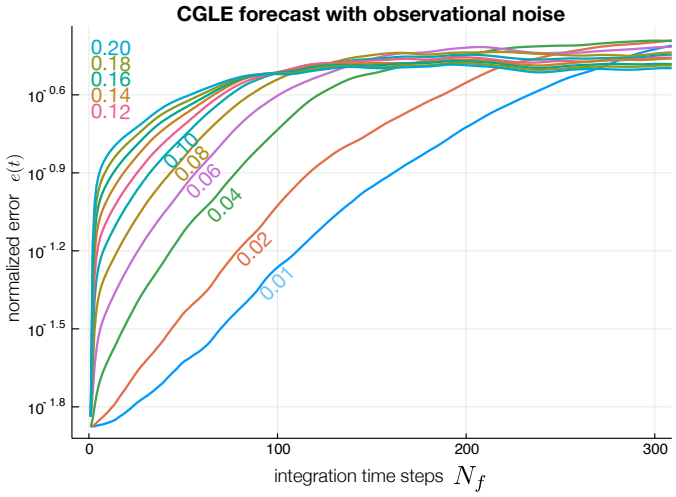

FIGURE 5.4.: Normalized forecast error according to Eq. 5.23. The colored numbers indicate the standard deviation of the noise used for the trial with the normalized error in the same color. The CGLE has a mean standard deviation (in time) of $\sigma \approx 1.3$.

TABLE 5.1.: Integration time step at which the normalized error $e(t)$ first passes 0.3 and 0.2 for various values of observational noise σ.

σ	0.01	0.02	0.04	0.06	0.08	0.1	0.12	0.14	0.16	0.18	0.2
$t_{0.3}$	259	209	147	125	106	97	95	92	90	88	89
$t_{0.2}$	207	161	106	83	69	59	54	46	40	35	30

5.6.3. CGLE with Incomplete Data

With the approach introduced in Sec. 5.5 accurate forecasts can even be made with incomplete data. For this purpose, we only trained the NPDE with data from the (64×128)-sized upper half of the spatial field (see Fig. 5.2). The learn domain ξ was set to be 20 grid points away from the boundary of the known domain ζ and is thus (44×108)-sized. The results are presented in Fig. 5.5. The valid time is $N_f = 333$ integration time steps or $5.57\lambda_{max}t$. The slightly lower threshold $e(t) = 0.3$ is reached at $N_f = 254$ integration time steps or $4.24\lambda_{max}t$. There is no significant difference between the accuracy inside and outside of the known domain as the almost identical evolution of the normalized error shows (Fig. 5.5).

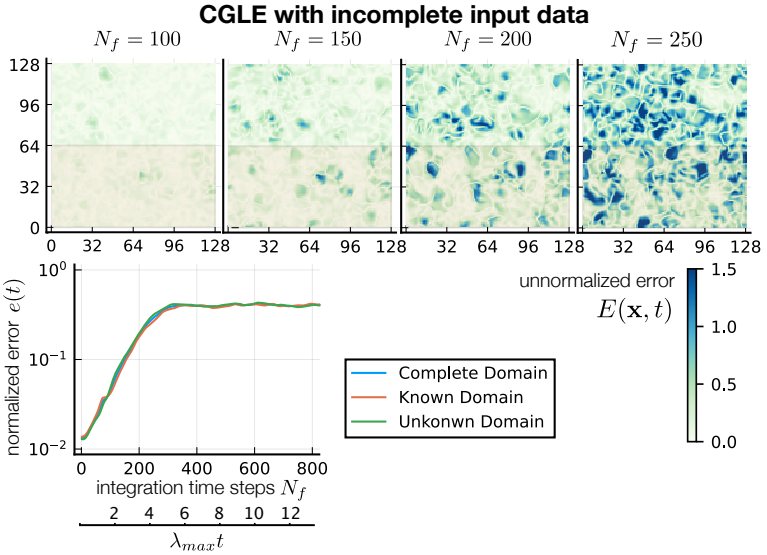

FIGURE 5.5.: CGLE forecast with incomplete input data from only the shaded area at the bottom of the spatial field. Also shown is the evolution of the normalized error $e(t)$ of the complete spatiotemporal field, only inside the known domain and outside the known domain.

TABLE 5.2.: Parameters used for the CGLE and KS NPDEs

	CGLE	KS
n	128×128	4096
L	192×192	1160
Δt time step	0.1	0.02
N_t length of training set	25	25
γ L1-regularization (loss function)	10^{-5}	10^{-5}
system parameters	$\alpha = 2$	
	$\beta = -1$	

5.6.4. Kuramoto-Sivashinsky Equation

The Kuramoto-Sivashinsky (KS) equation

$$\partial_t u = -\partial_{xxxx} u - \partial_{xx} u - u\partial_x u. \tag{5.24}$$

is another example of a spatiotemporally chaotic partial differential equation. The equation was derived independently by Kuramoto [106] when investigating chaotic reaction-diffusion equations and by Sivashinsky [211] to describe instabilities in laminar flame fronts. Several further applications have been found (e.g. trapped ion modes in plasma [49]) demonstrating the prototypical natural of the KS equation. Again, we solve the PDE with periodic boundary conditions and a finite difference scheme. The investigated system domain has a length of $L = 1,160$ and is discritized to 4,096 grid points, resulting in an intergrid spacing of $\Delta x \approx 0.28$ (see Tab. 5.2 for a full overview of all parameters). The initial conditions are drawn uniformly random from $[-0.005; 0.005]$. The system has a maximum Lyapunov exponent of $\lambda_{max} = 0.08$, clearly indicating its chaotic nature. After integrating the system for a sufficiently long time, the transient is discarded and the next 25 time steps at time intervals $\Delta t = 0.02$ are saved for the training. Further time steps are saved for validation and testing. For demonstrating the NPDE approach, we purposefully 'forget' the second derivative term of Eq. 5.24, which is chosen to ensure better comparability with the results reported by Pathak et al. [161] with the hybrid reservoir approach. The NPDE for the KS system reads

$$\partial_t u = -\partial_{xxxx} u - u\partial_x u - \mathcal{N}_{KS}(u). \tag{5.25}$$

The ANN $\mathcal{N}_{KS}$ comprises of four of the Nabla layers that we introduced in Sec. 5.4 and three dense layers with a skip connection (see Fig. 5.1). The four Nabla layers are chosen so that derivatives up to the fourth order could be modelled with the network and the skip connection is added to ensure better trainability of this deeper network. Including the additional penalties of the Nabla layers the loss function that is minimized during training becomes

$$\mathcal{L}(\Theta) = \sum_{i_t, \mathbf{x}} (u(\mathbf{x}, i_t) - \hat{u}(\mathbf{x}, i_t))^2 + \sum_{i=1}^{4} \max(\theta_i^6 - 1, -\theta_i^4 + \theta_i^2) + \gamma \sum_{i=5}^{N_\Theta} ||\theta_i||; \tag{5.26}$$

where the first four parameters $[\theta_1, ...\theta_4]$ are the parameters of the Nabla layers and the remaining elements of Θ are the parameters of the ResNet. During the training procedure two of the Nabla layers parameters quickly converge to 0 and two to 1, correctly identifying the second derivative of the missing term. The results of the NPDE are shown in Fig. 5.6 and 5.7. As visible in Fig. 5.7 the normalized error increases exponentially with increasing t. The valid time t_v is 2891 time steps which, given a maximum Lyapunov exponent $\lambda_{max} = 0.08$, is equivalent to $4.63\lambda_{max}t$. In comparison the hybrid reservoir can predict accurately up to a valid time of $N_f = 52$

/ $0.08\lambda_{max}t$, again failing to make any meaningful long-term prediction with the short training data. We found that especially for the KS system, the forecast profits from smaller time step Δt. This became most apparent when replacing the fourth derivative term as is shown in the Appendix Sec. C.1. In this case a larger time step Δt, e.g. $\Delta t = 0.1$ fails to result in meaningful forecasts which is due to the KS system being very sensitive to even the smallest changes to this term. However, using $\Delta t = 0.02$ leads to similar forecasts horizon as shown here for the second derivative term. This is due to how sensitive chaotic systems like the KS system can be to small deviations.

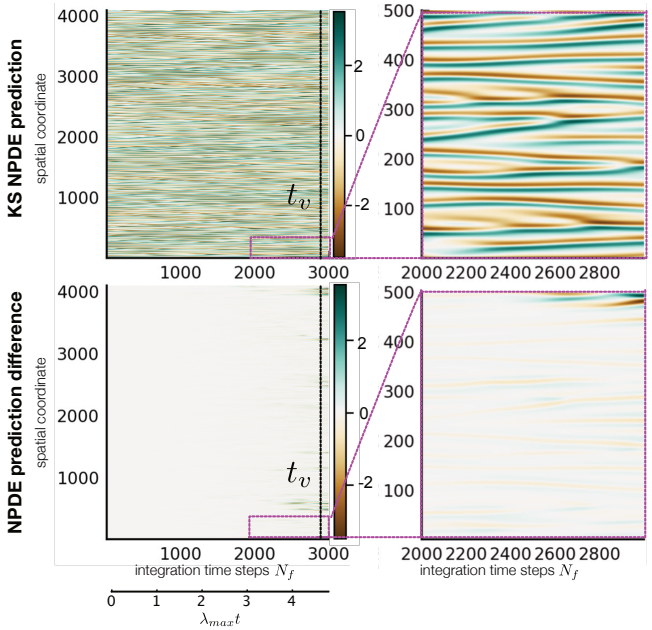

FIGURE 5.6.: NPDE forecasts for the Kuramoto-Sivashinsky equation. Predictions of the NPDE in the top row and difference to the true values in the bottom row. The right-hand-side panels show a detailed view of the area marked in pink in the large plots on the left. The valid time t_v is marked with the dashed line in the difference plots.

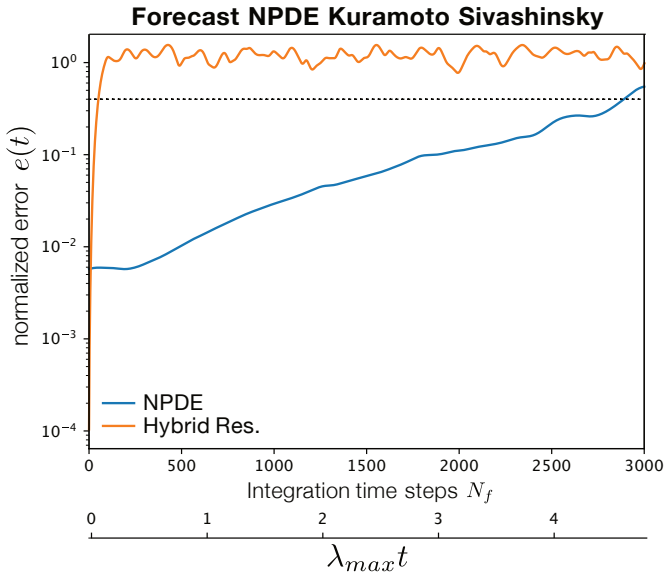

FIGURE 5.7.: Evolution of the normalized error $e(t)$ for the NPDE model for the KS equation. The upper x axis is given in units of integration time steps with $\Delta t = 0.02$ and the lower axis is in units of the Lyapunov time ($\lambda_{max} = 0.08$. The dashed line marks $e(t) = 0.4$.

5.6.5. Bistable Climate Toy Model

In Sec. 4.2.2 we introduced and analysed the Bistable Climate Toy Model (BCTM) with MCBB. The BCTM is constructed by coupling a zero dimensional energy balance model (EBM) to a Lorenz96 model (L96). With the help of MCBB we identified the two competing attractors of the models, one corresponding to a cold and one to a warm state of the energy balance model. These two attractors will, in general, exhibit different properties, e.g. different maximum Lyapunov exponents. The maximum Lyapunov exponents computed with the method of Benettin et al. [18] (implementation of DynamicalSystems.jl [53]) are $\lambda_{max}^{(\text{cold})} \approx 1.04$ for the cold and $\lambda_{max}^{(\text{warm})} \approx 2.60$ for the warm state. The larger Lyapunov exponent of the warm state shows that, as expected, the Lorenz96 sub-model is more chaotic for larger values of the forcing. When we want to predict the model's behavior, we have to be aware of that, and evaluate predictions on both attractors separately. MCBB also classifies all initial conditions used by the algorithms to either of the attractors. In this way, we have many possible initial conditions for predictions on these attractors. Technically the BCTM is an ODE and not a PDE, but the Lorenz96 model has strong similarities to a discritized PDE. Therefore, although we have an Neural Ordinary Differential Equation (NODE), all previously described techniques for NPDEs apply here as well. For demonstrating the approach on the BCTM we "forget" the equation of the EBM and replace it with an ANN. In this case this is an artificial example, but in many observational scenarios and models, one has incomplete models those deficiencies can be corrected with the NODE approach. In our case replacing the EBM with an ANN is supposed to mirror setups of more realistic models in which one probably has much better knowledge of the governing equations of the atmosphere than the energy balance.

The ANN $\mathcal{N}_{EBM}$ is set up to have the same input variables as the EBM in Eq. 4.18

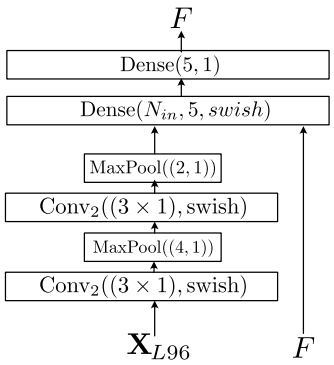

FIGURE 5.8.: ANN setup used to replace the EBM in the NODE. Convolutional layers with two filters, i.e. channels, a (3×1) kernel and a swish activation function are used on the L96 dimensions, the output of these layers and the old forcing value F are used as inputs of two densely connected layers. N_{in} is chosen to have the correct input dimension which depends on the dimension of the L96 model.

has arguments: all variables of the L96 sub-model and the EBM itself. Due to the spatial input, convolutional layers are best suited. Fig. 5.8 shows the ANN used. The convolutional layers have only the L96 dimensions as inputs, whereas the forcing F, the result of the EBM itself, skips these layers and inputs directly into the densely connected layers. The swish activation function [169] $\text{swish}(x) = x/(1 + \exp(-x))$ is used as an activation function and MaxPooling layers reduce the dimension. By replacing the EBM the full NODE reads

$$\begin{aligned} \dot{F} &= \mathcal{N}(\mathbf{X}, F; \Theta) \\ \dot{X}_n &= (X_{n+1} - X_{n-2})\, X_{n-1} - X_n + F; \end{aligned} \tag{5.27}$$

where Θ are the parameters of all ANN layers. The same loss function and optimization routines as for the CGLE are used. Similar to earlier results for the CGLE and KS, we found that integrating the NODE for long time spans does not significantly decrease the loss on neither the training nor the validation set, but increases the computational complexity massively. Therefore, the NODE is only integrated for $\Delta t = 0.05$ with only one time step saved. As training data two separated trajectories, each 100 time steps long (at $\Delta t = 0.05$), are used. These trajectories are integrated from initial conditions drawn randomly, one from each state within the basins identified by MCBB, i.e. the two shaded areas shown in Fig. 4.15. The initial 2000 time steps are discarded to avoid transient dynamics and the following 100 time steps of each of the two trajectories are used as the training set. Subsequent time steps of each of the trajectories are saved as validation set. Thus, the NODE is trained to model the full system with both attractors. The training data is generated with the same system parameters as in Sec. 4.2.2.

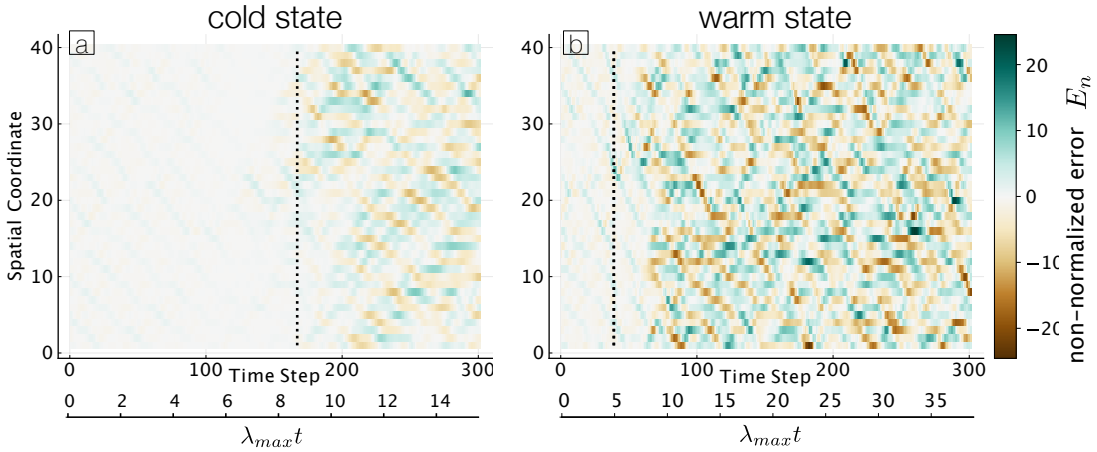

FIGURE 5.9.: NODE predictions of the Bistable Climate Toy Model, the non-normalized error $E_n(i_t)$ of the L96 dimensions is shown. (a) shows a prediction on the cold state, (b) the warm state. The valid time t_v is marked with the dashed line.

We evaluate the non-normalized error on the L96 dimensions

$$E_n(i_t) = X_n(i_t) - \hat{X}_n(i_t) \tag{5.28}$$

and the normalized error $e(t)$ (see Eq. 5.20) on the L96 dimensions as well. Similar to how the NODE was trained with data from both attractors, we also predict and evaluate trajectories from both attractors. Fig. 5.9 shows the trajectories of the NODE that were integrated from initial conditions of the first time step outside of the training dataset for both attractors. As expected the valid time is smaller for the more chaotic warm state than for the cold state. For the cold state the valid time 169 time steps or $8.52\lambda_{max}t$ and for the warm state it is 39 time steps or $5.02\lambda_{max}$.

5.7. Discussion

With the three prototypical applications, the CGLE, the KS and the BCTM we demonstrate that with Neural Partial Differential Equations one is able to forecasts partially known high-dimensional chaotic systems, even when datasets available for training are extremely short and spatially incomplete.

The NPDE approach excels in particular when the ANN is set up to model a function of a spatiotemporal field and/or its derivatives like in the CGLE and KS example. In this case, the NPDE approach makes use of the ergodicity of such systems and is thus able to train and make accurate forecast not despite but because these systems are high dimensional. The ANN is set up to model the function that is the same on the whole spatial domain. Despite the short time series, the large amount of spatial information give us thus enough data to train the ANN. The forecast horizon of the NPDE is much longer than the dataset used for training itself and as the

differential equation is modelled directly, one can also make predictions from arbitrary initial conditions. These are even possible when the training data is corrupted by observational noise. The CGLE system we investigated is 16,384-dimensional, whereas the KS system is 4,096-dimensional. The NPDEs are optimized on GPUs and thus the approach is scalable and increasing the dimension further is certainly possible. The key challenges that we identified: high-dimensionality, chaotic behaviour, short time series and incomplete data are all successfully tackled by using NPDEs.

As shown, NPDEs are also useful in cases where only incomplete data is available. With only half of the spatial information available for training the NPDE, the forecast length still exceeds the length of the training datasets by an order of magnitude. While this approach seems to be limited to systems without significant long-range interactions, it is still a powerful tool that enables predictions even when the spatial domain training data is incomplete.

In contrast to other hybrid modelling approaches like hybrid reservoir, the NPDEs can predict multiple steps at once without a recursive loop by increasing the integration length. For the systems that we investigated, increasing the integration length for the training made only a very small difference which makes sense as these systems do not have any form of memory. When investigating non-Markovian systems, the possibility to increase the integration length could be helpful though.

The application to the BCTM is different to those to the CGLE and KS. Here, we replaced one sub-model of the BCTM, the energy balance model with an ANN. With this setup we cannot profit in the same way from the ergodicity of the system as we do for the CGLE and KS. Therefore the forecast length gets smaller, but still remains of about the same order of magnitude as we have training data. While in terms of integration steps, the forecast lengths differs on both attractors, in terms of the Lyapunov time the forecast length is similar.

Given that the universal differential equations approach and the accompanying software [165] is extremely flexible, it also allows for a plenitude of other setups. For example, one could make the parameters of the known model trainable as well and extend it to chaotic, stochastic partial differential equations.

5.8. Outlook

So far, we only used theoretical setups with the NPDE approaches where we purposefully forgot a part of the equation and modelled it with an ANN. The goal of these tests is of course the apply them to observational data and models which describe them. For future research we identified two major possible areas of application. In these cases the NPDE approach has the potential to improve existing models.

Firstly, in nonlinear optics there are experiments which can be described very closely by the CGLE and the related Swift-Hohenberg equation [220]. One example are localized structures in liquid crystal light valves with optical feedback [48]. These experiments follow the modified CGLE or Swift-Hohenberg relatively closely and could be a good starting point for an NPDE investigation where the data-driven part of

the NPDE would model previously neglected higher order terms and other unknown influences.

However, more important for the research presented in this thesis are applications in climate science. Here, one possible approach would be to model atmospheric dynamics with the NPDEs, for example with the quasigeostrophic model in three layers (QG3) [139]. While being less complex than a typical general circulation model, it is much easier to implement and manipulate while still retaining a fairly realistic climatology for the northern hemisphere winter, especially its low-frequency variability. It has been used e.g. to study atmospheric blocking events [129]. We thus have a candidate model that we can turn into a NPDE and observational data available which the model resembles relatively closely.

Applying hybrid modelling approaches as described in this chapter to observational data has, as far as is known, not been done before, but seems certainly possible and it would be a substantial advancement of hybrid modelling as a whole. It is not completely clear if the NPDE approach that uses the ergodicity of the system like we demonstrated for the CGLE and KS would work. Potentially, for observational data one would need to use a combination of different neural networks architectures, one similar to those we used for the KS and CGLE and one which would work globally on the complete spatiotemporal field like for the BCTM. Pre-training the model on model data e.g. from CMIP5 also seems possible. If such a hybrid QG3 model is successful it could for example directly serve as a replacement for the atmospheric component of Earth Models of Intermediate Complexity (EMICs), but more importantly serve as a proof-of-concept so that even larger models could be converted to hybrid models.

Summary

When predicting complex systems one typically relies on differential equations which can often be incomplete, missing unknown influences or higher order effects. In this chapter we were integrating artificial neural networks directly into differential equations to fill deficiencies of high-dimensional models. The resulting Neural Partial Differential Equations (NPDEs) cannot be trained using the regular backpropagation algorithm but use algorithms such as adjoint-based sensitivity analysis. Training the NPDE is also possible for chaotic, high-dimensional systems when the integration time during training is very short. If this is the case, the NPDE can even make accurate forecasts when only short, incomplete and noisy training data is available as we demonstrated on three paradigmatic examples. For these examples we choose the Complex Ginsburg-Landau equation, a reaction-diffusion type PDE, the Kuramoto-Sivashinsky equation and the Bistable Climate Toy Model that we first introduced in the last chapter.

6. Discussion

The study of complex systems is interdisciplinary, not only in its applications, the fields where we find those systems in, but also in the methods that we can use to analyse them: elements of network and dynamical systems are most often the basis of investigations but they can be combined with machine learning methods to deal with the large amounts of data and the high-dimensionality that usually comes along with many complex systems. All of these aspects come hand in hand when dealing with complex systems. A network structure naturally arises as the constituents of the system are coupled to each other and we've seen one possible approach to recover a form of network from climate data. The couplings themselves and the individual dynamics are usually nonlinear and as shown phenomena such as phase coherence can be inferred from climate data as well. Additionally, complex system, especially in climate science, exhibit due to their nonlinearity multistable regimes and complex basin structure. The high-dimensionality also implies large amounts of data that can be efficiently analysed with machine learning methods. Within this thesis three different approaches were considered.

In the first part of the thesis, a complex network approach was taken to analyse the variability of the low-level circulation of the South American Monsoon System. The low-level circulation was encoded into a network structure to study the most important wind paths and their variability during active and break phases of the monsoon and due to the El Niño-Southern Oscillation especially highlighting the importance of the South American low-level jet and cross-equatorial flow. The network study also pointed us to the influence of the Rossby wave train on the low-level circulation and precipitation. We focused on this relationship by setting up a conceptual model that corroborates the hypothesis that the dominant precipitation variability is caused by a wave train and by proving phase coherence between the wave train and the precipitation in the regions most affected by the variability. This approach also showed how methods from network and dynamical systems theory can be used in conjunction to analyse climate systems. Networks identify spatiotemporal patterns and the most important regions for further investigations that can be performed by, among others, proving phase coherence.

Subsequently, we turned our attention to directly investigate the behaviour of high-dimensional dynamical systems, with the aim in mind to apply our methods to climate models. For this purpose, first Monte Carlo Basin Bifurcation analysis (MCBB) was introduced. By combining random sampling with clustering techniques, MCBB is able to discover the largest basins of attraction of a dynamical system and track their volume when control parameters of the system are changed. With the Neural Partial Differential Equations (NPDE), we then explored how artificial neural networks can be

integrated into differential equation to model only partially known dynamical systems. On synthetic examples the NPDE was able to forecast those systems for time spans that exceed the training dataset by more than an order of magnitude, thus promising great capability for future applications in more realistic settings. Bundling together Monte Carlo Basin Bifurcation Analysis and Neural Partial Differential Equations can be seen as a two-part approach to analyse and predict dynamical systems as a basic knowledge of the attractors of a system is often required to make meaningful numerical predictions of the system that respect its physical constraints. We demonstrated this two-part approach on the Bistable Climate Toy Model that we first introduced, then identified its attractors, the cold and warm state, with MCBB and consequently used that knowledge when using the NPDE approach to forecast the model. As already discussed separately in Sec. 4.1.10 and 5.8, for both approaches, MCBB and NPDE, we demonstrated them first on paradigmatic examples from various disciplines. By that we were showcasing the wide applications of these methods beyond just climate science before we turned our attention on models from climate science itself. Both the conceptual model for tipping cascades and the Bistable Climate Toy Model, are, as the names already suggest, conceptual models that do not try to accurately model an actual climate system. However, this will be just the first step towards more realistic models.

In conclusion, two approaches, combining physics with machine learning, were pursued in this thesis to investigate complex systems in climate dynamics and other disciplines: 1) complex networks and phase synchronization techniques to uncover and identify spatiotemporal variability patterns in climate data and investigate their cause, 2) MCBB and NPDEs to analyse and forecast dynamical systems.

These approaches are already in themselves an ideal starting point for further investigations. Aside from this, the first part of the analysis, the study of the South American Monsoon System, can also be further deepened. Based on the results that prove the strong relation between the Rossby wave trains, the low-level circulation and precipitation, first the temporal evolution can be further evaluated. This could e.g. be done in terms of analysing the conditions when the coherence between the Rossby waves and precipitation is less pronounced. This knowledge could potentially then also be used in a forecast model, again also using machine learning techniques, to predict precipitation or its extremes based on e.g the Rossby wave state on the one hand and also the low-level jet strength as an indicator for the active and break phases on the other hand. It also seems possible to bring in knowledge of atmospheric models into this potential analysis by utilizing influence or Green's functions as outlined e.g. by Grimm and Silva Dias [81, e.g] to determine potential areas where atmospheric observables can serve as precursors. Artificial neural networks that were used in the later part of the thesis could also potentially be used for the forecast model.

As already outlined in Sec. 5.8, both, MCBB and NPDE, offer the potential to apply them to more sophisticated atmosphere or climate models. For MCBB, aside from advancing the method itself further with e.g. the already outlined modified clustering algorithm, it would be particularly interesting to investigate its applications to partial

differential equations. Systems from atmospheric dynamics could also be one example there. Even more promising is the further applications of the NPDE approach. For the first step the quasigeostrophic model from Marshall and Molteni [139] seems ideal. In a first step, one could use a synthetic setup similar to those shown in this thesis with the model. But later, as the quasigeostrophic model exhibits a fairly realistic climatology of the northern hemisphere winter, it could potentially be used for a NPDE setup with observational data. Showing that such a hybrid model substantially improves a model with observational data would be a major advancement and could subsequently applied to even more realistic models. In order to so one could consider pre-training it with model data such as from CMIP to ensure that the hybrid model is able to deliver accurate forecasts on the observational data as well.

Both of the further avenues of research sketched out in the last paragraphs show how one can further combine knowledge that we have of complex systems like those in climate with data-driven approaches to advance predictions or the understanding of the system in question and carry on with the core ideas of this thesis.

Appendices

A. Data Analysis of the South American Monsoon System

A.1. Streamflow networks

A.1.1. Pseudocode

Algorithm 2 Computation of the edge list of the streamflow network using the simulation method, as presented in [MG1]

$\mathbf{\Delta} \leftarrow$ spatial distances of all nodes to each other
$\boldsymbol{\gamma} \leftarrow$ angles between the spatial positions of all nodes to each other
for $i \in$ nodes **do**
  $u_d \leftarrow \frac{1}{2}\left(d_m + d_z\left(\lambda\right)\right)$ ▷ calculate distance uncertainty
  for $t \in$ time series **do** ▷ compute hit counts of actual wind time series
    $d \leftarrow \left|\mathbf{v}_i\left(t\right)\right| \cdot T + u_d$
    for $j \in$ nodes **do** ▷ depending on the used grid it is possible to limit the set of nodes j has to loop over based on additional geometrical considerations
      if $d > \Delta_{ij}$ **then**
        if $\gamma_{ij} \in [\theta_i - u_\theta, \theta_i + u_\theta]$ **then**
          $h_{ij} \leftarrow h_{ij} + 1$
  for $k \in [0, N_{stat}]$ **do** ▷ compute hit counts of surrogates
    for $t \in$ time series **do**
      $d \leftarrow \left|\mathbf{v}_i\left(t\right)\right| \cdot T + u_d$
      for $j \in$ nodes **do** ▷ it is possible to limit the set of nodes j has to loop over (see above)
        if $d > \Delta_{ij}$ **then**
          $\beta \leftarrow$ random uniformly distributed number $\in [-\pi, \pi]$
          if $\gamma_j \in [\beta - u_\theta, \beta_i + u_\theta]$ **then**
            $\eta_{ij}^{(k)} \leftarrow \eta_{ij}^{(k)} + 1$
  for $j \in$ nodes **do** ▷ evaluate surrogates and set links
    if $h_{ij} > 0$ **then**
      $\mu \leftarrow$ mean of $\eta_{ij}^{(k)}$ with respect to k
      $\sigma \leftarrow$ standard deviation of $\eta_{ij}^{(k)}$ with respect to k
      if $h_{ij} > \mu + n \cdot \sigma$ **then**
        add (i, j) to edge list $\mathbf{E}$

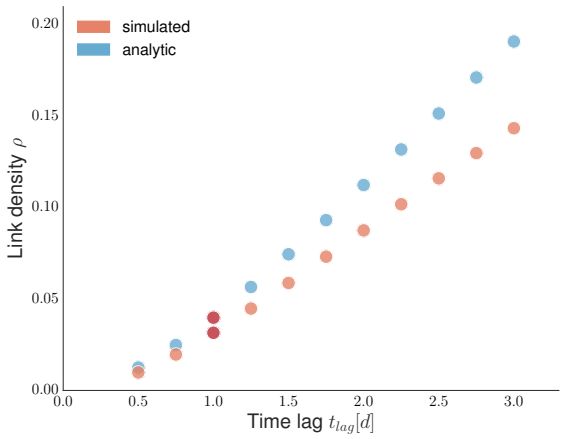

FIGURE A.1.: Dependency of the link density of the delay time T for the simulated and the semi-analytic streamflow network. The calculations were done with $n = 2$, respectively $\psi = 0.05$. It shows that the link density increases for the semi-analytic method slightly stronger than for the simulation method. For both methods a delay time of one day (red dot) is picked for further computations.

A.1.2. Parameter Sensitivity

Additional to the reasoning for the parameters presented in Sec. 3.3.2, here additional results concerning the parameter sensitivity are presented that largely follow the appendix of [MG1].

The travel time T governs the radius of the circle section ($|(u_i(t), v_i(t))| \cdot T + u_{d_i}(\lambda)$) that is used to calculate the network links. Hence, it is directly linked to the out-degree of all nodes and thus the link density of the whole network. Since we introduced the additional distance uncertainty u_{d_i}, $d_i(t) \geq u_{d_i}$ so that even small values for T should allow to connected path through the network along the flow of the wind that we can analyse with path-based measures like the betweenness. For both methods, the simulation and the semi-analytic method, the link density increases monotonously, in an almost linear way for larger travel times as seen Fig. A.1. A travel distance of one day results in a link density large enough for the network to include enough interesting features and is therefore chosen for all constructed streamflow networks.

The angle uncertainty u_θ governs the central angle of the circle section. It affects the out-degree of all nodes as well. However, the angle uncertainty also affect paths through the network and the overall structure as we argue in the Sec. 3.3.2. Fig. A.2 shows the dependency of the link density of the network on u_θ. For both network types an fixed uncertainty of $u_\theta = \frac{\pi}{6}$ is chosen. Fig. A.3 and A.4 justify this choice as even a reasonably large variation to u_θ only has small effects on the centrality measures.

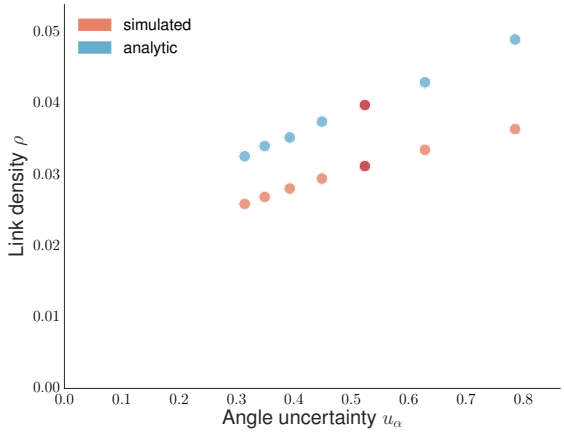

FIGURE A.2.: Dependency of the link density of the angle uncertainty u_θ for the simulated and the semi-analytic streamflow network. The calculations were done with the 1985-2010 MERRA dataset for South America and with $n = 2$ respectively $\psi = 0.05$. It shows that the link density increases in an almost linear way for both methods. The red dots show the angle uncertainty $u_\theta = \pi/6$ picked for further computations.

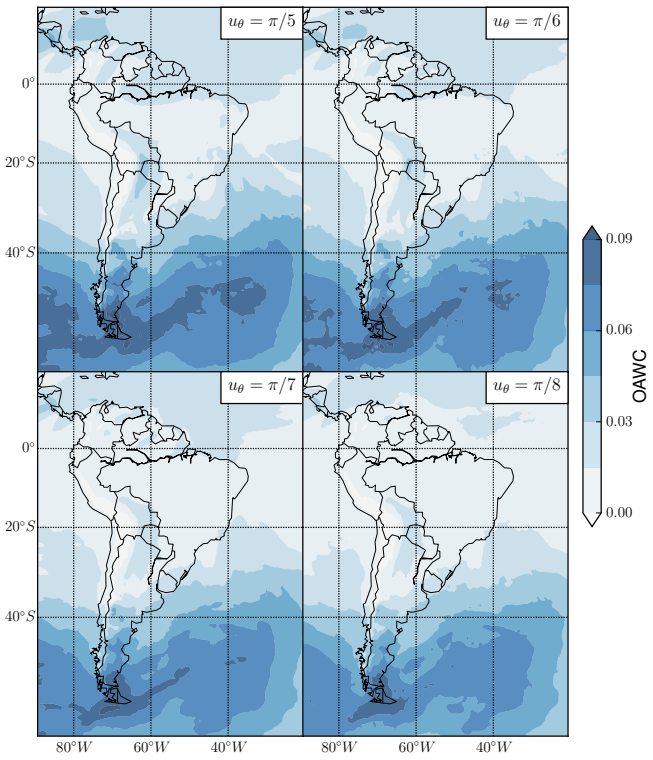

FIGURE A.3.: Out-area weighted connectivity of streamflow networks using the simulation method. All networks were computed using DJF data and the same parameters except for the angle uncertainty u_θ. u_θ was varied to investigate the qualitative behaviour of the OAWC with changing u_θ. The OAWC is very robust to small changes of u_θ.

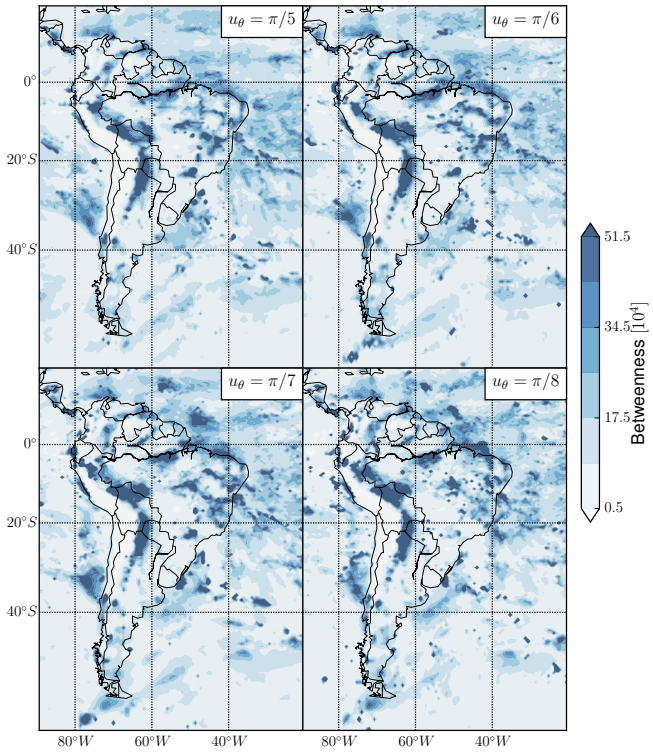

FIGURE A.4.: Betweenness of streamflow networks for different values of u_θ similar to Fig. A.3. Note that also for this measure, variations around the value $\pi/6$ do not affect the qualitative characteristics of the resulting betweenness centralility distribution.

A.1.3. Selected Hit Count Statistic

TABLE A.1.: Kolmogorov-Smirnov statistic of the distributions of the surrogate hit counts in Figure A.5.

Figure	$d_{crit}(\alpha = 0.001)^1$	d_{max}
(a)	0.1949	0.1024
(b)	0.0872	0.0680
(c)	0.0872	0.0657
(d)	0.0872	0.0703

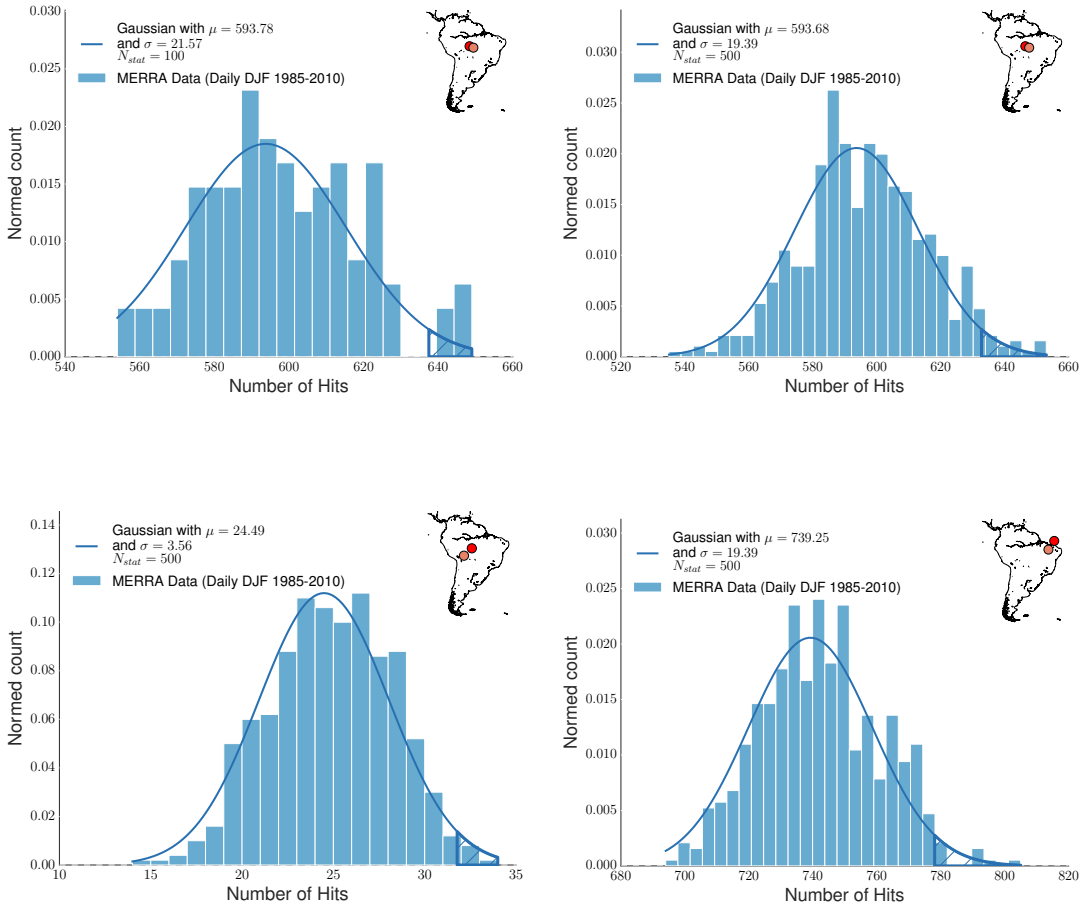

FIGURE A.5.: Histograms of the distribution of the hit count surrogates for different locations in South America. The distribution is approximately normally distributed when there are only few hits when looking at larger distances (bottom-left panel) and also for large hit counts when smaller distances are chosen (bottom-right panel). The results of a Kolmogorov-Smirnov test are shown in table A.1. Both top-row panels show the surrogate distribution between the same locations, only with a different number of surrogates. Apparently already as few as 100 surrogates can be enough to get a good estimate for a significance threshold. The significance threshold $\mu_{\eta,ij} + n \cdot \sigma_{\eta,ij}$ itself is marked in every panel with a dark blue line.

A.1.4. Reference Region for Active and Break Phases

The investigation of the active and break phases of the SAMS in Sec. 3.4 uses a reference region in Beni and Santa Cruz (BSC) in Bolivia in order to distinguish between the active and break phases of the SAMS. This region is shifted southward by 4° latitude from the reference region in Rondônia (9°-13°S, 60°-64°W) that was used in the initial description of the active and break SAMS phases by [94]. Here, we use a

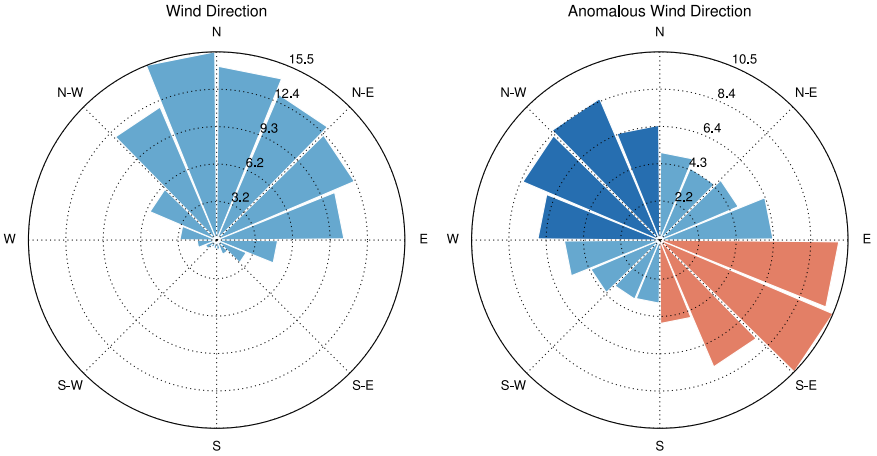

FIGURE A.6.: Histograms of wind directions at 850 hPa in the Brazilian state of Rondônia (9°-13°S, 60°-64°W). This is the same as Fig. 3.7 but with a northward shifted reference region that is identical to the study of [94].

different data source, MERRA, whereas Jones and Carvalho [94] used NCEP/NCAR data. While the NCEP/NCAR wind field in Rondônia exhibits an overall westerly wind regime in Rondônia, the MERRA wind field exhibits a broader, northerly wind regime in Rondônia during DJF (see Fig. A.6). Nonetheless, the anomaly wind field of the MERRA data in Rondônia exhibits a westerly and an easterly regime as well. By shifting the reference region southward to BSC, we obtain an overall westerly wind direction distribution (Fig. 3.7). Furthermore, active phases occur more often and are on average 0.5 d longer when BSC instead of Rondônia is used as reference region. In Sec. 3.4.1 we found that the geopotential height at 850 hPa in the southern Atlantic is connected to the active and break phases as well. The difference between the mean geopotential height at 850 hPa in the southern Atlantic is larger when using BSC as the reference region ($\Delta\mathrm{GPH}_{850} = 34.2\,\mathrm{m}$ versus $\Delta\mathrm{GPH}_{850} = 48.2\,\mathrm{m}$). The $\Delta\mathrm{GPH}_{850}$ for the BSC reference region is larger than the standard deviation of the geopotential height in the southern Atlantic, $\sigma_{\mathrm{GPH850}} = 45.1\,\mathrm{m}$, whereas the $\Delta\mathrm{GPH}_{850}$ for the Rondônia region would be smaller than the standard deviation.

We tested the further robustness of the results by shifting the reference region BSC along the eastern slopes of the Andes in Bolivia. The north-western region (NW) (15°-10°S, 69°-63°) and the south-eastern region (SE) (21°-15°S, 62°-56°W) induce active and break phases with a much larger coincidence to the studied phases with the reference region in BSC than to the phases with the reference region in Rondônia (see Tab. A.2 and A.3). The values of $\Delta\mathrm{GPH}_{850}$ and the overall qualitative structure of the streamflow networks is very similar as well. The results are therefore robust to a shift of the BSC reference region along the north-west to south-east axis following the eastern slopes of the Andes.

TABLE A.2.: Coincidence of the active phases determined with different reference regions. This coincidence is calculated as $C_{AB} = \frac{|A \cap B|}{|A|}$, where A and B denote the sets of numbered time steps that are part of the active regime for the corresponding reference region. $|A|$ is the amount of elements in the set A. As in general $|A| \neq |B|$, it follows that $C_{AB} \neq C_{BA}$. The reference regions are Beni and Santa Cruz (BSC) as used in this investigation, Rondônia (RON) as used by Jones and Carvalho [94], as well as the regions obtained by shifting BSC further south-east (SE) and north-west (NW). Precise coordinates of the latter two regions, which only serve the purpose of testing robustness, are specified in Sec. A.1.4.

	BSC	RON	SE	NW
Beni and Santa Cruz (BSC)	1	0.49	0.69	0.72
Rondônia (RON)	0.71	1	0.52	0.80
South-East (SE)	0.90	0.47	1	0.70
North-West (NW)	0.78	0.60	0.58	1

TABLE A.3.: Coincidence of the break regimes of different reference regions. The naming of the reference regions and the calculations follow those of Tab. A.2.

	BSC	RON	SE	NW
Beni and Santa Cruz (BSC)	1	0.54	0.65	0.66
Rondônia (RON)	0.53	1	0.42	0.65
South-East (SE)	0.82	0.54	1	0.60
North-West (NW)	0.68	0.68	0.49	1

A.2. Phase Coherence between Precipitation in South America and Rossby Waves

The additional results and the extended information on the conceptual model follows the supplementary material of the publication [MG3].

A.2.1. Conceptual Model

The full equations of the conceptual model are formulated using the centered coordinates

$$\xi = \varphi - \varphi_0 \tag{A.1}$$

$$\nu = \lambda - \lambda_0 \tag{A.2}$$

and the coefficients

$$a = \frac{\cos^2\theta}{2\sigma_\xi^2} + \frac{\sin^2\theta}{2\sigma_\nu^2} \tag{A.3}$$

$$b = -\frac{\sin 2\theta}{4\sigma_\xi^2} + \frac{\sin 2\theta}{4\sigma_\nu^2} \tag{A.4}$$

$$c = \frac{\sin^2\theta}{2\sigma_\xi^2} + \frac{\cos^2\theta}{2\sigma_\nu^2} \tag{A.5}$$

that use the propagation direction θ and the standard deviations σ_ξ and σ_ν in the model data equation

$$P_M\left(\xi(\varphi), \nu(\lambda), t\right) = \exp\left(-\left(a\xi^2 + 2b\xi\nu + c\nu^2\right)\right) \sin\left(\left(2\pi\left(\cos\theta\cdot\xi + \sin\theta\cdot\nu\right)\right)/L - \omega t\right). \tag{A.6}$$

While the wavelength L is another parameter of the model, the (temporal) frequency is kept at $\omega = 1/40\,\mathrm{d}$ as it does not affect the spatial structure of the resulting EOFs. The full set of parameters is thus $(\varphi_0, \lambda_0, K, \sigma_\xi, \sigma_\nu, \theta)$. We then calculate the model $\mathrm{EOF}_i^{(M)}$ and fit it to the data by numerically minimizing the least square error to the observed data $\mathrm{EOF}_i^{(D)}$

$$\mathrm{LSE}\left(\varphi_0, \lambda_0, , \sigma_\xi, \sigma_\nu, \theta\right) = \sum_{\varphi,\lambda}\sum_{i=1}^{2}\left(\mathrm{EOF}_i^{(M)}\left(\varphi,\lambda\right) - \mathrm{EOF}_i^{(D)}\left(\varphi,\lambda\right)\right). \tag{A.7}$$

As a single function evaluation can take a few seconds on a current processor, this is obviously a computationally relative expensive minimization that does very likely exhibit multiple local minima. The Nelder-Mead implementation of Python's scipy is used with initial parameter guesses chosen by hand to be already relatively close to being a good fit.

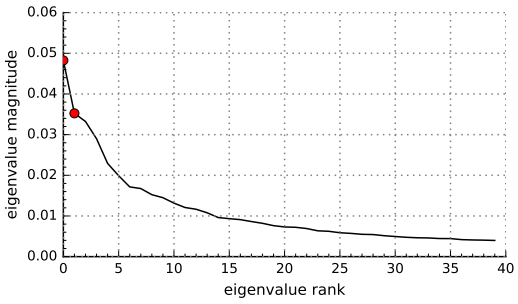

FIGURE A.7.: Eigenvalue spectrum of the PCA performed with precipitation anomlies from MERRA2 shown in Fig. 2. The red circles indicate the two leading EOFs that are further investigated with the conceptual model.

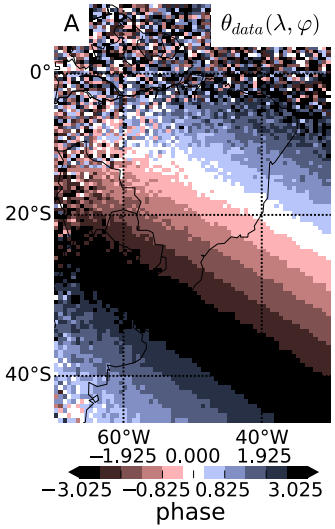

FIGURE A.8.: Spatial Phase of the first COEF of the conceptual model.

A.2.2. Monte Carlo SSA

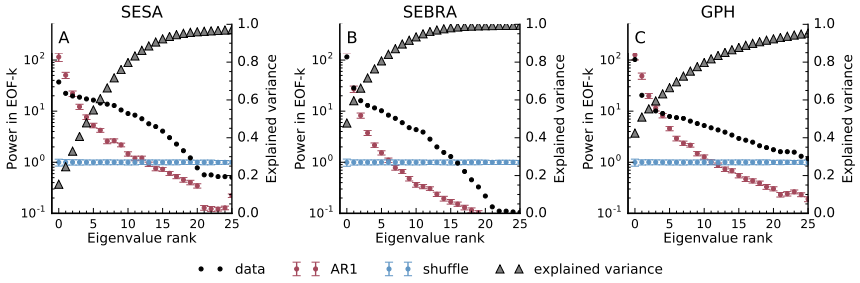

FIGURE A.9.: Singular Spectrum Analysis (SSA) of all three investigated observables. 1000 AR1 and shuffle surrogates are generated for each of the observables and can serve as significance tests for the SSA components.

A.2.3. Additional Results for Phase Differences

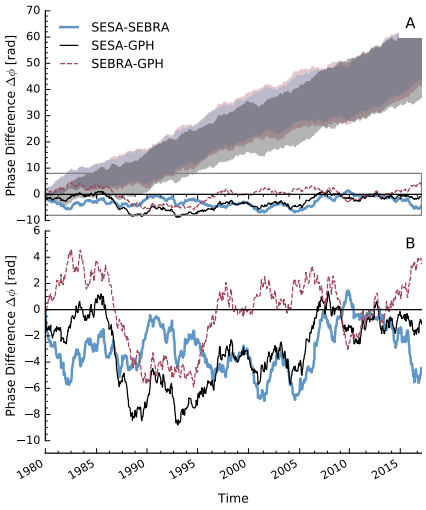

FIGURE A.10.: Phase Difference time series results analogous to Fig. 3.23, presented in the main text. These results feature AR1 surrogates instead of the AR2 surrogates presented in the main text.

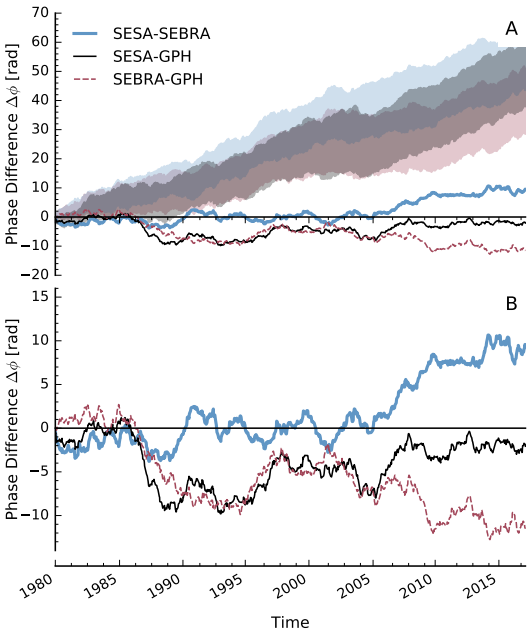

FIGURE A.11.: Phase Difference time series results analogous to Fig. 3.23, presented in the main text. These results were computed with the third and fourth SSA component included in the analysis.

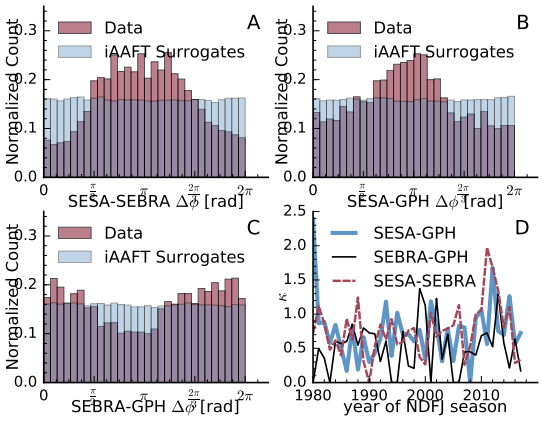

FIGURE A.12.: Phase Difference histogram results analogous to Fig. 3.24, presented in the main text. These results were computed with the third and fourth SSA component included in the analysis.

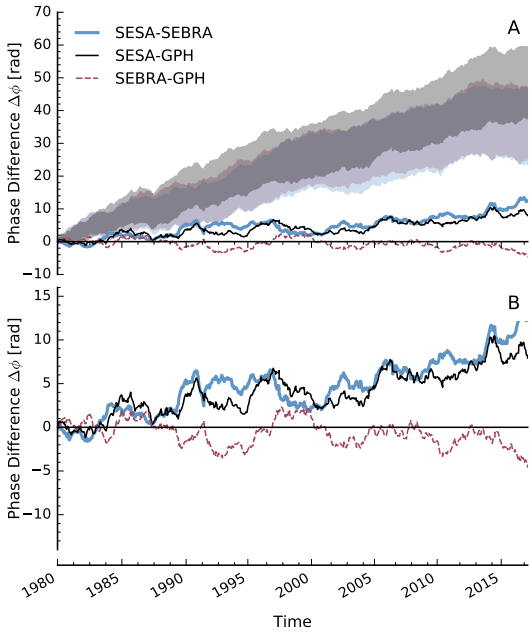

FIGURE A.13.: Phase Difference time series results analogous to Fig. 3.23. These results were computed with a 10-50 day Bandpass-Lanczos Filter with 1501 weights instead of the SSA.

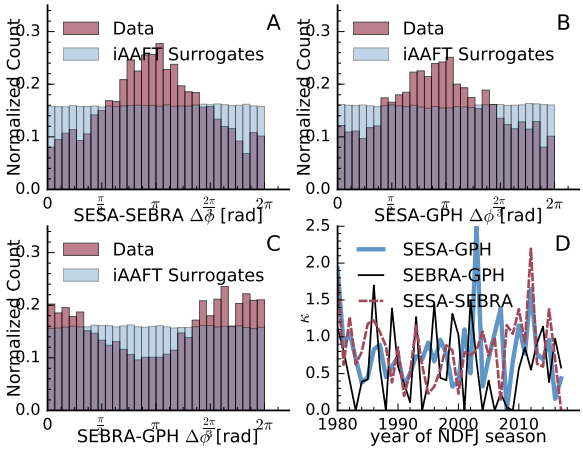

FIGURE A.14.: Phase Difference histogram results analogous to Fig. 3.24. These results were computed with a 10-50 day Bandpass-Lanczos Filter with 1501 weights instead of the SSA.

B. Monte Carlo Basin Bifurcation Analysis

The additional results and the sensitivity study on initial conditions that is presented here, follows the appendix of the publication [MG5].

B.1. Dependence on initial conditions

During the sampling step of MCBB there is often a natural choice, given the parametrization and coordinates used, for the distribution of the initial conditions, and it is typical in basin studies to use a uniform distribution in a box. However, there is no a priori reason to expect that the limit of infinite box size converges, but experience shows that often plausible ranges for the box are naturally given by the system and the results don't depend heavily on box size (or even on substituting a normal distribution for the box). To further investigate this, the distribution of the initial conditions of the frequencies of the second order Kuramoto model is changed which is presented in Sec. III.B. Fig. B.1 shows results for uniform distributions with different bounds ($[-\pi, \pi]$, as shown in the main text, $[-5\pi, \pi]$ and $[-10\pi, 10\pi]$) and a normal distribution with mean 0 and standard deviation π. All other parameters (e.g. the clustering parameter ϵ_{DB}) are kept constant. Qualitatively the results are very similar: they show an unsynchronized regime (violet), a fully synchronized regime (blue) and several partially synchronized states. Quantitatively they differ. The broader the distributions of the frequencies gets, the later the fully synchronized states becomes the only existing asymptotic states. This behaviour can be expected from a second order Kuramoto system: with initial frequencies very far apart from each other, it will synchronize less well.

B.2. BBClustering

For the MCBB results presented in this thesis DBSCAN (see Sec. 2.3.5) is used to find the classes of asymptotic states. In the following, a specialized density-based clustering algorithm, Basin Bifurcation Clustering (BBClustering), is outlined that could be used in future research to replace DBSCAN. The basis of BBClustering is an additional continuation of the integration. As described in Sec. 4.1.4, $\delta_i^{\pm} = D(\rho^i, \rho^{i\pm})$ is the distance of the i-th trial to a continuation with the control parameter shifted by $\pm\delta p \approx \pm < \min_j(||p^{(i)} - p^{(j)}||) >_i$. BBClustering is based on DBSCAN but computes

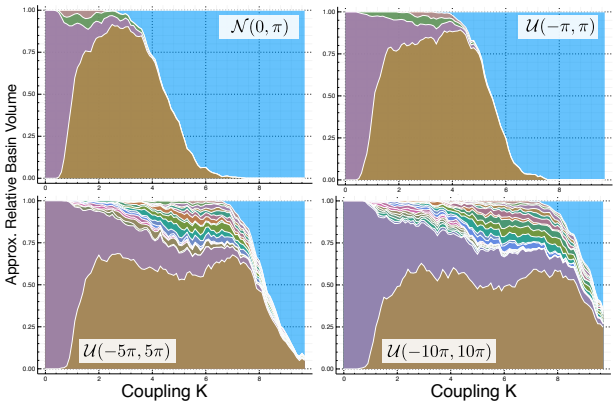

FIGURE B.1.: Results for the second order Kuramoto with different distributions of initial conditions.

the neighbourhood of each sample through the results of the continuation. A sample j is considered to be a neighbour of i if

$$D_{ij} \cdot \left(\frac{\delta p}{||p_i - p_j||} \right) < k \cdot \frac{1}{2} (\min_{\pm}(\delta_i^{\pm}) + \min_{\pm}(\delta_j^{\pm})). \tag{B.1}$$

As sketched in Fig. B.2, this criterion is based on the rationale that the continuation response $\delta^{\pm}$ will be strongly asymmetric when the state becomes unstable in one direction. Two samples belong to the same asymptotic state when the distance D_{ij} is about the same as the mean of the smaller continuation response. k is a parameter remaining in this clustering method, governing how fine or coarse the clusters should be resolved. In contrast to the standard DBSCAN algorithm, BBClustering features an adaptive neighbourhood criterion based on the continuation response. The remaining part of the algorithm is identical to DBSCAN and as outlined in Sec. 2.3.5. MCBB.jl (see Sec. B.4) features an implementation of BBClustering.

B.3. Additional Results and Resources

B.3.1. Logistic Map

While MCBB is designed with high-dimensional systems in mind, it also works in the fringe case of a one dimensional system such as the logistic map $x_{n+1} = rx_n(1 - x_n)$. Fig. B.3 shows the approximate relative basin volume computed with MCBB compared to the bifurcation diagram. It was computed using the mean, standard deviation and Kullbach-Leibler divergence as statistics with the weights 1, 0.5 and 0.5. The major bifurcation points are reproduced. The stable regions inside the chaotic regime form separate clusters, while most of the chaotic regime is grouped into to distinct clusters, one before and one after the larger stable region around $r \approx 3.8$.

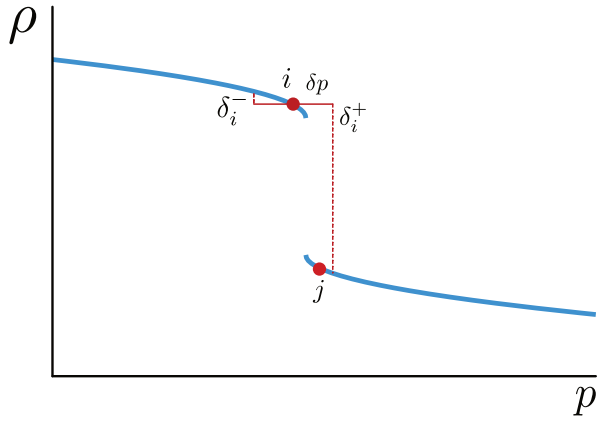

FIGURE B.2.: Sketch of the rational behind the neighourhood criterion of BBClustering.

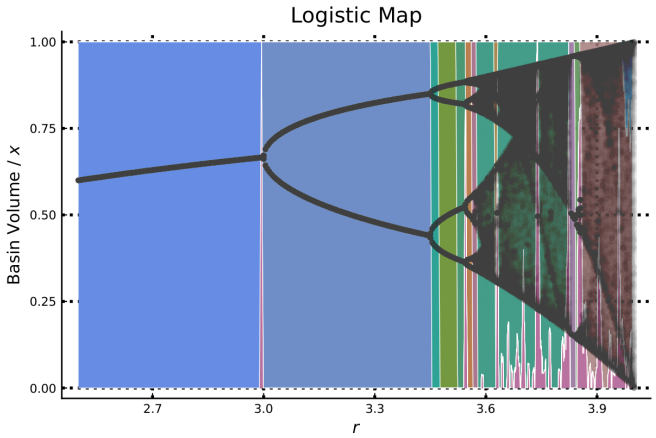

FIGURE B.3.: Basin Volume computed with MCBB and Bifurcation diagram of a logistic map.

B.3.2. Stuart-Landau Oscillator Network

Additionally to the results presented in Sec. 4.1.9 for the Stuart-Landau oscillator network, one can also further inspect the other clusters. In Fig. B.4 and B.5 show results for the classes of asymptotic states not shown in the main text. These are the outlier cluster, the travelling wave (TW) and oscillation death (OD) states. The Julia package (see Sec. B.4) also allows for further other visualizations and inspections of the measures and the clusters. The documentation of the package explains these in more detail.

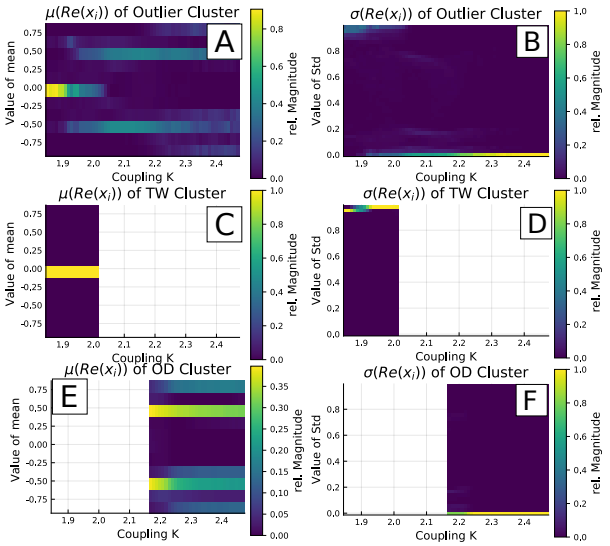

FIGURE B.4.: Further analysis on the clusters also shown in Fig. 4.7. (A),(B),(E),(F) are sliding window histograms fits of the denoted measures for trials with parameters within the respective window. (C) and (D) are example trajectories of trials within these clusters.

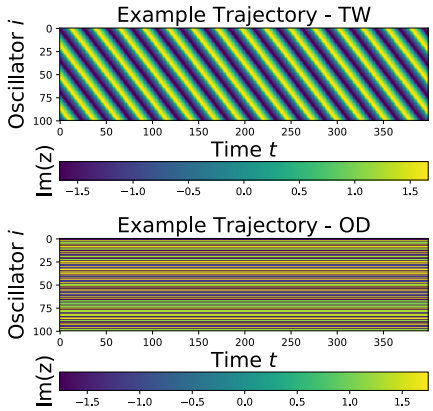

FIGURE B.5.: Further analysis on the clusters also shown in Fig. 4.7. (A),(B),(E),(F) are sliding window histograms fits of the denoted measures for trials with parameters within the respective window. (C) and (D) are example trajectories of trials within these clusters.

B.3.3. Conceptual Model for Tipping Cascades

TABLE B.1.: Further parameters of the conceptual tipping model for tipping cascades presented in Sec. 4.2.1. The link strength s_{ij} has a specific link strength range and a specific physical process that is connected to the respective interaction and given below. The link strength ranges are scaled from literature values [105, 112] such that they can be used in the model (Eq. 4.15). For a more in depth description please be referred to Wunderling et al. [249]. This table itself is taken from the publication Wunderling et al. [MG7].

Interaction	**Link strength range s_{ij} (a.u.)**	**Process**
Greenland → AMOC	$[+1; +10]$	Freshwater inflow
AMOC → Greenland	$[-1; -10]$	AMOC breakdown, Greenland cooling
Greenland → West Antarctica	$[+1; +10]$	Grounding line retreat
ENSO → Amazon rainforest	$[+1; +10]$	Drying over Amazonia
ENSO → West Antarctica	$[+1; +5]$	Warming of Ross and Amundsen seas
AMOC → Amazon rainforest	$[\pm 2; \pm 4]$	Changes in hydrological cycle
West Antarctica → AMOC	$[\pm 1; \pm 3]$	Increase in meridional salinity gradient (−), Fast advection of freshwater anomaly to North Atlantic (+)
AMOC → ENSO	$[+1; +2]$	Cooling of North-East tropical Pacific with thermocline shoaling and weakening of annual cycle in EEP
West Antarctica → Greenland	$[+1; +2]$	Grounding line retreat
ENSO → AMOC	$[-1; -2]$	Enhanced water vapor transport to Pacific
AMOC → West Antarctica	$[+1; +1.5]$	Heat accumulation in Southern Ocean
Amazon rainforest → ENSO	$[\pm 1; \pm 1.5]$	Changes in tropical moisture supply

B.4. Julia Package

The MCBB algorithm is implemented in Julia. The package can be installed directly from the GitHub repository `https://github.com/maximilian-gelbrecht/MCBB.jl/`. The package makes uses Julia's DifferentialEquations.jl library [40]. There is an extensive documentation available that explains the package with some tutorials.

C. Neural Partial Differential Equations

The additional results presented here, follow the supplementary material of the publication [MG2].

C.1. Kuramoto Sivashinsky - 4th Derivative Term

In the main text, in Sec. 5.6.4, when investigating the Kuramoto Sivashinsky equation (KS) we replaced the second order term with an ANN, here show additional results to proof the robustness of the approach. For this purpose we replace the term with the fourth order derivative with an ANN:

$$\partial_t u = \mathcal{N}_{KS}(u) - u\partial_x u - \partial_{xx} u. \tag{C.1}$$

When investigating this setup, it became even more apparent that small values for the integration time step Δt are needed. Whereas the training fails for $\Delta t = 0.1$, the results shown in Fig. C.1 for $\Delta t = 0.02$ are similar to those reported in the main text for the second derivative term. The valid time t_v is 2953 time steps which, given a maximum Lyapunov exponents $\lambda_{max} = 0.08$, is equivalent to $4.72\lambda_{max}t$.

C.2. Benchmarks

C.2.1. Convolutional Neural Network

The results of the NPDE forecast are compared to a CNN (see Sec. 2.4). This CNN is set up with a bottleneck, meaning that the first convolutional and pooling layers reduce the dimension of the input before subsequent layers extend the dimension back to the full size of the field. It makes forecasts by using a recursive loop in which the output of the CNN is fed back as input for the next time step. This architecture showed to be successful in approximating complex spatiotemporal fields, like simple global circulation models [195]. The CNN consists of three convolutional layers with 3×3-sized kernel, each with 8 channels and each followed by a 2×2 max pooling layer. The dimension is reduced, this is the so-called 'bottleneck' of the CNN. Then, three convolutional layers with 3×3-sized kernel each followed by an upsampling layer scale the dimension back to the input dimension. It is trained by minimizing the one-step-ahead least-squared forecast error with a stochastic gradient descent method over 10000 epochs of the dataset.

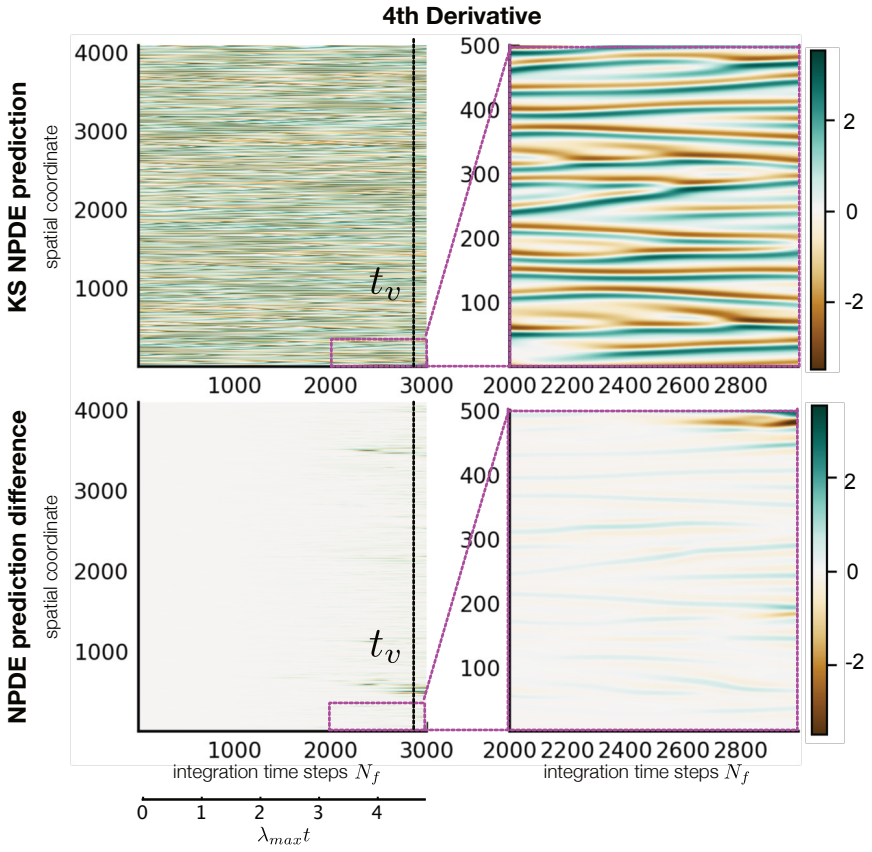

FIGURE C.1.: Results for the NPDE for the KS system according to Eq. C.1. The right hand panels show a zoomed in view of the area marked with the maganta rectangles in the left hand panels.

C.2.2. Hybrid Reservoir

Combining knowledge-based but incomplete models with a data-driven numerical model has previously been achieved with great success using reservoirs. Pathak et al. [161] showed that such a setup is able to forecast chaotic processes for very long times. However, in these examples very long input datasets were used. Here, we use the same basic setup as reported by Pathak et al. [161] with reservoir size $N = 20000$, spectral density $\rho = 0.4$, sparsity $< d >= 0.03$, input coefficient uniformly drawn from $[-0.5; 0.5]$ and regularization constant 10^{-4}. The knowledge-based model is the NPDE without the neural network, thus the PDE with one term missing. It was integrated using the LSODA solver from the Fortran ODEPACK library. While for longer training datasets a forecast horizon of several Lyapunov times can be achieved, it is much lower for the short training datasets explored in this thesis. For the 128×128-sized grid that is used for the CGLE and the 4096-dimensional KS discritization, one would need much larger reservoir sizes. These are potentially prohibitively large. We

therefore computed the hybrid reservoir comparisons on smaller grids, 50×50 for the CGLE and 128 for the KS.

List of Publications

[MG1] Maximilian Gelbrecht, Niklas Boers, and Jürgen Kurths. „A complex network representation of wind flows“. In: *Chaos: An Interdisciplinary Journal of Nonlinear Science* 27.3 (2017), p. 035808.

Author Contributions: MG, NB and JK conceived and designed the study. MG conducted the analysis. MG prepared the manuscript. All authors discussed the results and edited the manuscript.

[MG2] Maximilian Gelbrecht, Niklas Boers, and Jürgen Kurths. „Neural partial differential equations for chaotic systems“. In: *New Journal of Physics* 23.4 (Apr. 2021), p. 043005.

Author Contributions: MG conceived and carried out the study. MG wrote the manuscript. MG, NB, JK discussed the results and edited manuscript.

[MG3] Maximilian Gelbrecht, Niklas Boers, and Jürgen Kurths. „Phase coherence between precipitation in South America and Rossby waves“. In: *Science Advances* 4.12 (2018).

Author Contributions: MG and NB conceived and designed the study. MG conducted the analysis. MG and NB prepared the manuscript. All authors discussed the results and edited the manuscript.

[MG4] Maximilian Gelbrecht, Niklas Boers, and Jürgen Kurths. „Variability of the Low-Level Circulation of the South American Monsoon Analysed with Complex Networks“. In: *(accepted at) European Physical Journal Special Topics* (2020).

Author Contributions: MG and NB conceived the study. MG conducted the analysis and wrote the manuscript. MG, NB, JK discussed the results and edited manuscript.

[MG5] Maximilian Gelbrecht, Jürgen Kurths, and Frank Hellmann. „Monte Carlo basin bifurcation analysis“. In: *New Journal of Physics* 22.3 (Mar. 2020), p. 033032.

Author Contributions: FH conceived the idea of the method. MG and FH conceived the research and details of the method. MG and FH designed the analyses. MG wrote the software library. MG and FH conducted the analyses. MG and FH prepared the manuscript. JK supervised the study. All authors discussed the results and the manuscript.

[MG6] Maximilian Gelbrecht, Valerio Lucarini, Niklas Boers, and Jürgen Kurths. „Analysis of a bistable climate toy model with physics-based machine learning methods“. In: *(accepted at) European Physical Journal Special Topics* (2020).

Author Contributions: MG designed the study, conducted the analysis and prepared the manuscript. VL set up the Toy Model itself. All authors discussed the results and edited the manuscript.

[MG7] Nico Wunderling, Maximilian Gelbrecht, Ricarda Winkelmann, Jürgen Kurths, and Jonathon F Donges. „Basin stability and limit cycles in a conceptual model for climate tipping cascades“. In: *New Journal of Physics* (2020).

Author Contributions: NW, RW and JFD designed the study. NW conducted the basin stability simulation runs and prepared the figures for the part on basin stability (not shown here). MG conducted the simulation runs and prepared the figures for the part on oscillatory states. All authors discussed the results of the paper and NW led the writing with input from all authors. In this thesis, the model is briefly summarized and the contribution from MG from this paper is shown. Additional results are presented that replace the basin stability results from the paper with MCBB results from MG
.

Bibliography

[1] Ralph Abraham, Alexander Keith, Matthew Koebbe, and Gottfried Mayer-Kress. „Computational unfolding of double-cusp models of opinion formation“. In: *Int. J. Bifurc. Chaos* 1.02 (1991), pp. 417–430.

[2] Rafail Abramov. „A Simple Stochastic Parameterization for Reduced Models of Multiscale Dynamics“. In: *Fluids* 1.1 (2016).

[3] Rafail V. Abramov. „Leading Order Response of Statistical Averages of a Dynamical System to Small Stochastic Perturbations“. In: *Journal of Statistical Physics* 166.6 (2017), pp. 1483–1508.

[4] Rafail V. Abramov and Andrew J. Majda. „New Approximations and Tests of Linear Fluctuation-Response for Chaotic Nonlinear Forced-Dissipative Dynamical Systems“. In: *Journal of Nonlinear Science* 18.3 (2008), pp. 303–341.

[5] Daniel M. Abrams and Steven H. Strogatz. „Chimera States for Coupled Oscillators“. In: *Phys. Rev. Lett.* 93 (17 Oct. 2004), p. 174102.

[6] M. R. Allen and L. A. Smith. *Monte Carlo SSA: detecting irregular oscillations in the presence of colored noise*. 1996.

[7] Ethem Alpaydin. *Introduction to Machine Learning*. 3rd ed. Adaptive Computation and Machine Learning. Cambridge, MA: MIT Press, 2014.

[8] A.A. Andronov, E.A. Leontovich, I.I. Gordon, and A.G. Maier. *Theory of Bifurcations of Dynamical Systems on a Plane*. Israel Program Sci. Transl., 1971.

[9] John Argyris, Gunter Faust, and Maria Haase. *Die Erforschung des Chaos*. vieweg, 1995.

[10] H. M. Arnold, I. M. Moroz, and T. N. Palmer. „Stochastic parametrizations and model uncertainty in the Lorenz system“. In: *Philosophical Transactions of the Royal Society A: Mathematical, Physical and Engineering Sciences* 371.1991 (2013), p. 20110479.

[11] Sabine Auer, Kirsten Kleis, Paul Schultz, Jürgen Kurths, and Frank Hellmann. „The impact of model detail on power grid resilience measures“. In: *The European Physical Journal Special Topics* 225.3 (2016), pp. 609–625.

[12] A Babloyantz and A Destexhe. „Low-dimensional chaos in an instance of epilepsy“. In: *Proceedings of the National Academy of Sciences* 83.10 (1986), pp. 3513–3517.

[13] Aldo Balestrino, Andrea Caiti, and Emanuele Crisostomi. „Entropy of Curves for Nonlinear Systems Classification“. In: *IFAC Proceedings Volumes* 40.12 (2007). 7th IFAC Symposium on Nonlinear Control Systems, pp. 72–77.

[14] T. P. Barnett. *Interaction of the Monsoon and Pacific Trade Wind System at Interannual Time Scales. Part III: A Partial Anatomy of the Southern Oscillation*. 1984.

[15] Robbin Bastiaansen, Arjen Doelman, Maarten B. Eppinga, and Max Rietkerk. „The effect of climate change on the resilience of ecosystems with adaptive spatial pattern formation“. In: *Ecology Letters* 23.3 (2020), pp. 414–429.

[16] Peter Bauer, Alan Thorpe, and Gilbert Brunet. „The quiet revolution of numerical weather prediction“. In: *Nature* 525.7567 (2015), pp. 47–55.

[17] Atilim Gunes Baydin, Barak A. Pearlmutter, Alexey Andreyevich Radul, and Jeffrey Mark Siskind. „Automatic Differentiation in Machine Learning: a Survey“. In: *Journal of Machine Learning Research* 18.153 (2018), pp. 1–43.

[18] Giancarlo Benettin, Luigi Galgani, Antonio Giorgilli, and Jean-Marie Strelcyn. „Lyapunov Characteristic Exponents for smooth dynamical systems and for hamiltonian systems; A method for computing all of them. Part 2: Numerical application“. In: *Meccanica* 15.1 (1980), pp. 21–30.

[19] Arthur R Bergen and David J Hill. „A structure preserving model for power system stability analysis“. In: *IEEE Transactions on Power Apparatus and Systems* 1 (1981), pp. 25–35.

[20] R. Blender and V. Lucarini. „Nambu representation of an extended Lorenz model with viscous heating“. In: *Physica D: Nonlinear Phenomena* 243.1 (2013), pp. 86–91.

[21] Tamás Bódai. „Extreme Value Analysis in Dynamical Systems: Two Case Studies“. In: *Nonlinear and Stochastic Climate Dynamics*. Ed. by Christian L. E. Franzke and Terence J. O'Kane. Cambridge University Press, 2017, pp. 392–429.

[22] Tamás Bódai and Valerio Lucarini. „Rough basin boundaries in high dimension: Can we classify them experimentally?“ In: *Chaos: An Interdisciplinary Journal of Nonlinear Science* 30.10 (2020), p. 103105.

[23] N Boers, B Bookhagen, H M J Barbosa, N Marwan, J Kurths, and J a Marengo. „Prediction of extreme floods in the eastern Central Andes based on a complex networks approach.“ In: *Nature communications* 5.1993 (2014), p. 5199.

[24] N. Boers, B. Bookhagen, H.M.J. Barbosa, N. Marwan, J. Kurths, and J.A. Marengo. „Prediction of extreme floods in the eastern Central Andes based on a complex networks approach“. In: *Natur Communications* 5.5199 (2014).

[25] Niklas Boers, Henrique M. J. Barbosa, Bodo Bookhagen, José A. Marengo, Norbert Marwan, and Jürgen Kurths. „Propagation of Strong Rainfall Events from Southeastern South America to the Central Andes“. In: *Journal of Climate* 28.19 (2015), pp. 7641–7658.

[26] Niklas Boers, Henrique M.J. Barbosa, Bodo Bookhagen, Jose A. Marengo, Norbert Marwan, and Jurgen Kurths. „Propagation of Strong Rainfall Events from Southeastern South America to the Central Andes“. In: *Journal of Climate* 28.19 (2015), pp. 7641–7658.

[27] Niklas Boers, Bodo Bookhagen, Norbert Marwan, and Jürgen Kurths. „Spatiotemporal characteristics and synchronization of extreme rainfall in South America with focus on the Andes Mountain range“. In: *Climate Dynamics* 46.1 (Jan. 2016), pp. 601–617.

[28] Niklas Boers, Bodo Bookhagen, Norbert Marwan, and Jürgen Kurths. „Spatiotemporal characteristics and synchronization of extreme rainfall in South America with focus on the Andes Mountain range“. In: *Climate Dynamics* 46.1 (2016), pp. 601–617.

[29] Niklas Boers, Bodo Bookhagen, Norbert Marwan, Jürgen Kurths, and José Marengo. „Complex networks identify spatial patterns of extreme rainfall events of the South American Monsoon System“. In: *Geophysical Research Letters* 40.16 (2013), pp. 4386–4392.

[30] Niklas Boers, Bedartha Goswami, Aljoscha Rheinwalt, Bodo Bookhagen, Brian Hoskins, and Jürgen Kurths. „Complex networks reveal global pattern of extreme-rainfall teleconnections“. In: *Nature* 566.7744 (Feb. 2019), pp. 373–377.

[31] Niklas Boers and Aljoscha Rheinwalt. „The South American rainfall dipole: A complex network analysis of extreme events“. In: *Geophysical Research Letters* 41 (2014), pp. 1–9.

[32] Niklas Boers, Aljoscha Rheinwalt, Bodo Bookhagen, Henrique M. J. Barbosa, Norbert Marwan, José Marengo, and Jürgen Kurths. „The South American rainfall dipole: A complex network analysis of extreme events“. In: *Geophysical Research Letters* 41.20 (2014), pp. 7397–7405.

[33] William D. Bonner. „Climatology of the Low Level Jet“. In: *Monthly Weather Review* 96.12 (1968), pp. 833–850.

[34] Carlos R. Mechoso Brant Liebmann. „The South American Monsoon System“. In: *The Global Monsoon System: Research and Forecast*. Ed. by Chih-Pei Chang, Yihui Ding, Ngar-Cheung Lau, Richard H. Johnson, Bin Wanga, and Tetsuzo Yasunari. World Scientific, 2011. Chap. 9, pp. 137–157.

[35] H. Broer, C. Simó, and R. Vitolo. „Bifurcations and strange attractors in the Lorenz-84 climate model with seasonal forcing“. In: *Nonlinearity* 15 (2002), pp. 1205–1267.

[36] D. S. Broomhead and Gregory P. King. „Extracting qualitative dynamics from experimental data“. In: *Physica D: Nonlinear Phenomena* 20.2-3 (1986), pp. 217–236.

[37] Charles D Brummitt, George Barnett, and Raissa M D'Souza. „Coupled catastrophes: sudden shifts cascade and hop among interdependent systems“. In: *J. Roy. Soc. Interface* 12.112 (2015), p. 20150712.

[38] Steven L. Brunton, Joshua L. Proctor, and J. Nathan Kutz. „Discovering governing equations from data by sparse identification of nonlinear dynamical systems“. In: *Proceedings of the National Academy of Sciences* 113.15 (2016), pp. 3932–3937.

[39] M. I. Budyko. „The effect of solar radiation variations on the climate of the Earth“. In: *Tellus* 21.5 (1969), pp. 611–619.

[40] Rackauskas C. and Nie Q. „DifferentialEquations.jl – A Performant and Feature-Rich Ecosystem for Solving Differential Equations in Julia“. In: *Journal of Open Research Software* 5(1):15 (2017).

[41] Levke Caesar, Stefan Rahmstorf, Alexander Robinson, G Feulner, and V Saba. „Observed fingerprint of a weakening Atlantic Ocean overturning circulation“. In: *Nature* 556.7700 (2018), pp. 191–196.

[42] M. Carlu, F. Ginelli, V. Lucarini, and A. Politi. „Lyapunov analysis of multiscale dynamics: the slow bundle of the two-scale Lorenz 96 model“. In: *Nonlinear Processes in Geophysics* 26.2 (2019), pp. 73–89.

[43] L. M. V. Carvalho, C. Jones, and B. Liebmann. „The South Atlantic Convergence Zone: Intesity, form, persistence, and relationships with intraseasonal to interanual activity and extreme rainfall.“ In: *Journal of Climate* 17 (2004), pp. 88–108.

[44] A. Chattopadhyay, P. Hassanzadeh, and D. Subramanian. „Data-driven predictions of a multiscale Lorenz 96 chaotic system using machine-learning methods: reservoir computing, artificial neural network, and long short-term memory network“. In: *Nonlinear Processes in Geophysics* 27.3 (2020), pp. 373–389.

[45] Ricky T. Q. Chen, Yulia Rubanova, Jesse Bettencourt, and David Duvenaud. *Neural Ordinary Differential Equations*. 2018.

[46] Catrin Ciemer, Niklas Boers, Marina Hirota, Jürgen Kurths, Finn Müller-Hansen, Rafael S. Oliveira, and Ricarda Winkelmann. „Higher resilience to climatic disturbances in tropical vegetation exposed to more variable rainfall“. In: *Nature Geoscience* 12.3 (2019), pp. 174–179.

[47] Allan J. Clarke. „El Niño Physics and El Niño Predictability“. In: *Annual Review of Marine Science* 6.1 (2014). PMID: 24405425, pp. 79–99.

[48] M. G. Clerc, A. Petrossian, and S. Residori. „Bouncing localized structures in a liquid-crystal light-valve experiment“. In: *Phys. Rev. E* 71 (1 Jan. 2005), p. 015205.

[49] B.I. Cohen, J.A. Krommes, W.M. Tang, and M.N. Rosenbluth. „Non-linear saturation of the dissipative trapped-ion mode by mode coupling“. In: *Nuclear Fusion* 16.6 (Dec. 1976), pp. 971–992.

[50] Michel Crucifix. „Oscillators and relaxation phenomena in Pleistocene climate theory“. In: *Philos. Trans. Royal Soc. A* 370.1962 (2012), pp. 1140–1165.

[51] Christopher Alexander Castro Cunningham and Iracema Fonseca de Albuquerque Cavalcanti. „Intraseasonal modes of variability affecting the South Atlantic Convergence Zone“. In: *International Journal of Climatology* 26.9 (2006), pp. 1165–1180.

[52] G. Cybenko. „Approximation by superpositions of a sigmoidal function“. In: *Mathematics of Control, Signals and Systems* 2.4 (1989), pp. 303–314.

[53] George Datseris. „DynamicalSystems.jl: A Julia software library for chaos and nonlinear dynamics“. In: *Journal of Open Source Software* 3.23 (Mar. 2018), p. 598.

[54] Asim Kumer Dey, Yulia R Gel, and H Vincent Poor. „Motif-based analysis of power grid robustness under attacks“. In: *2017 IEEE Global Conference on Signal and Information Processing (GlobalSIP)*. IEEE. 2017, pp. 1015–1019.

[55] Peter Ditlevsen, Takahito Mitsui, and Michel Crucifix. „Crossover and peaks in the Pleistocene climate spectrum; understanding from simple ice age models“. In: *Clim. Dynam.* 54.3 (2020), pp. 1801–1818.

[56] P. S. Dodds and D. J. Watts. „A generalized model of social and biological contagion“. In: *Journal of Theoretical Biology* 232.4 (2005), pp. 587–604.

[57] Peter Sheridan Dodds and Duncan J. Watts. „Universal behavior in a generalized model of contagion“. In: *Physical Review Letters* 92.21 (2004), pp. 1–4.

[58] Eusebius J. Doedel. *AUTO-07P : Continuation and Bifurcation Software for Ordinary Differential Equations*. `http://indy.cs.concordia.ca/auto/`. Concordia University Montreal, Canada. 2007.

[59] F. J. Donges, Y. Zou, N. Marwan, and J. Kurths. „Complex networks in climate dynamics“. In: *The European Physical Journal Special Topics* 174.1 (2009), pp. 157–179.

[60] Wansuo Duan and Zhenhua Huo. „An Approach to Generating Mutually Independent Initial Perturbations for Ensemble Forecasts: Orthogonal Conditional Nonlinear Optimal Perturbations“. In: *Journal of the Atmospheric Sciences* 73.3 (Feb. 2016), pp. 997–1014.

[61] Claude E. Duchon. „Lanczos Filtering in One and Two Dimensions“. In: *Journal of Applied Meteorology* 18.8 (Aug. 1979), pp. 1016–1022.

[62] Witold Dzwinel, Jacek Kitowski, and Jacek Mościński. „“Checker Board” Periodic Boundary Conditions in Molecular Dynamics Codes“. In: *Molecular Simulation* 7.3-4 (1991), pp. 171–179.

[63] J. -P. Eckmann and D. Ruelle. „Ergodic theory of chaos and strange attractors“. In: *Rev. Mod. Phys.* 57 (3 June 1985), pp. 617–656.

[64] Ronald M. Errico. „What Is an Adjoint Model?“ In: *Bulletin of the American Meteorological Society* 78.11 (Nov. 1997), pp. 2577–2592.

[65] Martin Ester, Xiaowei Xu, Hans - peter Kriegel, and Jorg Sander. „Density-based algorithm for discovering clusters in large spatial databases with noise“. In: *Proceedings Of The Acm Sigkdd International Conference On Knowledge Discovery And Data Mining* pages (1996), pp. 226–231.

[66] V. Eyring, S. Bony, G. A. Meehl, C. A. Senior, B. Stevens, R. J. Stouffer, and K. E. Taylor. „Overview of the Coupled Model Intercomparison Project Phase 6 (CMIP6) experimental design and organization“. In: *Geoscientific Model Development* 9.5 (2016), pp. 1937–1958.

[67] B. Farley and W. Clark. „Simulation of self-organizing systems by digital computer“. In: *Transactions of the IRE Professional Group on Information Theory* 4.4 (1954), pp. 76–84.

[68] Juergen Fell and Nikolai Axmacher. „The role of phase synchronization in memory processes“. In: *Nature Reviews Neuroscience* 12.2 (Feb. 2011), pp. 105–118.

[69] Rosana Nieto Ferreira, Thomas M. Rickenbach, Dirceu L. Herdies, and Leila M. V. Carvalho. „Variability of South American Convective Cloud Systems and Tropospheric Circulation during January–March 1998 and 1999“. In: *Monthly Weather Review* 131.5 (2003), pp. 961–973.

[70] Giovanni Filatrella, Arne Hejde Nielsen, and Niels Falsig Pedersen. „Analysis of a power grid using a Kuramoto-like model“. In: *The European Physical Journal B* 61.4 (2008), pp. 485–491.

[71] N.I. Fisher. *Statistical Analysis of circular data*. Cambridge University Press, 1993.

[72] Félix-Antoine Fortin, Francois-Michel De Rainville, Marc-André Gardner, Marc Parizeau, and Christian Gagné. „DEAP : Evolutionary Algorithms Made Easy“. In: *Journal of Machine Learning Research* 13 (2012), pp. 2171–2175.

[73] Kunihiko Fukushima. „Neocognitron: A self-organizing neural network model for a mechanism of pattern recognition unaffected by shift in position“. In: *Biological Cybernetics* 36.4 (1980), pp. 193–202.

[74] Dennis Gabor. „Theory of communication. Part 1: The analysis of information“. In: *Journal of the Institution of Electrical Engineers-Part III: Radio and Communication Engineering* 93.26 (1946), pp. 429–441.

[75] G. Gallavotti and V. Lucarini. „Equivalence of Non-equilibrium Ensembles and Representation of Friction in Turbulent Flows : The Lorenz 96 Model“. In: *Journal of Statistical Physics* 156 (2014), pp. 1027–1065.

[76] Vladimir Garcia-Morales and Katharina Krischer. „The complex Ginzburg–Landau equation: an introduction“. In: *Contemporary Physics* 53.2 (2012), pp. 79–95.

[77] Rene D. Garreud. „Cold Air Incursions over Subtropical South America: Mean Structure and Dynamics“. In: *Monthly Weather Review* 128.7 (2000), pp. 2544–2559.

[78] M. Ghil. „Advanced spectral methods for climatic time series“. In: *Reviews of Geophysics* 40.1 (2002), p. 1003.

[79] Ian Goodfellow, Yoshua Bengio, and Aaron Courville. *Deep Learning*. `http://www.deeplearningbook.org`. MIT Press, 2016.

[80] Celso Grebogi, Edward Ott, Steven Pelikan, and James A. Yorke. „Strange attractors that are not chaotic“. In: *Physica D: Nonlinear Phenomena* 13.1 (1984), pp. 261–268.

[81] Alice M. Grimm and Pedro L. Silva Dias. „Analysis of Tropical–Extratropical Interactions with Influence Functions of a Barotropic Model“. In: 52 (1995), pp. 3538–3555.

[82] Eldad Haber, Lars Ruthotto, Elliot Holtham, and Seong-Hwan Jun. *Learning across scales - A multiscale method for Convolution Neural Networks*. 2017.

[83] S. Hallerberg, D. Pazó, J.M. López, and M.A. Rodriguez. „Logarithmic bred vectors in spatiotemporal chaos: Structure and growth“. In: *Physical Review E - Statistical, Nonlinear, and Soft Matter Physics* 81.6 (2010), pp. 1–8.

[84] Kaiming He, Xiangyu Zhang, Shaoqing Ren, and Jian Sun. *Deep Residual Learning for Image Recognition*. 2015.

[85] J. Heitzig, J. F. Donges, Y. Zou, N. Marwan, and J. Kurths. „Node-weighted measures for complex networks with spatially embedded, sampled, or differently sized nodes“. In: *The European Physical Journal B* 85.1 (2012), pp. 1–22.

[86] Frank Hellmann, Paul Schultz, Carsten Grabow, Jobst Heitzig, and Jürgen Kurths. „Survivability of deterministic dynamical systems“. In: *Scientific reports* 6 (2016), p. 29654.

[87] Sebastian Herzog, Florentin Wörgötter, and Ulrich Parlitz. „Data-Driven Modeling and Prediction of Complex Spatio-Temporal Dynamics in Excitable Media“. In: *Frontiers in Applied Mathematics and Statistics* 4 (2018), p. 60.

[88] Marina Hirota, Milena Holmgren, Egbert H. Van Nes, and Marten Scheffer. „Global Resilience of Tropical Forest and Savanna to Critical Transitions“. In: *Science* 334.6053 (2011), pp. 232–235.

[89] Sepp Hochreiter. „The Vanishing Gradient Problem during Learning Recurrent Neural Nets and Problem Solutions“. In: *Int. J. Uncertain. Fuzziness Knowl.-Based Syst.* 6.2 (Apr. 1998), pp. 107–116.

[90] Paul F. Hoffman and Daniel P. Schrag. „The snowball Earth hypothesis: testing the limits of global change“. In: *Terra Nova* 14.3 (2002), pp. 129–155.

[91] J.D. Horel. *Complex Principal Component Analysis: Theory and Examples.* 1984.

[92] Kurt Hornik. „Approximation capabilities of multilayer feedforward networks“. In: *Neural Networks* 4.2 (1991), pp. 251–257.

[93] Guannan Hu, Tamás Bódai, and Valerio Lucarini. „Effects of stochastic parametrization on extreme value statistics“. In: *Chaos: An Interdisciplinary Journal of Nonlinear Science* 29.8 (2019), p. 083102.

[94] Charles Jones and Leila M. V. Carvalho. „Active and Break Phases in the South American Monsoon System“. In: *Journal of Climate* 15.8 (Apr. 2002), pp. 905–914.

[95] A. Karimi and M. R. Paul. „Extensive chaos in the Lorenz-96 model“. In: *Chaos: An Interdisciplinary Journal of Nonlinear Science* 20 (2010), p. 043105.

[96] D. L. van Kekem and A. E. Sterk. „Wave propagation in the Lorenz-96 model“. In: *Nonlinear Processes in Geophysics* 25.2 (2018), pp. 301–314.

[97] Dirk L. van Kekem and Alef E. Sterk. „Symmetries in the Lorenz-96 Model“. In: *International Journal of Bifurcation and Chaos* 29.01 (2019), p. 1950008.

[98] John Kerin and Hans Engler. *On the Lorenz '96 Model and Some Generalizations.* 2020.

[99] J. Kiefer and J. Wolfowitz. „Stochastic Estimation of the Maximum of a Regression Function“. In: *Ann. Math. Statist.* 23.3 (Sept. 1952), pp. 462–466.

[100] Heetae Kim, Sang Hoon Lee, and Petter Holme. „Building blocks of the basin stability of power grids“. In: *Physical Review E* 93.6 (2016), p. 062318.

[101] Diederik P. Kingma and Jimmy Ba. *Adam: A Method for Stochastic Optimization.* 2014.

[102] Joseph L Kirschvink. „Late Proterozoic low-latitude global glaciation: the snowball Earth“. In: (1992).

[103] Aneta Koseska, Evgeny Volkov, and Jürgen Kurths. „Oscillation quenching mechanisms: Amplitude vs. oscillation death“. In: *Physics Reports* 531.4 (2013). Oscillation quenching mechanisms: Amplitude vs. oscillation death, pp. 173–199.

[104] Hans-Peter Kriegel, Peer Kröger, Jörg Sander, and Arthur Zimek. „Density-based clustering“. In: *WIREs Data Mining Knowl Discov* 1 (2011), pp. 231–240.

[105] Elmar Kriegler, Jim W Hall, Hermann Held, Richard Dawson, and Hans Joachim Schellnhuber. „Imprecise probability assessment of tipping points in the climate system“. In: *Proc. Natl. Acad. Sci.* 106.13 (2009), pp. 5041–5046.

[106] Yoshiki Kuramoto. „Diffusion-Induced Chaos in Reaction Systems“. In: *Progress of Theoretical Physics Supplement* 64 (Feb. 1978), pp. 346–367.

[107] Yoshiki Kuramoto. „Self-entrainment of a population of coupled non-linear oscillators“. In: *International Symposium on Mathematical Problems in Theoretical Physics*. Ed. by Huzihiro Araki. Berlin, Heidelberg: Springer Berlin Heidelberg, 1975, pp. 420–422.

[108] L. D. Landau. „On the problem of turbulence“. In: *Doklady Akademii Nauk SSSR* (1944), 44: 339–342.

[109] N. Le Carrer and P. L. Green. „A possibilistic interpretation of ensemble forecasts: experiments on the imperfect Lorenz 96 system“. In: *Advances in Science and Research* 17 (2020), pp. 39–45.

[110] J. D. Lenters and K. H. Cook. „Summertime Precipitation Variability over South America: Role of the Large-Scale Circulation“. In: *Monthly Weather Review* 127.3 (1999), pp. 409–431.

[111] Timothy M Lenton, Johan Rockström, Owen Gaffney, Stefan Rahmstorf, Katherine Richardson, Will Steffen, and Hans Joachim Schellnhuber. *Climate tipping points—too risky to bet against*. 2019.

[112] Timothy M Lenton and Hywel TP Williams. „On the origin of planetary-scale tipping points“. In: *Trends Ecol. Evol.* 28.7 (2013), pp. 380–382.

[113] Timothy M. Lenton, Hermann Held, Elmar Kriegler, Jim W. Hall, Wolfgang Lucht, Stefan Rahmstorf, and Hans Joachim Schellnhuber. „Tipping elements in the Earth's climate system“. In: *Proceedings of the National Academy of Sciences* 105.6 (2008), pp. 1786–1793.

[114] Brant Liebmann, George N. Kiladis, Carolina S. Vera, A. Celeste Saulo, and Leila M V Carvalho. „Subseasonal variations of rainfall in South America in the vicinity of the low-level jet east of the Andes and comparison to those in the South Atlantic convergence zone“. In: *Journal of Climate* 17.19 (2004), pp. 3829–3842.

[115] Michael Lindner and Frank Hellmann. „Stochastic basins of attraction and generalized committor functions“. In: *Phys. Rev. E* 100 (2 Aug. 2019), p. 022124.

[116] Seppo Linnainmaa. „Taylor expansion of the accumulated rounding error“. In: *BIT Numerical Mathematics* 16.2 (1976), pp. 146–160.

[117] S. Lloyd. „Least squares quantization in PCM“. In: *IEEE Transactions on Information Theory* 28.2 (1982), pp. 129–137.

[118] Edward N. Lorenz. „Designing Chaotic Models“. In: *Journal of the Atmospheric Sciences* 62.5 (May 2005), pp. 1574–1587.

[119] Edward N. Lorenz. „Deterministic Nonperiodic Flow“. In: *Journal of the Atmospheric Sciences* 20.2 (Mar. 1963), pp. 130–141.

[120] Edward N. Lorenz. „Predictability: a problem partly solved“. In: *Seminar on Predictability, 4-8 September 1995*. Vol. 1. ECMWF. Shinfield Park, Reading: ECMWF, 1995, pp. 1–18.

[121] Edward N. Lorenz. „The physical bases of climate and climate modelling. Climate predictability“. In: *GARP Publication Series*. WMO, 1975, pp. 132–136.

[122] Edward N. Lorenz. „The predictability of a flow which possesses many scales of motion“. In: *Tellus* 21.3 (1969), pp. 289–307.

[123] Ilya Loshchilov and Frank Hutter. *Decoupled Weight Decay Regularization*. 2017.

[124] Jürgen Hedderich Lothar Sachs. *Angewandte Statistik*. 13th. Berlin, Heidelberg: Springer Verlag, 2009.

[125] V. Lucarini and S. Sarno. „A statistical mechanical approach for the computation of the climatic response to general forcings“. In: *Nonlinear Processes in Geophysics* 18.1 (2011), pp. 7–28.

[126] Valerio Lucarini. „Stochastic Perturbations to Dynamical Systems: A Response Theory Approach“. In: *Journal of Statistical Physics* 146.4 (2012), pp. 774–786.

[127] Valerio Lucarini and Tamás Bódai. „Global stability properties of the climate: Melancholia states, invariant measures, and phase transitions“. In: *Nonlinearity* 33.9 (June 2020), R59–R92.

[128] Valerio Lucarini and Tamás Bódai. „Transitions across Melancholia States in a Climate Model: Reconciling the Deterministic and Stochastic Points of View“. In: *Phys. Rev. Lett.* 122 (15 Apr. 2019), p. 158701.

[129] Valerio Lucarini and Andrey Gritsun. „A new mathematical framework for atmospheric blocking events“. In: *Climate Dynamics* 54.1 (Jan. 2020), pp. 575–598.

[130] William W. Lytton. „Computer modelling of epilepsy“. In: *Nature Reviews Neuroscience* 6 (2008).

[131] Jan Machowski, Janusz Bialek, and Jim Bumby. *Power System Dynamics: Stability and Control, 2nd Edition*. Wiley, 2008.

[132] Nishant Malik, Bodo Bookhagen, Norbert Marwan, and Jürgen Kurths. „Analysis of spatial and temporal extreme monsoonal rainfall over South Asia using complex networks“. In: *Climate Dynamics* 39.3 (2012), pp. 971–987.

[133] Debsankha Manik, Martin Rohden, Henrik Ronellenfitsch, Xiaozhu Zhang, Sarah Hallerberg, Dirk Witthaut, and Marc Timme. „Network susceptibilities: Theory and applications“. In: *Physical Review E* 95.1 (2017), p. 012319.

[134] D Maraun and J Kurths. „Epochs of phase coherence between El Nino/Southern Oscillation and Indian monsoon“. In: *Geophysical Research Letters* 32 (2005), pp. 2–6.

[135] J. A. Marengo et al. „Recent developments on the South American monsoon system“. In: *International Journal of Climatology* 32.1 (2012), pp. 1–21.

[136] Jose A. Marengo, Michael W. Douglas, and Pedro L. Silva Dias. „The South American low-level jet east of the Andes during the 1999 LBA-TRMM and LBA-WET AMC campaign“. In: *Journal of Geophysical Research: Atmospheres* 107.D20 (2002). 8079, LBA 47-1–LBA 47-11.

[137] Jose A. Marengo, Wagner R. Soares, Celeste Saulo, and Matilde Nicolini. „Climatology of the Low-Level Jet East of the Andes as Derived from the NCEP–NCAR Reanalyses: Characteristics and Temporal Variability“. In: *Journal of Climate* 17.12 (2004), pp. 2261–2280.

[138] Jose A. Marengo, Wagner R. Soares, Celeste Saulo, and Matilde Nicolini. „Climatology of the low-level jet east of the Andes as derived from the NCEP-NCAR reanalyses: Characteristics and temporal variability“. In: *Journal of Climate* 17.12 (2004), pp. 2261–2280.

[139] John Marshall and Franco Molteni. „Toward a Dynamical Understanding of Planetary-Scale Flow Regimes“. In: *Journal of the Atmospheric Sciences* 50.12 (June 1993), pp. 1792–1818.

[140] Robert M. May. „Thresholds and breakpoints in ecosystems with a multiplicity of stable states“. In: *Nature* 269.5628 (1977), pp. 471–477.

[141] Peter J Menck, Jobst Heitzig, Jürgen Kurths, and Hans Joachim Schellnhuber. „How dead ends undermine power grid stability“. In: *Nature communications* 5 (2014), p. 3969.

[142] Jun Meng, Jingfang Fan, Josef Ludescher, Ankit Agarwal, Xiaosong Chen, Armin Bunde, Jürgen Kurths, and Hans Joachim Schellnhuber. „Complexity-based approach for El Niño magnitude forecasting before the spring predictability barrier“. In: *Proceedings of the National Academy of Sciences* 117.1 (2020), pp. 177–183.

[143] Nora Molkenthin, Kira Rehfeld, Norbert Marwan, and Jürgen Kurths. „Networks from Flows - From Dynamics to Topology“. In: *Scientific Reports* 4 (Feb. 2014).

[144] Adilson E Motter, Seth A Myers, Marian Anghel, and Takashi Nishikawa. „Spontaneous synchrony in power-grid networks“. In: *Nature Physics* 9.3 (2013), p. 191.

[145] Adilson E. Motter and David K. Campbell. „Chaos at fifty“. In: *Physics Today* 66.5 (May 2013), pp. 27–33.

[146] J. D. Murray. *Mathematical Biology: I. An Introduction, Third Edition*. Springer, 2002.

[147] Alan C. Newell and J. A. Whitehead. „Finite bandwidth, finite amplitude convection“. In: *Journal of Fluid Mechanics* 38.2 (1969), pp. 279–303.

[148] M. Newman. *Networks: An Introduction*. OUP Oxford, 2010.

[149] Gregoire Nicolis and Catherine Nicolis. *Foundations of Complex Systems: Nonlinear Dynamics, Statistical Physics, Information and Prediction*. World Scientific, 2007.

[150] Rosana Nieto-Ferreira and Thomas M. Rickenbach. „Regionality of monsoon onset in South America: A three-stage conceptual model“. In: *International Journal of Climatology* 31.9 (2011), pp. 1309–1321.

[151] Rosana Nieto-Ferreira, Thomas M. Rickenbach, and Emily A. Wright. „The role of cold fronts in the onset of the monsoon season in the South Atlantic convergence zone.“ In: *Quarterly Journal of the Royal Meteorological Society* 137 (2001), pp. 908–922.

[152] Julia Nogues-Paegle and Kingtse C. Mo. „Alternating Wet and Dry Conditions over South America during Summer“. In: *Monthly Weather Review* 125 (1997), pp. 279–291.

[153] D. Orrell. „Model Error and Predictability over Different Timescales in the Lorenz '96 Systems“. In: *Journal of the Atmospheric Sciences* 60.17 (2003), pp. 2219–2228.

[154] D. Orrell and L.A. Smith. „Visualising bifurcations in high dimensional systems: The spectral bifurcation diagram“. In: *International Journal of Bifurcation and Chaos* 13.10 (2003), pp. 3015–3027.

[155] Grigory V Osipov, Bambi Hu, Changsong Zhou, and Mikhail V Ivanchenko. „Three Types of Transitions to Phase Synchronization in Coupled Chaotic Oscillators“. In: *Physical Review Letters* 16.JULY (2003), pp. 1–4.

[156] E. Ott. *Chaos in Dynamical Systems*. Cambridge, England: Cambridge University Press, 1993.

[157] Edward Ott. *Chaos in Dynamical Systems*. Cambridge University Press, 1993.

[158] Julia N. Paegle, Lee A. Byerle, and Kingtse C. Mo. „Intraseasonal Modulation of South American Summer Precipitation“. In: *Monthly Weather Review* 128.3 (2000), pp. 837–850.

[159] Shaowu Pan and Karthik Duraisamy. „Long-Time Predictive Modeling of Nonlinear Dynamical Systems Using Neural Networks“. In: *Complexity* 2018 (Dec. 2018), p. 4801012.

[160] Jaideep Pathak, Brian Hunt, Michelle Girvan, Zhixin Lu, and Edward Ott. „Model-Free Prediction of Large Spatiotemporally Chaotic Systems from Data: A Reservoir Computing Approach“. In: *Phys. Rev. Lett.* 120 (2 Jan. 2018), p. 024102.

[161] Jaideep Pathak, Alexander Wikner, Rebeckah Fussell, Sarthak Chandra, Brian R. Hunt, Michelle Girvan, and Edward Ott. „Hybrid forecasting of chaotic processes: Using machine learning in conjunction with a knowledge-based model“. In: *Chaos: An Interdisciplinary Journal of Nonlinear Science* 28.4 (2018), p. 041101.

[162] Diego Pazó, Ivan G. Szendro, Juan M. López, and Miguel A. Rodriguez. „Structure of characteristic Lyapunov vectors in spatiotemporal chaos“. In: *Phys. Rev. E* 78 (1 June 2008), p. 016209.

[163] Arkady Pikovsky, Jurgen Kurths, Michael Rosenblum, and Jürgen Kurths. *Synchronization: a universal concept in nonlinear sciences*. Vol. 12. Cambridge university press, 2003.

[164] Lev Semenovich Pontryagin, V G Boltyanskii, R V Gamkrelidze, and E F Mishchenko. *The mathematical theory of optimal processes*. Wiley, 1962.

[165] Christopher Rackauckas, Yingbo Ma, Julius Martensen, Collin Warner, Kirill Zubov, Rohit Supekar, Dominic Skinner, Ali Ramadhan, and Alan Edelman. *Universal Differential Equations for Scientific Machine Learning*. 2020.

[166] Maziar Raissi, Paris Perdikaris, and George Em Karniadakis. *Physics Informed Deep Learning (Part I): Data-driven Solutions of Nonlinear Partial Differential Equations*. 2017.

[167] M. Rajeevan, Sulochana Gadgil, and Jyoti Bhate. „Active and break spells of the Indian summer monsoon“. In: *Journal of Earth System Science* 119.3 (2010), pp. 229–247.

[168] Sarbendu Rakshit, Bidesh K. Bera, Matjaz Perc, and Dibakar Ghosh. „Basin stability for chimera states“. In: *Scientific Reports* 7.1 (2017), p. 2412.

[169] Prajit Ramachandran, Barret Zoph, and Quoc V. Le. *Searching for Activation Functions*. 2017.

[170] K. Ramamurthy. „Monsoon of India: Some aspects of the 'break' in the Indian southwest monsoon during July and August“. In: *Forecasting Manual 1-57 No. IV 18.3, India Met. Dept.* (1969).

[171] Markus Reichstein, Gustau Camps-Valls, Bjorn Stevens, Martin Jung, Joachim Denzler, Nuno Carvalhais, and Prabhat. „Deep learning and process understanding for data-driven Earth system science“. In: *Nature* 566.7743 (2019), pp. 195–204.

[172] A. Rheinwalt, N. Marwan, J. Kurths, P. Werner, and F.-W. Gerstengarbe. „Boundary effects in network measures of spatially embedded networks“. In: *EPL (Europhysics Letters)* 100 (Oct. 2012), p. 28002.

[173] Aljosha Rheinwalt, Bedartha Goswami, Niklas Boers, Jobst Heitzig, Norbert Marwan, R. Krishnan, and Jürgen Kurths. „Teleconnections in Climate Networks: A Network-of-Networks Approach to Investigate the Influence of Sea Surface Temperature Variability on Monsoon Systems“. In: *Machine Learning and Data Mining Approaches to Climate Science*. Ed. by Valliappa Lakshmanan, Eric Gilleland, Amy McGovern, and Martin Tingley. Springer, 2015, pp. 23–33.

[174] Michele M. Rienecker et al. „MERRA: NASA's modern-era retrospective analysis for research and applications“. In: *Journal of Climate* 24.14 (2011), pp. 3624–3648.

[175] N. Rochester, J. Holland, L. Haibt, and W. Duda. „Tests on a cell assembly theory of the action of the brain, using a large digital computer“. In: *IRE Transactions on Information Theory* 2.3 (1956), pp. 80–93.

[176] Francisco A Rodrigues, Thomas K DM Peron, Peng Ji, and Jürgen Kurths. „The Kuramoto model in complex networks“. In: *Physics Reports* 610 (2016), pp. 1–98.

[177] Víctor Rodríguez-Méndez, Víctor M. Eguíluz, Emilio Hernández-García, and José J. Ramasco. „Percolation-based precursors of transitions in extended systems“. In: *Scientific Reports* 6 (July 2016).

[178] M. J. Rodwell and B. J. Hoskins. „Subtropical Anticyclones and Summer Monsoons“. In: *Journal of Climate* 14.15 (2001), pp. 3192–3211.

[179] Martin Rohden, Andreas Sorge, Dirk Witthaut, and Marc Timme. „Impact of network topology on synchrony of oscillatory power grids“. In: *Chaos: An Interdisciplinary Journal of Nonlinear Science* 24.1 (2014), p. 013123.

[180] Chester F Ropelewski and Michael S Halpert. „Global and regional scale precipitation patterns associated with the El Niño/Southern Oscillation“. In: *Monthly weather review* 115.8 (1987), pp. 1606–1626.

[181] F. Rosenblatt. „The perceptron: A probabilistic model for information storage and organization in the brain“. In: *Psychological Review* 65.6 (1958).

[182] M G Rosenblum, a S Pikovsky, and J Kurths. „Phase synchronization of chaotic oscillators“. In: *Physical Review Letters* 76.11 (1996), pp. 1804–1807.

[183] David Ruelle. „A review of linear response theory for general differentiable dynamical systems“. In: *Nonlinearity* 22.4 (2009), p. 855.

[184] David Ruelle. „Differentiation of SRB states“. In: *Communications in Mathematical Physics* 187.1 (1997), pp. 227–241.

[185] David E. Rumelhart, Geoffrey E. Hinton, and Ronald J. Williams. „Learning representations by back-propagating errors“. In: *Nature* 323.6088 (1986), pp. 533–536.

[186] Lars Ruthotto and Eldad Haber. *Deep Neural Networks Motivated by Partial Differential Equations*. 2018.

[187] Murry L. Salby. *Physics of the Atmosphere and Climate*. 2nd. Cambridge: Cambridge University Press, 2012.

[188] P. Salio, M. Nicolini, and A. C. Saulo. „Chaco low-level jet events characterization during the austral summer season“. In: *Journal of Geophysical Research: Atmospheres* 107.D24 (2002). 4816, ACL 32-1–ACL 32-17.

[189] Paola Salio and Matilde Nicolini. „Seasonal Characterization of the Diurnal Cycle of Convection Frequency over South America under Different Low-Jet Conditions“. In: *Proceedings of 8 ICSHMO*. 2006, pp. 1157–1162.

[190] K. Sathiyadevi, V. K. Chandrasekar, and D. V. Senthilkumar. „Stable amplitude chimera in a network of coupled Stuart-Landau oscillators“. In: *Phys. Rev. E* 98 (3 Sept. 2018), p. 032301.

[191] A. Celeste Saulo, Marcelo E. Seluchi, and Matilde Nicolini. „A Case Study of a Chaco Low-Level Jet Event“. In: *Monthly Weather Review* 132.11 (2004), pp. 2669–2683.

[192] Garima Saxena, Awadhesh Prasad, and Ram Ramaswamy. „Amplitude death: The emergence of stationarity in coupled nonlinear systems“. In: *Physics Reports* 521.5 (2012). Amplitude Death: The Emergence of Stationarity in Coupled Nonlinear Systems, pp. 205–228.

[193] Benjamin Schäfer, Moritz Matthiae, Xiaozhu Zhang, Martin Rohden, Marc Timme, and Dirk Witthaut. „Escape routes, weak links, and desynchronization in fluctuation-driven networks“. In: *Physical Review E* 95.6 (2017), p. 060203.

[194] Hans Joachim Schellnhuber, Stefan Rahmstorf, and Ricarda Winkelmann. „Why the right climate target was agreed in Paris“. In: *Nat. Clim. Change* 6.7 (2016), p. 649.

[195] S. Scher. „Toward Data-Driven Weather and Climate Forecasting: Approximating a Simple General Circulation Model With Deep Learning“. In: *Geophysical Research Letters* 45.22 (2018), pp. 12, 616–12, 622.

[196] Katrin Schmietendorf, Joachim Peinke, and Oliver Kamps. „The impact of turbulent renewable energy production on power grid stability and quality“. In: *The European Physical Journal B* 90.11 (2017), p. 222.

[197] Alfons Schnitzler and Joachim Gross. „Normal and pathological oscillatory communication in the brain“. In: *Nature Reviews Neuroscience* 6.4 (Apr. 2005), pp. 285–296.

[198] Thomas Schreiber and Andreas Schmitz. „Improved surrogate data for nonlinearity tests“. In: *Physical Review Letters* 77.4 (1996), pp. 635–638.

[199] Paul Schultz, Jobst Heitzig, and Jürgen Kurths. „Detours around basin stability in power networks“. In: *New Journal of Physics* 16.12 (2014), p. 125001.

[200] Jean-Luc Schwartz, Nicolas Grimault, Jean-Michel Hupé, Brian C. J. Moore, and Daniel Pressnitzer. „Multistability in perception: binding sensory modalities, an overview“. In: *Philosophical Transactions of the Royal Society B: Biological Sciences* 367.1591 (2012), pp. 896–905.

[201] William D. Sellers. „A Global Climatic Model Based on the Energy Balance of the Earth-Atmosphere System“. In: *Journal of Applied Meteorology* 8.3 (June 1969), pp. 392–400.

[202] Enrico Ser-Giacomi, Vincent Rossi, Cristóbal López, and Emilio Hernández-García. „Flow networks: A characterization of geophysical fluid transport“. In: *Chaos: An Interdisciplinary Journal of Nonlinear Science* 25.3 (2015), p. 036404.

[203] Enrico Ser-Giacomi, Ruggero Vasile, Irene Recuerda, Emilio Hernández-García, and Cristóbal López. „Dominant transport pathways in an atmospheric blocking event“. In: *Chaos: An Interdisciplinary Journal of Nonlinear Science* 25.8 (2015), p. 087413.

[204] Yurdanur Sezginer Unal and Michael Ghil. „Interannual and interdecadal oscillation patterns in sea level“. In: *Climate Dynamics* 11.5 (1995), pp. 255–278.

[205] P.R. Shukla et al. *IPCC, 2019: Climate Change and Land: an IPCC special report on climate change, desertification, land degradation, sustainable land management, food security, and greenhouse gas fluxes in terrestrial ecosystems*. 2019.

[206] G. A. M. Silva and T. Ambrizzi. *Inter-El Niño variability and its impact on the South American low-level jet east of the Andes during austral summer - two case studies*. Feb. 2006.

[207] G. A. M. Silva, T. Ambrizzi, and J. A. Marengo. „Observational evidences on the modulation of the South American Low Level Jet east of the Andes according the ENSO variability“. In: *Annales Geophysicae* 27.2 (2009), pp. 645–657.

[208] David Silver et al. „Mastering the game of Go with deep neural networks and tree search“. In: *Nature* 529.7587 (2016), pp. 484–489.

[209] Jose Ricardo Siqueira and Luiz Augusto Toledo Machado. „Influence of the Frontal Systems on the Day-to-Day Convection Variability over South America“. In: *Journal of Climate* 17.9 (2004), pp. 1754–1766.

[210] Jose Ricardo Siqueira, William B. Rossow, Luiz Augusto Toledo Machado, and Cindy Pearl. „Structural Characteristics of Convective Systems over South America Related to Cold-Frontal Incursions“. In: *Monthly Weather Review* 133.5 (2005), pp. 1045–1064.

[211] G. I. Sivashinsky. „Nonlinear analysis of hydrodynamic instability in laminar flames—I. Derivation of basic equations“. In: *Acta Astronautica* 4.11 (Jan. 1977), pp. 1177–1206.

[212] P. Smole, D.A. Baxter, and J.H. Byrne. „Mathematical Modeling of Gene Networks“. In: *Neuron* 26 (2000), pp. 567–580.

[213] Casper Kaae Sønderby, Lasse Espeholt, Jonathan Heek, Mostafa Dehghani, Avital Oliver, Tim Salimans, Shreya Agrawal, Jason Hickey, and Nal Kalchbrenner. *MetNet: A Neural Weather Model for Precipitation Forecasting*. 2020.

[214] Will Steffen, Johan Rockström, Katherine Richardson, Timothy M Lenton, Carl Folke, Diana Liverman, Colin P Summerhayes, Anthony D Barnosky, Sarah E Cornell, Michel Crucifix, et al. „Trajectories of the Earth System in the Anthropocene“. In: *Proc. Natl. Acad. Sci.* 115.33 (2018), pp. 8252–8259.

[215] A. E. Sterk and D. L. van Kekem. „Predictability of Extreme Waves in the Lorenz-96 Model Near Intermittency and Quasi-Periodicity“. In: *Complexity* 2017 (2017), p. 9419024.

[216] Veronika Stolbova, Elena Surovyatkina, Bodo Bookhagen, and Jürgen Kurths. „Tipping elements of the Indian monsoon: Prediction of onset and withdrawal“. In: *Geophysical Research Letters* 43.8 (2016), pp. 3982–3990.

[217] Hans Von Storch and Francis W Zwiers. „Statistical Analysis in Climate Research“. In: *Journal of the American Statistical Association* 95 (1999), p. 1375.

[218] Steven H. Strogatz. *Nonlinear Dynamics and Chaos. With Applications to Physics, Biology, Chemistry, and Engineering*. Westview, 2015.

[219] J. T. Stuart. „On the non-linear mechanics of wave disturbances in stable and unstable parallel flows Part 1. The basic behaviour in plane Poiseuille flow“. In: *Journal of Fluid Mechanics* 9.3 (1960), pp. 353–370.

[220] J. Swift and P. C. Hohenberg. „Hydrodynamic fluctuations at the convective instability“. In: *Phys. Rev. A* 15 (1 Jan. 1977), pp. 319–328.

[221] M. Thiel, M.C. Romano, Jürgen Kurths, M. Rolfs, and R. Kliegl. „Twin Surrogates to Test for Complex Synchronisation“. In: *Europhysics Letters* 75 (2006).

[222] Ch. Tsitouras. „Runge-Kutta Pairs of Order 5(4) Satisfying Only the First Column Simplifying Assumption“. In: *Comput. Math. Appl.* 62.2 (July 2011), pp. 770–775.

[223] A.A. Tsonis and P.J. Roebber. „The architecture of the climate network“. In: *Physica A: Statistical Mechanics and its Applications* 333 (2004), pp. 497–504.

[224] Anastasios A. Tsonis and Kyle L. Swanson. „Topology and Predictability of El Niño and La Niña Networks“. In: *Phys. Rev. Lett.* 100 (22 June 2008), p. 228502.

[225] Anastasios A. Tsonis, Kyle L. Swanson, and Paul J. Roebber. „What Do Networks Have to Do with Climate?“ In: *Bulletin of the American Meteorological Society* 87.5 (2006), pp. 585–595.

[226] Liubov Tupikina, Nora Molkenthin, Cristóbal López, Emilio Hernández-García, Norbert Marwan, and Jürgen Kurths. „Correlation Networks from Flows. The Case of Forced and Time-Dependent Advection-Diffusion Dynamics“. In: *PLOS ONE* 11.4 (Apr. 2016), pp. 1–12.

[227] Dirk L. van Kekem and Alef E. Sterk. „Travelling waves and their bifurcations in the Lorenz-96 model“. In: *Physica D: Nonlinear Phenomena* 367 (2018), pp. 38–60.

[228] R Vautard and Michael Ghil. „Singular spectrum analysis in nonlinear dynamics, with applications to paleoclimatic time series“. In: *Physica D: Nonlinear Phenomena* 35.3 (1989), pp. 395–424.

[229] Robert Vautard, Pascal Yiou, and Michael Ghil. „Singular-spectrum analysis: A toolkit for short, noisy chaotic signals“. In: *Physica D: Nonlinear Phenomena* 58.1 (1992), pp. 95–126.

[230] C. Vera et al. „The South American Low-Level Jet Experiment“. In: *Bulletin of the American Meteorological Society* 87.1 (2006), pp. 63–77.

[231] Carolina Vera et al. „Toward a unified view of the American monsoon systems“. In: *Journal of Climate* 19.20 (2006), pp. 4977–5000.

[232] Jan Viebahn and Henk A. Dijkstra. „Critical Transition Analysis of the Deterministic Wind-Driven Ocean Circulation — A Flux-Based Network Approach“. In: *International Journal of Bifurcation and Chaos* 24.02 (2014), p. 1430007.

[233] G. Vissio. „Statistical mechanical methods for parametrization in geophysical fluid dynamics“. In: *Reports on Earth System Science* 212 (2018).

[234] G. Vissio and V. Lucarini. „A proof of concept for scale-adaptive parametrizations: the case of the Lorenz '96 model“. In: *Quarterly Journal of the Royal Meteorological Society* 144 (2018), pp. 63–75.

[235] Vissio, Gabriele and Lucarini, Valerio. „Mechanics and thermodynamics of a new minimal model of the atmosphere“. In: *Eur. Phys. J. Plus* 135.10 (2020), p. 807.

[236] Athanasios Voulodimos, Nikolaos Doulamis, Anastasios Doulamis, and Eftychios Protopapadakis. „Deep Learning for Computer Vision: A Brief Review“. In: *Computational Intelligence and Neuroscience* 2018 (Feb. 2018), p. 7068349.

[237] Yi-Hui Wang, Gudrun Magnusdottir, Hal Stern, Xu Tian, and Yaming Yu. „Uncertainty Estimates of the EOF-Derived North Atlantic Oscillation“. In: *Journal of Climate* 27.3 (Jan. 2014), pp. 1290–1301.

[238] J. Watson. „On the non-linear mechanics of wave disturbances in stable and unstable parallel flows Part 2. The development of a solution for plane Poiseuille flow and for plane Couette flow“. In: *Journal of Fluid Mechanics* 9.3 (1960), pp. 371–389.

[239] Duncan J. Watts and Steven H. Strogatz. „Collective dynamics of 'small-world' networks“. In: *Nature* 393 (1998), p. 440.

[240] P. J. Webster, V. O. Magaña, T. N. Palmer, J. Shukla, R. A. Tomas, M. Yanai, and T. Yasunari. „Monsoons: Processes, predictability, and the prospects for prediction“. In: *Journal of Geophysical Research: Oceans (1978–2012)* 103.C7 (June 1998), pp. 14451–14510.

[241] E Weinan. „A Proposal on Machine Learning via Dynamical Systems“. In: *Communications in Mathematics and Statistics* 5.1 (2017), pp. 1–11.

[242] P.J. Werbos. *Beyond Regression: New Tools for Prediction and Analysis in the Behavioral Sciences*. Harvard University, 1975.

[243] Marc Wiedermann, Alexander Radebach, Jonathan F. Donges, Jürgen Kurths, and Reik V. Donner. „A climate network-based index to discriminate different types of El Niño and La Niña“. In: *Geophysical Research Letters* 43.13 (2016). 2016GL069119, pp. 7176–7185.

[244] Alexander Wikner, Jaideep Pathak, Brian Hunt, Michelle Girvan, Troy Arcomano, Istvan Szunyogh, Andrew Pomerance, and Edward Ott. „Combining machine learning with knowledge-based modeling for scalable forecasting and subgrid-scale closure of large, complex, spatiotemporal systems“. In: *Chaos: An Interdisciplinary Journal of Nonlinear Science* 30.5 (2020), p. 053111.

[245] D. S. Wilks. „Comparison of ensemble-MOS methods in the Lorenz '96 setting“. In: *Meteorological Applications* 13.3 (2006), pp. 243–256.

[246] D.S. Wilks. „Effects of stochastic parametrizations in the Lorenz '96 system“. In: *Quarterly Journal of the Royal Meteorological Society* 131.606 (2005), pp. 389–407.

[247] Klaus Wolter and Michael S. Timlin. „El Niño/Southern Oscillation behaviour since 1871 as diagnosed in an extended multivariate ENSO index (MEI.ext)“. In: *International Journal of Climatology* 31.7 (2011), pp. 1074–1087.

[248] Zhaohua Wu, Norden E Huang, and Biospheric Processes. „Ensemble Empirical Mode Decomposition: A Noise Assisted Data Analysis Method“. In: *Advances in Adaptive Data Analysis* 1.1 (2009).

[249] Nico Wunderling, F. Jonathan Donges, Jürgen Kurths, and Ricarda Winkelmann. „Interacting tipping elements increase risk of climate domino effects under global warming“. In: *Earth Syst. Dynam. Disc. (Preprint doi: 10.5194/esd-2020-18)* (2020).

[250] K. Yamasaki, A. Gozolchiani, and S. Havlin. „Climate Networks around the Globe are Significantly Affected by El Niño“. In: *Phys. Rev. Lett.* 100 (22 June 2008), p. 228501.

[251] Chidong Zhang. „Madden-Julian Oscillation“. In: *Reviews of Geophysics* 43.2 (2005).

[252] Fuqing Zhang, Y. Qiang Sun, Linus Magnusson, Roberto Buizza, Shian-Jiann Lin, Jan-Huey Chen, and Kerry Emanuel. „What Is the Predictability Limit of Midlatitude Weather?“ In: *Journal of the Atmospheric Sciences* 76.4 (Apr. 2019), pp. 1077–1091.

[253] Dong Zhou, Avi Gozolchiani, Yosef Ashkenazy, and Shlomo Havlin. „Teleconnection Paths via Climate Network Direct Link Detection“. In: *Physical Review Letters* 115.26 (2015).

[254] Jiayu Zhou and K-M. Lau. „Does a Monsoon Climate Exist over South America?“ In: *Journal of Climate* 11.5 (1998), pp. 1020–1040.